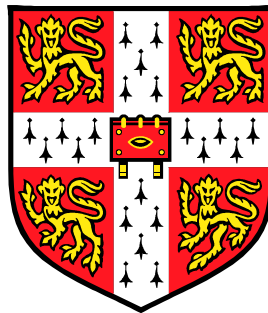


# Development of (RE)BaCuO Coated Conductors by Liquid Phase Epitaxy

*Yee Siau Cheng*

Emmanuel College  
Cambridge



A dissertation submitted for the degree of  
Doctor of Philosophy at the University of Cambridge

January 2002

致給：  
敬愛的父母及姐姐

## Preface

I declare that, except where otherwise stated, this dissertation is the result of my own work carried out in the Department of Materials Science and Metallurgy, University of Cambridge, and includes nothing that is the outcome of work done in collaboration. No part of this dissertation has been submitted at Cambridge or any other university for a degree, diploma, or other qualification. Except where reference is made, the work described is original. This dissertation does not exceed 60,000 words.

Y.S. Cheng

January 2002

## Acknowledgements

There are a lot of people whom I would like to thank, but first and foremost, I would like to thank Prof Jan Evetts for his supervision, guidance, patience, and support throughout the years.

I am extremely grateful to Dr Ahmed Kuršumović for his advice and insight on this project, as well as teaching me some of his remarkable all-round skills. A big thank you is owed to Dr Rumun Tomov for providing me with endless supplies of PLD samples.

Thanks are extended to Dr Bartek Glowacki for all the arrangements at the *IRC in Superconductivity*; to Mr Eric Robinson for his technical assistance at the *IRC*; to Dr Mary Vickers, Dr Annette Bramley & Mr Andrew Moss, for their help with XRD; to Dr Peter Berghuis, Dr John Durrell & Mr Ashish Garg for their help with the AFM; to Dr Bernhard Zeimetz for his help with the resistive  $T_c$  probe; to Dr Frank Kahlmann, Mr James Ransley & Mr David Ansell for their help with the inductive  $T_c$  probe at the *IRC*; to Mrs Karen Butler for her help with SEM EDX; to Frank & Dr Ed Tarte for the YBCO seeded SrTiO<sub>3</sub>; to Dr Zoe Barber for all her support; to Dr Gavin Burnell & Dr Dae-Joon Kang for their assistance and patience on all my computer-related problems; and to John, Ashish, Dr Veni Madhav Adyam & Mr Aldo Faisal for proof reading this dissertation.

For a lot of excellent data, I am indebted to Dr Alexander Vostner, Dr Susi Tönies, Dr Yunfeng Sun, and Prof Harald Weber at ATI in Vienna, Austria for the transport measurements; to Dr Ausanio Tuissi & Dr Elena Villa of CNR-TEMPE in Italy for the Ni-based metallic tapes; to Mr Sibe Mennema (now in this group) & Prof Henny Zandbergen at Delft University of Technology in the Netherlands for the TEM/HREM work; and to Dr Xiaoding Qi & Dr Judith MacManus-Driscoll at Imperial College in London for the ICP-AES measurements.

I would like to express my gratitude towards the *George & Lilian Schiff Foundation*, the *Overseas Research Students Award*, and the *Cambridge Commonwealth Trust* for financial support. I am also very grateful to the *Cambridge Philosophical Society* and *Emmanuel College* for assistance towards the cost of attending the *ISTEC-MRS Superconductivity Workshop* in Honolulu, as well as support for my final few months in Cambridge.

A very, very special thank to Dr Graeme M.C. Lee at DalTech, Halifax, Canada, without him, I would not be here.

Throughout the years in Cambridge I have made a lot of friends who have spiced up the social scene. I especially enjoyed the company of Adnan & Ashish for the countless number of *kebab* or *Kadhai chicken* nights with our home-made wines and all the fruitful discussions (sometimes) and fierce debates (normally useless). Special thanks to Ashish for being my "bridge" to the Indian community (hence Indian food!) in Cambridge and teaching me some

"wonderful" Hindi phrases, *dhanyavad!* Kind hospitality (i.e. food & drinks!) from Sandipon & Sonia, Mahesh & Pallavi, and Ashesha are much appreciated. The influence of Indian community has also forced me to learn the "mysterious" game of cricket, and thanks to Ashish, Adnan, Jakka, Mahesh, Pallavi, and Sandipon, I can now follow cricket games (and their passionate conversations) smoothly. Various parties with housemates at Park Lodge and Parkside (especially Aldo, Bill, Curtis, Ludwig, Peng Peng, and Sushmita (a.k.a. *Ullu*)) are memorable. I also treasure the endless support and encouragement from friends abroad, especially Li Na (who is always like a sister to me), Rasha (together with Mohammed & little Haneen), Woon S.J. & Brian Sahely (who share similar views on many world issues), and my "brothers" – especially Ee Khoon, Kok Leong, and Chon Keat.

The atmosphere in the lab would not be the same without people like (in no particular order) Ashish *the F-BMG*, Adnan *Royale Latifa*, José *Gandu* Prieto, Debbie *Spaghetina* Morecroft, Brian *Black-hole* Pang, *Old-man* Ru-men (with his words of "encouragement" for delivering "mega-amps" conductors), and Mikee *Lobster-boy* Hogg, as well as those without "colourful" nicknames: Robert Hadfield, Rachel Speaks, Vassilka Tsaneva (*super-mom*), Dennis Leung, Sibe, Maria Glew, and Laura Leder. The "group" trip to Scotland in August 2001 was particularly fun; the daily "paper-ball war", the never-ending ringing phone & buzzer (especially · – – ·) in the lab are memorable; and the "post-docs vs. PhD students" basketball game will be unforgettable. At this point, I would also like to express my appreciation to my office-mates (Ashish, Mike, Cliff Elwell, Moon-Ho Jo) for their co-operation over the years.

A big shout outs to the *Emmanuel College Basketball Team* (Marcel, Dan, Yoav, Alkis, Tom, James S., Elisabeth, Nick, Chris, Mike P., Oscar×2, Allen) for the many fun (albeit physical) games and making me the MVP (mainly due to the standard of British basketball, I think!); as well as the *CUMSA Basketball Team* (Yizhao, Fred, Renjie, Nelson, Steve, Yongqing, Roy) for the fun & super-physical matches at the *Nottingham Games*. Special thanks to Robert and Brian P. for introducing me (and getting me addicted) to the spirited *Ultimate Frisbee* and also to some fellow "flatballers" – Rich T., Graham B., Ben B., Anna, Dora, Helen, Roshan, Luke, Jon – thanks for the coaching, fine "flatball", and fun at the tournaments.

And to all the people (local & fellow travellers alike) whom I met while travelling, in particular in Tunisia (صلات من الجزائر؛ فاطمة، ناجية، ليلى، طاهر، عماد، مريم، عبد الكريم من تطاوين) – thanks for the hospitality – شكرا، Egypt (Bitten, Dawn, Simone, Alison, Mark, Jane & Stewart) and Turkey (Lisa, Jo, Tanja) – thank you for sharing the passion to travel and the spirit of never-stop-exploring.

Finally, the tremendous support and love from my parents and sister 曉漫, whom I have only seen once or twice in the past 3 years, can never be put in texts – thank you and I love you all more than words can express.

鍾欲曉

۱۵ بنابر ۲۰۰۲

## Summary

Since the discovery of high-temperature superconductors, there has been a worldwide effort towards the development of processes for fabricating coated conductors for power applications. Most of these processes are based on vapour phase deposition techniques that have relatively low growth rates. A high-rate processing route was proposed based on the observation of high growth rate of (RE)Ba<sub>2</sub>Cu<sub>3</sub>O<sub>7- $\delta$</sub>  superconducting compounds (RE = rare-earth element) from a flux supersaturated with one or more RE elements by *liquid phase epitaxy* (LPE).

LPE has been successfully used to grow YBCO thick films with both *c*- and *a,b*-orientations on (110) NdGaO<sub>3</sub> substrates and pure *c*-oriented films on YBCO seeded (100) MgO and (100) SrTiO<sub>3</sub> under carefully controlled growth temperature and undercooling. The film growth mode (*c*- or *a,b*-oriented) is determined by the growth rate, which is directly related to the level of RE supersaturation that could be controlled by the undercooling used along with the amount of total RE solubility in the solution. The LPE grown films were highly epitaxial and biaxially aligned with good in-plane and out-of-plane textures. YBCO thick films grown on NdGaO<sub>3</sub> by LPE showed high  $T_c$  of ~92 K and zero-field  $J_c$  at 77 K of  $2.5 \times 10^5$  A/cm<sup>2</sup>.

The initial growth of YBCO was found to be a multi-nucleation process. However, above a critical film thickness, dislocations started to form as a lattice-misfit stress relieving mechanism that led to step formation and spiral growth around dislocation cores. The growth kinetics from an unstirred solution was found to obey a  $\sqrt{t}$  law, whereas the growth rate from a stirred solution (substrate rotation) was found to have two growth stages with initial-transient and steady-state regimes. The transient regime extended to ~180 s with  $\sqrt{t}$  growth kinetics. In the steady-state regime, diffusion across an established diffusion boundary layer led to a linear increase of film thickness with time. Detailed study of the film growth confirmed the presence of interface kinetics that limited the growth on a competitive basis with volume diffusion in the solution. Furthermore, film growth on seeded substrates was found to be dependent on the stability of the seed layers where the mechanism of the dissolution of seed films was investigated.

The major obstacle towards continuous deposition of coated conductor in long lengths by LPE is the lack of non-vacuum techniques capable of producing long lengths of suitably buffered substrate or a closely-matched substrate where YBCO can be deposited directly. However, despite the lack of suitably buffered and/or seeded substrates in long lengths, continuous metallic tape processing had been tested at a preliminary level showing scalability of the process.

# Contents

Acknowledgements	iv
Summary	vi
<b>Chapter I Introduction</b>	<b>1</b>
1.1 Background	1
1.2 Objectives and Aims	3
1.3 Overview of the Dissertation	3
References	4
<b>Chapter II Superconductivity</b>	<b>5</b>
2.1 Basic Physical Phenomena of Superconductivity	5
2.1.1 <i>Zero resistance</i>	5
2.1.2 <i>Meissner effect</i>	6
2.1.3 <i>The London penetration depth</i>	7
2.1.4 <i>The Ginzburg-Landau penetration depth and coherence length</i>	7
2.1.5 <i>Type I and type II superconductors</i>	7
2.2 High Temperature Superconductors	8
2.2.1 <i>Crystal structure and stoichiometry of YBCO</i>	8
2.2.2 <i>Other HTS materials</i>	11
2.2.3 <i>Anisotropy</i>	11
2.3 Flux Vortices and Pinning in Type II Superconductors	12
2.3.1 <i>Flux vortices</i>	12
2.3.2 <i>Flux flow</i>	14
2.3.3 <i>Flux pinning</i>	14
2.3.4 <i>Flux creep</i>	15
2.3.5 <i>Irreversibility line</i>	15
2.4 Electric Power Applications of HTS	16
2.4.1 <i>Power generator and electric motor</i>	16
2.4.2 <i>Energy storage</i>	16
2.4.3 <i>Electrical transmission and distribution</i>	17
2.5 Summary	18
References	18
<b>Chapter III Crystal Growth from High-Temperature Solutions</b>	<b>20</b>
3.1 Theory of Solution Growth	20
3.1.1 <i>Supersaturation and driving force</i>	21
3.1.2 <i>Nucleation</i>	21
3.1.3 <i>Growth</i>	25
3.1.4 <i>Solute-diffusion boundary layer</i>	27
3.1.5 <i>Generation of a growth spiral</i>	28
3.1.6 <i>The BCF theory</i>	29
3.1.7 <i>Non-Archimedian spirals</i>	31
3.2 Epitaxy	32
3.3 Liquid Phase Epitaxy	33
3.3.1 <i>The basis of LPE</i>	33
3.3.2 <i>Experimental techniques</i>	34
3.3.3 <i>LPE growth model</i>	35
3.4 LPE of YBCO	37
3.4.1 <i>Peritectic reaction</i>	37
3.4.2 <i>Phase diagram and solubility curves</i>	38
3.4.3 <i>The principles in LPE of REBCO</i>	39
3.4.4 <i>LPE growth mechanism</i>	41
References	41

<b>Chapter IV</b>	<b>A Review in Coated Conductor Development</b>	<b>44</b>
4.1	Introduction	44
4.2	Substrates	45
4.2.1	<i>Untextured metallic substrates</i>	48
4.2.2	<i>Textured metallic substrates</i>	48
4.3	Buffer Layers	50
4.3.1	<i>IBAD buffer</i>	50
4.3.2	<i>Inclined substrate deposition</i>	51
4.3.3	<i>Ceramic buffer on RABiTS</i>	52
4.3.4	<i>Metallic buffer on RABiTS</i>	54
4.3.5	<i>Self-oxidation epitaxy</i>	54
4.4	Superconducting Layer	55
4.4.1	<i>Thin film</i>	55
4.4.2	<i>Thick film</i>	56
4.5	Studies of Grain Boundaries as Weak Links Using Bicrystals	58
4.6	Summary of Coated Conductor Development	60
4.7	Liquid Phase Epitaxy of REBCO	60
4.7.1	<i>Early LPE of REBCO</i>	61
4.7.2	<i>Nucleation and growth of REBCO by LPE</i>	62
4.7.2(a)	Nucleation and growth of YBCO on NdGaO <sub>3</sub>	62
4.7.2(b)	Nucleation and growth of NdBCO on NdGaO <sub>3</sub>	64
4.7.2(c)	Nucleation and growth on seeded substrates	64
4.7.2(d)	Crystalline orientation of the LPE grown films	68
4.7.2(e)	Factors affecting the LPE growth rate	69
4.7.3	<i>Lowering the growth temperature</i>	70
4.7.4	<i>Recent developments</i>	72
4.7.5	<i>Transport properties</i>	75
4.7.6	<i>Crack formation</i>	76
4.8	Summary of the LPE of REBCO	78
	References	79
<b>Chapter V</b>	<b>Experimental Details</b>	<b>89</b>
5.1	Sample Preparation	89
5.1.1	<i>Starting materials</i>	89
5.1.2	<i>Furnace set-up</i>	90
5.1.2(a)	Box furnace with thermal-gradient crucible operating in air	91
5.1.2(b)	Box furnace operating in air using step-cooling mode	92
5.1.2(c)	Controlled-atmosphere furnace with thermal-gradient crucible	92
5.1.3	<i>Growth conditions</i>	93
5.1.4	<i>Film growth</i>	94
5.1.5	<i>Oxygenation</i>	95
5.2	Characterisation	95
5.2.1	<i>X-ray diffraction</i>	95
5.2.1(a)	Diffractionmeter	95
5.2.1(b)	Texture goniometer	96
5.2.2	<i>Optical microscopy</i>	96
5.2.3	<i>Electron microscopy</i>	97
5.2.4	<i>Atomic force microscopy</i>	97
5.2.5	<i>T<sub>c</sub> measurement</i>	97
5.2.5(a)	Resistive transition	97
5.2.5(b)	Inductive T <sub>c</sub> measurement	98
5.2.6	<i>Transport J<sub>c</sub></i>	98
5.3	RE Solubility Measurement	99
	References	99

<b>Chapter VI</b>	<b>Growth of YBCO on NdGaO<sub>3</sub></b>	<b>101</b>
6.1	Crystalline Orientation	101
6.2	Growth Rate Dependence	104
6.3	Nucleation and Growth Mechanism	107
6.3.1	<i>Steady-state growth</i>	108
6.4	Growth Kinetics	111
6.4.1	<i>Unstirred solution and stirred solution transient growth</i>	111
6.4.2	<i>Stirred solution steady-state growth</i>	115
6.5	Growth at Reduced Temperature in Air	119
6.5.1	<i>Growth from Ba-Cu-O-F flux in air</i>	120
6.5.2	<i>Growth from Ba-Cu-O-Ag flux in air</i>	122
6.5.3	<i>Growth from Ba-Cu-O-F-Ag flux in air</i>	122
6.5.4	<i>Growth rate dependence</i>	122
6.6	Microstructural Analyses	123
6.6.1	<i>TEM and HREM analyses</i>	128
6.7	Transport Properties	130
6.7.1	<i>Critical temperatures</i>	130
6.7.2	<i>Critical currents</i>	131
6.8	Summary	133
	References	134
<b>Chapter VII</b>	<b>Growth of Mixed (Y,RE)BCO on NdGaO<sub>3</sub></b>	<b>136</b>
7.1	Undercooling Growth Windows of Various REBCO Systems	136
7.2	Growth of NdBCO and (Y,Nd)BCO from Unstirred Solutions	138
7.3	Growth of SmBCO and (Y,Sm)BCO from Unstirred Solutions	143
7.4	The Effects of the Presence of Multiple REs	144
7.5	Summary	146
	References	146
<b>Chapter VIII</b>	<b>Growth on Seeded Single Crystalline Substrates</b>	<b>147</b>
8.1	X-Ray Characterisation	147
8.2	Stability of the Seed Layer	150
8.2.1	<i>Surface modification of the seed layer prior to the LPE growth</i>	152
8.3	Growth Mechanism	156
8.4	Surface Morphology of LPE Grown YBCO	157
8.5	Transport Properties and Mg Contamination	158
8.6	Summary	161
	References	161
<b>Chapter IX</b>	<b>Growth on Metallic Substrates</b>	<b>163</b>
9.1	Growth of YBCO on Metallic Substrates in Air	163
9.2	Growth under Controlled Atmosphere	164
9.3	Summary	166
	References	166
<b>Chapter X</b>	<b>Conclusions and Future Outlook</b>	<b>167</b>
10.1	Conclusions	167
10.2	Future Outlook	169
	References	170
<b>Appendix:</b>	<b>Flux Calculation</b>	<b>171</b>
<b>List of Publications and Conference Presentations</b>		<b>173</b>

*This chapter introduces the topics of study – coated conductor & liquid phase epitaxy – and presents the research objectives as well as an outline of the dissertation.*

## **1.1 Background**

The discovery of the family of cuprate superconductors that become superconducting when placed in liquid nitrogen ~15 years ago [1] marked the beginning of the high-temperature superconductivity (HTS) era. The widespread perception of the remarkable potential of these cuprates for novel technological applications, be it for energy and power applications, for levitation of trains, in medicine for MRI (Magnetic Resonance Imaging) tomography, or for SQUIDs (Superconducting Quantum Interference Devices) in magnetic encephalography, has encouraged intense research worldwide.

The first generation superconducting wires and tapes have not yet made a significant contribution to industrial applications due to severe limitations in current-carrying capability at high temperatures and modest magnetic fields. The so-called "second generation" superconducting tape with its potentially high-current carrying capability in relatively high magnetic fields has encouraged its development for large-scale industrial applications. This second generation superconducting tape is referred to as coated conductor.

A coated conductor usually consists of three layers: substrate, buffer layer (if necessary), and superconductor. If long lengths of coated conductor can be reliably and cost-effectively fabricated, the HTS materials may be able to replace conventional low-temperature superconductors in many applications such as magnets for MRI tomography. Such

replacement would save a significant amount of operating cost such as cryogen consumption in the long run.

As a superconductor conducts electric current without any power dissipation, there are enormous efforts towards the development of processes for fabricating coated conductors for energy and power applications. These developments have been based on the  $\text{REBa}_2\text{Cu}_3\text{O}_{7-\delta}$  (REBCO or RE123 where RE = rare-earth element) family of superconductors that is considered the most promising candidate for a cost-effective HTS conductor. This is mainly because REBCO type compounds, when compared to other HTS materials, are capable of carrying high electric currents at high magnetic fields and temperatures.

Most REBCO coated conductor fabrication methods are based on vapour-phase deposition techniques that have relatively low growth rates due to the low impingement rate of atoms at the growth interface. Although technically sound, there is a concern that such processes may not be financially viable for many applications. On the other hand, the impingement rate of atoms for REBCO grown from solution is typically several orders of magnitude greater than for growth from vapour phase. This offers remarkable potential for high-rate production of REBCO via liquid-phase processes.

The *liquid phase epitaxy* (LPE) method was first developed for thin film growth of semiconductors and oxides for optoelectronics [2]. LPE involves the undercooling of a molten flux supersaturated with solutes and in the presence of a suitable substrate (e.g., small lattice mismatch), the desired phase would nucleate and grow. Growing HTS materials by the one-step LPE method was pioneered by Scheel *et al.* [3] who surveyed the essential problems and difficulties connected with the epitaxial growth of YBCO films. LPE of REBCO is more difficult than the traditional LPE of semiconductor and garnet films since the solubility of RE elements in the melt is very low, hence nucleation and growth is more difficult. Furthermore, at the high growth temperature of LPE, metallic substrates, which are preferred for coated conductor applications due to their flexibility and availability in long lengths, could have detrimental effect on the REBCO layer.

The LPE technique, already with the advantages of its high growth rate and being a non-vacuum process, has another edge over vapour-phase techniques as it is capable of growing thick films without degradation in the crystallinity.

## 1.2 Objectives and Aims

The primary objective of the research is to develop a novel process for the continuous high-rate production of low-cost high critical current coated conductors on metallic and ceramic substrates. This research aims to generate new scientific and technical knowledge regarding the growth of REBCO by LPE. An improved understanding will be obtained for: (i) nucleation process on various substrates including REBCO seeded substrates, (ii) high-rate epitaxial growth of REBCO, including transient and steady-state growth, and (iii) parameters that govern the growth.

## 1.3 Overview of the Dissertation

This dissertation presents the background information and results of the work as outlined in the research objectives above. The dissertation is organised in the following manner:

- Chapter II presents a brief introduction into the subject of superconductivity where some basic phenomena of superconductivity are described;
- Chapter III focuses on the theory of crystal growth from high-temperature solutions and the principles of LPE;
- Chapter IV summarises the development of coated conductor technology worldwide;
- Chapter V describes the experimental details of sample preparation and characterisation;
- Chapter VI presents results from the growth of YBCO on NdGaO<sub>3</sub> single crystalline substrates including the nucleation, growth mechanism, and growth kinetics;
- Chapter VII presents results from the growth of mixed (Y,RE)BCO on NdGaO<sub>3</sub> single crystalline substrates including the cumulative effect of multiple RE solubility on film growth;
- Chapter VIII presents results from the growth of YBCO on seeded single crystalline substrates (MgO and SrTiO<sub>3</sub>) including the surface modification of seed layer prior to LPE growth;
- Chapter IX presents results from the growth of YBCO on metallic substrates with various buffer architectures; and
- Chapter X summarises the present findings and provides an outlook for coated conductor development via LPE.

**References**

- 1 M. K. Wu, J. R. Ashburn, C. J. Torng, P. H. Hor, R. L. Meng, L. Gao, Z. J. Huang, Y. Q. Wang, and C. W. Chu, *Phys. Rev. Lett.* **58** (1987) 908.
- 2 B. M. Small, E. A. Giess, and R. Ghez, in *Handbook of Crystal Growth*, edited by D. T. J. Hurle, Vol. 3a (North-Holland, Amsterdam, 1994).
- 3 H. J. Scheel, M. Berkowski, and B. Chabot, *J. Crystal Growth* **115** (1991) 19.

<b>Chapter I Introduction</b>	<b>1</b>
1.1 Background	1
1.2 Objectives and Aims	3
1.3 Overview of the Dissertation	3
References	4

*This chapter presents an introduction to the subject of superconductivity. The chapter starts with descriptions of the basic phenomena of superconductivity, follows by the properties of the  $\text{YBa}_2\text{Cu}_3\text{O}_{7.8}$  superconducting material, and then discusses some potential electric power applications. Since in-depth theories of superconductivity are beyond the scope of this work, they will not be reviewed here.*

## **2.1 Basic Physical Phenomena of Superconductivity**

A superconductor is a material that offers zero electrical resistance and perfect diamagnetism when it is cooled below its critical temperature  $T_c$ . Besides temperature, there exists a critical value of applied magnetic field,  $B_c$  (for type I superconductors; see §2.1.5 later), above which the superconductivity would be suppressed. This implies that there is only a finite amount of electric current that can be carried in a superconductor before the *self-field* generated by the current exceeds  $B_c$ . Hence, in addition to temperature and magnetic field, there is also an upper limit to the current flowing through the material, known as the critical current  $I_c$ , which is usually expressed in current per unit area or critical current density  $J_c$ .

### **2.1.1 Zero resistance**

The characteristic resistive transition of a superconductor is an abrupt drop of resistance at  $T_c$ . The resistance is now known to be exactly zero, not just a small value below its transition temperature. This zero resistance phenomenon of superconductivity can be best demonstrated by a persistent current experiment in a superconducting ring as shown in Fig. 2.1. Once set up, such current would continue to flow without measurable decrease indefinitely.

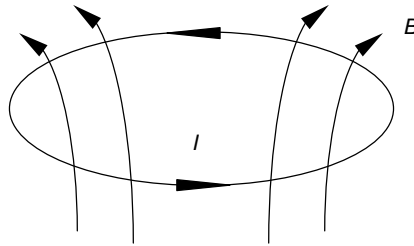


**Fig. 2.1** Schematic of persistent current experiment.

### 2.1.2 Meissner effect

Another characteristic of a superconductor that is less widely recognised is its ability to expel magnetic flux from its interior when it is cooled below  $T_c$ . This phenomenon, known as the *Meissner effect*, occurs when the material enters the superconducting state. The presence of a magnetic field sets up electric shielding currents on the surface of the superconductor, producing a magnetic field of equal magnitude but opposite in direction to the external applied field. This results in complete cancellation of magnetic flux within the sample.

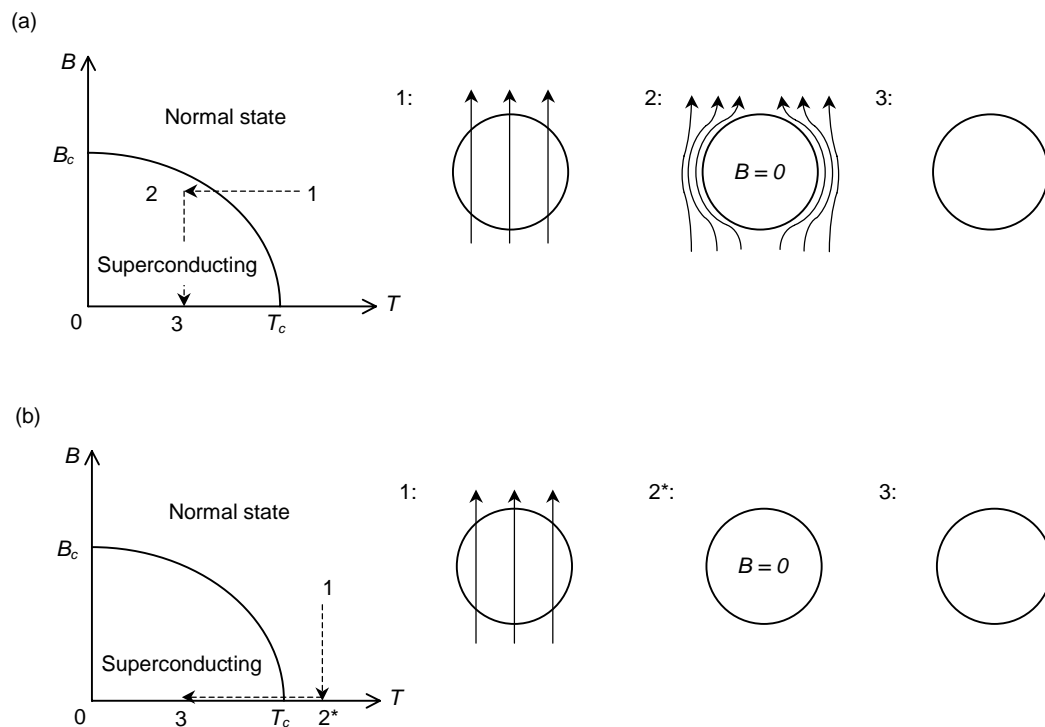


**Fig. 2.2** Schematic of the Meissner effect showing that the final state of superconductor is independent of its thermodynamic path. Adapted from ref. [1].

Unlike a material with infinite electric conductivity, the final state of a superconductor for a given temperature and magnetic field is independent of the thermodynamic path (sequence of

cooling and applying magnetic field) followed to reach such state, which implies that the superconducting state is a true thermodynamic equilibrium state. This concept is illustrated in Fig. 2.2.

### **2.1.3 The London penetration depth**

After studying the relationship between applied magnetic field and current flow within a superconductor, the London brothers [2] attempted to explain the Meissner effect and suggested that magnetic flux did penetrate a small distance underneath the surface despite the opposing currents. They predicted that the applied magnetic field would penetrate into the superconductor over a mean distance of  $\lambda_L$ , known as the London penetration depth, and decrease exponentially along the  $x$  direction according to  $B = B_0 \exp(-x/\lambda_L)$ .

### **2.1.4 The Ginzburg-Landau penetration depth and coherence length**

In 1950, Ginzburg and Landau [3] proposed a theory describing the superconducting electrons by a complex wavefunction  $\psi(x)$  such that  $n_s = |\psi(x)|^2$ , where  $n_s$  is the number density of superconducting electrons. The Ginzburg-Landau equations lead to two characteristic lengths: the G-L penetration depth  $\lambda_{GL}$  and the coherence length  $\xi_{GL}$ . The penetration depth, like the London penetration depth, is the characteristic length for the decay of the magnetic field in a superconductor. The coherence length may be described as the length scale over which the order parameter  $\psi$  varies.

### **2.1.5 Type I and type II superconductors**

In 1957, Abrikosov [4] showed that solutions of the Ginzburg-Landau equations fall into two distinct categories according to the ratio  $\kappa = \lambda_{GL}/\xi_{GL}$ . For  $\kappa < 1/\sqrt{2}$ , the superconductor allows magnetic flux to penetrate at and beyond the critical field ( $B_c$ ). The superconductor thus transforms from the Meissner state to normal state with an abrupt loss of superconductivity – so-called type I behaviour. Since the current-carrying capacity is low for type I superconductors, which are pure metallic elements, these materials have limited potential in large-scale magnetic and electric applications.

In type II superconductors ( $\kappa > 1/\sqrt{2}$ ), the Meissner state is followed by a "mixed state" before reverting to the normal state in an increasing field. With an increasing magnetic field, flux will start to penetrate into the material at a lower critical field  $B_{c1}$ , which marks the beginning of the "mixed state". Flux penetration increases until the magnetic field reaches an upper

critical field  $B_{c2}$ , where the superconductor is fully penetrated, before it restores to the normal state. In other words, magnetic fields can co-exist with superconductivity in type II superconductors. Type II superconductors, which are metal alloys and compounds, have a much higher current-carrying capacity and are thus attractive to magnet technology and power applications.

## 2.2 High Temperature Superconductors

The high temperature superconductors discovered to date are all oxides containing the crucial transition element copper (thus the term cuprates). These copper oxides exist in the crystal structure in the form of sheets or planes that play an important role in superconductivity. Since this work is limited to REBCO type superconductor, only properties of REBCO will be described in details.

### 2.2.1 Crystal structure and stoichiometry of YBCO

All HTS materials have characteristic layered structures. The unit cell of YBCO type superconductor is a complex, layered perovskite centred on a Y layer. The perovskite structure has the general formula of  $ABO_3$ . The structure can be cubic (idealised), tetragonal, or orthorhombic depending on its temperature, which is material specific. This structure was first found in the mineral perovskite,  $CaTiO_3$ , which has a tetragonal structure at room temperature. Fig. 2.3 shows an idealised unit cell of  $CaTiO_3$  in which the Ca and O atoms combine to form a close-packed cubic structure with the smaller Ti atom in octahedral interstice.

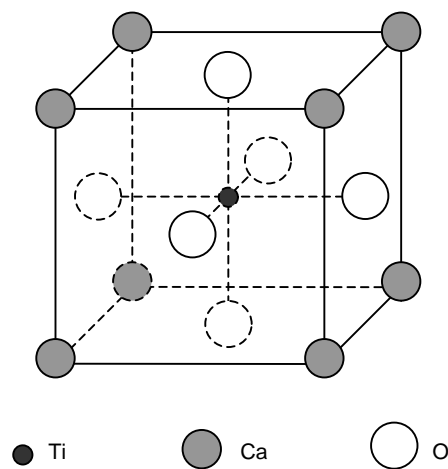


**Fig. 2.3** The ideal cubic perovskite structure [5].

Changes in temperature alter the coordination of the Ti atoms with its neighbouring oxygen ions, and this modifies the crystal structure of the material. For the ease of illustration, Fig. 2.4(a) shows a redrawn ideal cubic perovskite with a Ca atom at the body-centred position while Fig. 2.4(b) shows the tetragonal perovskite structure.

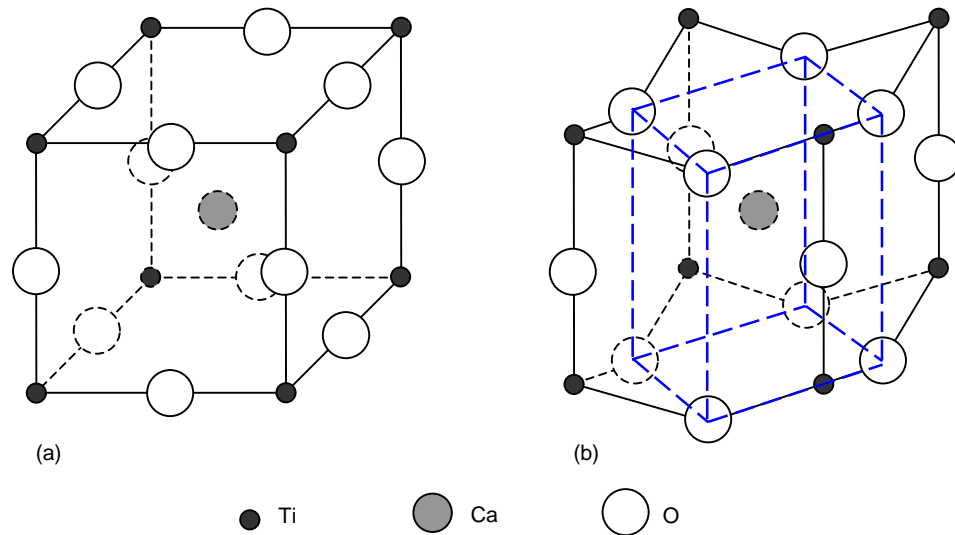


**Fig. 2.4** (a) Cubic perovskite and (b) tetragonal perovskite [6].

The crystal structure of YBCO consists of three perovskite-like unit cells where Cu atoms are equivalent to Ti atoms and by substituting one Y atom for every third Ba atom, Y and Ba atoms are equivalent to Ca atoms in the  $\text{CaTiO}_3$  structure. As shown in Fig. 2.5, the centre of a YBCO unit cell has two  $\text{CuO}_2$  planes that sandwich an Y atom in between. Above and below these  $\text{CuO}_2$  planes, there is a  $\text{BaO}_2$  layer and on top of that lies a Cu-O basal plane with variable oxygen content.

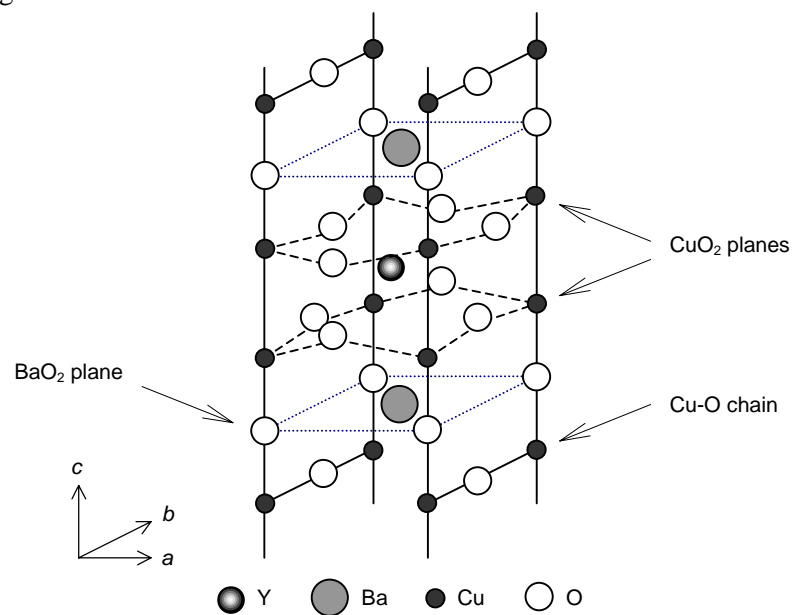


**Fig. 2.5** The orthorhombic unit cell of YBCO [6].

Since these Cu-O basal planes have missing oxygen atoms, they are known as *Cu-O chains*. Crystal structures of other REBCO compounds are identical to YBCO with substitution of the relevant rare-earth element for yttrium atoms.

The stoichiometry of  $\text{YBa}_2\text{Cu}_3\text{O}_{7-\delta}$  depends on temperature and oxygen partial pressure. The change in oxygen content would modify the crystal structure and superconductivity of YBCO. As synthesised at high temperatures, YBCO has a tetragonal structure with a  $\delta$  value varying from 0.7 to 1 that is not superconducting. By oxidation,  $\delta$  can be reduced to 0.1 or less, and by cooling through the phase transition range around  $650^\circ\text{C}$ , YBCO becomes orthorhombic. Only this oxidised phase is superconducting at about 92 K. The variation of oxygen content in YBCO is shown in Fig. 2.6. The plot shows that  $\text{YBa}_2\text{Cu}_3\text{O}_{7-\delta}$  is not superconducting for  $\delta > 0.56$  and  $T_c$  rises rapidly as oxygen content increases until it reaches a maximum  $T_c$  of 93 K for  $\delta = 0.08$ .

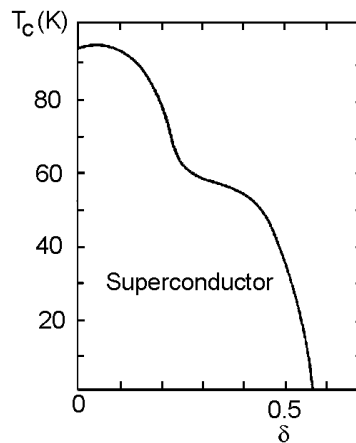


**Fig. 2.6** The effect of oxygen content on the  $T_c$  of  $\text{YBa}_2\text{Cu}_3\text{O}_{7-\delta}$  [7].

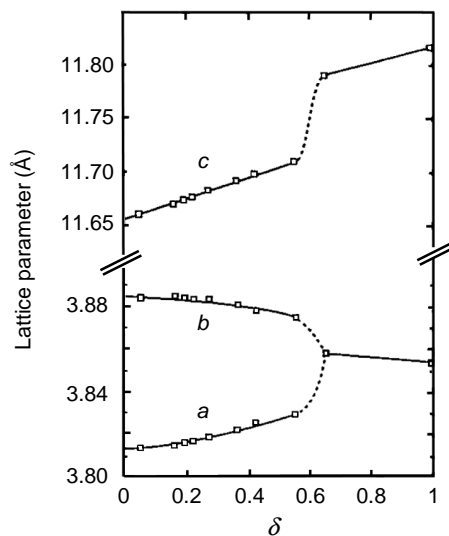


**Fig. 2.7** Lattice parameters of YBCO as a function of oxygen content. Adapted from ref. [8].

As oxygen atoms are incorporated into the tetragonal structure, the splitting of the tetragonal  $a$ -axis (=  $b$ -axis) to the orthorhombic  $a$  and  $b$  axes as well as the transition-induced change of the  $c$  lattice parameter lead to strain. The variation of the lattice parameters of YBCO with oxygen content is shown in Fig. 2.7. The tetragonal-orthorhombic transition occurs at around  $\delta = 0.6$ .

### 2.2.2 Other HTS materials

In addition to REBCO, the other superconductors discovered to date having a  $T_c$  above 77 K are Bi-, Tl-, and Hg-containing compounds. Bi-compounds, which are based on  $\text{Bi}_2\text{Sr}_2\text{Ca}_n\text{Cu}_{n+1}\text{O}_{6+2n}$  (BSCCO) where  $n$  is an integer, are extremely anisotropic. The structures of  $n = 1$  and  $n = 2$  are generally known as Bi-2212 and Bi-2223 respectively. BSCCO is limited in many applications due to its low irreversible field  $B_{irr}$  (see §2.3.5 later).

There are two types of HTS containing Tl:  $\text{Tl}_2\text{Ba}_2\text{Ca}_n\text{Cu}_{n+1}\text{O}_{2n+6}$  that has similar crystal structure and inter-layer spacing to BSCCO and  $\text{TlX}_2\text{Ca}_{n-1}\text{Cu}_n\text{O}_{2n+3}$  ( $X = \text{Ba}$  or  $\text{Sr}$ ) with single Tl-O layer. Film fabrication for Tl-compounds is usually a two-step process involving the deposition of an amorphous precursor film, which may or may not contain Tl, followed by heat treatment in the presence of thallos oxide vapour to form the crystalline superconducting structure [9]. The fabrication of Tl-compounds involves a delicate balance between the high processing temperature and the high volatility and toxicity of Tl at these temperatures.

The Hg-based compound,  $\text{HgBa}_2\text{Ca}_2\text{Cu}_3\text{O}_9$  or Hg-1223, has the highest  $T_c$  among all superconductors discovered to date at 135.5 K under atmospheric pressure [10] and 164 K under high pressure up to 45 GPa [11]. However, studies of Hg-based compounds, like Tl-compounds, are limited partly due to the toxicity of Tl and Hg and complexity in the processing techniques. Furthermore, both Tl- and Hg-based compounds have lower normalised irreversibility lines  $B_{irr}$  (see Fig. 2.12 later) than REBCO type materials.

### 2.2.3 Anisotropy

It is well known that most HTS materials are highly anisotropic. There is no exception for REBCO compounds; it is widely agreed that superconductivity takes place inside the  $\text{CuO}_2$  sheets, which lie within the  $a,b$ -plane. Thus, it is desirable to fabricate a coated conductor such that its  $a,b$ -plane lies within the direction of current flow for high-current applications.

Besides correct orientation, current flow within these  $\text{CuO}_2$  planes is also very sensitive to the mismatch of grains where the grain boundaries act as *weak links*. Weak link is a term used to describe the behaviour of an electric current as it crosses a non-superconducting region. It has been experimentally shown [12] that  $J_c$  of REBCO type superconductors drops significantly for grain boundary angles greater than about  $5-7^\circ$ . *Biaxially textured* superconducting materials are superconductors that have the desired microstructures with  $a,b$ -planes in the direction of current flow and have low angle grain boundaries.

## 2.3 Flux Vortices and Pinning in Type II Superconductors

For most of the applications outlined later in §2.4, the magnetic fields would likely be in between  $B_{c1}$  and  $B_{c2}$ . Therefore, it is necessary to understand the behaviour of type II superconductors in magnetic fields.

### 2.3.1 Flux vortices

In the "mixed state" of type II superconductors, the magnetic field penetrates the superconductor as single-quantum magnetic flux lines, called *flux vortices*. The vortex, a cylinder with a core of radius  $\zeta$  contains a region of suppressed order parameter that decreases to zero at the vortex centre, while the local magnetic field rises to a maximum as shown in Fig. 2.8.

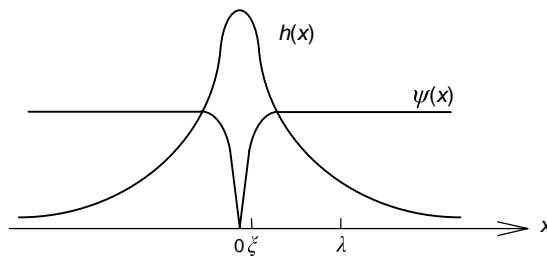


**Fig. 2.8** Variation of order parameter and local flux density for a single flux vortex [13].

Abrikosov [4] predicted that the vortices arrange as an approximately regular lattice known as the *flux line lattice*. However, Essmann and Trauble [14] confirmed experimentally that the arrangement with lowest free energy state is in fact a triangular lattice.

Due to the anisotropy in HTS materials, the structure of flux vortices changes depending on the differences in the coherence length and penetration depth in the  $a,b$ - and  $c$ -directions. The vortex cores having radii  $\zeta_{ab}$  and  $\zeta_c$  in the  $a,b$ - and  $c$ -directions, respectively, are shown in Fig.

2.9. The approximate ratios of the dimensions in Fig. 2.9 for YBCO are  $\zeta_{ab} \approx 5\zeta_c$ ,  $\lambda_c \approx 5\lambda_{ab}$ , and  $\lambda_{ab} \approx 100\zeta_c$  [14].

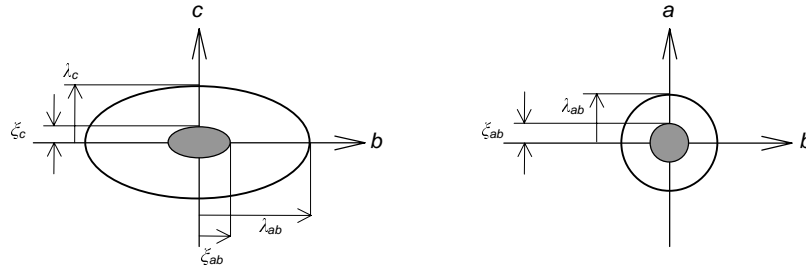


**Fig. 2.9** Schematic of vortices along the  $a$ -axis and  $c$ -axis of a uniaxially anisotropic type II superconductor. The shaded region represents the vortex core and the outer perimeter is a line of constant field. Adapted from ref. [13].

In addition to this anisotropy, the layered nature of REBCO materials is also important to the vortex structure. If the coherence length is significantly larger than the interplanar lattice spacing, the homogeneous 3-dimensional description holds. However, if  $\zeta_c$  is smaller than the interplanar spacing, the  $\text{CuO}_2$  planes in REBCO materials are no longer well coupled and the material is best described as a stack of superconducting planes. The description of the flux vortices must then be modified in order to take into account the fact that they are localised within the planes, resulting in an array of pancakes [15] that are confined to the superconducting planes and only weakly coupled to their neighbours. For a magnetic field that is parallel to the  $c$ -direction, the flux pancakes form a simple stack, if the field is parallel to the  $a, b$ -plane, vortices may form between the superconducting planes. These so-called *Josephson vortices* have no normal cores and thus do not strongly suppress the order parameter in the adjacent superconducting planes. For a magnetic field at an intermediate angle, the vortex can be described as a combination of pancake vortices in the  $c$ -direction, which are confined within the  $\text{CuO}_2$  planes, connected by Josephson vortices in the  $a, b$ -plane as illustrated in Fig. 2.10.

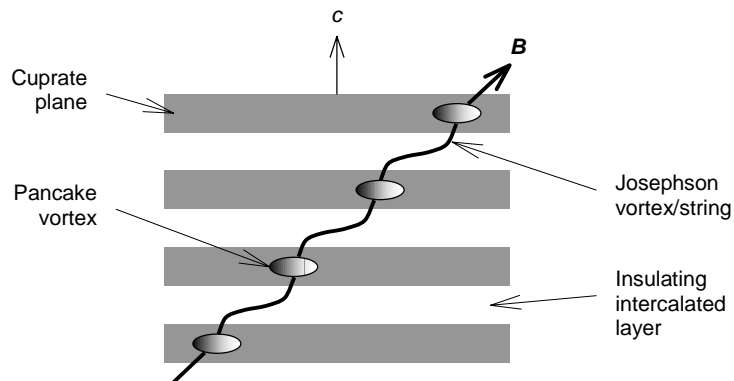


**Fig. 2.10** A flux vortex in an anisotropic layered REBCO superconductor. Adapted from ref. [16].

### 2.3.2 Flux flow

In the presence of a macroscopic transport current, a flux vortex is subjected to a Lorentz force per unit length as  $f_L = \Phi_0 \mathbf{J} \times \mathbf{n}$ , where  $\mathbf{J}$  is the current density,  $\mathbf{n}$  is a unit vector along the flux line, and  $\Phi_0$  is the flux quantum. The Lorentz force density over a number of vortices is given as:

$$\mathbf{F}_L = \mathbf{J} \times \mathbf{B}. \quad (2.1)$$

This force tends to move the flux lines in a transverse direction to the current flow, inducing an electric field, which is normal to both the movement and the field direction, of magnitude [17]:

$$\mathbf{E} = \mathbf{B} \times \mathbf{v} \quad (2.2)$$

where  $\mathbf{v}$  is the velocity of the moving flux line. This acts like a resistive voltage and power is dissipated, which leads to heating and further degrades the performance.

A simple model of flux flow assuming a viscous drag coefficient  $\eta$  such that the viscous force per unit length of a vortex line moving with velocity  $\mathbf{v}$  is  $-\eta \mathbf{v}$  leads to a force balance equation:

$$\Phi_0 \mathbf{J} = -\eta \mathbf{v}, \quad (2.3)$$

and the flux flow resistivity,  $\rho_f$ , defined as  $\mathbf{E} = \rho_f \mathbf{J}$  is given by [18]:

$$\rho_f = \frac{B \Phi_0}{\eta}. \quad (2.4)$$

Fig. 2.11 shows a schematic  $E$ - $J$  characteristic for linear flux flow.

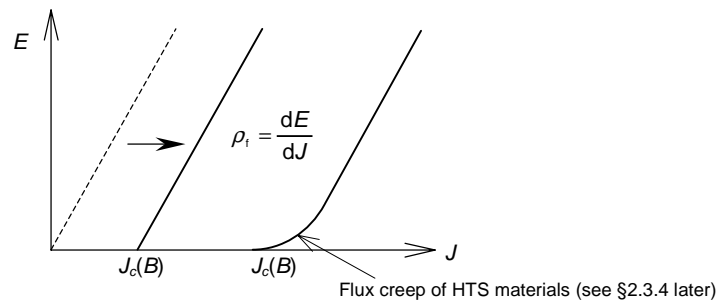


**Fig. 2.11** Schematic  $E$ - $J$  characteristic for flux flow and flux creep of HTS materials.

### 2.3.3 Flux pinning

In order to minimise dissipation due to flux flow as soon as vortices enter type II superconductors beyond  $B_{c1}$ , a force opposing to the Lorentz force is necessary to pin the vortices in place. Such *pinning centres*, which prevent the motion of flux lines (or vortices), can be provided by defects. These defects locally change the free energy of the flux line

lattice, by which the flux lines are trapped. Pinning centres may be point defects such as impurities or vacancies, and line defects such as edge or screw dislocations.

The critical current density ( $J_c$ ) is then defined by the balance of the pinning and Lorentz forces,  $F_p = F_L$ , where  $F_p$  is the volume summation over all microstructural pinning defects in the strongly interacting network of flux lines [19]. Ideally, a type II superconductor can carry a dissipation-free current density at  $J < J_c$ . When  $J$  exceeds  $J_c$ , a superconductor switches into a dissipative, vortex-flow state driven by Lorentz force. Large critical currents have been achieved by proper treatment during fabrication that yields optimal defect morphology in the material and enable a superconductor to carry transport current densities with minimum dissipation of  $10^4$ - $10^6$  A/cm<sup>2</sup> in fields as strong as 20 T [20]. The degree of pinning varies among the HTS materials, with YBCO having more effective pinning sites as compared to Bi- and Tl-containing compounds, leading to higher  $J_c$ .

### 2.3.4 Flux creep

At finite temperature, flux lines may jump from one pinning configuration to another by overcoming the energy barrier due to thermal fluctuations, resulting in energy dissipation. The net flux movement is zero in the absence of a current; however, in the presence of even a small current, there is a net flux motion in the direction of Lorentz force. As the current increases, the number of forward jump increases while the backward jump decreases, leading to an increase in net flux movement.

The effect of thermal-activated flux creep tend to dominate the early stages of dissipation in HTS materials due to the fact that the activation energy is smaller for conventional type II materials and because they are usually used at higher temperatures, hence the thermal energy is greater. This thermal-activated flux creep causes a significant curvature of the  $E$ - $J$  characteristic around  $J_c$  as shown in Fig. 2.11.

### 2.3.5 Irreversibility line

For type II superconductors, there is a magnetic field that is usually more important than  $B_{c1}$  and  $B_{c2}$ : the irreversibility field  $B_{irr}$ , which is the field above which flux pinning becomes ineffective and moving flux lines cause dissipation. The position of the *irreversibility line*, which describes the variation of  $B_{irr}$  with temperature as shown in Fig. 2.12, is material dependent.

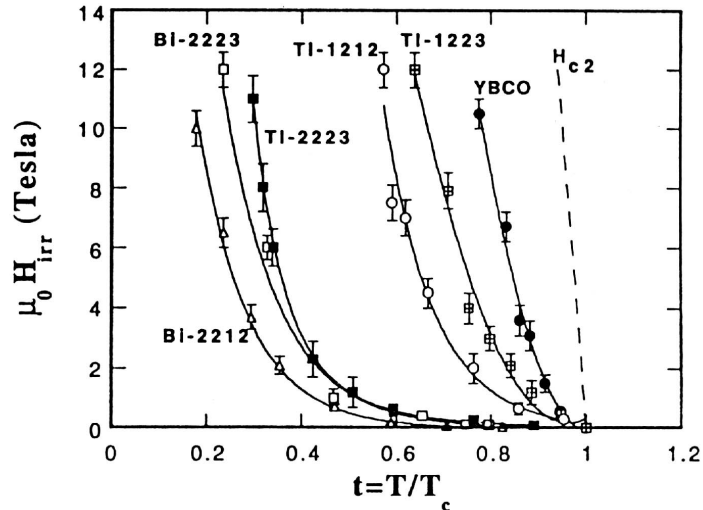


Fig. 2.12 The position of the irreversibility line for various HTS materials [8].

## 2.4 Electric Power Applications of HTS

Most electrical applications using HTS are based on its high  $J_c$  values that are not obtainable using conventional materials. HTS materials have several advantages over low  $T_c$  superconductors (LTS) as they have higher  $B_{irr}$  and potential savings in cryogen consumption costs and reducing the design complexity of cryogenic system.

### 2.4.1 Power generator and electric motor

HTS generators and motors have the advantages of higher power density, higher efficiency, smaller size and weight, due to the capability of producing high magnetic fields from the loss-less superconducting winding and hence smaller rotor coils.

Electric motors consume large amount of electricity, thus there is a lot of interests in utilising superconductors to improve its efficiency. However, electric motors are generally rather efficient [21], therefore HTS motors have to be even more efficient to offset the cost of their cryogenic system.

### 2.4.2 Energy storage

There are two types of energy storage systems that could potentially benefit from using superconductors: superconducting magnetic energy storage (SMES) and superconducting flywheels. Such applications in energy storage would be useful for meeting peak-hour electricity demand and as an emergency power source. In SMES, energy is stored in the

magnetic field produced by superconducting coils that carry a large DC current with zero resistive losses; the current will persist for as long as the coil is kept below its  $T_c$ . On the other hand, a superconducting flywheel is based on the principle of the Meissner effect that produces an extremely low-friction bearing. Electrical energy is used to spin the flywheel and cut off when it reaches its top speed such that the energy is stored in rotational kinetic form by the spinning flywheel with very low frictional or air-drag losses (when housed in a vacuum).

### **2.4.3 Electrical transmission and distribution**

As the demand for electrical power is increasing, one of the challenges for the utility industry is to find new ways to transport large amount of power from the generation plant to consumers. The market in electrical transmission and distribution is large especially in urban areas where the demand of electricity is increasing while there is limited clearance for overhead cables. Thus, using underground HTS cables capable of carrying three to five times more power than copper cables of the same size, and thus using existing rights of way is an attractive solution [22]. Furthermore, significant portions of the existing cables are ageing and need replacement in the near future. Not only that HTS cables can transmit electricity with minimal resistive losses, in addition, the liquid nitrogen used to cool underground HTS cables is less expensive and presents less environmental risk than the dielectric oil used in copper cables [22].

HTS transformers offer many benefits over conventional power transformers for utility applications. The major practical advantage is the reduction in weight and size, as the losses in the windings are significantly reduced allowing smaller number of ampere-turns used. This, in turn, reduces the iron-core losses due to the smaller amount of generated magnetic flux. HTS transformers are expected to be half the weight and size of conventional ones, which would, among others, reduce the area required for a power substation, ease the transportation, and replace the dielectric oil with environmental friendly and non-flammable liquid nitrogen.

Another application of superconductors in electrical transmission is the fault current limiter (FCL) that uses the superconducting-normal (SN) transition of a superconductor to reduce the fault current in an electric circuit. In the event of a fault current, the  $J_c$  of the superconductor is exceeded whereby the material turns into its normal state that limits the large fault current. The FCL is capable of reducing a fault current nearly instantaneously and is highly sought since the increasing power consumption and demand make it useable where the short-circuit capacity of power system would exceed the capacity of a conventional circuit breaker. HTS

materials connected in series are very effective in controlling rising fault currents within milliseconds since the SN transition can occur in less than 1 ms [21].

## 2.5 Summary

The discovery of superconducting materials with  $T_c$  greater than the boiling point of liquid nitrogen has created a wide range of potential applications. One such application is in the electric power industry such as power generation, energy storage, and power transmission. Nevertheless, there are still many obstacles to be overcome before HTS materials can be competitive with the existing components made of non-superconducting or LTS materials. HTS compounds are more complex, anisotropic, and brittle than LTS materials, which are mostly pure metals or metal alloys. However, besides the potential savings in cryogen consumption costs, HTS materials are capable of carrying larger currents in higher magnetic fields, which make them attractive candidates for many applications.

## References

- 1 A. C. Rose-Innes and E. H. Rhoderick, *Introduction to Superconductivity*, 2<sup>nd</sup> edition (Pergamon, Oxford, 1988).
- 2 F. and H. London, *Proc. Royal Soc. A* **149** (1935) 71.
- 3 V. L. Ginzburg and L. D. Landau, *Zh. Eksp. Teor. Fiz.* **20** (1950) 1064.
- 4 A. Abrikosov, *Zh. Eksp. Teor. Fiz.* **32** (1957) 1442.
- 5 W. D. Kingery, H. K. Bowen, and D. R. Uhlmann, *Introduction to Ceramics* (John Wiley & Sons, New York, 1976).
- 6 C. P. Poole Jr., T. Datta, and H. A. Farach, *Copper Oxide Superconductors* (John Wiley & Sons, New York, 1988).
- 7 M. Cyrot and D. Pavuna, *Introduction to Superconductivity and High  $T_c$  Materials* (World Scientific, London, 1995).
- 8 J. R. Waldram, *Superconductivity of Metals and Cuprates* (IoP Publishing, London, 1996).
- 9 A. P. Bramley, J. D. O'Connor, and C. R. M. Grovenor, *Supercond. Sci. Tech.* **12** (1999) R57.
- 10 A. Schilling, M. Cantoni, J. D. Guo, and H. R. Ott, *Nature* **363** (1993) 55.
- 11 L. Gao, Y. Y. Xue, F. Chen, Q. Xiong, R. J. Meng, D. Ramirez, C. W. Chu, J. H. Eggert, and H. K. Mao, *Phys. Rev. B* **50** (1993) 4260.
- 12 D. Dimos, P. Chaudhari, J. Mannhart, and F. K. Le Goues, *Phys. Rev. Lett.* **61** (1988) 219.
- 13 M. Tinkham, *Introduction to Superconductivity*, 2<sup>nd</sup> edition (McGraw-Hill, Singapore, 1996).
- 14 D. N. Zheng, A. M. Campbell, J. D. Johnson, J. R. Cooper, F. J. Blunt, F. J. Porch, and P. A. Freeman, *Phys. Rev. B* **49** (1994) 1417.
- 15 J. R. Clem, *Phys. Rev. B* **43** (1991) 7837.

- 16 J. H. Durrell, PhD Dissertation, University of Cambridge, Cambridge (2001).
- 17 B. D. Josephson, *Phys. Lett.* **1** (1962) 251.
- 18 J. Bardeen and M. J. Stephen, *Phys. Rev. A* **140** (1965) 1197.
- 19 D. Larbalestier, A. Gurevich, D. M. Feldmann, and A. Polyanskii, *Nature* **414** (2001) 368.
- 20 P. H. Kes, in *Concise Encyclopedia of Magnetic & Superconducting Materials*, edited by J. E. Evetts (Pergamon, Oxford, 1992).
- 21 T. P. Sheahen, *Introduction to High-Temperature Superconductivity* (Plenum, New York, 1994).
- 22 J. G. Daley and J. S. Badin, *Extended Abstracts of the 5<sup>th</sup> ISTEK-MRS Intl. Workshop on Superconductivity* (Honolulu HI, USA, 2001) 2.

<b>Chapter II Superconductivity</b>	<b>5</b>
2.1 Basic Physical Phenomena of Superconductivity	5
2.1.1 <i>Zero resistance</i>	5
2.1.2 <i>Meissner effect</i>	6
2.1.3 <i>The London penetration depth</i>	7
2.1.4 <i>The Ginzburg-Landau penetration depth and coherence length</i>	7
2.1.5 <i>Type I and type II superconductors</i>	7
2.2 High Temperature Superconductors	8
2.2.1 <i>Crystal structure and stoichiometry of YBCO</i>	8
2.2.2 <i>Other HTS materials</i>	11
2.2.3 <i>Anisotropy</i>	11
2.3 Flux Vortices and Pinning in Type II Superconductors	12
2.3.1 <i>Flux vortices</i>	12
2.3.2 <i>Flux flow</i>	14
2.3.3 <i>Flux pinning</i>	14
2.3.4 <i>Flux creep</i>	15
2.3.5 <i>Irreversibility line</i>	15
2.4 Electric Power Applications of HTS	16
2.4.1 <i>Power generator and electric motor</i>	16
2.4.2 <i>Energy storage</i>	16
2.4.3 <i>Electrical transmission and distribution</i>	17
2.5 Summary	18
References	18

---

## Chapter III Crystal Growth from High-Temperature Solutions

---

*Selected theories of crystal growth from high-temperature solutions are reviewed in this chapter, in particular the principle of liquid phase epitaxy, which includes a growth model that was developed based on the LPE of garnet films.*

### 3.1 Theory of Solution Growth

Single crystals may be produced from solid, liquid, or vapour phase. In the case of growth from the liquid phase, crystals may be grown from a pure melt or a solution; the latter may be further subdivided into aqueous and non-aqueous solutions. It is important to distinguish between crystal growth from pure melt and that from solutions.

Unlike crystal growth from pure melt, in the growth of crystals from solution, the constituents of the materials to be crystallised dissolve in a suitable solvent (water in the case of aqueous solution) and crystallisation occurs as the solution becomes critically supersaturated with solute. The solvent can be an element, a compound, or a combination of compounds. Usually, the solute is an element or a compound with a melting point generally higher than that of the solvent with an exception when the crystal to be grown is of eutectic composition. The supersaturation may be promoted by evaporation of the solvent, by cooling the solution, or by a transport process in which the solute is made to flow from a hotter to a cooler region. The major advantage of using a solvent is that crystal growth could take place at a lower temperature than that required for growth from pure melt.

Crystal growth from high-temperature solutions, as referred to in this chapter, is growth from non-aqueous solutions at elevated temperatures. Though, the terms "high temperature" and

"solution" are not definite; most experiments concerned are normally in the range from 300-1800°C and the solute concentration is usually up to 30% in terms of either molar or weight fraction [1]. High-temperature solution growth has been especially valuable in cases for materials with high melting points, high vapour pressures, or which decompose before melting, or melt incongruently. LPE is one of the techniques used for growing crystals from high-temperature solutions.

### 3.1.1 Supersaturation and driving force

A system has a minimum free energy at its equilibrium state. A melt at a temperature below its melting point or a solution below the temperature at which it is saturated with solute can decrease its free energy by precipitating solid. The energy made available evolves as *latent heat*. Hence, the driving force for crystallisation can be considered as the decrease in free energy difference between the solid and the supersaturated or supercooled liquid. This driving force is discussed as the chemical potential in vapour phase growth and as relative supersaturation  $\sigma$  in solution growth as follows [2]:

$$\sigma = \frac{C_L - C_e}{C_e} = \frac{\Phi \Delta T}{RT^2} \quad (3.1)$$

where  $C_L$  and  $C_e$  are the actual (bulk solution) and the equilibrium concentrations respectively,  $\Phi$  is the molar heat of solution,  $\Delta T$  is the undercooling, and  $R$  and  $T$  denotes universal gas constant and absolute temperature respectively.

Crystal growth involves two major processes: nucleation and growth. The formation of nuclei of the crystalline phase in a supersaturated liquid is the initial stage of crystallisation. Growth is the subsequent process by which these nuclei attain macroscopic dimensions.

### 3.1.2 Nucleation

*Homogeneous* nucleation is referred to as the formation of nuclei through composition fluctuations of the solute where solute atoms cluster together to form a solid phase. On the other hand, *heterogeneous* nucleation occurs when nuclei are formed at a solid interface or other favourable centres that differs from the nucleus phase.

In the case of homogeneous nucleation, fluctuations within a supersaturated solution give rise to small clusters of molecules, known as "embryos". The probability that an embryo will grow to form a stable nucleus depends on the change in free energy associated with its growth

or decay. The change in Gibbs free energy  $\Delta G$  associated with the formation of a spherical embryo of radius  $r$  can be simplified as [1]:

$$\Delta G = 4\pi r^2 \gamma - \frac{4}{3}\pi r^3 \Delta G_V \quad (3.2)$$

where  $\gamma$  is the interfacial surface energy of the solid-liquid interface and  $\Delta G_V$  represents the difference in the Gibbs free energy per unit volume between the solid and liquid phases.

As  $r$  increases from zero, the Gibbs free energy increases up to a critical value  $\Delta G^*$  at  $r = r^*$  and then decreases, thus  $r^*$  represents the minimum radius of a stable nucleus. The value of  $r^*$  is given by differentiation of Eqn. (3.2) as:

$$r^* = \frac{2\gamma}{\Delta G_V}. \quad (3.3)$$

The form of Eqn. (3.3) is similar for non-spherical shaped nuclei except that the numerical factor will be different.

The corresponding value of  $\Delta G$  in Eqn. (3.2) for a nucleus of critical size is given as:

$$\Delta G^* = \frac{16\pi\gamma^3}{3\Delta G_V^2}. \quad (3.4)$$

The relation between  $\Delta G$  and  $r$  can be illustrated as in Fig. 3.1.

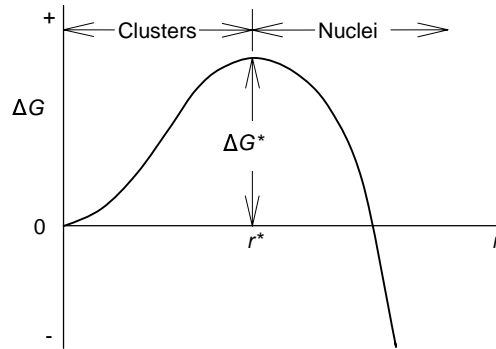


**Fig. 3.1** Free-energy barrier to nucleation. Adapted from ref. [3].

The critical radius  $r^*$  may be related to the relative supersaturation  $\sigma$  in the system as [1]:

$$r^* = \frac{2\gamma V_M}{RT\sigma} \quad (3.5)$$

where  $V_M$  is the molar volume. Eqn. (3.5) shows that an increase in supersaturation will decrease  $r^*$  and therefore favour nucleation. The thermodynamic barrier to the formation of a critical nucleus decreases rapidly with increasing undercooling.

The nucleation rate  $dN/dt$ , defined as the number of critical nuclei generated in a unit volume per second, is given by [4]:

$$\frac{dN}{dt} = N_o n^* \exp\left(\frac{-\Delta G^*}{k_B T}\right) \quad (3.6)$$

where  $N_o$  is the number of available sites for nucleation,  $n^*$  denotes the rate at which atoms are added to a nucleus, and  $k_B$  is the Boltzmann's constant. Upon cooling below the melting point  $T_m$ , the nucleation is slow until some temperature  $T_n$  is reached at which the nucleation rate increases rapidly as illustrated in Fig. 3.2.

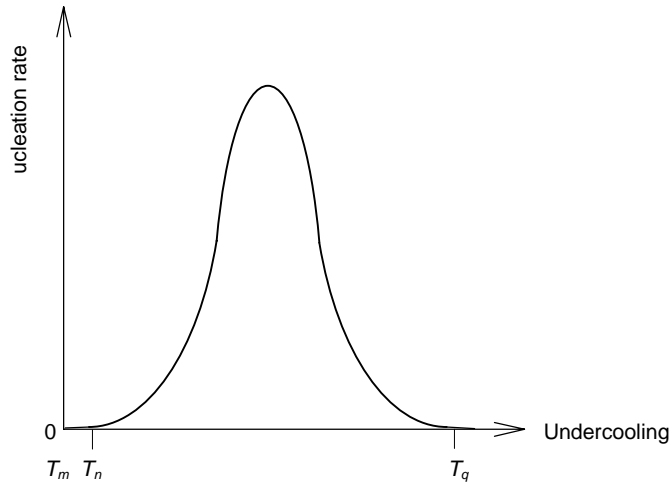


**Fig. 3.2** Temperature dependence of nucleation rate [1].

The metastable region between  $T_m$  and  $T_n$  in Fig. 3.2 depends on factors such as the purity of the melt and the presence of dust or other particles that may act as centres for nucleation. The nucleation rate continues to rise until a maximum value before declining due to a slowing down in the kinetics as the temperature is decreased, the rate will eventually become zero at some temperature  $T_q$ . If the melt is cooled to  $T_q$  without any crystallisation, a glass will form. A similar curve to Fig. 3.2 applies to nucleation from solutions.

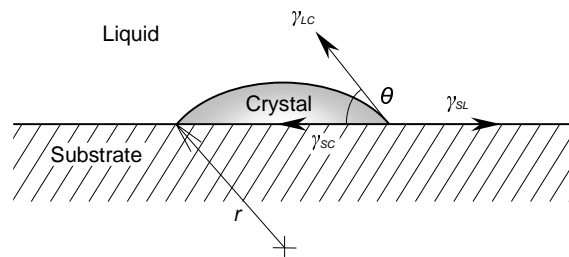


**Fig. 3.3** Formation of a cluster on a substrate. Adapted from ref. [3].

In the presence of a solid surface or other favourable centre such as foreign particles, the nucleation rate increases due to a reduction in the interfacial free energy. If the nucleus takes

the form of a cap from a sphere of radius  $r$  such that the contact angle made by the nucleus on the foreign substrate is  $\theta$  as shown in Fig. 3.3, equilibrium is attained when

$$\gamma_{SL} - \gamma_{SC} = \gamma_{LC} \cos\theta \quad (3.7)$$

where  $\gamma_{SL}$ ,  $\gamma_{SC}$ ,  $\gamma_{LC}$  are the surface energies of substrate-liquid, substrate-cluster, and liquid-cluster respectively.

The corresponding  $r^*$  and  $\Delta G^*$  are given as [5]:

$$r^* = \frac{2\gamma \sin\theta}{\Delta G_V}, \quad (3.8)$$

and

$$\Delta G_{Hetero}^* = \Delta G_{Homo}^* \left[ \frac{(1 - \cos\theta)^2 (2 + \cos\theta)}{4} \right]. \quad (3.9)$$

The free-energy barrier is dependent on the contact angle;  $\Delta G^*$  will disappear altogether if  $\theta$  is zero, that is, when the growing solid "wets" the substrate.

In the case of nucleation around a foreign particle of radius  $r_p$ , the value of the critical nucleus is the same as for homogeneous nucleation (Eqn. (3.3)) but the value of  $\Delta G^*$  is different and is given by [4]:

$$\Delta G^* = \frac{16\pi\gamma^3}{3\Delta G_V} + \frac{4}{3}\pi r_p^3 \Delta G_V - 4\pi r_p^2 \gamma_{LS}, \quad (3.10)$$

where  $\gamma_{LS}$  is the interfacial energy between the liquid and the foreign particle.

The free energy in heterogeneous nucleation (Eqns. (3.9) and (3.10)) is usually less than that required for homogeneous nucleation (Eqn. (3.4)), i.e. heterogeneous nucleation is easier to accomplish.

The classical theory of crystal growth is similar to the nucleation theory given above where the nucleation occurs on a crystal surface. Therefore, in such a "two-dimensional nucleation theory", it is more convenient to treat a cylindrical embryo of radius  $\rho_c$  and of height  $a$  as one growth unit. The critical radius of this 2-D nucleation is given as [1]:

$$\rho_c = \frac{\gamma_m a}{k_B T \sigma} \quad (3.11)$$

where  $\gamma_m$  is the energy per growth unit (e.g., unit cell) on the edge of the cylindrical nucleus.

### 3.1.3 Growth

Crystal growth involves processes where atoms or molecules are integrated into the crystal. There is no definite mechanism in crystal growth; different materials grow by different mechanisms and different faces of the same material grow differently.

There are three classical growth modes for thin film: (i) Volmer-Webber (V-W or island), (ii) Frank-van der Merwe (F-M or layer-by-layer), and (iii) Stranski-Krastanov (S-K) as illustrated schematically in Fig. 3.4. Island growth occurs when the smallest stable nuclei form on the substrate and grow in three dimensions to form islands. This happens when the atoms or molecules deposited are more strongly bound to each other than to the substrate (non-wetting behaviour). In contrast, in layer growth mode the smallest stable nuclei extend two-dimensionally which results in the formation of planar layers, due to their wetting behaviour. The S-K or layer-plus-island growth mode is a combination of the previous two mechanisms. In this case, after the formation of one or more layers, succeeding layer growth becomes unfavourable and islands form.

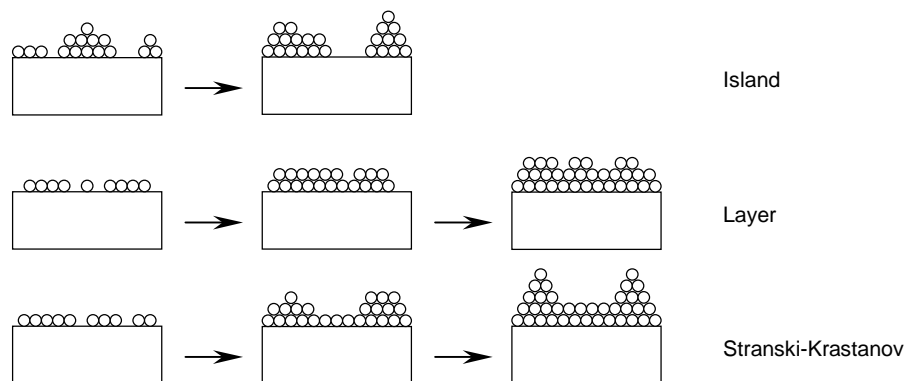


**Fig. 3.4** Basic modes of thin-film growth. Adapted from ref. [6].

In general, the process of crystal growth from solution may be treated as a combination of *mass transfer* and *surface kinetics* processes as summarised in Table 3.1.

**Table 3.1** Stages in crystal growth from a solution.

<i>Mass Transfer</i>	i.	Transport of solute atoms from the bulk of solution to the solute-diffusion boundary layer.
	ii.	Volume diffusion through this boundary layer.
<i>Surface Kinetics</i>	iii.	Adsorption on the crystal surface.
	iv.	Surface diffusion.
	v.	Attachment into a step.
	vi.	Diffusion along the step.
	vii.	Integration into the crystal at the kink in the step.

If the surface kinetic mechanisms are rapid as compared to the mass transport, the growth rate will become mass-transport controlled and vice-versa.

Following Brice [7] as well as Hillig and Turnbull [8], faces where crystals grow can be divided into two classes: *rough* and *singular* (or atomically smooth). Nucleation is generally not necessary for growth on rough faces, as atoms or molecules can be added at any position (e.g., kinks) on these faces, which grow more or less uniformly. The probability that an atom will become part of that surface is dependent on the bonding energy  $W_B$  exponentially as  $\exp(nW_B/k_B T)$  [1] where  $k_B$  and  $T$  are Boltzmann's constant and temperature, respectively, whereas  $n$  denotes the number of bonds form. The number  $n$  is more than one for an atom incorporating into a kink on a rough surface since more than one bonds has to be formed at a kink as compared to flat (smooth) surface. Therefore, it can be concluded that atomically rough surfaces have a much higher rate of growth than atomically flat surfaces.

Rough surfaces tend to remain rough as long as the atom is added in a way that provides a new kink site for the attachment of subsequent atoms. On the other hand, on a smooth surface, the rate-limiting step will be the addition of a new atom or group of atoms on that surface, since this group will form a layer with "rough" edges at which atoms can be integrated relatively easily until the layer covers the whole crystal face and the surface is smooth again.

If the Jackson's  $\alpha$  factor, which allows to evaluate the roughness of an interface [9], of a crystal is different for different faces, the crystal may readily develop straight edges. These straight edges are associated to the smooth (slow-growing) faces, since the rough (fast-growing) faces are eliminated as illustrated Fig. 3.5.

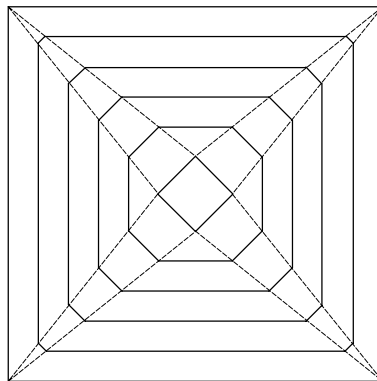


**Fig. 3.5** The fast growing faces ( $45^\circ$  lines) are eventually replaced by the slower growing faces (vertical and horizontal lines) [4].

### 3.1.4 Solute-diffusion boundary layer

It is important to distinguish between a solute-diffusion boundary layer and a hydrodynamic boundary layer. The latter is a layer that is considered stagnant because of adhesion to the crystal surface while the remaining liquid flows pass this surface. The boundary layer that will be discussed in this section is the solute-diffusion boundary layer.

The rate of solute transport per unit area  $J$  in the  $x$  direction, normal to the surface considered, is given by Fick's first law as:

$$J = -D \frac{dC}{dx} \quad (3.12)$$

where  $D$  is the diffusion coefficient of the solute in a solution with concentration  $C$ .

Considering a simple approximation of mass transport from a solution to a growth interface, where the bulk solution is perfectly stirred and yet there exists a solute-diffusion boundary layer near the solid-liquid interface. When a crystal is rotated in solution, the boundary layer thickness  $\delta$  is given by [10]:

$$\delta \approx 2^{2/3} D^{1/3} \nu^{1/6} \omega^{-1/2} \quad (3.13)$$

where  $\omega$  is the angular velocity of the crystal rotation and  $\nu$  is the kinematic viscosity of the solution. The stirring pattern for a rotating crystal/substrate in a stationary crucible can be approximated as shown in Fig. 3.6.

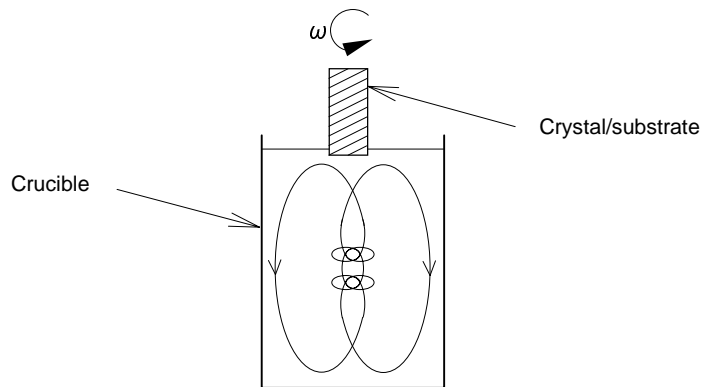


**Fig. 3.6** Stirring pattern for a rotating crystal in a stationary crucible. Adapted from ref. [4].

The solute concentration at the solid-liquid interface will approximate that of the equilibrium value  $C_e$ , provided that the kinetic process is extremely rapid compared to the volume diffusion. If the solute concentration gradient is uniform over the boundary layer, the linear crystal growth rate  $F$  in a volume-diffusion limited growth is related to  $\delta$  as [1]:

$$F = \frac{D}{\delta} \frac{(C_L - C_e)}{\rho} \quad (3.14a)$$

where  $\rho$  is the density of the crystal and  $C_L - C_e$  denotes the overall supersaturation, or in terms of relative supersaturation  $\sigma$  as:

$$F = \frac{D}{\delta} \frac{C_e \sigma}{\rho}. \quad (3.14b)$$

Hence, the steady-state growth rate in a stirred system depends on the overall supersaturation, diffusion coefficient of solute in the solution, and thickness of the solute-diffusion boundary layer. The substrate rotation rate will affect the boundary layer thickness according to Eqn. (3.13), which decreases with increasing rotation rate whereby the growth rate will increase accordingly. From Eqns. (3.13) and (3.14), it follows that there is a linear dependence of the growth rate  $F$  on  $\omega^{1/2}$ .

### 3.1.5 Generation of a growth spiral

Frank [11] showed that screw dislocation acts as a continuous source of steps on the surface of a crystal and the presence of the step associated with such a dislocation eliminates the need for surface nucleation, resulting in nucleation-free growth. Fig. 3.7(a) shows the face of a crystal with a screw dislocation emerging at  $P$ .

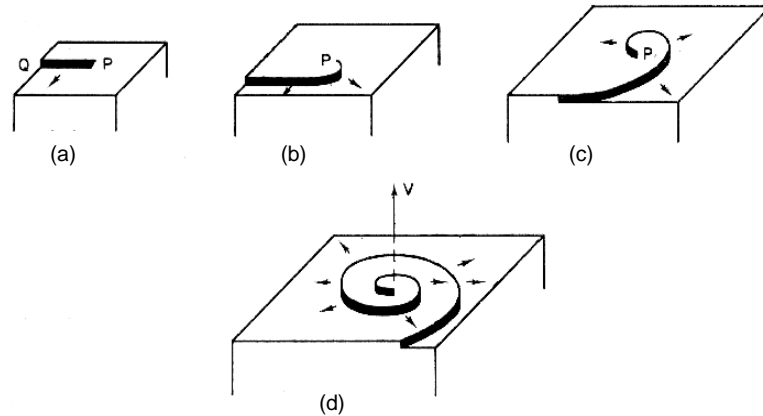


**Fig. 3.7** Development of a spiral [1].

Molecules are incorporated into the crystal at the step  $PQ$  (Fig. 3.7) of approximately monomolecular height with an initial growth normal to the step as indicated by the arrow. The emergence of the screw dislocation at  $P$  fixes this point so that the growth rate is zero here whereas elsewhere the step grows in such a way that its linear velocity is constant while angular velocity decreases with the distance from  $P$ . As the crystal grows, the step winds

itself up into a spiral with its centre at  $P$ . The spiral growth will continue until the separation of the adjacent layers at the centre is in the order of the radius  $\rho_c$  of the critical nucleus (Eqn. (3.11)).

### 3.1.6 The BCF theory

A theory of crystal growth including the mechanism of step generation and of transport into the step was given by Burton, Cabrera, and Frank [12], which is known as the BCF theory. As an approximation to the behaviour of a real growth spiral, BCF used the equation for an Archimedian spiral:

$$r = 2 \rho_c \theta \quad (3.15)$$

where  $r$  and  $\theta$  are the coordinates of any point on the spiral as indicated in Fig. 3.8.

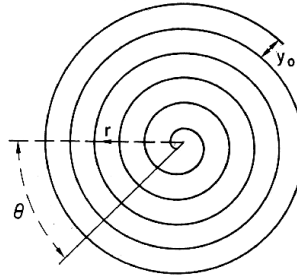


Fig. 3.8 An Archimedian growth spiral [1].

The distance  $y_0$  between the steps of the spiral is given as:

$$y_0 = 2 \rho_c (\theta + 2\pi) - \theta = 4\pi \rho_c . \quad (3.16)$$

In order to take into account the effect of non-Archimedian spirals due to the occurrence of dislocation pairs or groups (see §3.1.7 later), BCF introduces a factor  $\varepsilon$  such that:

$$y_0 = \frac{4\pi \rho_c}{\varepsilon} . \quad (3.17)$$

In the case of a group of dislocations with the same sign,  $\varepsilon$  can be as great as the number of dislocations contained in it. A group of  $S$  dislocations of the same sign, arranged on an array of length  $L$ , has an activity of  $\varepsilon$  times that of a single dislocation, and the value for  $\varepsilon$  are:

$$\varepsilon = S \quad \text{if} \quad 2\pi \rho_c \gg L , \quad (3.18a)$$

$$\varepsilon = S/2 \quad \text{if} \quad 2\pi \rho_c = L , \quad (3.18b)$$

$$\varepsilon = 2\pi \rho_c S/L \quad \text{if} \quad 2\pi \rho_c \ll L . \quad (3.18c)$$

If the dislocations are arranged on a circle, the length  $L$  can be replaced by  $\frac{1}{2}P$  where  $P$  is the perimeter of the group of dislocations.

However, Cabrera and Levine [13] give a more rigorous approach on the interstep distance as:

$$y_o \approx \frac{19\rho_c}{\varepsilon} = \frac{19\gamma_m a}{\varepsilon k_B T \sigma}. \quad (3.19)$$

When a spiral step is rough, containing a high density of kink sites, the step advances isotropically, with equal velocity in all direction, resulting in a spiral with circular shape. On the other hand, when the spiral step is smooth, with low density of kink sites, the advancing rate is strongly dependent on the stronger bonds within the surface (e.g., directional variation in  $\gamma$ ), resulting in anisotropic growth that leads to a polygonised spiral. A polygonised spiral may grow by a different mechanism than round ones since a smooth edge has less kink sites for attachment of growth units. Mutaftschiev [14] suggested that an interstep distance of a fully polygonised spiral originated from a single screw dislocation is related to the radius of critical nucleus  $\rho_c$  as:

$$y_o = 8\rho_c. \quad (3.20)$$

The second part of the BCF theory deals with the transport of atoms or molecules from the bulk of the solution to kinks in the steps of a spiral. Assuming that the growth rate is controlled by solute diffusion through the diffusion boundary layer adjacent to the growth surface whereby the molecules enter the kinks directly rather than by entering an adsorption layer and undergoing surface diffusion. The justification for this assumption was that the coefficient of volume diffusion ( $\sim 10^{-5}$  cm<sup>2</sup>/s) is normally much higher than the coefficient of surface diffusion ( $\sim 10^{-8}$  cm<sup>2</sup>/s) for molecules in solution so that any diffusion in a direction parallel to the crystal surface might be expected to occur in the boundary layer [1]. If the flow rate of solute atoms or molecules to the kinks is governed by diffusion through the boundary layer, the net flux reaching the steps, which governs the rate of advance, will be proportional to the supersaturation  $\sigma$ . The linear rate of advance of the step  $f_{st}$  is related to the interstep distance  $y_o$ , the overall growth rate  $F$  (Eqn. (3.14)), and step height  $h$  as [12]:

$$f_{st} = \frac{F y_o}{h}. \quad (3.21)$$

The theory predicts a quadratic growth curve  $F(\sigma)$  for low values of supersaturation with a gradual transition to a linear relationship as the supersaturation is increased above a critical value.

### 3.1.7 Non-Archimedian spirals

The growth spiral, as discussed in the BCF theory in previous section, has been assumed to be of approximately Archimedian shape with single screw dislocation origin. However, dislocations often exist in pairs or groups; therefore, spirals originating from such centres usually have more complex shapes and their growth mechanism may differ from the simpler case considered in §3.1.5.

According to BCF [12], if the growth centre is a pair of dislocations of the same sign separated by a distance greater than  $2\pi\rho_c$ , the resulting spiral will have the shape shown in Fig. 3.9. The two sections will be fed with steps from the two centres with activity similar to that of a single spiral. If the separation is much less than  $\rho_c$ , the centre effectively generates two spirals, each with the same step velocity  $f_{st}$ , hence, the activity will be twice that of a single spiral.

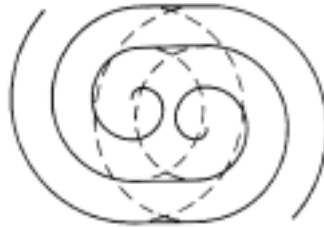


**Fig. 3.9** Growth spiral due to a pair of dislocations of same sign [12].

When a pair of dislocations of opposite sign are separated by a distance greater than  $2\pi\rho_c$ , the steps join up to form closed loops as shown in Fig. 3.10.

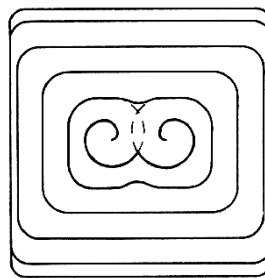


**Fig. 3.10** Layers due to a pair of dislocations of opposite sign [12].

Frequently, the spirals and growth features observed experimentally are not of unit-cell dimensions but may consist of 100-10000 unit cells, which are referred to as *macrospirals* with "bunching" steps. The formation of large steps by bunching is governed by kinetics rather than by thermodynamics [15,16]. Bunching has higher probability to occur in impure solutions since impurity molecules rejected by the crystal interface tend to impede the motion

of steps; highly immobile impurity ions may become incorporated into the crystal at the resulting macro-steps. In order to take into account step bunching, Klemenz and Scheel [17] introduced a variable  $m$  corresponding to  $m$ -fold activity of these step edges and modified Eqn. (3.19) to:

$$y_o = \frac{19\rho_c m}{\varepsilon} = \frac{19\gamma_m a m}{\varepsilon k_B T \sigma}. \quad (3.22)$$

### 3.2 Epitaxy

The term *epitaxy* implies the alignment of the crystal lattice of each layer of the grown film with the lattice of the substrate. *Homoepitaxy* refers to the case where the film and the substrate are of the same chemical composition whereas *heteroepitaxy* refers to the case where the film and the substrate are composed of different materials.

The lattice parameters are perfectly matched in homoepitaxy and therefore there is no interfacial bond straining. In the case of heteroepitaxy, the interface is essentially like that of homoepitaxy if the lattice mismatch is very small. However, when the film and substrate lattice parameters differ more significantly, either edge dislocation defects form at a small distance from the interface, for instant,  $\sim 20$  nm for  $c$ -oriented YBCO [18] (relaxed), or the two lattices strain to accommodate their crystallographic difference (strained) as illustrated in Fig. 3.11.

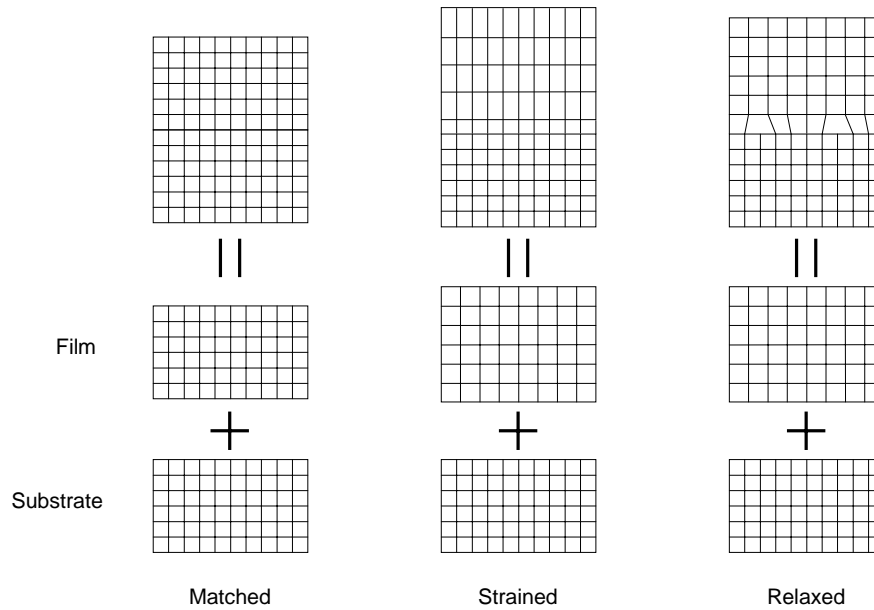


**Fig. 3.11** Schematic illustration of lattice-matched, strained, and relaxed heteroepitaxy structures. *Homoepitaxy is structurally very similar to lattice-matched heteroepitaxy [6].*

Epitaxial films can be grown from vapour phase (VPE) or liquid phase (e.g., LPE) processes. VPE processes such as physical and chemical vapour deposition (PVD and CVD) are the most widely used methods in growing thin epitaxial films. On the other hand, LPE technique has the advantages in that its equipment is simpler (e.g., does not require a high vacuum system) and higher growth rate of several orders in magnitude can be achieved [19].

### 3.3 Liquid Phase Epitaxy

*Liquid phase epitaxy* is a process by which an epitaxial layer of crystalline material is deposited from a saturated or supersaturated solution onto a suitable substrate. The substrate should have similar lattice parameters and linear thermal expansion coefficient to the material to be deposited, if the mismatch is excessive, strains will be introduced into the film leading to misfit dislocation or crack formations.

#### 3.3.1 The basis of LPE

The process of LPE has four stages:

- i. Producing a solution containing a quantity of solute corresponding to a saturation temperature  $T_s$ .
- ii. Cooling this solution to the growth temperature  $T_g$  producing an undercooling supersaturation corresponding to  $\Delta T (= T_s - T_g)$ .
- iii. Bringing the solution and the substrate into contact for an appropriate period of time for the layer thickness required where solution and/or substrate rotation can be used.
- iv. Terminating the growth by separating the solution from the substrate/film.

The order of stages (ii) and (iii) can be interchanged and the cooling can be started (or continued) after the solution and the substrate are brought into contact. Cooling of the solution to promote supersaturation may be in continuous or in a single step mode, or a combination of these two. Stages (iii) and (iv) require certain mechanical movement of the solution and/or the substrate. After growing a layer with the desired thickness, the substrate is removed and it is important to ensure that the surface is free from any drops of excess solution.

The deposition rate for epitaxial growth on flat substrates is normally limited by the rate at which the solute diffuses from the bulk of the solution to the solid-liquid interface. Hence, relative motion between the solution and the substrate is normally used to introduce forced convection in order to increase growth rate by reducing the thickness of the solute-diffusion

boundary layer. A horizontal or vertical rotating disc method is a convenient way to introduce such forced convection. However, the latter may cause significant turbulence depending on the substrate dimension and rotation rate.

It is usually assumed that interface kinetic is extremely rapid in LPE and nucleation may be expected to occur uniformly over the whole substrate area. Therefore, it is particularly important to have homogeneity of both temperature and solute distribution over the substrate surface to ensure uniform growth. Stirring the solution will lead to a more uniform growth as long as turbulence with non-uniform flow patterns is avoided.

The film growth rate depends on the method used to create the supersaturation, among which step-cooling, ramp-cooling, transient-mode LPE (TMLE), and steady-state growth have been used. In the step-cooling mode, the temperature of the initially saturated solution is lowered to a new value to produce a supersaturation. Using this method, the increase in film thickness was found [20,21] to be a function of the square root of growth time for the growth of semiconductor oxide films. However, it has not been reported if this  $\sqrt{t}$  growth kinetics is also observed in the growth of REBCO by LPE.

In the ramp-cooling mode, the temperature is reduced continuously by a programmable temperature controller after the substrate is immersed into the flux. In this case, the film thickness was found [20,21] to grow as  $t^{3/2}$  and continued to increase with time as a result of constant supersaturation maintained by the continuous cooling.

In TMLE growth, the flux is kept at the growth temperature (e.g., 1000°C) while the substrate is slowly lowered from room temperature until it reaches a temperature (e.g., 980°C) equivalent to the desired undercooling (e.g., 20°C) before film growth takes place. The advantage of this method is a greatly enhanced nucleation and rapid initial growth driven by the high local supersaturation. However, the exact level of supersaturation is hard to control and measure.

### **3.3.2 Experimental techniques**

The experimental set-up for LPE growth can be categorised by the motion of either the solution or substrate as tilting, rotating, dipping, or sliding technique as illustrated schematically in Fig. 3.12.

The earliest experimental designs for LPE growth are based on tilting motion with either tilting the entire furnace or just the crucible in order to bring the solution into contact with the substrate to initiate growth and in the reverse way to terminate growth. A more effective method is to rotate the crucible about a horizontal axis, allowing the substrate to be moved from a horizontal position for growth and to a vertical position for solution removal.

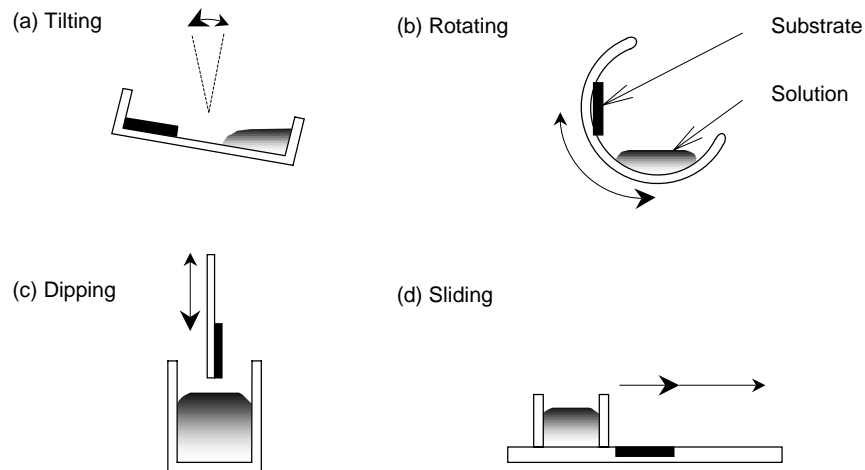


**Fig. 3.12** Experimental techniques to start (large arrow) and finish (small arrow) LPE growth.

Adapted from ref. [22].

In the case of dipping technique, the substrate, which can be placed in either horizontal or vertical position, is lowered into the solution for growth and lifted to end growth. The vertical substrate position may introduce a temperature gradient (hence a supersaturation gradient) across the substrate from top to bottom if the melt is not uniformly heated. In a horizontal rotating disc method, the boundary layer thickness is considerably reduced at the ends of the substrate as compared to the middle. Consequently, the epitaxial film grown is thicker at the edges than that in the middle.

A more advanced technique that is widely used in semiconductor industry is the sliding method. This technique enables one or more solutions (with different compositions such as different dopants for semiconductor multilayers) to be brought into contact with the substrate and then to be removed without relying on gravitational force for residual solution removal.

### 3.3.3 LPE growth model

In solution growth, the growth rate is generally controlled partly by volume diffusion through the boundary layer with thickness  $\delta$ , and partly by interface kinetics [1]. Furthermore, it is generally assumed that volume diffusion is a much faster process than surface diffusion as

discussed in §3.1.6. The model used to describe the growth of bulk crystals from solutions can be applied to LPE.

There exist different relations that may be used to express the growth rate  $F$  in terms of a kinetic reaction as:

$$F = k(C_i - C_e)^n \quad (3.23)$$

where  $C_i - C_e$  is the difference between the concentrations at the interface  $C_i$  and the equilibrium (saturation)  $C_e$  in the solution for a given temperature,  $k$  denotes the reaction constant that is temperature dependent, and  $n$  represents the order of the reaction.

Ghez and Giess [23] developed a growth model for LPE of garnet films with a rotating substrate based on first order kinetics ( $n = 1$ ). Both interface kinetics and volume diffusion processes were taken into account in the analysis, which yielded a steady-state growth rate that takes a modified form of Eqn. (3.14) as:

$$F = \frac{D}{\delta} \frac{(C_L - C_e)}{\rho} \frac{1}{1+R}. \quad (3.24)$$

The dimensionless parameter  $R = D/\delta k$  reflects the relative importance of volume diffusion to surface kinetics as the rate-limiting process.

In the case of fast interface kinetics ( $R \ll 1$ ), the growth rate is volume-diffusion limited, varying linearly with the supersaturation, and increasing as a function of square root of the substrate rotation rate  $\omega$ , through  $\delta$ . The results of Ghez and Giess [23] showed a negative intercept at the origin in the expression of the film thickness dependence on the square root of growth time, yielding a quantitative estimation of the surface reaction constant  $k$ .

The growth rate will increase with increasing substrate rotation rate, which reduces the boundary layer thickness until a critical value is reached where the growth becomes controlled by interface kinetics. Hence, at high supersaturation and high rotation rate, the steady-state growth rate will reach a maximum constant value for a given solute/solvent system, which is controlled by surface kinetics. On the other hand, at medium supersaturation, the growth rate may depend on both volume diffusion and surface kinetics processes as well as substrate rotation rate, whereas at low supersaturation, the volume diffusion process becomes predominant.

The formation of the Y123 phase was suggested by several researchers [24-26] to be proceeded by solute diffusion between the Y211 particles dispersed in the liquid phase and

the growing Y123 interface; that is, the rate-limiting step in such a reaction is the yttrium diffusion rate in the liquid. The diffusion coefficient  $D$  for yttrium in the flux (with different compositions) reported ranges from 1.0 to  $2.5 \times 10^{-12}$  m<sup>2</sup>/s by Gautier-Picard *et al.* [27], to  $6 \times 10^{-11}$  m<sup>2</sup>/s by Cima *et al.* [25], and  $45 \times 10^{-11}$  m<sup>2</sup>/s by Athur *et al.* [28]. However, the growth model developed usually oversimplified by assuming that solute diffusion is the rate-determining step in the reaction. In contrast, Nakamura *et al.* [29] suggested a mixed control of solute diffusion through the liquid phase and interface kinetics for melt-textured bulk crystal growth. Nevertheless, no studies involving both solute diffusion and interface kinetics, or similar detailed study by Ghez and Giess [23] have been done on the LPE of REBCO.

### 3.4 LPE of YBCO

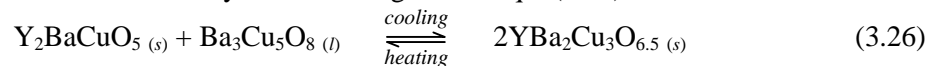
The LPE method was first developed for thin film growth of semiconductors and oxides for optoelectronics [30]. Growing HTS materials by LPE method was pioneered by Scheel *et al.* [31] who surveyed the essential problems and difficulties connected with the epitaxial growth of YBCO films. The principle behind LPE of YBCO lies in the peritectic reaction of the system.

#### 3.4.1 Peritectic reaction

The peritectic reaction is an isothermal reversible reaction in which a liquid phase reacts with a solid phase to produce a single (different) solid phase upon cooling through the peritectic temperature  $T_p$  as described below:



The peritectic reaction in YBCO system is analogised to Eqn. (3.25) as:



where  $\text{Y}_2\text{BaCuO}_5$  (Y211, a non-superconducting phase) reacts with  $\text{Ba}_3\text{Cu}_5\text{O}_8$  liquid to form Y123 upon cooling, or Y123 decomposes incongruently upon heating forming Y211 and  $\text{Ba}_3\text{Cu}_5\text{O}_8$  liquid (refer to the phase diagram in Fig. 3.13). Hence, a BaO-CuO solution containing yttrium solutes would be suitable for the growth of Y123 and the source of Y could come from compounds such as Y211 or  $\text{Y}_2\text{O}_3$ . Peritectic temperature of YBCO system reported varies from 1000°C [32] to 1005°C [33], and as high as 1020°C [34] in air. However,  $T_p$  between 1000-1005°C is widely used.

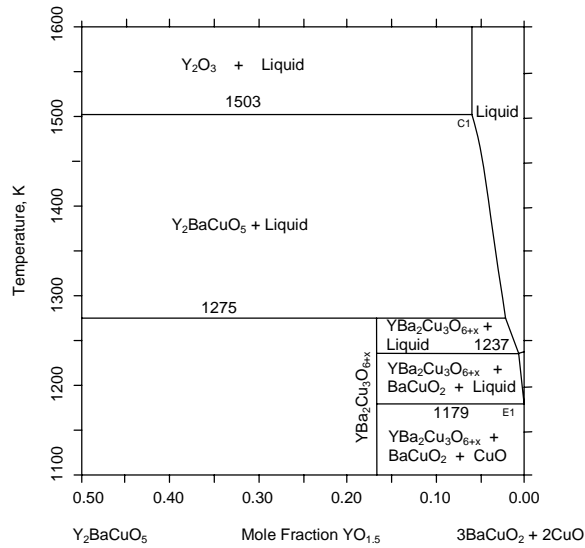


**Fig. 3.13** Pseudobinary phase diagram of  $YO_{1.5}$ -BaO- $CuO_x$  system at 0.21 atm  $O_2$  pressure [32].

### 3.4.2 Phase diagram and solubility curves

Knowledge of the phase relation, especially the primary crystallisation fields (PCF) and solubility curves, in the Y-Ba-Cu-O (or other RE) system is of fundamental importance for (Y/RE)BCO crystal growth. Due to the complexity of the ternary system ( $Y_2O_3$ -BaO-CuO) and peritectic reaction of YBCO, a reliable phase relation is difficult to obtain. This is demonstrated in Fig. 3.14, which shows the solubility curves of YBCO determined by several groups [33,35,36].

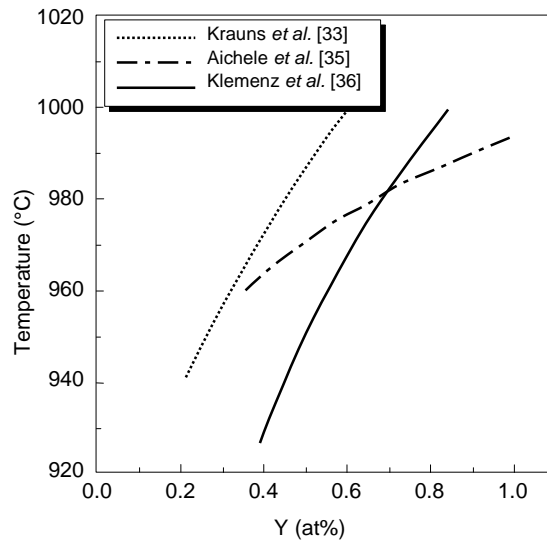


**Fig. 3.14** Solubility curves along pseudobinary sections through primary crystallisation field of YBCO in the  $Y_2O_3$ -BaO- $CuO_x$  system.

The strong scatter of solubility data in the literature is likely due to the different techniques, solution compositions (Ba:Cu ratio), and crucibles used, besides the difficulties in REBCO materials.

Fig. 3.15(a) shows a ternary phase diagram of Y211-CuO-BaCuO<sub>2</sub> system showing the PCF of Y123. For LPE (and crystal growth), experiments should be performed within the PCF. Ternary phase diagrams of other REBCO systems are not fundamentally different but the areas of PCF may vary; for instance, the PCF of NdBCO is much wider than that of YBCO.

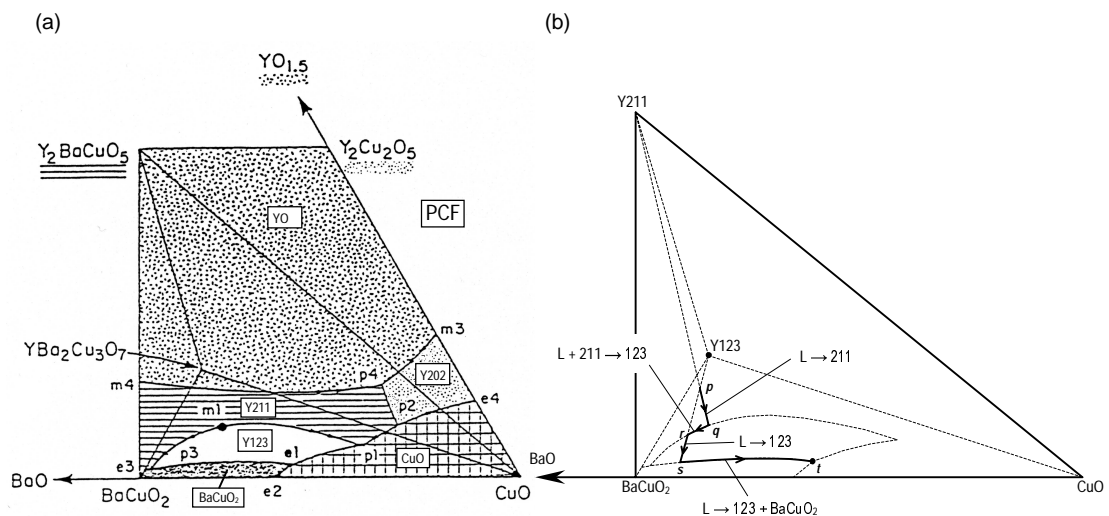


**Fig. 3.15** (a) Ternary phase diagram of Y211-CuO-BaCuO<sub>2</sub> showing the PCF of Y123 in air [37], and (b) a schematic ternary phase diagram of Y211-CuO-BaCuO<sub>2</sub> showing the path in cooling a melt of composition *p*, indicating by arrows in the direction of falling temperature. Adapted from ref. [38].

Fig. 3.15(b) illustrates the paths of liquid composition in cooling a melt of composition *p*. Upon cooling the liquid, solid phase Y211 crystallises out along *p-q*. From *q* to *r*, Y211 reacts with the liquid and forming Y123, i.e. peritectic reaction starts whereby Y211 reacts with liquid to form Y123 crystals around the Y211 particles. At *r*, all of Y211 has decomposed into Y123 but Y123 continues to crystallise from the liquid along *r-s*. Along *s-t*, Y123 and BaCuO<sub>2</sub> crystallise together and finally, at point *t*, the remaining liquid solidified via a eutectic reaction forming Y123, BaCuO<sub>2</sub> and CuO phases.

### 3.4.3 The principles in LPE of REBCO

The technique in LPE of YBCO (or REBCO) involves the undercooling of a molten flux supersaturated with one or more rare-earth elements in the presence of a suitable substrate.

The substrate is kept below  $T_p$  in order to nucleate the Y123 phase. Usually forced convection is induced by relative motion between the substrate and the flux in order to increase the growth rate by delivery of supersaturated solution to the growth interface.

Both nucleation and growth of the right phase (Y123) with the required  $c$ -axis orientation (for coated conductor applications) must be achieved. The solution is equilibrated at  $T_s$  (see Fig. 3.16) until some equilibrium concentration is reached (up to 0.6 at% for Y in Ba-Cu-O solution [33]). In the absence of seeds and agitation (stirring) this solution can be cooled, through the so-called Ostwald-Miers or *metastable* supersaturated region to  $T_{hom}$  where homogeneous nucleation will occur. The width of the Ostwald-Miers region decreases with an increasing degree of agitation, therefore smooth stirring is required to prevent spontaneous nucleation. The meta-stability occurs because a nucleus of critical size must be formed before crystal growth can take place.

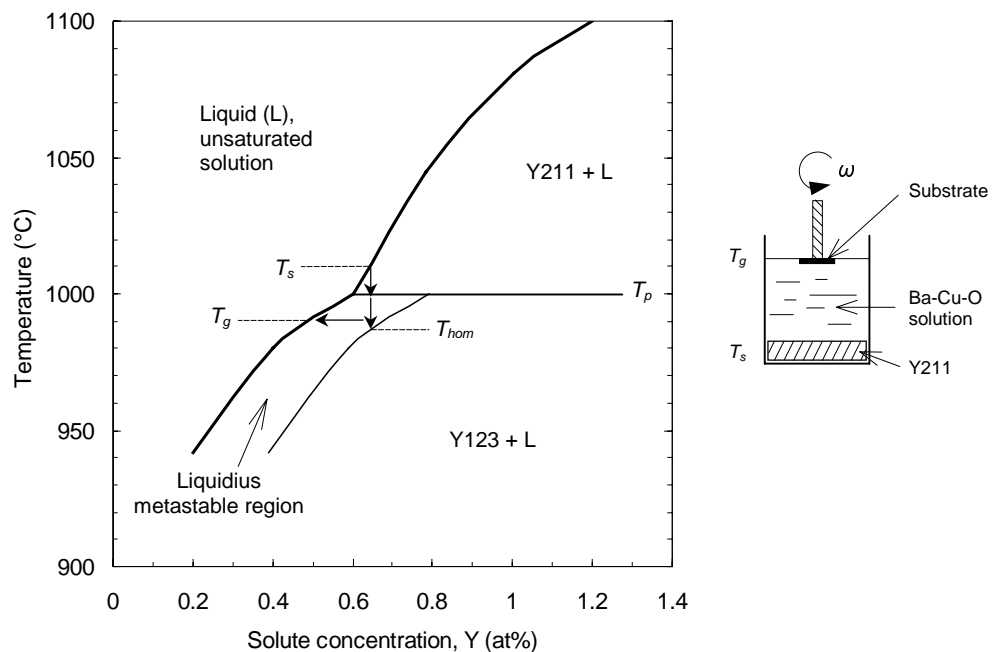


**Fig. 3.16** Yttrium solubility in Ba-Cu-O flux (solubility data from ref. [33]). The inset shows schematic of the experimental set-up with thermal-gradient crucible.

Heterogeneous nucleation usually occurs at some temperature above  $T_{hom}$ . Thus, in the presence of a seed or a substrate that is closely matched to the expected nucleating phase, nucleation will start at the seed or the substrate at some temperature  $T_g > T_{hom}$ . Nevertheless, heterogeneous nucleation will also occur at other potential nucleation sites such as dust particles or crucible wall. Therefore, it is essential to keep the growth solution as clean as possible from any foreign particles.

The experimental set-up with thermal-gradient crucible for growing YBCO by LPE consists of a crucible containing Y211 at the bottom and a Ba-Cu-O mixture on the top (see the inset in Fig. 3.16). Whilst the bottom of the crucible is maintained at a temperature a few degrees above  $T_p$  where the Y211 phase dissolves, the top of the crucible is at a temperature a few degrees below  $T_p$  where the Y123 phase is grown.

#### 3.4.4 LPE growth mechanism

Unlike vapour phase processes, LPE growth occurs near the thermodynamic equilibrium that has much lower driving force [2]. This low thermodynamic driving force in LPE allows the F-M (layer-by-layer) growth mechanism over macroscopic dimensions where screw dislocations or other defects act as sources of steps [35,39]. Nevertheless, in the growth of thick films for high current applications, since the surface flatness is not of major concern, as large a supersaturation as possible should be used in order to achieve the maximum growth rate since the growth rate is dependent on the level of supersaturation (Eqn. (3.14)).

Several researchers [40,41] found that the growth mode of the film changes from a multi-nucleation island growth to a spiral-step growth at screw dislocation centres. The mechanism of introducing the dislocations at the interface could be explained by the stress induced by strain due to the lattice misfit between the YBCO film and the substrate at the growth temperature [42].

Depending on the effective supersaturation and mass transport (convection or diffusion of the crystallising species), the growth-rate limiting factors can be of *surface kinetics* and/or *volume diffusion* as discussed in §3.1.3. Scheel *et al.* [2] argued that at low supersaturation  $\sigma$ , the rate-limiting factor is the surface kinetics leading to layer-by-layer growth and at intermediate  $\sigma$  step bunching occurs, whereas higher  $\sigma$  would result in 3-D nucleation. However, no experimental data from LPE of REBCO were used in the study.

#### References

- 1 D. Elwell and H. J. Scheel, *Crystal Growth from High-Temperature Solutions* (Academic Press, London, 1975).
- 2 H. J. Scheel, *Advances in Superconductivity VII* (Springer-Verlag, Tokyo, 1994) 29.
- 3 M. C. Flemings, *Solidification Processing* (McGraw-Hill, New York, 1974).
- 4 J. C. Brice, *The Growth of Crystals from Liquids*, Vol. XII (North-Holland, Amsterdam, 1973).

- 5 D. Dimos, P. Chaudhari, J. Mannhart, and F. K. Le Goues, *Phys. Rev. Lett.* **61** (1988) 219.
- 6 M. Ohring, *The Materials Science of Thin Films* (Academic Press, San Diego, 1992).
- 7 J. C. Brice, *Crystal Growth Processes* (Blackie Halsted, Glasgow, 1986).
- 8 W. B. Hillig and D. Turnbull, *J. Chem. Phys.* **24** (1956) 914.
- 9 K. A. Jackson, *Growth and Perfection of Crystals* (John Wiley & Sons, New York, 1958).
- 10 J. A. Burton, R. C. Prim, and W. P. Slichter, *J. Chem. Phys.* **21** (1953) 1987.
- 11 F. C. Frank, *Disc. Faraday Soc.* **5** (1949) 48.
- 12 W. K. Burton, N. Cabrera, and F. C. Frank, *Phi. Trans. A* **243** (1951) 299.
- 13 N. Cabrera and M. M. Levine, *Phil. Mag.* **1** (1956) 450.
- 14 B. Mutaftschiev, in *Dislocations in Solids*, edited by F. R. N. Nabarro (North-Holland, Amsterdam, 1980) 90.
- 15 N. Cabrera and D. A. Vermilyea, in *Growth and Perfection of Crystals*, edited by R. H. Doremus, B. W. Roberts, and D. Turnbull (John Wiley & Sons, New York, 1958) 393.
- 16 F. C. Frank, in *Growth and Perfection of Crystals*, edited by R. H. Doremus, B. W. Roberts, and D. Turnbull (John Wiley & Sons, New York, 1958) 411.
- 17 C. Klemenz and H. J. Scheel, *Physica C* **265** (1996) 126.
- 18 C. Klemenz, I. Utke, and H. J. Scheel, *J. Crystal Growth* **207** (1999) 62.
- 19 H. Nelson, *J. Crystal Growth* **27** (1974) 1.
- 20 M. G. Astles, *Liquid-Phase Epitaxial Growth of III-V Compound Semiconductor Materials and Their Device Applications* (IoP Publishing, Bristol, 1990).
- 21 R. L. Moon, in *Crystal Growth*, 2<sup>nd</sup> edition, edited by B. R. Pamplin (Pergamon Press, Oxford, 1980).
- 22 P. D. Greene, in *Advanced Crystal Growth*, edited by P. M. Dryburgh, B. Cockayne, and K. G. Barraclough (Prentice Hall, London, 1987).
- 23 R. Ghez and E. A. Giess, *MRS Bull.* **8** (1973) 31.
- 24 T. Izumi, Y. Nakamura, and Y. Shiohara, *J. Mater. Res.* **7** (1992) 1621.
- 25 M. J. Cima, M. C. Flemings, A. M. Figueredo, M. Nakade, H. Ishii, H. D. Brody, and J. S. Haggerty, *J. Appl. Phys.* **72** (1992) 179.
- 26 T. Izumi, Y. Nakamura, and Y. Shiohara, *J. Crystal Growth* **128** (1993) 757.
- 27 P. Gautier-Picard, E. Beaunon, and R. Tournier, *Physica C* **276** (1997) 35.
- 28 S. P. Athur, V. Selvamanickam, U. Balachandran, and K. Salama, *J. Mater. Res.* **11** (1996) 2976.
- 29 Y. Nakamura and Y. Shiohara, *J. Mater. Res.* **11** (1996) 2450.
- 30 B. M. Small, E. A. Giess, and R. Ghez, in *Handbook of Crystal Growth*, edited by D. T. J. Hurle, Vol. 3a (North-Holland, Amsterdam, 1994).
- 31 H. J. Scheel, M. Berkowski, and B. Chabot, *J. Crystal Growth* **115** (1991) 19.
- 32 B. J. Lee and D. N. Lee, *J. Am. Ceram. Soc.* **74** (1991) 78.
- 33 Ch. Krauns, M. Sumida, M. Tagami, Y. Yamada, and Y. Shiohara, *Z. Physik B* **96** (1994) 207.
- 34 W. Assmus and W. Schmidbauer, *Supercond. Sci. Tech.* **6** (1993) 555.
- 35 T. Aichele, S. Bornmann, C. Dubs, and P. Görnert, *Cryst. Res. Technol.* **32** (1997) 1145.
- 36 C. Klemenz and H. J. Scheel, *J. Crystal Growth* **129** (1993) 421.

- 37 M. Kambara, PhD Dissertation, University of Tokyo, Tokyo (1999).
- 38 S. Kawabata, H. Hoshizaki, N. Kawahara, H. Enami, T. Shinohara, and T. Imura, *Jpn. J. Appl. Phys. Pt 2-Lett.* **29** (1990) L1490.
- 39 H. J. Scheel, C. Klemenz, F. K. Reinhart, H. P. Lang, and H. J. Guntherodt, *Appl. Phys. Lett.* **65** (1994) 901.
- 40 T. Kitamura, S. Taniguchi, Y. Shiohara, I. Hirabayashi, S. Tanaka, Y. Sugawara, and Y. Ikuhara, *J. Crystal Growth* **158** (1996) 61.
- 41 T. Kitamura, I. Hirabayashi, S. Tanaka, Y. Sugawara, and Y. Ikuhara, *Appl. Phys. Lett.* **68** (1996) 2002.
- 42 T. Kitamura, Y. Sugawara, Y. Ikuhara, and I. Hirabayashi, *Advances in Superconductivity IX* (Springer-Verlag, Tokyo, 1996) 1077.

<b>Chapter III</b>	<b>Crystal Growth from High-Temperature Solutions</b>	<b>20</b>
3.1	Theory of Solution Growth	20
3.1.1	<i>Supersaturation and driving force</i>	21
3.1.2	<i>Nucleation</i>	21
3.1.3	<i>Growth</i>	25
3.1.4	<i>Solute-diffusion boundary layer</i>	27
3.1.5	<i>Generation of a growth spiral</i>	28
3.1.6	<i>The BCF theory</i>	29
3.1.7	<i>Non-Archimedean spirals</i>	31
3.2	Epitaxy	32
3.3	Liquid Phase Epitaxy	33
3.3.1	<i>The basis of LPE</i>	33
3.3.2	<i>Experimental techniques</i>	34
3.3.3	<i>LPE Growth Model</i>	35
3.4	LPE of YBCO	37
3.4.1	<i>Peritectic reaction</i>	37
3.4.2	<i>Phase diagram and solubility curves</i>	38
3.4.3	<i>The principles in LPE of REBCO</i>	39
3.4.4	<i>LPE growth mechanism</i>	41
	References	41

*This chapter presents an overview of the development in REBCO coated conductors and focuses on published results on the growth of REBCO type superconductors by the LPE method.*

#### **4.1 Introduction**

The most essential requirement of a coated conductor is that a superconducting layer is deposited on a substrate with both in-plane and out-of-plane texturing (biaxial alignment) of the grains. This is necessary because high angle grain boundaries create weak links that limit current flow.

The two major problems limiting the applications of conductors based on HTS materials are weak intragrain pinning and weak intergrain coupling [1]. As the origin of weak intragrain pinning is structural in nature, it is important to choose a material that has strong intrinsic flux pinning capability at high temperatures and magnetic fields. Despite the relative ease of fabrication, Bi-containing compounds have limited applications in high magnetic field at 77 K due to their intrinsically low irreversibility fields ( $B_{irr}$ , as shown in Fig. 2.12) [1,2]. Whilst Tl- and Hg-containing materials have higher  $B_{irr}$  than Bi compounds, low  $J_c$  values still remain due to the existent of weak-link dominated intergrain coupling problems [1,3]. In addition, both Tl and Hg are toxic and their production usually involves a second step for the incorporation of Tl or Hg into the crystal structure. Thus, REBCO type compounds remain the choice for coated conductor because of their high  $J_c$  at 77 K in the presence of high magnetic fields usually required for power applications, as well as their relative ease of fabrication among superconductors with high  $B_{irr}$ .

In recent years, there has been considerable progress in developing processes with the potential for fabricating long lengths of REBCO coated conductor. Such a conductor consists of a metallic substrate coated with a biaxially textured, non-reactive oxide buffer layer (e.g., YSZ, CeO<sub>2</sub>) and topped with a superconducting layer. There are two major approaches in preparing the buffered metallic tape, the first starts from an untextured metallic tape (e.g., Hastelloy) and uses advanced deposition techniques such as the so-called *ion beam assisted deposition* (IBAD) process [4] involving dual ion sources to grow the biaxially textured buffer layer and *inclined substrate deposition* (ISD) process [5].

The second approach starts with a biaxially textured metallic substrate tape made by a well-established thermo-mechanical process, known as the *rolling assisted biaxially textured substrate* (RABiTS) process, that was pioneered by Hitachi on textured Ag tape [6] and by Oak Ridge National Laboratory (ORNL) on textured Ni and Ni-alloy tapes [7,8]. Since the metallic substrate is biaxially textured, subsequent deposition of a textured buffer layer is relatively simple, among which the most straightforward method is to utilise the formation of biaxially textured native oxide on the RABiT substrates through controlled oxidation in the so-called *self-oxidation epitaxy* (SOE) process pioneered by Matsumoto *et al.* [9] in 1998.

The main differences in the first two approaches are that untextured tape requires a thicker buffer layer but uses a lower deposition temperature (~1 μm buffer at <100°C [10]) as compared to textured Ni tapes (20-50 nm buffer at 600-750°C [11]). RABiTS, especially SOE RABiTS, has the advantages of speed and relative simplicity over IBAD in terms of their potential industrial implementation.

## 4.2 Substrates

It is very crucial to choose a suitable substrate material in the production of coated conductor. The fundamental factors that affect the choice of substrate material include lattice mismatch (<0.1% [12]) with the superconductor, chemical compatibility, difference in thermal expansion coefficients (<10% [12]), suitable mechanical properties (e.g., ductility and strength), magnetic properties, and high-temperature stability, as well as size availability (length, width, and thickness) and cost effectiveness for large-scale production. In addition, it is preferable to use a thin (but strong) substrate in order to maximise the engineering critical current density  $J_{c,eng}$ , which is defined as current per total cross sectional area of superconductor and sheath. It is also desirable in certain applications, such as magnet windings, to have a mechanically flexible substrate.

Single crystalline ceramic substrates such as MgO, NdGaO<sub>3</sub>, SrTiO<sub>3</sub>, and yttria stabilised zirconia (YSZ) meet most of the criteria well, since they are chemically inert and stable at high temperatures. However, several factors, notably flexibility and availability in long lengths, prohibit the use of these ceramic substrates for large-scale applications. Metallic substrates have the obvious advantages where long lengths of flexible tapes may be produced if the thickness of the tape is kept below one hundred microns.

Among the metallic materials considered, several Ni-based alloys, developed for aerospace engine applications, have very good stability and oxidation resistance at elevated temperatures. Silver is another attractive candidate; since it is relatively inert and non-poisonous to REBCO, textured Ag tape usually does not require a buffer layer for PVD processes. However, Ag also has its major drawbacks such as its low melting point (~931°C in air) and extreme softness after annealing. High-temperature oxidation may be a problem for other metallic materials in consideration such as copper and steel.

Of the mechanical properties required by substrate materials, besides flexibility for certain applications as mentioned earlier, strength is of foremost importance. Reasonable high yield strength is necessarily in order to provide good mechanical support for handling of the conductor in various processing steps during and after deposition.

Difference in the thermal expansion coefficients of the substrate and superconductor is also important. Usually the substrate is much thicker than the film, thus, if assuming that both the substrate and film have similar Young's moduli, the substrate thermal expansion properties will determine that of the overall conductor. If the substrate has a smaller coefficient of thermal expansion than the film, the substrate will contract less than the film upon cooling from growth temperature, thus inducing a tensile stress on the film and vice-versa. If the tensile stress in the film is larger than what can be relieved by means of misfit dislocations and twin formation, the result is the creation of cracks on the film. Therefore, an ideal substrate should have a thermal expansion coefficient that matches or is slightly larger than the film.

Surface quality of substrates such as roughness, cleanliness, and grain boundary grooving played a significant role in the quality of YBCO grown. If the substrate is rough or has deep grooves between grains, smooth continuous YBCO layer cannot be grown. Although the surface cleanliness effect has not yet been fully studied, it is likely that any surface residue such as lubricant from the rolling process will interfere with film adhesion or the desired epitaxial growth.

For certain applications, conductive substrates are preferred as they can provide an electrical contact to the HTS layer. This would improve electrical stability where current would be able to locally transfer from the superconductor in the event of a failure in the HTS, hence, avoiding the creation of hot spots that could be detrimental. An alternative is to coat the HTS layer with a conducting shunt layer (e.g., Ag, Cu), which provides a measure of stability in the same way.

The magnetic properties of substrates could be important especially in cases where AC losses are of major concern in the applications. Usually substrate materials with minimum magnetic hysteresis loss are preferred. Table 4.1 presents properties of some of the commonly used substrates for YBCO.

**Table 4.1** Properties of some commonly used substrates for YBCO [13-16].

Substrate	Crystal structure	Lattice parameter <sup>†</sup> (Å)	Distance in unit cell for matching <sup>†</sup> (Å)	Misfit to YBCO <sup>†</sup> (%)	$\alpha^{\dagger}$ ( $10^{-6}/^{\circ}\text{C}$ )	m.p. ( $^{\circ}\text{C}$ )
Ideal	cubic/tetragonal	~3.85	-	-	13	<1700
NdGaO <sub>3</sub>	o.p.	$a = 5.43$ $b = 5.50$ $c = 7.70$	3.84 3.89	-0.26 +1.04	10	1750
SrTiO <sub>3</sub>	c.p.	3.91	3.91	+1.56	10.4	1920
LaAlO <sub>3</sub>	r.p.	3.79	3.79	-1.56	9-11	2100
MgO	cubic	4.21	4.21	+9.35	12.8-15.0*	2850
YSZ (Y <sub>2</sub> O <sub>3</sub> ) <sub>x</sub> (ZrO <sub>2</sub> ) <sub>1-x</sub>	cubic for $x = 0.08-0.4$	5.13-5.18	3.63-3.66	-(5.71-4.94)	11	2700
CeO <sub>2</sub>	cubic	5.41	3.83	-0.62	9.9-13.2*	2600
Ni	f.c.c.	3.52	3.52	-8.57	13.4-17.4*	1455
NiCr	f.c.c.	3.54	3.54	-8.05	11	~1430
NiV	f.c.c.	3.52	3.52	-8.57	11	~1425
NiFe	f.c.c.	3.59	3.59	-6.75	9.4-17*	~1450
NiCrW	f.c.c.	3.55	3.55	-7.79	11	~1440
CuNi	f.c.c.	3.58	3.58	-7.01	16.2	~1240
Ag	f.c.c.	4.08	4.08	+5.97	25.9*	931
Hastelloy	f.c.c.	3.52	3.52	-8.57	12.8	1325-1370

Keys: <sup>†</sup> values at room temperature unless otherwise stated;  $\alpha$  = coefficient of thermal expansion (\* denotes values at 1000 K); m.p. = melting point; o.p. = orthorhombic perovskite; c.p. = cubic perovskite; r.p. = rhombohedral perovskite; f.c.c. = face-centred cubic

### **4.2.1 Untextured metallic substrates**

With the development of the IBAD technique where biaxially aligned films may be deposited onto untextured substrates, the choice of metallic substrate materials becomes rather large. Commercially available materials remain a sensible choice and thus there is a lack of an optimum substrate candidate for IBAD route, as different groups choose to use different materials available.

Commercially available polycrystalline metallic substrates including various Ni-based alloys – Hastelloy, Inconel 601, Rene 41 – and stainless steel SS304 were investigated by Yin *et al.* [17]. Several researchers have also investigated other commercial alloys such as Inconel 625 [18,19] and stainless steel [20,21]. However, Hastelloy remains a popular choice and has been investigated by several groups [4,20,22-24].

### **4.2.2 Textured metallic substrates**

An alternative to producing a biaxially textured buffer layer on polycrystalline substrates is to produce a textured substrate itself whereby subsequent buffer and HTS depositions would be more straightforward. In order to deposit REBCO with (001) orientation, the most suitable texture for substrates with cubic symmetry is cube texture  $\{100\}\langle 001\rangle$ .

The RABiTS technique involves deformation of metal ingot via rolling and follows by an annealing step to develop the desired textures. Hence, the basic requirement for RABiTS materials is metals that can generate the desired textures by the rolling and recrystallisation process.

The technique was first developed using pure Ni [7] and Ag [6]. Ni is well suited as substrate material due to the easy formation of sharp cubic texture and its high oxygen resistance; however, its ferromagnetism and low tensile strength have to be overcome. Biaxially textured Ni tapes are now available in hundreds of meter length [25].

Over the years, various Ni-based alloys have been developed as suitable substrates for coated conductor applications. The main drives behind the development of Ni-based alloys are to improve its mechanical properties, to increase its oxidation resistance if possible, and to produce a non-magnetic substrate. Reger *et al.* [26] studied all possible alloying elements based on its solid solubility in Ni, cost, ability to reduce the Curie temperature below 77 K, as well as its ability to form sharp cubic texture in Ni solid solution and retain the FCC structure. They concluded that Cr, V, and Cu were the three alloying elements that would form cube

texture as sharp as pure Ni. In addition, they also showed that Cr and V alloying improved tensile strength. Hence, NiCr and NiV alloys remain the popular Ni-alloy tapes under investigation [27,28].

Other Ni alloys have also been explored. NiW textured tapes with improved yield strength and reduced magnetism have recently been reported by ORNL [29] and Eickmeyer *et al.* [30]. NiFe is another substrate material that exhibits sharp cube texture that was developed and used in the Brite-Euram MUST project [31]; it is now commercially available in kilometre length. However, the development of NiFe has been largely limited to the same group [32-37] and has not made significant breakthrough as a candidate for coated conductor applications.

The search for better-textured substrate materials has moved beyond binary alloys; recently, Tuissi *et al.* [38] have developed two Ni-based ternary alloys, NiCrW and NiCrV, with improved yield strength, magnetic properties, and oxygen resistance.

In recent years, the Japanese have developed high-strength clad-type composite tapes by inserting a core metal rod into a Ni pipe or sandwiching a core metal sheet between two Ag plates and subsequently cold rolled and annealed as in the RABiTS process. The core metal is usually stronger and/or has better magnetic property in order to improve its performance without losing the biaxial textures of the original tape on the outer layers. Furukawa Electric [39] has produced 30-m long Ni-clad/Ni-20%Cr (Ni/NiCr) and Ni-clad/austenitic stainless steel (Ni/SS) substrates with improved strength and reduced magnetic hysteresis loss. The in-plane full-width-at-half-maximum (FWHM) values of X-ray scans of these Ni-clad tapes are in the order of 15-23°.

Silver has the advantages of being a good electrical conductor and non-poisonous to HTS materials. There has been intensive research on Ag as a possible coated conductor substrate [17,40-50]. However, it has several drawbacks including low melting point (931°C in air), high raw material cost, and poor mechanical properties. Toshiba Corp. recently reported [48,49] a 100-m long of Ag-0.1wt%Cu/Ag-10wt%Ni/Ag-0.1wt%Cu clad tape with improved strength. Up to 1 m of the tape has been deposited with YBCO directly without buffer layer by PLD with YBCO in-plane FWHM of 23°. The average transport  $J_c$  reported was 0.12 MA/cm<sup>2</sup> with  $J_c$  above 10<sup>5</sup> A/cm<sup>2</sup> throughout the entire 1 m length. The higher material cost of Ag over Ni and Ni-alloy tapes may be compensated by the elimination of additional processing steps for buffer layers.

Similar reinforced Ag composite ribbons have also been developed by Suo *et al.* [51]. They examined the possibility of using AgMg, Ni, or Ni alloys as a reinforced core for Ag tapes and succeeded in producing  $\{110\}\langle 011\rangle$  Ag tapes with Ni core having in-plane FWHM of 10-15°. A very thin Cu intermediate sheath was used in between the Ag outer layer and the reinforced core in order to improve the bonding between the two layers prior to deformation (rolling). The total amount of Ag used in the composite tape was reported to be reduced by up to 40% as compared to pure Ag tape.

The textures of Ag that are suitable for coated conductor applications are the cube texture  $\{100\}\langle 001\rangle$ ,  $\{100\}\langle 011\rangle$ ,  $\{110\}\langle 110\rangle$ , and  $\{110\}\langle 001\rangle$ . Doi *et al.* [50] reported that out of the four possible cubic Ag textures, NdBCO would only grow on  $\{100\}\langle 001\rangle$  texture while YBCO would only grow on  $\{110\}\langle 110\rangle$ .

### 4.3 Buffer Layers

Due to chemical incompatibility and large lattice mismatch between the substrate and the superconductor such as in the case of Ni and YBCO, buffer layer(s) is usually required in order to prevent chemical reaction and reduce lattice mismatch with YBCO. The functions of the buffer as a chemical barrier include the prevention of metal atom diffusing into the superconductor as well as preventing oxygen diffusion through to the buffer/substrate interface that may oxidise the metallic substrate. In order to be an effective barrier, it is important that the buffer is free of cracks, which usually cause by stress induced through differential thermal contraction. Thus, buffer material having a closely matched thermal expansion coefficient with the substrate and superconductor is desired.

The basic requirements for a buffer layer are to be biaxially textured with suitable lattice parameters and non-reactive with the HTS layer. The crystallographic orientation of the buffer generally requires a  $\{100\}$  cube texture. Both metallic (e.g., Ag, Pd) and ceramic (e.g., YSZ, CeO<sub>2</sub>) materials have been used as buffer layers.

#### 4.3.1 IBAD buffer

The application of IBAD technique to coated conductor was first addressed by Iijima *et al.* [4] in 1992. The technique involves the use of an O + Ar ion beam to control the orientation of film growth. Using an IBAD technique, a thin film can be grown even on a polycrystalline substrate whereby the resulting biaxially aligned buffer can be used as a template for subsequent REBCO deposition.

YSZ was the focus in the early studies of IBAD buffer since its lattice parameters are a reasonable match with YBCO. The YSZ texture was found to be developed gradually and only reached the desired alignment at a thickness of 1  $\mu\text{m}$  [22,52]. Even though early work by Iijima *et al.* and Reade *et al.* [53] show poor buffer in-plane FWHM values of about  $30^\circ$ , however,  $J_c$  values of the YBCO deposited were in the order of  $0.5 \text{ MA/cm}^2$ .

Improvements have been made over the years and in-plane FWHM values of  $9\text{-}15^\circ$  are now achievable with a  $J_c$  of  $0.76 \text{ MA/cm}^2$  on short sample [54]. Recently, the same workers reported [55] a 10-m long Ni-alloy tape with IBAD-YSZ buffer having in-plane FWHM of  $10\text{-}20^\circ$ . A YBCO layer is deposited by PLD on this buffered tape with in-plane FWHM of  $9^\circ$  and has an average transport  $J_c$  of  $0.4 \text{ MA/cm}^2$ .

Another suitable buffer material for IBAD process is MgO. It appears that MgO has the advantage where only a very thin film is needed in order to achieve similar texture as in YSZ. Los Alamos National Laboratory [56] is developing IBAD-MgO buffer on up to 1-m long metallic substrates, as they claimed that only 10 nm of MgO (or 1 %) is needed to achieve IBAD-YSZ texture, which is approximately 100 times faster. PLD YBCO films with in-plane FWHM of  $4.5\text{-}10^\circ$  on IBAD-MgO/Ni-alloy substrates and transport  $J_c$  of 0.1 to  $>1 \text{ MA/cm}^2$ , depending on the substrate roughness, were reported.

Due to its close lattice matching with YBCO ( $<1\%$ ),  $\text{CeO}_2$  has been investigated via IBAD route but without much success [57]. Nevertheless, there is more success in using  $\text{CeO}_2$  as a cap layer to improve the lattice matching between IBAD-YSZ or MgO with YBCO. Holesinger *et al.* [58] showed that by adding a 30 nm  $\text{CeO}_2$  cap layer onto 700 nm IBAD-YSZ the  $J_c$  improved from 0.6 to  $1 \text{ MA/cm}^2$  with an overall critical current improvement from 100 A to 200 A. They also demonstrated that a cap layer that is too thick will reduce  $J_c$  as  $\text{CeO}_2$  grows thicker, it becomes rougher and more porous.

Despite the seemingly intensive research and positive results via IBAD route, the technique has a major drawback as being a vacuum process that may not be cost effective for industrial-scale production.

#### **4.3.2 Inclined substrate deposition**

Another technique that leads to in-plane alignment of films on untextured substrates is a similar method without ion beam assistance called *inclined substrate deposition* (ISD). Hasegawa *et al.* [5] first reported the method in 1996 using off-axis pulsed laser ablation

whereby biaxially aligned YSZ is deposited on untextured Ni-alloy substrates with a deposition rate of 0.5  $\mu\text{m}/\text{min}$ . The same researchers have also used this ISD technique to prepare a MgO film on metallic tapes as a buffer for LPE processed REBCO [59].

Sumitomo Electric [60,61] recently reported a 10-m long YSZ-buffered Ni-alloy tape prepared by reel-to-reel ISD with  $J_c$  of 0.05-0.2 MA/cm<sup>2</sup> throughout the tape. The tape moving speed was 1.2 m/h and the HTS deposition rate reportedly could be raised to 3  $\mu\text{m}/\text{min}$  by using an industrial scale 200 W, 660 mJ laser at 150 Hz. However, the  $J_c$  of the 10-m long tape dropped below 10<sup>5</sup> A/cm<sup>2</sup> at positions corresponding to target changing, thus, reducing the "effective" length to about 4-m pieces.

### 4.3.3 Ceramic buffer on RABiTS

Besides IBAD and ISD techniques, ordinary PLD has been widely used to deposit ceramic buffer layers. Since CeO<sub>2</sub> has a good lattice matching with YBCO, it has been widely used as a buffer layer in various single crystalline and metallic substrates. In 1997, Paranthaman *et al.* [62] and He *et al.* [11] first showed that epitaxial CeO<sub>2</sub> could be deposited on Ni substrates where they also found that CeO<sub>2</sub> film thicker than 50 nm cracked extensively. It was initially thought to be due to differential thermal contraction; however, Oh *et al.* [63] observed that there were substantially less cracks when depositing on Pt tapes and concluded that lattice matching is a more significant factor in determining crack formation.

Nevertheless, problems associated with CeO<sub>2</sub> cracking may be overcome by depositing a layer of YSZ on top [7]; thus Ni/CeO<sub>2</sub>/YSZ/YBCO became a standard architecture of early coated conductor studies. The best buffer architecture now appears to be CeO<sub>2</sub>/YSZ/CeO<sub>2</sub>. Since YSZ does not have very good lattice matching with YBCO as compared to CeO<sub>2</sub>, a second CeO<sub>2</sub> layer is added on top of the YSZ. The topmost CeO<sub>2</sub> layer is sometimes substituted with a RE<sub>2</sub>O<sub>3</sub> layer, which has relatively good lattice matching with YBCO.

Several groups have attempted these CeO<sub>2</sub>/YSZ or CeO<sub>2</sub>/YSZ/CeO<sub>2</sub> buffer architectures on different metallic substrate materials. Attempts by Holzapfel *et al.* [64] on NiCr tape were without much success due to the formation of a passive Cr<sub>2</sub>O<sub>3</sub> layer prior to CeO<sub>2</sub> deposition. Similar problem where native oxide formation preventing good epitaxial CeO<sub>2</sub> layer was faced by Boffa *et al.* [65] when trying on pure Ni tape; nevertheless, they solved the problem by using a Pd intermediate layer. On the other hand, Jackson *et al.* [66] showed that the Pd layer is unnecessary under different growth atmospheres such as using forming gas (H<sub>2</sub> in Ar). Using a forming gas, Tomov *et al.* were able to produce the buffer layers on NiV [67]

and NiFe [36] tapes with in-plane FWHM values of around  $9^\circ$  on the latter; however, the (111) growth component could not be eliminated completely. Bramley *et al.* [68] were able to produce similar buffer layers with better textures on NiFe with in-plane FWHM of  $3\text{-}4^\circ$ . Recently, Tomov *et al.* [69] have successfully deposited the  $\text{CeO}_2/\text{YSZ}/\text{Y}_2\text{O}_3$  buffer architecture without the need of a forming gas on the newly developed NiCrW ternary alloy tape [38]. The in-plane FWHM was  $10^\circ$  and they could completely eliminate the (111) growth components. In addition, Takahashi *et al.* [70] showed that  $\text{CeO}_2$  could also be grown on pure Ag almost without any (111) growth components. Whilst PLD could produce high quality layers, the technique is again a vacuum process that would be difficult to scale up.

RE oxides ( $\text{RE}_2\text{O}_3$ ) are another set of buffer candidates that have been widely studied. ORNL leads the field in RE oxide studies where they have investigated a wide range of oxides including  $\text{Y}_2\text{O}_3$ ,  $\text{Yb}_2\text{O}_3$ ,  $\text{Gd}_2\text{O}_3$ , and  $\text{Eu}_2\text{O}_3$  [71-73]. They deposited the  $\text{RE}_2\text{O}_3$  layer via either vacuum [71] or solution techniques such as sol-gel and spin or dip coating [72,73] and capped it with either YSZ and/or  $\text{CeO}_2$  layers via vacuum process. The best RE oxide for buffer layer reported is  $\text{Yb}_2\text{O}_3$ , possibly due to its close lattice matching with Ni. The other RE oxides are closer to YBCO. Buffer layers deposited via sol-gel process tend to produce lower  $J_c$  values ( $0.2 \text{ MA/cm}^2$ ) than those made by vacuum techniques ( $1.1 \text{ MA/cm}^2$ ) due to high porosity. This approach by ORNL involves multiple steps including vacuum, non-vacuum, and heat treatment processes, which would inevitably slow down the overall production time. This complication was probably the reason why the research on  $\text{RE}_2\text{O}_3$  buffer by ORNL seems to have ceased after the year 2000.

Ideally, the best process would be one that requires minimum or no buffer layers. With a lattice parameter in between Ni and YBCO,  $\text{Y}_2\text{O}_3$  has been studied as a possible single-buffer material by Ichinose *et al.* [74-76] using electron-beam (e-beam) evaporation. Well-textured  $\text{Y}_2\text{O}_3$  with in-plane and out-of-plane FWHM values of  $11^\circ$  and  $3^\circ$  respectively are reported. A relatively smooth film was produced but there is the evidence of (111) growth components present at grain boundaries, which could weaken the intergrain coupling.

There are many other ceramic buffer materials being considered including  $\text{LaNiO}_3$  [77-80],  $\text{Ni/LaNiO}_3/\text{SrRuO}_3$  [81,82], and  $\text{NdGaO}_3$  [83]; however, no significant breakthrough has been made in terms of quality, speed, and scalability.

#### 4.3.4 **Metallic buffer on RABiTS**

The metallic buffer on the other hand has not been widely studied even though they have the obvious advantages over ceramic materials in terms of ductility and electrical conductivity. The former advantage could be crucial where cracks induced by differential thermal contraction is causing a major problem. Metallic materials also have the advantage that the buffer deposition is usually taking place in reducing atmosphere or under UHV (ultra high vacuum) conditions. This decreases the risk of substrate oxidation.

It appears that Ag is the only metal suitable as the topmost buffer material because of its non-poisonous nature to REBCO. However, due to its large lattice mismatch (>13%) with Ni and Ni-alloys, other metals such as Pt and Pd are required as an intermediate layer [84,85].

#### 4.3.5 **Self-oxidation epitaxy**

A simple, scaleable, and cost effective route of buffer fabrication is to oxidise the metallic substrates and form a native oxide layer that functions as buffer layer. The technique involves controlled oxidation of the metallic tape in order to reproduce the biaxial alignment of the substrate onto the oxide buffer.

The oxidation of metallic tape as a buffer was first considered by Ginsbach *et al.* [86] in 1991 in which Ni sheets were oxidised to form NiO, but they were unable to produce the desired cube texture. Nevertheless, they did demonstrate that YBCO could be grown on NiO single crystals and estimated that a NiO layer of ~10  $\mu\text{m}$  thick is required to prevent Ni diffusion through the layer. It was not until 1998 when Matsumoto *et al.* [9] successfully produced an epitaxial NiO on Ni that more intensive research on the process they termed *self-oxidation epitaxy* (SOE) buffer took off.

The preferred growth orientations of SOE NiO on (100) Ni are (100) NiO and (111) NiO [87]. It was found that (100) NiO becomes dominant at elevated temperature above 1000°C in air [9]. Initial attempts of YBCO deposited on SOE NiO revealed low  $J_c$  (less than 0.1 MA/cm<sup>2</sup>). It was suggested that this might be caused by Ni inter-diffusion [88]. The same researchers [89,90] have thus added a thin oxide cap layer (MgO, YSZ, CeO<sub>2</sub>) between the NiO and YBCO and improved the  $J_c$  to 0.3-0.5 MA/cm<sup>2</sup>.

Recently, Watanabe *et al.* [39] reported a 30-m long SOE NiO buffer on their clad-type Ni/NiCr and Ni/SS tapes with the NiO in-plane FWHM in the order of 19°; however, only a

low  $J_c$  value of  $10^4$  A/cm<sup>2</sup> was obtained. Further work is required for SOE buffer layer to reach the level of performance of other buffer materials.

Several researchers have also been working on Ni-alloy tapes. Boffa *et al.* [91] have developed a cube textured NiO layer by oxidising NiV in 10 mTorr pure O<sub>2</sub> at 700°C for 30 minutes. The  $J_c$  of the YBCO deposited with a CeO<sub>2</sub> cap layer was 0.6 MA/cm<sup>2</sup>. Rutter *et al.* [33] used an additional step where the uncontrolled surface oxide on the NiFe tape was first removed before SOE was subsequently carried out, yielding a cube textured iron nickel oxide layer with a FWHM of 8°. Lockman *et al.* [92,93] reported a cube textured SOE NiO buffer on Ni-alloy tapes by oxidising NiCr at 1050°C for up to 1 hour and NiV at very high temperatures (up to 1275°C) for up to 3 hours.

## 4.4 Superconducting Layer

The fabrication of the superconducting layer can be broadly categorised into thin film and thick film techniques. The principal difference between the two categories is not necessarily the film thickness but the conditions used in growing the film.

### 4.4.1 Thin film

Thin film depositions usually utilise physical vapour deposition (PVD) techniques where the film grows at atomic-scale increment. Examples of these processes include pulsed laser ablation, sputtering, and e-beam evaporation. Most of the researchers worldwide deposit YBCO using one of these methods and high quality YBCO can now be consistently produced.

Early studies of YBCO coated conductors have been based on thin film technologies (PVD) as very high critical current densities were obtainable. These  $J_c$  values are usually  $>10^6$  A/cm<sup>2</sup> at 77 K and  $>10^7$  A/cm<sup>2</sup> at 4 K; fine-scale defects induced during growth are responsible for these high  $J_c$  values. Despite high  $J_c$  values, there is a widespread concern that such vapour phase technique may not be financially viable for many applications mainly due to its slow processing rate and the requirement of a vacuum system; the latter may cause difficulties in scaling-up production.

Another problem is that there exists an upper limit to the film thickness over which the desired *c*-axis oriented epitaxial growth can be maintained [1,13]. Presently most processes with buffered substrate tapes prepared by IBAD or RABiTS routes deposit the superconducting layer using a vapour deposition method. The YBCO thickness is usually

less than 1- $\mu\text{m}$  thick such that even with a critical current density in the order of  $10^5$ - $10^6$   $\text{A}/\text{cm}^2$ , the  $J_{c,eng}$  is still unacceptably low ( $10^3$ - $10^4$   $\text{A}/\text{cm}^2$ ) for electric power applications. Efforts made to increase the YBCO thickness to several microns could result in an intrinsically low-rate high-cost production route.

#### 4.4.2 Thick film

Thick film processes on the other hand are not very well established. Various thick film methods such as liquid phase epitaxy and its variations, ultrasonic spray pyrolysis, and *ex-situ*  $\text{BaF}_2$  processes have only been developed in recent years. The reasons for adopting these thick film processes are speed, scalability, and lower cost.

The most promising route for high-rate processing of REBCO seems to be by LPE as it is a one-step process capable of growing high quality films at high growth rates. The other thick film routes usually involve two processing steps whereby a precursor layer is first deposited either by ultrasonic spray pyrolysis, sol-gel spin or dip coating, or *ex-situ*  $\text{BaF}_2$  processes *etc.* This precursor layer is subsequently heat treated to crystallise the REBCO layer in order to obtain the desired biaxial textures.

Ultrasonic spray pyrolysis is a method whereby a nitrate or carboxylate precursor solution of the superconducting constituents is sprayed onto a substrate at elevated temperature [94-98]. Film composition is controlled empirically by adjusting the cation ratios in the solution, flow rate, and substrate temperature. Further heat treatment is required to improve film crystallinity and to optimise the microstructure. The growth rate of this process is in the order of 0.7-1  $\mu\text{m}/\text{min}$  [97]. This technique was primarily used for  $\text{TlBa}_2\text{Ca}_2\text{Cu}_3\text{O}_9$  (Tl-1223) [6,41] and  $\text{HgBa}_2\text{Ca}_2\text{Cu}_3\text{O}_8$  (Hg-1223) [99] compounds. Hitachi [41] reported a one-meter length Tl-1223 film on Ag tape with  $J_c$  of  $9 \times 10^4$   $\text{A}/\text{cm}^2$  at 77 K, 0 T. Initial attempt of YBCO deposition on Ag tape has been reported to have a large FWHM value of about  $20^\circ$  [96] even though results on single crystalline  $\text{LaAlO}_3$  shows a sharp texture with in-plane FWHM of  $\sim 3^\circ$  [97,98]. The main problems associated with spray pyrolysis are high porosity and rough surfaces on the YBCO layers.

In the *ex-situ*  $\text{BaF}_2$  process, the precursor film is co-evaporated by e-beam from Y, Cu, and  $\text{BaF}_2$  sources that follows by an *ex-situ* heat treatment process under controlled humidified atmosphere. The exact mechanism of the heat treatment process is still under investigation; however, Solovyov *et al.* [100] proposed that the metal-oxifluoride precursor decomposes as temperature increases in the presence of  $\text{H}_2\text{O}$  vapour while releasing HF, and the decomposed

precursor product is converted into Y123 phase. Hence, it is important for the conversion process to go to completion, which is generally a straightforward process for short samples. However, problems arose for longer samples where non-uniform YBCO conversion is reported [101]; this is thought to be due to the built-up of HF to a saturation level, leaving part of the precursor film un-reacted.

Metalorganic deposition using trifluoroacetate salt (TFA-MOD) is a better known sol-gel route attempted by several groups towards coated conductor fabrication [102-105]. Spin or dip coating is usually used to deposit the precursors that are then calcined under various different O<sub>2</sub> and Ar partial pressures. High  $J_c$  values ranging from 6.7 MA/cm<sup>2</sup> [105] to 7.5 MA/cm<sup>2</sup> [106] on single crystalline LaAlO<sub>3</sub> substrates and 1.7 MA/cm<sup>2</sup> on IBAD-YSZ on Hastelloy [107] have been reported. Nonetheless, all these high  $J_c$  films were very thin, ranging from 85 nm to 180 nm, resulting in low  $J_{c,eng}$ . Even with a recent result on a 3-cm long Hastelloy tape with  $J_c$  of 2.5 MA/cm<sup>2</sup>, the YBCO film was only 230 nm thick [108].

There is also research on processes similar to LPE with the aim to avoid the high-temperature Ba-Cu-O flux used in the LPE process. Hirabayashi *et al.* [109,110] proposed a process similar to LPE called *vapour-liquid-solid* (VLS) growth that is a combination of LPE and metalorganic chemical vapour deposition (MOCVD) processes. They first observed a quasi-liquid layer on the substrate at 750°C in MOCVD process, which is a temperature of the lower bound for growth in a Ag-saturated Ba-Cu-O-F flux under low partial O<sub>2</sub> pressure (see §4.7.3 for modification of growth condition to lower growth temperature). They proposed a process such that the source material for growth is generated in vapour phase while the growth is carried out in liquid phase. It is essentially a LPE growth with the Y-Ba-Cu-O source supplied from the vapour phase. This is to ensure the high growth rate from a liquid phase while keeping the processing temperature low (750°C). In VLS growth, the source vapour has to be first condensed onto the surface liquid layer and followed by crystallisation at the liquid-solid interface. Their results [109,111] showed that the VLS growth rate was five times higher than that of the conventional vapour-phase process. However, the growth rate (500 nm/h) is still very slow when compared to LPE process.

Recently, Jo *et al.* [112] reported a newly developed two-step *in-situ* liquid-vapour process similar to LPE to grow YBCO at relatively low substrate temperatures (800-900°C) with a growth rate of 1-10 nm/s. The YBCO film was deposited by e-beam evaporation from Y, Ba, and Cu sources at relatively low O<sub>2</sub> pressure. For the two-step growth, they reported that the liquid flux initial layer with a composition of Y<sub>0.03</sub>Ba<sub>0.37</sub>Cu<sub>0.6</sub> liquid layer was first formed on

the substrate and sequentially stoichiometric  $\text{YBa}_2\text{Cu}_3$  vapour was incorporated onto the liquid fluxed film. However, a non-uniform YBCO coverage was observed.

#### 4.5 Studies of Grain Boundaries as Weak Links Using Bicrystals

Applications of coated conductor require a highly aligned superconducting layer in order to minimise weak links caused by high angle grain boundaries (GBs). Systematic studies of artificial GBs in the form of bicrystals were pioneered by Dimos *et al.* [113]. A lot of work in this area has been done in thin films grown by PVD techniques. The  $J_c$  across GBs as a function of misorientation angle  $\theta$  shows that  $J_c(\theta)$  values are almost constant up to  $\sim 7\text{-}8^\circ$  and then decrease exponentially (see Fig. 4.1).

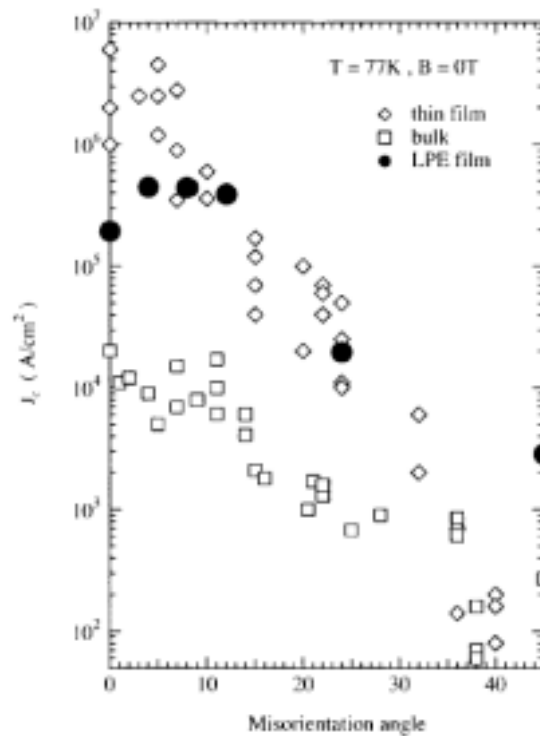


**Fig. 4.1** Dependence of  $J_c(\text{GB})$  on misorientation angle for bicrystals (adapted from ref. [114]). Thin film and bulk bicrystals data are from ref. [115].

Geometrically, a GB is characterised by two parameters: the relative misorientation angle of the adjoining grains and the facet plane of the boundary. Most of the GB characterisations in the past have been focusing on the misorientation angle. However, it has been pointed out recently [116-118] that  $J_c$  through different facets may vary dramatically. Hence, a single facet GB is necessary to obtain the intrinsic transport property dependence on the misorientation angles.

It is thought that the meandering of GBs in PVD films was due to the initial 3-dimensional (3-D) island nucleation and could be reduced by lowering the growth rate by means of using a smaller supersaturation (thermodynamic driving force) such that 2-D nucleation will take place [119,120]. Although the LPE technique has a much higher growth rate than PVD techniques, it has a much lower effective supersaturation level, and is thus ideal for growing large single-faceted GBs with 2-D nucleation.

In recent years, there has been several reports on the studies of YBCO grown on bicrystals via LPE [114,121-125]. Takagi *et al.* [121] first reported LPE grown YBCO on a 24° [001]-tilt MgO bicrystal. Transport measurements on straight single-faceted GB showed zero-field intergrain  $J_c$  of  $1.4 \times 10^4$  A/cm<sup>2</sup> at 77 K, which was one order in magnitude lower than the intragrain  $J_c$  of  $\sim 10^5$  A/cm<sup>2</sup>. Nonetheless, these inter- and intragrain  $J_c$  values are one order in magnitude lower than that in films grown by PVD techniques such as PLD.

Bicrystals with different misorientation angles were also explored. Wen *et al.* [114] investigated LPE grown YBCO films on 4°, 8°, 12°, 16°, 24°, 36°, and 45° [001]-tilt MgO bicrystals. All bicrystals used contained a seed layer prepared by PLD prior to the LPE growth. They confirmed that straight single-faceted GBs with 10-30  $\mu$ m were easily found on the LPE films. High-resolution electron microscopic (HREM) studies revealed that GBs with misorientation angles of 4°, 8°, 12°, 16°, and 45° were single facets at the atomic scale. While the 24° and 36° GBs were faceted at several nanometers scale. The studies also revealed that as the misorientation angle increased, the length of single facet region decreased and meandering increased [123]. Fig. 4.1 shows that the  $J_c$  values of LPE bicrystal films were almost constant up to  $\sim 12^\circ$  misorientation angle and dropped exponentially thereafter. This is thought to be because the GBs in bicrystal films  $< 12^\circ$  misorientation having almost no meandering microfacet structures within the 30- $\mu$ m strip width of the films used for the transport measurements.

Studies of bicrystal Josephson junctions in LPE grown YBCO films by Eltsev *et al.* [124,125] showed that selected samples demonstrated regular magnetic interference patterns, in contrast to PVD thin films, suggesting a better quality of the GB in LPE bicrystals compared to PVD samples.

## 4.6 Summary of Coated Conductor Development

The development of coated conductor technology has been reviewed. Clearly, there are still a lot of scientific and technological barriers to be overcome before long lengths of high  $J_c$  coated conductor can be produced commercially.

As for substrates, it remains unclear what is the best metallic candidate most suitable for coated conductor applications. Ni-alloy tapes seem to have advantages over pure Ni in terms of mechanical strength and oxidation resistance; however, the sharpness of texture in Ni alloys appears to be less superior than to pure Ni. And depending on the application, the ferromagnetism of substrates such as in pure Ni and NiFe could be beneficial. Ag has a major advantage over Ni or Ni-alloy tapes: the possibility of eliminating the need of a buffer layer. However, its poor mechanical properties and low melting point still remain as hurdles to be overcome.

In the area of buffer development, the optimum buffer layer(s) also remains unclear. The ideal situation would be a coated conductor without buffer layer, if not minimum buffer layer(s) deposited by non-vacuum processes. There are many buffer materials being investigated and all have potential advantages and disadvantages in terms of the ease of fabrication and fulfilling the functions of a buffer layer.

Whilst a high  $J_c$  superconducting layer can be reliably produced by various PVD techniques, there are major difficulties in transferring the technology to large-scale commercial production. High-speed, non-vacuum processes capable of fabricating thick films seem to be the most hopeful option for potential industrial implementation. Among these processes, LPE stands out as the most promising method in producing high-quality REBCO thick films at high growth rates as will be reviewed in the remainder of this chapter.

## 4.7 Liquid Phase Epitaxy of REBCO

LPE is one of the most promising routes for REBCO coated conductor fabrication as it has very high growth rates, typically one to two orders higher than that of vapour-phase deposition techniques, and being a non-vacuum process makes it an attractive candidate for possible industrial implementation.

Among the film preparation methods, LPE is one of the most promising growth techniques for preparing relatively thick films of high quality because the film is grown near the

thermodynamic equilibrium. However, due to incongruent melting, REBCOs are predominantly grown from high-temperature solutions. Apart from the high growth temperature, the LPE of REBCO poses another challenge: as the solubility of RE elements in the flux is very low, nucleation and growth is more difficult than the traditional LPE of semiconductors and garnet films.

#### 4.7.1 Early LPE of REBCO

Growing HTS compounds via the LPE technique started back in the late 1980s and early 1990s such as Bi-2212 [126-128] and Tl-1223/-1324 [129]. There are only few reports [130,131] on LPE of YBCO with relatively low  $T_c$  (61-85 K) in the early 1990s. It was Scheel *et al.* [13], having worked with LPE of semiconductor and optoelectronic films, who first presented details of the essential problems, difficulties, and possibility of growing HTS materials via LPE method in 1991. Since then, there has been intensive research worldwide on LPE of REBCO, first in Europe and later followed by the Japanese group at ISTEC. Early LPE of REBCO for coated conductor applications focused mainly on single crystalline substrates, since they were easier to grow on and thus can provide fundamental scientific knowledge about the process.

Early work on LPE of REBCO by Scheel *et al.* in Lausanne, Switzerland was intended for tunnel-devices (with  $a,b$ -axes orientation) rather than coated conductors. As LPE growth occurs near the thermodynamic equilibrium, extremely flat YBCO surfaces can be made for device applications by using low supersaturation for the LPE growth [132-134]. The same group also pioneered in finding suitable single-crystalline substrates for the process from their expertise in crystal growth [135]. They used BaO-CuO-RE<sub>2</sub>O<sub>3</sub> as starting materials in Al<sub>2</sub>O<sub>3</sub> or YSZ crucibles and started the film growth when the desired undercooling was reached using ramp cooling (at 0.3°C/h).

The research group in Jena, Germany, with experience in LPE of garnet films, started working on LPE of REBCO in the early 1990s and explored the undercooling "window" (or temperature range) for different growth orientations using various flux compositions. They also used a BaO-CuO-Y<sub>2</sub>O<sub>3</sub> flux in YSZ crucible and achieved the desired undercooling by means of step or ramp cooling. They first reported [136,137] that using a flux composition of Ba:Cu = 3:7, pure  $c$ -axis oriented growth only occurred with an undercooling of  $\leq 0.5^\circ\text{C}$  while an undercooling between 0.5 and 2°C lead to a mix  $a,b$ - and  $c$ -axis oriented film. However, they later reported [138] that an undercooling of  $\leq 2^\circ\text{C}$  resulted in  $c$ -axis oriented growth with the same flux composition of Ba:Cu = 3:7, while an undercooling between 3 and 14°C,

depending on the  $Y_2O_3$  concentration, would lead to pure  $a,b$ -axes oriented films. They also reported [139] using a  $CuO-BaCO_3-Y_2O_3$  mixture for the flux and grew  $a,b$ -axes oriented YBCO films at 960-970°C by means of ramp cooling (0.7-3°C/h) to achieve the desired supersaturation for growth. It remains unclear if the flux composition was the major factor leading to the different undercooling windows for  $c$ -oriented growth. They also observed that there could be significant a melt-back of the  $NdGaO_3$  substrates if the growth temperature was above the liquidus line and thus resulted in a mixed (Y,Nd)BCO film with reduced  $T_c$  [140].

The Japanese approach use a modified *top-seeded solution growth* (TSSG) method. A thermal-gradient crucible is used such that the bottom of the crucible is kept above  $T_p$  whereby a Y211 pellet dissolves while the top is kept below  $T_p$  where the Y123 phase grows on a suitable substrate. In order to avoid contamination, a  $RE_2O_3$  crucible is used. The advantage of this set-up is that the Y source is constantly supplied by natural thermal convection and is enhanced with forced convection by means of substrate or crucible rotation; hence, film growth can be carried out continuously. The Y source originates either from the Y211 pellet placed at the bottom of the crucible or from the  $Y_2O_3$  crucible.

As mentioned earlier, the most important factor governing LPE growth is the lattice mismatch of the substrate material with the growing phase. Different single-crystalline substrate materials were explored using LPE method at the early stage including (001)  $NdGaO_3$  [141], (110)  $NdGaO_3$  [132,137,139,142], (001)  $LaGaO_3$  [135,139], (110)  $La_xNd_{1-x}GaO_3$  [143], (100) sapphire [131], (001)  $LaAlO_3$  [144], (100)  $MgO$  [145-148], (100) YSZ [149], and (001)  $PrBa_2Cu_3O_{7-\delta}$  [150].

#### **4.7.2 Nucleation and growth of REBCO by LPE**

The mechanism of nucleation and growth of REBCO via LPE method has been widely studied and varied slightly depending on the type of films and substrates. This section has been divided into five sub-sections, which includes the nucleation and growth processes of YBCO and NdBCO on  $NdGaO_3$  substrates as well as seeded  $MgO$  substrates. The final two sub-sections discuss the factors affecting the film growth mode ( $c$ - or  $a,b$ -oriented) such as the undercooling (supersaturation level) used.

##### **4.7.2(a) Nucleation and growth of YBCO on $NdGaO_3$**

Kitamura *et al.* [151] observed that the LPE process on YBCO started from a transient heteroepitaxial multi-nucleation growth and changed into a steady-state homoepitaxial spiral-step growth. The driving force of the initial growth was thought to be local supersaturation

caused by the temperature difference between the substrate and the flux in the non-steady state growth and that the later growth is the supersaturation realised by convection. Their results showed two growth stages where the initial growth before 180 s was very rapid but soon slowed down to very low rates before eventually growing at an almost constant rate of  $\sim 2 \mu\text{m}/\text{min}$  as shown in Fig. 4.2.

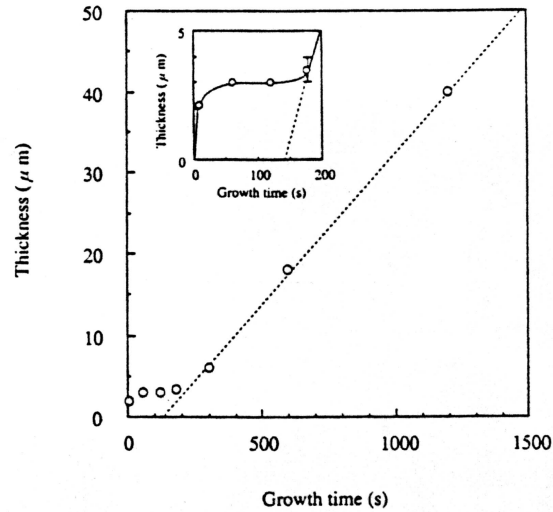


**Fig. 4.2** The growth time dependence of film thickness of YBCO films showing two growth stages with initial and steady-state growth [151].

It is thought [151] that the large supersaturation due to the difference in substrate and flux temperatures, even after prolonged equilibrium, was the cause of the initial rapid growth. Very slow growth was then observed due to depletion of Y solutes at the growth interface after the YBCO film covered the entire substrate. Eventually, as forced convection induced by substrate rotation brought the Y source to the growth interface, the growth rate increased and reached a steady state as the continuous supply of Y solutes stabilised.

AFM image showed the presence of growth islands on plate-like crystallites [151]. The islands on *c*-oriented film were about 12 nm in height, which corresponds to about ten unit cells of YBCO, while the plate-like crystallites were in the order of 20-30 nm thick. This indicates that the precipitates were formed on the plate-like crystallite and continued to grow until they formed a new layer. The mechanism of the initial growth was described as the repetition of these crystallisation processes.

Kitamura *et al.* [151] observed the presence of spiral-step bunching in the later growth stage. From this result, it is thought that the growth mode changed from the initial transient growth

to spiral-step growth around screw dislocation cores. This spiral-step growth mode is regarded as a homoepitaxial growth on top of the initially grown YBCO.

The difference of the growth mode, be it multi-nucleation or spiral-step, is dominated by the driving force for crystal growth: the chemical potential difference  $\Delta\mu$  between the solute and the flux. In order to form the nuclei, the new surface energy of the critical nucleus must be compensated. In contrast, the spiral-step growth occurs with the attachment of the solute to the steps and the source of the step is the screw dislocation. There is no disadvantage in the formation of critical nuclei in the case of spiral growth. Thus, the growth mode of the later growth may be selected to be the spiral growth, which gives a possibility of growth at lower driving forces.

Kitamura *et al.* [152] also reported that the growth mechanism of *a,b*-oriented YBCO films consisted of three stages: (i) nucleation and island growth, (ii) lateral growth of island, and (iii) layer formation due to coalescence of the islands. The repetition of island growth and coalescence thickened the film.

#### **4.7.2(b) Nucleation and growth of NdBCO on NdGaO<sub>3</sub>**

The LPE growth of NdBCO also showed two growth stages with initial transient and steady-state modes. However, in contrast to YBCO, the initial rapid transient growth was only about 10 s before entering the transition stage that lasted until  $t = 30$  s [153-155]. Furthermore, NdBCO growth showed a negative growth rate in the transition period between the two growth modes when the films were grown using transient-mode LPE (TMLE).

Takagi *et al.* [155] observed that when the NdBCO films were grown in the TMLE mode, the top surface of the films was characterised by structures with step heights varying over several to some ten unit cells along the *c*-axis and with many small-angle tilt boundaries. In contrast, when the films were grown in a step-cooling mode, spiral steps with the height of a mono-unit cell were observed on the top surface and small-angle tilt boundaries were reported to be greatly reduced. They concluded that the growth mechanism in the TMLE was mainly dominated by the lateral growth of macro-steps, whereas it was dominated by the spiral-step growth of micro-steps in the step-cooling mode.

#### **4.7.2(c) Nucleation and growth on seeded substrates**

Earlier reports of films grown on MgO [145-148] and YSZ [149] substrates by the Japanese group at ISTEC did not mention the presence of a YBCO seeding layer. However, they later claimed that no LPE growth could be achieved without the seed layer of YBCO on MgO,

YSZ, SrTiO<sub>3</sub>, Ag, and Ni-based substrates due to high degree of lattice mismatch [156-159]. These seed layers are usually grown by PVD techniques such as PLD and ratio-frequency (rf) thermal plasma evaporation.

It has been noted [160-162] that two orientations of seed grains exist on the MgO substrates that are 45° misoriented. The epitaxial relations are: [100] or [010]<sub>YBCO</sub> || [100]<sub>MgO</sub> and [110]<sub>YBCO</sub> || [100]<sub>MgO</sub>, denoted as 0°- and 45°-oriented grains respectively. The presence of these two in-plane grain orientations was reported [163] to be observed even on *c*-axis oriented YBCO films grown by LPE on (100) MgO substrates. The  $J_c$  values varied significantly between films with only 0° grains and those with both 0° and 45° grains whereby the 45° angle grain boundaries act as weak links in transporting current and resulting in a  $J_c$  value nearly two orders of magnitude lower.

Ishida *et al.* [160] and Kakimoto *et al.* [161] observed that initially the seed layer on MgO partially dissolved in the flux prior to LPE growth. Results showed that the 45° oriented grains preferentially dissolved into the oxide flux prior to that of 0° oriented grains. They concluded that only grains exceeding the critical size served as nuclei while the smaller ones dissolved. The remaining islands of nuclei eventually extended laterally and coalesced with one another to form fully covered film. The resultant LPE grown YBCO films only have the 0°-oriented grains. It is thought that this partial dissolution of the seed grains improved the crystallinity of the LPE films.

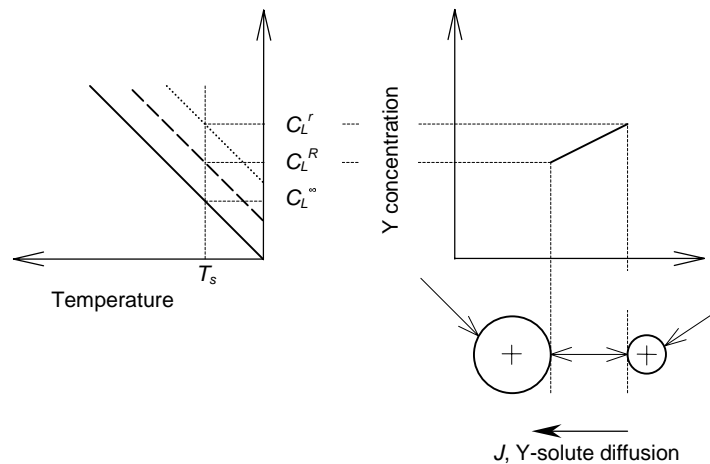


**Fig. 4.3** Schematic images of the basic idea for the coarsening mechanism due to the curvature difference in two platelet YBCO grains. Adapted from ref. [161].

Ishida *et al.* [160] attempted to explain the driving force of this preferential dissolution by the coarsening mechanism due to curvature difference in two platelet YBCO grains. When a grain has a certain curvature, the dissolution temperature of the grain decreases by the

difference of the curvature from the bulk of infinite radius of curvature as shown in Fig. 4.3. Different interfacial Y concentrations could be assumed for different radii of the grains at the same temperature ( $T_s$ ). As the curvature of the grain becomes small (large radius), the interfacial Y concentration of the grain also becomes small. When two grains have different curvatures, the diffusion of Y solutes from the small grain to the large one takes place due to the difference in Y concentration between the grains. Consequently, a smaller grain dissolves and a larger one grows and average radius increases.

Nevertheless, Kakimoto *et al.* [161] also observed similar preferential dissolution of the 45°-oriented grains even when both the 0°- and 45°-oriented grains have similar grain sizes. Hence, they argued that the phenomenon could not be explained by the coarsening mechanism due to curvature difference alone. They suggested that the difference in the interfacial energy between the two different kinds of grains with the MgO substrates might have contributed to the preferential dissolution. Izumi *et al.* [164] investigated further and developed a growth model based on the difference in curvatures and bonding energies between the seed grains and the MgO substrate as driving forces for growth. The model agreed well with experimental results showing the preferential dissolution of 45°-oriented grains.

Nomura *et al.* [165] observed a preference in growth orientation of REBCO on seeded MgO substrates. In the case of YBCO, it was revealed that the <100> directions of YBCO grew along the <100> directions of YBCO seeded MgO (0° orientation); whereas in the case of NdBCO, it was found that the <100> directions of NdBCO crystal grew along the <110> directions of NdBCO seeded MgO (45° orientation). Based on the model developed by Izumi *et al.* mentioned above [164], Nomura *et al.* incorporated the Coulomb force into the interfacial bonding energy, as they argued that both the film and substrate are ionic crystals. Their calculations of Coulomb force density based on the O-lattice theory by Bollmann [166] showed two attractive forces exist for the lattices of YBCO and MgO at 0° and 45° orientations and the magnitude of the force was larger at 0° than at 45° orientation. In the case of NdBCO, there is only one attractive force between the lattices of NdBCO and MgO at 45°. All calculations agreed well with the experimental results.

Kai *et al.* [167] investigated the stability of YBCO seed film on MgO buffered Hastelloy tapes in a MgO-saturated Ba-Cu-O flux. They found that the YBCO seed layer was more unstable in the flux when it was deposited on MgO buffer layer as compared to MgO single crystal. This is thought to be due to the larger bonding energy in the seed film on single crystal, which has better in-plane alignment when compared to seed film on MgO buffer

layer. Furthermore, YBCO seed layer prepared by PLD with a target containing MgO showed improved stability in the MgO-saturated flux. They explained this observation from the thermodynamic stability point of view.

The difference in the mechanisms of YBCO homoepitaxial and heteroepitaxial growths has been studied by Nomura *et al.* [168,169]. They observed that when growing on YBCO substrates (homoepitaxial growth), a lot of small crystallite islands were generated within several tens of ms; whereas in the case of heteroepitaxial growth on seeded MgO substrates, partial melt-back of the seed grains as mentioned earlier was observed. Even though the MgO substrates were seeded with YBCO, they argued that the bare substrate was exposed due to partial dissolution of the seed layer and hence it was justified as heteroepitaxial growth. Furthermore, in the case of homoepitaxial growth, the slope angle of LPE grown island as defined in Fig. 4.4 increased up to  $\sim 10^\circ$  within the initial 0.1 s and gradually decreased to  $\sim 0.2^\circ$  with increasing growth time. In contrast, in the case of heteroepitaxial growth, the slope angle of the grain increased from  $\sim 10^\circ$  to  $\sim 60^\circ$  with increasing time and saturated at  $\sim 60^\circ$  until full coverage of the film on the MgO surface.

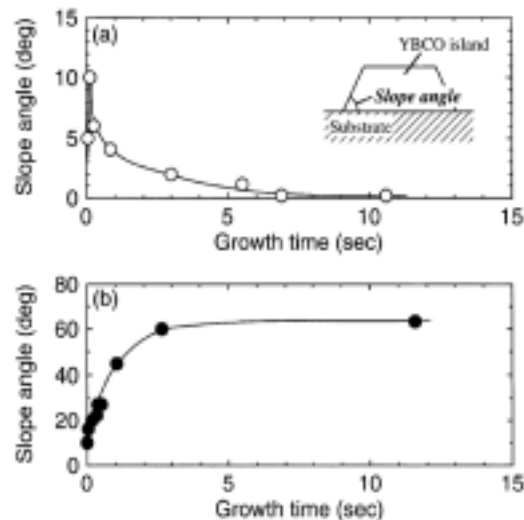


**Fig. 4.4** Slope angle of LPE grown islands as a function of growth time for (a) homoepitaxial growth, and (b) heteroepitaxial growth [168].

They explained this phenomenon by considering the difference in the lateral growth rates between the homo- and heteroepitaxial growth interfaces where they found that the lateral growth rate on YBCO substrate was twice as fast as that on MgO substrate. They also found that the heteroepitaxial interface strongly affected the quality of the LPE film, as flux might be trapped in between when two grains with high slope angles met.

#### 4.7.2(d) *Crystalline orientation of the LPE grown films*

In conventional PVD techniques, the crystalline orientation of deposited YBCO film is determined by the choice of substrate material and its growth temperature [170]. On the other hand, film orientation in LPE growth is controlled by changing the flux composition, growth temperature, and supersaturation level.

On the most widely used (110) NdGaO<sub>3</sub> substrates, *c*-axis oriented YBCO film grow epitaxially such that the {001} planes of YBCO are parallel with the substrate surface, i.e.  $[001]_{\text{YBCO}} \parallel [110]_{\text{NdGaO}_3}$ ; whereas *a,b*-orientation implies film growth with the *c*-axis of YBCO parallel with the substrate surface, i.e.  $[001]_{\text{YBCO}} \perp [110]_{\text{NdGaO}_3}$ .

Kitamura *et al.* [151,170,171] reported that in the case of copper-poor flux compositions (Ba:Cu = 3.0:5.0 and 3.0:6.0), only *c*-axis oriented growth was observed; whereas both *c*-axis and *a,b*-axes oriented films were obtained using the flux of copper-rich compositions (Ba:Cu = 3.0:6.5 and 3.0:7.0). In the latter case, the crystalline orientation of YBCO films was reported [170] to be dependent on the growth temperature where *c*-axis oriented films were obtained at lower growth temperature (975-980°C) while the films showed *a,b*-axes orientation at higher growth temperature (983-995°C). The transition range in crystalline orientation of YBCO films was reported [170] to be as narrow as 3°C.

The YBCO films are *c*-axis oriented under low supersaturation conditions and *a,b*-axes oriented under high supersaturation. This is because the driving force required for nucleation differs according to variations in the crystal interface where a larger driving force is required for the two-dimensional nucleation and growth of *a,b*-oriented film as compared to the spiral-step growth of *c*-oriented film, and the driving force depends on the degree of solute supersaturation. In addition, according to the inversely proportional relationship between supersaturation and step interval for spiral-step growth mode, low supersaturation leads to a very long step interval corresponding to a more atomically flat surface. The equilibrium concentration of Y in the flux is reported [171] to be increasing with higher copper content, and the increase in the copper content caused supersaturation to increase. This is probably the reason why Kitamura *et al.* observed *a,b*-oriented films in copper-rich flux composition but not in copper-poor flux.

In contrast, two other groups [134,138] reported that for a copper-rich flux with Ba:Cu = 3:7, *c*-axis oriented films were grown at higher temperature and those of *a,b*-axes orientation at lower growth temperature, which is consistent with the growth by PVD techniques. In

addition, Klemenz [172] reported that *c*-axis growth was observed at low supersaturation and if the supersaturation was increased ( $\Delta T \geq 3^\circ\text{C}$ ), mixed *a,b/c*-oriented or pure *a,b*-oriented films were obtained.

In the case of seeded YSZ, due to its low thermal conductivity it is difficult to remove the latent heat of solidification of YBCO at the growth interface. Taniguchi *et al.* [149] increased the initial temperature difference (or undercooling) to  $>50^\circ\text{C}$  and successfully grew *c*-oriented YBCO films.

In-plane textures of coated film are an important feature for potential coated conductor applications. Typical FWHM values of X-ray rocking curves reported on either (005) or (006) peaks of *c*-axis oriented YBCO of  $\sim 10\ \mu\text{m}$  thick are  $0.21^\circ$  on  $\text{NdGaO}_3$  [138],  $0.44^\circ$  on seeded MgO [173], and  $0.8^\circ$  on seeded YSZ [174]. It has been consistently reported that FWHM decreases with increasing film thickness suggesting that either the crystallinity and/or the grain size increased with increasing thickness [147,151,173,175,176].

It remains unclear the exact factor(s) that determines the film growth mode (*c*- or *a,b*-oriented), be it the flux compositions, supersaturation levels, growth temperature, growth rate, or the combination of these factors. Furthermore, the rate-determining step is usually assumed to be the solute diffusion in the flux and the involvement of surface kinetics in LPE growth of REBCO films have not been investigated in details.

#### 4.7.2(e) *Factors affecting the LPE growth rate*

A major advantage of LPE is that growth rates are rapid. High quality *c*-axis oriented films at growth rates of about 2-3  $\mu\text{m}/\text{min}$  for YBCO [146,152] and as high as 10  $\mu\text{m}/\text{min}$  for NdBCO [155,177] have been reported. These values are at least one to two orders in magnitude higher than that of PVD techniques [132,146,173]. In addition to the method used to create the supersaturation (§3.3.1), the LPE growth rate is also a function of the supersaturation level, the flux composition, oxygen partial pressure, the growth temperature, and substrate rotation rate.

The growth rates are anisotropic with respect to the tetragonal YBCO phase with quick growing crystallographic *a,b*-direction and slow growing *c*-axis orientation [136]. Results from Nakamura *et al.* [178] showed that the growth rate of the {100} face (or *a,b*-axes orientation) has a quadratic dependence of undercooling, while that of the {001} shows a linear dependence. The dependence of substrate rotation rate to YBCO growth rate was observed by Nomura *et al.* [179] where higher substrate rotation rate lead to faster growth.

As the high growth rate of the NdBCO system was hard to control, in order to grow a film with thickness of 1-3  $\mu\text{m}$ , Krauns *et al.* [177] showed that the growth rate could be reduced from 10 to 4  $\mu\text{m}/\text{min}$  by changing flux composition, supersaturation, and growth temperature.

### 4.7.3 Lowering the growth temperature

Substrate reactivity causes serious problem in the formation of LPE films on metallic substrates for potential long-length coated conductor production. Most metals will react strongly with, or dissolve in, the highly corrosive Ba-Cu-O flux at the growth temperature of 970-1000°C in air. In fact, some ceramic substrate materials including YSZ and  $\text{SrTiO}_3$  are attacked by the flux at the growth temperature.

One method of reducing growth temperature is to incorporate fluoride into the flux as demonstrated by Yamada *et al.* [180]. They reported a decreased in the peritectic temperature of the YBCO system by  $\sim 30^\circ\text{C}$  and the eutectic temperature of more than  $50^\circ\text{C}$  by the addition of  $\text{BaF}_2$  into a Ba-Cu-O flux. Using this novel Ba-Cu-O-F flux, YBCO films have been reported to grow at reduced temperatures of 900-925°C on YBCO seeded YSZ [157,158,174], MgO [157-159,181],  $\text{SrTiO}_3$  [158], and Ag [156,159] substrates without causing deterioration in their superconductivity. Similar effects were also observed in NdBCO system where the growth temperature was lowered by as much as  $140^\circ\text{C}$  [157].

Figs. 4.5 and 4.6 show the relations between growth temperature and  $\text{BaF}_2$  concentrations for various flux compositions of YBCO and NdBCO systems, respectively.

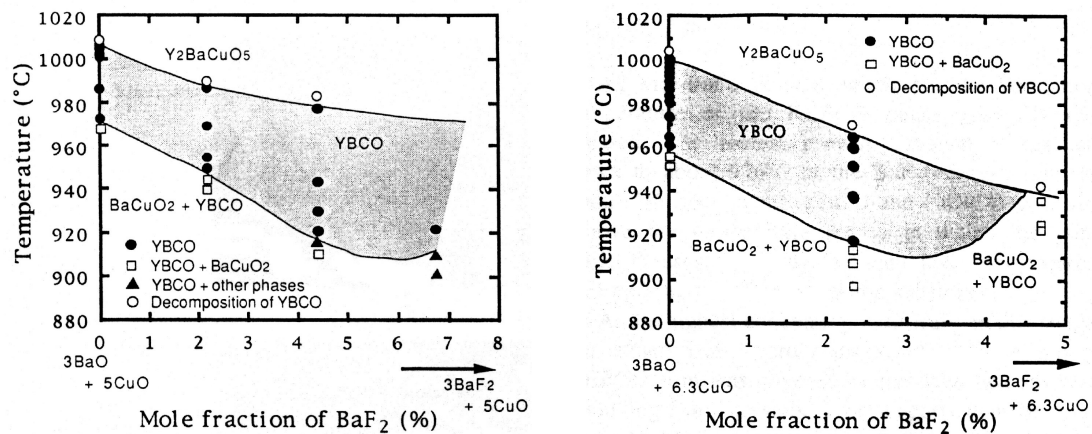


**Fig. 4.5** Relations between growth temperature and deposited phases as a function of the fluoride concentration in the solution for YBCO with (a) Ba:Cu = 3:5, and (b) Ba:Cu = 3:6.3 [157].

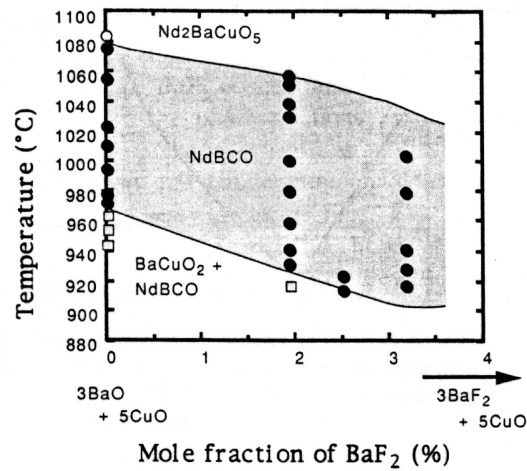


**Fig. 4.6** Relations between growth temperature and deposited phases as a function of the fluoride concentration in the solution for NdBCO with Ba:Cu = 3:5 [157].

Niiori *et al.* [159] observed that the addition of silver into a Ba-Cu-O-F flux altered the growth temperature whereby as the Ag content in the flux increased, the temperature for the primary phase region of Y123 phase decreased down to near 900°C. Fig. 4.7 shows the relation between growth temperature and deposited phases as a function of the atomic fraction of Ag in a Ba-Cu-O-F flux. Table 4.2 summarises the effects of several additives into the Ba-Cu-O flux.

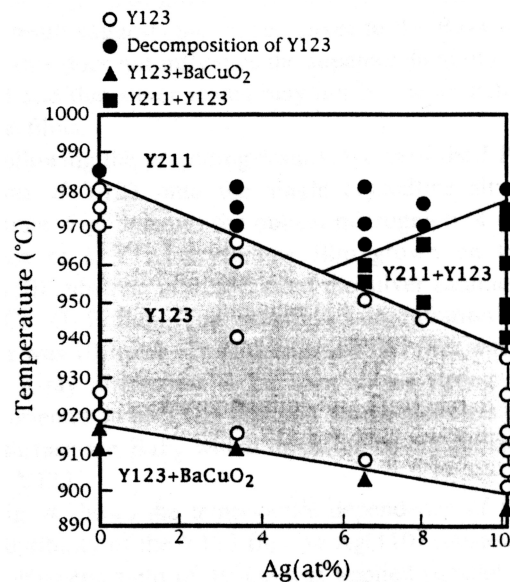


**Fig. 4.7** Relationship between growth temperature and deposited phases as a function of the atomic fraction of Ag in the flux (Ba:Cu = 3:5, BaF<sub>2</sub> = 4.5 mol%) [159].

**Table 4.2** Effects of additives into the Ba-Cu-O (Ba:Cu = 3:5) solvent. Adapted from ref. [182].

Additive	Growth temperature of YBCO	Remarks
BaF <sub>2</sub>	Decreased to 900-920°C	$T_c$ unchanged, nucleation depressed
LiF	Decreased to 890°C	$T_c$ degraded
Ag	Unchanged*	$T_c$ unchanged, silver dissolution depressed
BaF <sub>2</sub> + Ag	Decreased to 900-920°C	$T_c$ unchanged, silver dissolution depressed

\*In contrast, Maeda and Shiohara [183] reported that the addition of Ag alone decreased the  $T_p$  of YBCO system from ~1005°C to ~970°C; while Sakai *et al.* [184] observed a decrease in the decomposition temperature of YBCO by ~34°C with 10 mass% Ag doping.

Using a Ag-saturated Ba-Cu-O-F flux, Niiori *et al.* [156] succeeded in growing YBCO films on single crystalline (100) Ag and {100}<001> cubic textured Ag tape at temperatures as low as 889°C. They also found that a MgO buffer layer was very effective in eliminating the 45° misoriented grains as mentioned in §4.7.2(c) on (100) Ag. However, the deposition on Ag tape did not yield a uniform layer and contained a lot of flux inclusions.

Another method of controlling growth temperature is by changing the oxygen partial pressure ( $pO_2$ ) in the system. It is well known that the peritectic temperature of YBCO decreases with decreasing  $pO_2$  [185-188], this is also true for other REBCOs such as NdBCO [189]. Reduced  $pO_2$  processing has been used in single-crystal YBCO growth [190] and melt-processed  $LRE_{1+x}Ba_{2-x}Cu_3O_y$  (LRE = light rare-earth element such as La, Nd, Sm, Eu, Gd) [191]. By combining 1%  $pO_2$  and the additions of Ag and BaF<sub>2</sub> (3 mol%) into the flux, growth temperature as low as 850°C has been reported [192].

It was found that the melting temperatures of REBCO compounds decrease with decreasing RE ion radii with YbBCO having the lowest  $T_p$  of ~960°C in air [193]. Combining low  $pO_2$ , Ag addition, and mixing compositions and combinations of different RE elements, Qi *et al.* [144] have succeeded in reducing the LPE growth temperature to as low as 880°C using mixed RE systems of Y-Yb and Er-Yb.

#### 4.7.4 Recent developments

In recent years, the Japanese group at ISTECH has developed two different routes for LPE growth on metallic substrates: (i) double LPE layers construction, and (ii) LPE growth at reduced temperatures using Ag-saturated Ba-Cu-O-F flux and low  $pO_2$ .

ISTECH in Tokyo is developing a so-called "double LPE construction" with reel-to-reel configuration and tape speed of up to 1.2 m/h [194]. Two types of double LPE layer

architectures were proposed: (a) Ni/SOE-NiO/seed/LPE-REBa(Ni,Cu)O/LPE-YBCO (where RE = Nd or Sm) from a NiO-saturated flux [162,195], and (b) Hastelloy/PLD-MgO/seed/LPE-YBa(Mg,Cu)O/LPE-YBCO from a MgO-saturated flux [196,197]. In both cases, the metallic substrates were first deposited with a buffer layer (SOE-NiO or PLD-MgO) and a seed layer (by PVD technique). These tapes were then coated by LPE from fluxes saturated with either NiO or MgO, depending on the buffer material, leading to a non-superconducting layer with Ni or Mg partially substituting for Cu in YBCO. The tapes were then subjected to a standard LPE growth from a flux without NiO or MgO.

Izumi *et al.* [198] observed that the addition of NiO into the flux had decreased the  $T_p$  of YBCO and increased the crystallisation temperature of Ba-Cu-Ni-O compound, which made it difficult to grow YBCO crystals alone from the NiO-saturated flux. Hence, Ni-substituted REBCO that has a higher  $T_p$  (RE = Nd or Sm) was grown as the first LPE layer and followed by the LPE YBCO layer. The first double-LPE-layer architecture was initially tested on NiO and SrTiO<sub>3</sub> single-crystalline substrates with promising results showing sharp in-plane textures of the LPE processed YBCO films [199]. Recently, up to 10-cm long of the first LPE-SmBa(Ni,Cu)O layers on Ni/SOE-NiO with sharp in-plane texture have been reported [194,195]. However, Ni diffusion from the first to the second LPE layer caused severe degradation of the superconducting layer was observed [200].

On the other hand, the addition of MgO into the flux was found [196,201] to have negligible influence on both the Y solubility and  $T_p$  of YBCO. Without MgO in the flux, the MgO-buffered Hastelloy tape dissolved completely [202]. However, melt-back of the first LPE layer was very severe where 7 of the 12  $\mu\text{m}$  first LPE-YBa(Mg,Cu)O layer dissolved before LPE-YBCO nucleation; hence, NdBa(Mg,Cu)O was used as the first LPE layer as it has higher decomposition temperature [197,203]. Nevertheless, no transport  $J_c$  has been reported on metallic tapes via this route due to difficulty in annealing and measuring flux-covered samples. Furthermore, the double-LPE-layer architecture will inevitably reduce the overall  $J_{c,eng}$ .

ISTEC in Nagoya is focusing on lowering growth temperature (as low as 820°C) by the addition of both fluoride and silver, as well as utilising low  $p\text{O}_2$  for LPE growth [204,205]. Maeda *et al.* [199] reported growing an 8-cm long YBCO film on  $\{120\}\langle 2\bar{1}0\rangle$  textured Ag-0.1wt%Cu alloy tape using reel-to-reel system. Flux with Ba:Cu = 3:7 and 2%  $p\text{O}_2$  were chosen; Ag-Cu alloy tapes from Toshiba [204] and Ni/SOE-NiO tapes from Furukawa Electric [205] were used. The most successful achievement using this route was thus far on textured NiCr tapes (the lengths are not reported) with in-plane aligned,  $c$ -oriented film that

were grown at reduced temperature of  $\sim 820^\circ\text{C}$  from a Ba-Cu-O-F-Ag flux [206]. The films have zero-field transport  $J_c$  values at 77 K of 1.7-1.9 MA/cm<sup>2</sup>. However, the NiCr tape mentioned above required a rather complex buffer architecture (IBAD-YSZ and PLD-Y<sub>2</sub>O<sub>3</sub>) with a YBCO seed layer deposited by vacuum techniques.

Alternative buffer and/or seed layers have also been explored. There has been an interesting progress being made recently by Qi *et al.* [207-209] where they grew Nd<sub>2-x</sub>Ce<sub>x</sub>CuO<sub>4</sub> (where  $x = 0-0.15$ ) and NiO via a liquid-phase process similar to LPE, with high growth rates greater than 2  $\mu\text{m}/\text{min}$ , as a non-vacuum processed buffer for LPE processed REBCO. A focused heat source (infrared aided) was used to flux a vertically-fed, pressed and sintered rod of the oxide until liquid droplets were created and fell down to the moving substrate kept below at a lower temperature (800-900°C). Due to the wetting property of Cu-O flux, a smooth layer of the oxide buffer immediately covered the entire substrate. Initial attempts of Nd<sub>2-x</sub>Ce<sub>x</sub>CuO<sub>4</sub> buffer showed promising results with sharp cube texture and in-plane FWHM values of 0.8° and 5° on single crystalline LaAlO<sub>3</sub> and SOE Ni tapes, respectively. Since the lattice parameter of this Nd<sub>2</sub>CuO<sub>4</sub> (3.94 Å) closely matches that of YBCO ( $\sim 2.3\%$  misfit), it has been shown that YBCO can be grown directly by LPE without the need of a seed layer.

In order to prepare a high-quality seed layer on Ag tape, Huang *et al.* [210] explored the possibility of using Y-Ba-Fe-O (YBFO) as a seed for LPE, as they observed reaction between the YBCO and the Ag substrate at high temperature due to the existence of Cu atoms. They reported growing YBCO films via LPE on YBFO seeded MgO substrates. The YBFO seed, which has a FCC structure instead of Y123 structure, was grown by PLD and had a very uniform interface with the MgO substrate. However, the seed layer appeared to degrade severely after LPE process where the YBFO dramatically changed into a non-uniform, thicker polycrystalline Ba-Cu-O layer.

Kim *et al.* [83] recently reported a room temperature PLD of NdGaO<sub>3</sub> as a seed for LPE processed REBCO. Amorphous NdGaO<sub>3</sub> was first grown by PLD at room temperature on single crystalline substrates such as SrTiO<sub>3</sub> and LaAlO<sub>3</sub>, post-annealing is then followed to crystallise the NdGaO<sub>3</sub>. Using this NdGaO<sub>3</sub> layer without the need of a seed layer, YBCO (with in-plane FWHM of 9.4°) had been successfully grown by LPE from a Ag-saturated Ba-Cu-O-F flux with thickness up to 2.5  $\mu\text{m}$  without cracks. However, the LPE growth rate is reported to be only 0.25  $\mu\text{m}/\text{min}$  due to the low growth temperature (860°C). This approach may eliminate the need of a seed layer; however, the NdGaO<sub>3</sub> deposition was still carried out in a less-than-ideal vacuum process.

### 4.7.5 Transport properties

For power applications, it is crucial to obtain high  $J_c$  in coated conductors. Oxygen vacancies, grain boundaries, and dislocations have been found to be effective pinning centres for YBCO. It was reported [147,171,176] that the intragrain  $J_c$  for YBCO film on NdGaO<sub>3</sub> substrate was lower than that for film grown on MgO substrate where zero-field transport  $J_c$  values as high as  $10^5$ - $10^6$  A/cm<sup>2</sup> at 77 K have been reported on YBCO films grown on MgO substrates by LPE method whereas those on NdGaO<sub>3</sub> substrates are  $10^4$ - $10^5$  A/cm<sup>2</sup>. Miura *et al.* [147] suggested that the difference in  $J_c$  values in YBCO films grown on the two different substrates were not related to large misoriented grains but to the pinning mechanism of the magnetic flux. They concluded that a larger lattice mismatch between MgO and YBCO as compared to NdGaO<sub>3</sub> and YBCO, leads to higher concentration of defects, which act as pinning centres. It has been suggested that the stacking faults on the *a,b*-plane in the films on MgO substrates behave as field-induced pinning centres [148,211]. Table 4.3 summarises the transport properties of LPE processed REBCO films.

**Table 4.3** Transport properties of LPE processed REBCO on various substrate materials.

Film	Substrate	Method	$J_c$ (A/cm <sup>2</sup> )*	$T_c$ (K) <sup>†</sup>	References
YBCO	NdGaO <sub>3</sub>	ACS <sup>‡</sup>	NM <sup>§</sup>	90	Jena [139]
(Y,Nd)BCO	NdGaO <sub>3</sub>	ACS	NM	80	Jena [140]
YBCO	MgO	Transport	$1.1 \times 10^5$	85	ISTEC [146]
YBCO	NdGaO <sub>3</sub>	SQUID	$2.5 \times 10^5$	89	ISTEC [212]
	MgO		$1.5 \times 10^6$	88	
YBCO	YSZ	SQUID	$1.0 \times 10^5$ (at 1 T)	89.5	ISTEC [149]
YBCO (Ba-Cu-O-F flux)	YSZ	Magnetic	$>10^5$	90.5	ISTEC [158]
YBCO	NdGaO <sub>3</sub>	SQUID	$1.0 \times 10^5$	89.0	ISTEC [211]
	MgO		$1.0 \times 10^6$	88.9	
	YSZ		$1.0 \times 10^6$	89.2	
YBCO	MgO	Transport	$2.1 \times 10^6$	89-92	ISTEC [176]
NdBCO	MgO	SQUID	NM	80-93	ISTEC [213]
SmBCO	MgO	SQUID	$3 \times 10^4$	94	ISTEC [214]
YBCO (double LPE layers)	MgO	SQUID	$1.2 \times 10^5$	91	ISTEC [215]
YBCO	LaAlO <sub>3</sub>	Magnetic	$>10^5$	90	Qi <i>et al.</i> [144]
YBCO	MgO	Transport	$8 \times 10^3$	87-90	Vienna/Jena [216]
YBCO	NdGaO <sub>3</sub>	Transport	$2.5 \times 10^5$	91	Vienna/this work
	MgO		$1 \times 10^5$	84.4	[217]
YBCO (single crystal)	NiO	SQUID	$7.9 \times 10^4$	92.5	ISTEC [199]
YBCO (Ba-Cu-O-F-Ag flux)	NiCr	Transport	$1.9 \times 10^6$	NM	ISTEC [206]

Keys: \* zero-field  $J_c$  at 77 K unless otherwise stated; <sup>†</sup> onset  $T_c$ ; <sup>‡</sup> AC susceptibility; <sup>§</sup> not mentioned

Kitamura *et al.* [175] also suggested that there are two mechanisms for the introduction of dislocations at the growth interface where one is due to the stress induced by lattice misfit while the other is attributed to the tetragonal-orthorhombic transition during the cooling process upon film growth. These dislocation defects, which act as pinning centres, not only occurred at a small distance from the substrate/film interface, but also far from the substrate interface [148]. Despite this,  $J_c$  values generally decrease with increasing LPE film thickness as the defect density is thought to be decreasing with increasing distance from the film/substrate interface.

Yao *et al.* [218] observed that for NdBCO films grown on MgO substrates, the superconducting transition temperature varied according to the film thickness whereby thinner films have lower  $T_c$ . Their investigation revealed that the cause was Mg contamination from the MgO substrate via high-temperature diffusion during film growth.

#### **4.7.6 Crack formation**

Thicker films are preferred for coated conductors in order to obtain higher  $J_{c,eng}$ . However, crack formation is one of the most serious problems when thick crystalline YBCO films are formed on substrates that have significant differential thermal expansion coefficients from the film.

Stress may be induced in the film due to differential thermal expansion, tetragonal-orthorhombic transition, and/or strain generated by lattice misfit. If the stress in the film is larger than what can be relieved by means of misfit dislocations and twin formation, the result is the creation of cracks on the film. Below the critical thickness for dislocation formation the epitaxial film is able to relax elastically the misfit strain by surface ripple formation [212]. However, with increasing crystal and layer size as well as crystalline perfection, the strain caused by misfit and by cooling due to thermal expansion differences may be partially or completely relaxed by the formation of misfit dislocations, twins, or by microscopic cracks, depending on the elastic strain accommodation and on the oxidation/phase transition-induced strain [219].

If the film is cooled in  $N_2$  atmosphere from the growth temperature, the REBCO crystal should retain its tetragonal structure. Depending on the differential thermal expansion, for film thicknesses below the critical value for crack formation, the strain can be relaxed if the dislocation mobility is sufficient, or by bending [220]. When the film is cooled in air, oxidation takes place. Depending on the cooling rate and anisotropic oxidation rate

(coefficients of oxygen diffusion  $D_a = 10^{-13}$  cm<sup>2</sup>/s,  $D_b = 10^{-11}$  cm<sup>2</sup>/s, and  $D_c = 10^{-16}$  cm<sup>2</sup>/s [221]), a partially oxidised/twinned film is obtained. The strain can be accommodated by twinning and cracking if the film is thicker than the critical value for crack formation.

Further oxygenation of the film is usually required for it to become superconducting. During this oxygenation, the phase transition from tetragonal to orthorhombic and splitting of the  $a$ - and  $b$ -axis leads to the formation of {110} twins that partially relax the strain. The remaining effective strain is accommodated by crack formation. Klemenz *et al.* [135,220] observed that these cracks propagated directionally. It was typical for  $a,b$ -oriented films on (110) NdGaO<sub>3</sub> to have cracks developed along the [001] direction of the YBCO film, and along the [100]/[010] direction for  $c$ -oriented films. They suggested that this directionality could be due to a preferred cleavage direction, or to some degree of uniaxiality in the stress. Their study revealed [220] that the cross-hatch {110} twin patterns observed on  $c$ -oriented films are more effective to relieve the strain than those in  $a,b$ -oriented films.

Olsson *et al.* [222] reported facing difficulty in growing crack-free YBCO and PrBCO films on (110) SrTiO<sub>3</sub> substrates by PLD technique back in 1991. They went around the problem by developing a model that predicted the crack spacing as a function of deposition temperature and film thickness. Results showed that the critical crack-free film thickness varied inversely with the deposition temperature from ~0.05 to 0.25 μm in a range of 700 to 500°C. Thus by controlling the deposition temperature adequately, they were able to deposit crack-free films.

Nevertheless, it is harder to control the crack formation in LPE processed films, as the complete mechanism of crack formation of LPE films is not yet fully understood. Aichele *et al.* [223] suggested that crack formation in the LPE grown REBCO films is due to the stress induced by the difference in thermal expansion coefficients of the substrate and the film during cooling after the film growth rather than due to lattice misfit during the growth. The basis of this argument is that the cracks are observed running over the growth steps and the spirals. Based on theoretical model and experimental results, they reported a critical film thickness of 0.17 and 0.22 μm, respectively, for the  $a,b$ -axes oriented YBCO grown on NdGaO<sub>3</sub> substrates. The critical thickness were 0.41 (modelling) and 0.46 μm (experimental) for films grown on lower-misfit (110) SrPrGaO<sub>4</sub> substrates.

Kawashima *et al.* [224] reported that as-grown films on YBCO seeded SrTiO<sub>3</sub> substrates by LPE had no visible cracks for film thickness up to 4 μm, whereas oxygenated films showed apparent crack propagation leading to the estimated critical thickness of about 1.35 μm. On

the other hand, they reported that films grown on MgO substrates have never shown any cracks even after oxygenation. They concluded that the closely matched thermal expansion coefficients between YBCO and MgO played an important role in determining the formation of cracks. They also suggested that the observed increased resistivity with increasing YBCO film thickness on YBCO films with no visible cracks might be caused by the creation of microcracks in the films. It was suggested [225] that microcracks, which are very short in length, do not completely obstruct the current path but increase the resistivity by decreasing the effective cross section and increasing the effective length of the current path. Kawashima *et al.* [224] and Yamada *et al.* [225] tried to deposit a MgO buffer layer between YBCO and SrTiO<sub>3</sub> substrate with the intention to increase the critical crack-free thickness on SrTiO<sub>3</sub> substrate, but the MgO layer did not show sufficient effect on suppressing the crack formation.

Kita *et al.* [226] reported growing a tetragonal  $Y_{0.75}Ca_{0.07}Ba_{1.63}La_{0.30}Cu_3O_x$  film on (110) NdGaO<sub>3</sub> substrate with no visible cracks on *c*-axis oriented film up to a thickness of 20 μm due to smaller difference in their coefficients of thermal expansion. However, the substitutions seem to have significantly suppressed its superconductivity with an onset  $T_c$  of 80.2 K.

There appears to be no theoretical studies on crack formation for REBCO films grown on metallic substrates, probably due to the lack of experimental data.

#### 4.8 Summary of the LPE of REBCO

Many of the fundamental issues such as the growth mechanism, dependence of crystalline orientations and growth rate by LPE have been studied using single crystalline substrates, especially on NdGaO<sub>3</sub> where REBCO films can be grown directly. The same group at ISTEK in Japan has largely carried out most of these studies. However, the exact factor(s) that determines the film growth mode (*c*- or *a,b*-oriented) remains unclear, be it the flux compositions, supersaturation level, growth temperature, growth rate, or the combination of these factors. Furthermore, the rate-determining step is usually assumed to be the solute diffusion rate in the flux and the involvement of surface kinetics in film growth by LPE has not been investigated in details. In addition, studies of the growth mechanism of YBCO on seeded MgO substrates have been restricted to the ISTEK group. Therefore, studies have been made in this work in an attempt to clarify some of these uncertainties.

Attempts to grow YBCO films on metallic substrates by LPE have had limited success, with the most promising results by Yamada *et al.* [206] on NiCr tapes grown at reduced temperature of  $\sim 820^\circ\text{C}$  from a Ba-Cu-O-F-Ag flux having zero-field transport  $J_c$  at 77 K as high as  $1.9 \text{ MA/cm}^2$ . However, the NiCr tapes used had a rather complex buffer and seed layers prepared using PVD techniques that may cause major concerns towards large-scale industrial implementation such as the scale-up of vacuum systems and its low deposition rates. Nevertheless, the promising results from the recent developments of  $\text{Nd}_{2-x}\text{Ce}_x\text{CuO}_4$  buffer layer by Qi *et al.* [207-209] using non-vacuum technique, together with the high  $J_c$  LPE processed films by Yamada *et al.* [206], have shown a promising future for the development of REBCO coated conductor by LPE.

## References

- 1 J. L. MacManus-Driscoll, *Annu. Rev. Mater. Sci.* **28** (1998) 421.
- 2 D. Larbalestier, A. Gurevich, D. M. Feldmann, and A. Polyanskii, *Nature* **414** (2001) 368.
- 3 T. P. Sheahen, *Introduction to High-Temperature Superconductivity* (Plenum, New York, 1994).
- 4 Y. Iijima, N. Tanabe, O. Kohno, and Y. Ikeno, *Appl. Phys. Lett.* **60** (1992) 769.
- 5 K. Hasegawa, K. Fujino, H. Mukai, M. Konishi, K. Hayashi, K. Sato, S. Honjo, Y. Sato, H. Ishii, and Y. Iwata, *Appl. Supercond.* **4** (1996) 487.
- 6 T. J. Doi, T. Yuasa, T. Ozawa, and K. Hihashiyama, *Advances in Superconductivity VII* (Springer-Verlag, Tokyo, 1994) 447.
- 7 D. P. Norton, A. Goyal, J. D. Budai, D. K. Christen, D. M. Kroeger, E. D. Specht, Q. He, B. Saffian, M. Paranthaman, C. E. Klabunde, D. F. Lee, B. C. Sales, and F. A. List, *Science* **274** (1996) 755.
- 8 A. Goyal, D. P. Norton, J. D. Budai, M. Paranthaman, E. D. Specht, D. M. Kroeger, D. K. Christen, Q. He, B. Saffian, F. A. List, D. F. Lee, P. M. Martin, C. E. Klabunde, E. Hartfield, and V. K. Sikka, *Appl. Phys. Lett.* **69** (1996) 1795.
- 9 K. Matsumoto, Y. Niiori, I. Hirabayashi, N. Koshizuka, T. Watanabe, Y. Tanaka, and M. Ikeda, *Advances in Superconductivity XI* (Springer-Verlag, Tokyo, 1999) 611.
- 10 X. D. Wu, S. R. Foltyn, P. Arendt, J. Townsend, C. Adams, I. H. Campbell, P. Tiwari, Y. Coulter, and D. E. Peterson, *Appl. Phys. Lett.* **65** (1994) 1961.
- 11 Q. He, D. K. Christen, J. D. Budai, E. D. Specht, D. F. Lee, A. Goyal, D. P. Norton, M. Paranthaman, F. A. List, and D. M. Kroeger, *Physica C* **275** (1997) 155.
- 12 I. Utke, C. Klemenz, H. J. Scheel, M. Sasaura, and S. Miyazawa, *J. Crystal Growth* **174** (1997) 806.
- 13 H. J. Scheel, M. Berkowski, and B. Chabot, *J. Crystal Growth* **115** (1991) 19.
- 14 H. J. Scheel, M. Berkowski, and B. Chabot, *Physica C* **185** (1991) 2095.
- 15 E. Villa, private communication.
- 16 M. Vickers, private communication.
- 17 E. Yin, M. Rubin, and M. Dixon, *J. Mater. Res.* **7** (1992) 1636.

- 18 E. Y. Shou, S. M. Gong, Y. J. Mao, M. P. Yuan, H. Zhang, J. Yuan, G. Q. Yang, X. H. Liu, and S. C. Zou, *Physica C* **282** (1997) 617.
- 19 J. R. Groves, P. N. Arendt, S. R. Foltyn, R. F. de Paula, C. P. Wnag, and R. H. Hammond, *IEEE Trans. Appl. Supercond.* **9** (1999) 1964.
- 20 M. P. Chudzik, R. Erck, M. T. Lanagan, and C. R. Kannewurf, *IEEE Trans. Appl. Supercond.* **9** (1999) 1490.
- 21 A. Usoskin, J. Knoke, F. Garcia-Moreno, A. Issaev, J. Dzick, S. Sievers, and H. C. Freyhardt, *IEEE Trans. Appl. Supercond.* **11** (2001) 3385.
- 22 W. A. J. Quinton, W. Y. Liang, F. Baudenbacher, D. T. Foord, A. P. Bramley, and S. B. Newcomb, *IEEE Trans. Appl. Supercond.* **9** (1999) 1498.
- 23 F. Yang, E. Narumi, S. Patel, and D. T. Shaw, *Physica C* **244** (1995) 299.
- 24 M. Bauer, R. Semerad, and H. Kinder, *IEEE Trans. Appl. Supercond.* **9** (1999) 1502.
- 25 W. B. Robbins, *Extended Abstracts of the 5<sup>th</sup> ISTE C-MRS Intl. Workshop on Superconductivity* (Honolulu HI, USA, 2001) 17.
- 26 N. Reger, B. de Boer, J. Eickemeyer, R. Opitz, B. Holzapfel, and L. Schultz, *Inst. Phys. Conf. Ser. No. 167* (IoP Publishing, 2000) 331.
- 27 R. M. Nekkanti, V. Seetharaman, L. Brunke, I. Maartense, D. Dempsey, G. Kozlowski, D. Tomich, R. Biggers, T. Peterson, P. Barnes, and C. E. Oberly, *IEEE Trans. Appl. Supercond.* **11** (2001) 3321.
- 28 C. L. H. Thieme, S. Annavarapu, W. Zhang, V. Prunier, L. Fritzemeier, Q. Li, U. Schoop, M. W. Rupich, M. Gopal, S. R. Foltyn, and T. Holesinger, *IEEE Trans. Appl. Supercond.* **11** (2001) 3329.
- 29 M. P. Paranthaman, S. Sathyamurthy, T. Aytug, D. B. Beach, A. Goyal, B. W. Kang, R. Feenstra, D. K. Christen, D. F. Lee, P. M. Martin, L. Heatherly Jr., and D. M. Kroeger, *Extended Abstracts of the 5<sup>th</sup> ISTE C-MRS Intl. Workshop on Superconductivity* (Honolulu HI, USA, 2001) 87.
- 30 J. Eickmeyer, D. Selbmann, R. Opitz, H. Wendrock, E. Maher, U. Miller, and W. Prusseit, *Proc. 5<sup>th</sup> European Conf. on Appl. Supercond.* (Copenhagen, Denmark, 2001) in press.
- 31 B. A. Glowacki, M. Vickers, and E. Maher, *Materials World* **6** (1998) 683.
- 32 N. A. Rutter, M. E. Vickers, Z. H. Barber, A. P. Bramley, B. A. Glowacki, J. E. Evetts, and E. Maher, *Inst. Phys. Conf. Ser. No. 167* (IoP Publishing, 2000) 403.
- 33 N. A. Rutter, B. A. Glowacki, J. H. Durrell, J. E. Evetts, H. te Lintel, R. de Gryse, and J. Denul, *Inst. Phys. Conf. Ser. No. 167* (IoP Publishing, 2000) 407.
- 34 N. A. Rutter, B. A. Glowacki, and J. E. Evetts, *Supercond. Sci. Tech.* **13** (2000) L25.
- 35 N. A. Rutter and B. A. Glowacki, *IEEE Trans. Appl. Supercond.* **11** (2001) 2730.
- 36 R. I. Tomov, A. Kursumovic, M. Majoros, D.-J. Kang, B. A. Glowacki, and J. E. Evetts, *Supercond. Sci. Tech.*, in press.
- 37 B. A. Glowacki, M. Vickers, N. A. Rutter, E. Maher, F. Pasotti, A. Baldini, and R. Major, *J. Mat. Sci.* **37** (2002) 157.
- 38 A. Tuissi, E. Villa, R. I. Tomov, and J. E. Evetts, *Proc. 5<sup>th</sup> European Conf. on Appl. Supercond.* (Copenhagen, Denmark, 2001) in press.
- 39 T. Watanabe, Y. Ohashi, M. Ozaki, K. Yamamoto, T. Maeda, K. Wada, and I. Hirabayashi, *Extended Abstracts of the 5<sup>th</sup> ISTE C-MRS Intl. Workshop on Superconductivity* (Honolulu HI, USA, 2001) 21.
- 40 N. Zafar, J. J. Wells, A. Crossley, and J. L. MacManus-Driscoll, *Inst. Phys. Conf. Ser. No. 158* (IoP Publishing, 1998) 877.

- 41 T. J. Doi, *Supercond. Week* **9** (1995) 1.
- 42 H. L. Suo, J. Y. Genoud, G. Triscone, E. Walker, M. Schindl, R. Passerini, F. Cleton, M. L. Shou, and R. Flukiger, *Supercond. Sci. Tech.* **12** (1999) 624.
- 43 N. Sugiyama, T. Doi, T. Yuasa, H. Akata, T. Ozawa, K. Higashiyama, S. Kikuchi, and K. Osamura, *J. Jpn. Inst. Met.* **61** (1997) 985.
- 44 R. P. Wang, Y. L. Zhou, S. H. Pan, M. He, Z. H. Chen, and G. Z. Yang, *Physica C* **328** (1999) 37.
- 45 M. Schindl, J. Y. Genoud, H. Suo, M. Dhalle, E. Walker, and R. Flukiger, *IEEE Trans. Appl. Supercond.* **11** (2001) 3313.
- 46 T. A. Gladstone, J. C. Moore, V. N. Tsaneva, C. J. Eastell, A. J. Wilkinson, and C. R. M. Grovenor, *Inst. Phys. Conf. Ser. No. 167* (IoP Publishing, 2000) 355.
- 47 J. J. Wells, J. L. Macmanus-Driscoll, J. Y. Genoud, H. L. Suo, E. Walker, and R. Flukiger, *Supercond. Sci. Tech.* **13** (2000) 1390.
- 48 H. Yoshino, M. Yamazaki, and T. D. Thanh, *Extended Abstracts of the 5<sup>th</sup> ISTE-C-MRS Intl. Workshop on Superconductivity* (Honolulu HI, USA, 2001) 32.
- 49 M. Yamazaki, T. D. Thanh, and H. Yoshino, *Extended Abstracts of the 5<sup>th</sup> ISTE-C-MRS Intl. Workshop on Superconductivity* (Honolulu HI, USA, 2001) 93.
- 50 T. Doi, K. Onabe, T. Nishida, N. Manago, Y. Hakuraku, M. Okada, N. Kashima, and S. Nagaya, *Extended Abstracts of the 5<sup>th</sup> ISTE-C-MRS Intl. Workshop on Superconductivity* (Honolulu HI, USA, 2001) 36.
- 51 H. Suo, J.-Y. Genoud, M. Schindl, E. Walker, and R. Flukiger, *Supercond. Sci. Tech.* **14** (2001) 854.
- 52 H. C. Freyhardt, J. Hoffmann, J. Wiesmann, J. Dzick, K. Heinemann, A. Isaev, F. Garcia-Moreno, S. Sievers, and A. Usoskin, *IEEE Trans. Appl. Supercond.* **7** (1997) 1426.
- 53 R. P. Reade, P. Berdahl, R. E. Russo, and S. M. Garrison, *Appl. Phys. Lett.* **60** (1992) 769.
- 54 Y. Iijima, K. Kakimoto, and K. Takeda, *Physica C* **357** (2001) 952.
- 55 Y. Iijima, K. Kakimoto, K. Takeda, and T. Saitoh, *Extended Abstracts of the 5<sup>th</sup> ISTE-C-MRS Intl. Workshop on Superconductivity* (Honolulu HI, USA, 2001) 47.
- 56 J. R. Groves, P. N. Arendt, S. R. Foltyn, Q. Jia, T. G. Holesinger, H. Kung, R. F. de Paula, P. C. Dowden, E. J. Peterson, L. Stan, and L. A. Emmert, *Extended Abstracts of the 5<sup>th</sup> ISTE-C-MRS Intl. Workshop on Superconductivity* (Honolulu HI, USA, 2001) 43.
- 57 S. Gnanarajan, A. Katsaros, and N. Savvides, *Appl. Phys. Lett.* **70** (1997) 2816.
- 58 T. G. Holesinger, S. R. Foltyn, P. N. Arendt, H. Kung, Q. X. Jia, R. M. Dickerson, P. C. Dowden, R. F. de Paula, J. R. Groves, and J. Y. Coulter, *J. Mater. Res.* **15** (2000) 1110.
- 59 K. Hasegawa, N. Hobara, Y. Nakamura, T. Izumi, and Y. Shiohara, *Physica C* **354** (2001) 424.
- 60 K. Fujino, K. Muranaka, T. Taneda, K. Ohmatsu, H. Takei, Y. Sato, K. Matsuo, and Y. Takahashi, *Extended Abstracts of the 5<sup>th</sup> ISTE-C-MRS Intl. Workshop on Superconductivity* (Honolulu HI, USA, 2001) 61.
- 61 K. Ohmatsu, K. Muranaka, S. Hahakura, T. Taneda, K. Fujino, H. Takei, Y. Sato, K. Matsuo, and Y. Takahashi, *Physica C* **357** (2001) 946.
- 62 M. Paranthaman, A. Goyal, F. A. List, E. D. Specht, D. F. Lee, P. M. Martin, Q. He, D. K. Christen, D. P. Norton, J. D. Budai, and D. M. Kroeger, *Physica C* **275** (1997) 266.
- 63 S. Oh, J. Yoo, K. Lee, J. Kim, and D. Youm, *Physica C* **308** (1998) 91.

- 64 B. Holzapfel, L. Fernandez, M. A. Arranz, N. Reger, B. de Boer, J. Eickemeyer, and L. Schultz, *Inst. Phys. Conf. Ser. No. 167* (IoP Publishing, 2000) 419.
- 65 V. Boffa, T. Petrisor, S. Ceresara, L. Ciontea, F. Fabbri, and P. Scardi, *Physica C* **312** (1999) 202.
- 66 T. J. Jackson, C. H. Wang, B. A. Glowacki, J. A. Leake, R. E. Somekh, and J. E. Evetts, *Inst. Phys. Conf. Ser. No. 158* (IoP Publishing, 1998) 1073.
- 67 R. I. Tomov *et al.*, unpublished data.
- 68 A. P. Bramley *et al.*, unpublished data.
- 69 R. I. Tomov, A. Kursumovic, D. J. Kang, B. A. Glowacki, M. Majoros, J. E. Evetts, A. Tuissi, and E. Villa, *Proc. 5<sup>th</sup> European Conf. on Appl. Supercond.* (Copenhagen, Denmark, 2001) in press.
- 70 Y. Takahashi, K. Matsumoto, S. B. Kim, I. Hirabayashi, H. Akata, and K. Higashiyama, *IEEE Trans. Appl. Supercond.* **9** (1999) 2272.
- 71 M. Paranthaman, D. F. Lee, A. Goyal, E. D. Specht, P. M. Martin, X. Cui, J. E. Mathis, R. Feenstra, D. K. Christen, and D. M. Kroeger, *Supercond. Sci. Tech.* **12** (1999) 319.
- 72 M. Paranthaman, T. G. Chirayil, S. Sathyamurthy, D. B. Beach, A. Goyal, F. A. List, D. F. Lee, X. Cui, S. W. Lu, B. Kang, E. D. Specht, P. M. Martin, D. M. Kroeger, R. Feenstra, C. Cantoni, and D. K. Christen, *IEEE Trans. Appl. Supercond.* **11** (2001) 3146.
- 73 J. S. Morrell, Z. B. Xue, E. D. Specht, A. Goyal, P. M. Martin, D. F. Lee, R. Feenstra, D. T. Verebelyi, D. K. Christen, T. G. Chirayil, M. Paranthaman, C. E. Vallet, and D. B. Beach, *J. Mater. Res.* **15** (2000) 621.
- 74 A. Ichinose, A. Kikuchi, K. Tachikawa, and S. Akita, *Physica C* **302** (1998) 51.
- 75 A. Ichinose, G. Daniels, C. Y. Yang, D. C. Larbalestier, A. Kikuchi, K. Tachikawa, and S. Akita, *IEEE Trans. Appl. Supercond.* **9** (1999) 2280.
- 76 A. Ichinose, C. Y. Yang, D. C. Larbalestier, S. E. Babcock, A. Kikuchi, K. Tachikawa, and S. Akita, *Physica C* **324** (1999) 113.
- 77 T. A. Gladstone, J. C. Moore, A. J. Wilkinson, and C. R. M. Grovenor, *IEEE Trans. Appl. Supercond.* **9** (1999) 2252.
- 78 C. M. Carlson, P. A. Parilla, M. P. Siegal, D. S. Ginley, Y. T. Wang, R. D. Blaugher, J. C. Price, D. L. Overmyer, and E. L. Venturini, *Appl. Phys. Lett.* **75** (1999) 2479.
- 79 Q. He, D. K. Christen, R. Feenstra, D. P. Norton, M. Paranthaman, E. D. Specht, D. F. Lee, A. Goyal, and D. M. Kroeger, *Physica C* **314** (1999) 105.
- 80 T. Aytug, J. Z. Wu, B. W. Kang, D. T. Verebelyi, C. Cantoni, E. D. Specht, A. Goyal, M. Paranthaman, and D. K. Christen, *Physica C* **340** (2000) 33.
- 81 T. Aytug, J. Z. Wu, C. Cantoni, D. T. Verebelyi, E. D. Specht, M. Paranthaman, D. P. Norton, D. K. Christen, R. E. Ericson, and C. L. Thomas, *Appl. Phys. Lett.* **76** (2000) 760.
- 82 C. Cantoni, T. Aytug, D. T. Verebelyi, M. Paranthaman, E. D. Specht, D. P. Norton, and D. K. Christen, *IEEE Trans. Appl. Supercond.* **11** (2001) 3309.
- 83 S. B. Kim, T. Maeda, Y. Yamada, T. Suga, Y. Yamada, T. Watanabe, and I. Hirabayashi, *Extended Abstracts of the 5<sup>th</sup> ISTE-C-MRS Intl. Workshop on Superconductivity* (Honolulu HI, USA, 2001) 244.
- 84 A. Goyal, D. P. Norton, D. M. Kroeger, D. K. Christen, M. Paranthaman, E. D. Specht, J. D. Budai, Q. He, B. Saffian, F. A. List, D. F. Lee, E. Hatfield, P. M. Martin, C. E. Klabunde, J. Mathis, and C. Park, *J. Mater. Res.* **12** (1997) 2924.
- 85 N. A. Rutter and B. A. Glowacki, *J. Mat. Sci. Lett.* **18** (1999) 1661.

- 86 A. Ginsbach, R. Schneider, H. W. Grueninger, and G. Grabe, *IEEE Trans. Magn.* **27** (1991) 1410.
- 87 N. N. Khoi, W. W. Smeltzer, and J. D. Embury, *J. Electrochem. Soc.* **122** (1975) 1495.
- 88 K. Matsumoto, S. B. Kim, J. G. Wen, I. Hirabayashi, T. Watanabe, N. Uno, and M. Ikeda, *IEEE Trans. Appl. Supercond.* **9** (1999) 1539.
- 89 K. Matsumoto, S. B. Kim, I. Hirabayashi, T. Watanabe, N. Uno, and M. Ikeda, *Physica C* **330** (2000) 150.
- 90 T. Watanabe, K. Matsumoto, T. Maeda, T. Tanigawa, and I. Hirabayashi, *Physica C* **357-360** (2001) 914.
- 91 V. Boffa, T. Petrisor, G. Celentano, F. Fabbri, C. Annino, S. Ceresara, L. Ciontea, V. Galluzzi, U. Gambardella, G. Grimaldi, and A. Mancini, *Supercond. Sci. Tech.* **13** (2000) 1467.
- 92 Z. Lockman, W. Goldacker, R. Nast, B. de Boer, and J. L. MacManus-Driscoll, *IEEE Trans. Appl. Supercond.* **11** (2001) 3325.
- 93 Z. Lockman, W. Goldacker, R. Nast, B. de Boer, and J. L. MacManus-Driscoll, *Extended Abstracts of the 5<sup>th</sup> ISTECS-MRS Intl. Workshop on Superconductivity* (Honolulu HI, USA, 2001) 96.
- 94 D. M. Kroeger, A. Goyal, E. D. Specht, Z. L. Wang, and J. E. Tkaczyk, *Appl. Phys. Lett.* **64** (1994) 106.
- 95 Hitachi, *Supercond. Week* **9** (1995) 1.
- 96 J. J. Wells, A. Crossley, R. Sweeney, and J. L. MacManus-Driscoll, *IEEE Trans. Appl. Supercond.* **9** (1999) 1983.
- 97 A. Ferreri, J. A. G. Nelstrop, A. D. Caplin, and J. L. MacManus-Driscoll, *Physica C* **351** (2001) 58.
- 98 A. Ferreri, A. Berenov, and J. L. MacManus-Driscoll, *Extended Abstracts of the 5<sup>th</sup> ISTECS-MRS Intl. Workshop on Superconductivity* (Honolulu HI, USA, 2001) 114.
- 99 R. L. Meng, Y. Q. Wang, K. Lewis, C. Garcia, Y. Cao, and C. W. Chu, *J. Supercond.* **11** (1998) 181.
- 100 V. F. Solovyov, H. J. Weismann, L. Wu, Y. Zhu, and M. Suenaga, *Appl. Phys. Lett.* **76** (2000) 1911.
- 101 D. F. Lee, F. A. List, D. M. Kroeger, K. W. Childs, D. O'Neill, and W. B. Robbins, *Extended Abstracts of the 5<sup>th</sup> ISTECS-MRS Intl. Workshop on Superconductivity* (Honolulu HI, USA, 2001) 73.
- 102 A. Gupta, R. Jagannathan, E. I. Cooper, E. A. Giess, J. I. Landman, and B. W. Hussey, *Appl. Phys. Lett.* **52** (1988) 2077.
- 103 P. C. McIntyre and M. J. Cima, *J. Appl. Phys.* **70** (1995) 5263.
- 104 J. A. Smith, M. J. Cima, and N. Sonnenberg, *IEEE Trans. Appl. Supercond.* **9** (1999) 1531.
- 105 T. Araki, K. Yamagiwa, S. B. Kim, K. Matsumoto, and I. Hirabayashi, *Advances in Superconductivity XII* (Springer-Verlag, Tokyo, 2000) 610.
- 106 H. Kurosaki, T. Araki, T. Yuasa, S. B. Kim, Y. Yamada, I. Hirabayashi, Y. Iijima, and T. Saitou, *Extended Abstracts of the 5<sup>th</sup> ISTECS-MRS Intl. Workshop on Superconductivity* (Honolulu HI, USA, 2001) 131.
- 107 Y. Iijima, M. Hosaka, N. Sadakata, T. Saitoh, and O. Kohno, *J. Mater. Res.* **13** (1998) 3106.
- 108 T. Araki, H. Kurosaki, T. Yuasa, S. B. Kim, K. Yamagiwa, Y. Yamada, I. Hirabayashi, Y. Iijima, and K. Takeda, *Extended Abstracts of the 5<sup>th</sup> ISTECS-MRS Intl. Workshop on Superconductivity* (Honolulu HI, USA, 2001) 128.

- 109 I. Hirabayashi, Y. Yoshida, Y. Yamada, Y. Koike, and K. Matsumoto, *IEEE Trans. Appl. Supercond.* **9** (1999) 1979.
- 110 Y. Yoshida, Y. Ito, I. Hirabayashi, H. Nagai, and Y. Takai, *Appl. Phys. Lett.* **69** (1996) 845.
- 111 Y. Yoshida, I. Hirabayashi, and Y. Takai, *J. Crystal Growth* **229** (2001) 348.
- 112 W. Jo, T. Ohnishi, J. Huh, A. F. Marshall, R. H. Hammond, and M. R. Beasley, *Extended Abstracts of the 5<sup>th</sup> ISTECS-MRS Intl. Workshop on Superconductivity* (Honolulu HI, USA, 2001) 77.
- 113 D. Dimos, P. Chaudhari, and J. Mannhart, *Phys. Rev. B* **41** (1990) 4038.
- 114 J. G. Wen, T. Takagi, and N. Koshizuka, *Supercond. Sci. Tech.* **13** (2000) 820.
- 115 K. E. Gray, M. B. Field, and D. J. Miller, *Phys. Rev. B* **58** (1988) 954.
- 116 H. Hilgenkamp, J. Mannhart, and B. Meyer, *Phys. Rev. B* **53** (1996) 1458.
- 117 N. D. Browning, J. P. Buban, P. D. Nellist, D. P. Norton, M. F. Chisholm, and S. J. Pennycook, *Physica C* **294** (1998) 183.
- 118 S. Oktyabrsky, R. Kalyanaraman, K. Jafannadham, and J. Narayan, *J. Mater. Res.* **14** (1999) 2764.
- 119 D. J. Miller, T. A. Roberts, J. H. Kang, J. Talvacchio, D. B. Buchholz, and R. P. H. Chang, *Appl. Phys. Lett.* **66** (1995) 2561.
- 120 X. F. Zhang, V. R. Todt, and J. Talvacchio, *J. Mater. Res.* **11** (1996) 2440.
- 121 T. Takagi, J. G. Wen, T. Machi, K. Hashimoto, Y. Takahashi, T. Morishita, I. Hirabayashi, and N. Koshizuka, *IEEE Trans. Appl. Supercond.* **9** (1999) 2328.
- 122 N. Koshizuka, T. Takagi, J. G. Wen, T. Usagawa, Y. Eltsev, T. Machi, and K. Nakao, *Proc. 9<sup>th</sup> Intl. Workshop on Critical Currents* (Madison, Wisconsin, 1999) 85.
- 123 N. Koshizuka, T. Takagi, J. G. Wen, K. Nakao, T. Usagawa, Y. Eltsev, and T. Machi, *Physica C* **337** (2000) 1.
- 124 Y. Eltsev, K. Nakao, Y. Yamada, I. Hirabayashi, Y. Ishimaru, K. Tanabe, Y. Enomoto, J. G. Wen, and N. Koshizuka, *IEEE Trans. Appl. Supercond.* **11** (2001) 3784.
- 125 Y. Eltsev, K. Nakao, Y. Yamada, I. Hirabayashi, Y. Ishimaru, K. Tanabe, Y. Enomoto, J. G. Wen, and N. Koshizuka, *Physica C* **357-360** (2001) 1572.
- 126 H. Takeya and H. Takei, *Jpn. J. Appl. Phys. Pt 2-Lett.* **28** (1989) L1548.
- 127 G. Balestrino, V. Foglietti, M. Marinelli, E. Milani, A. Paoletti, P. Paroli, and G. Luce, *Solid State Commun.* **76** (1990) 503.
- 128 S. Narayanan, K. K. Raina, R. K. Pandey, and C. D. Brandle, *Mat. Lett.* **11** (1991) 212.
- 129 R. S. Liu, Y. T. Huang, P. T. Wu, and J. J. Chu, *Physica C* **156** (1988) 785.
- 130 R. F. Belt, J. Ings, and G. Diercks, *Appl. Phys. Lett.* **56** (1990) 1805.
- 131 L. H. Perng, T. S. Chin, K. C. Chen, and C. H. Lin, *Supercond. Sci. Tech.* **3** (1990) 233.
- 132 H. J. Scheel, C. Klemenz, F. K. Reinhart, H. P. Lang, and H. J. Guntherodt, *Appl. Phys. Lett.* **65** (1994) 901.
- 133 A. A. Chernov and H. J. Scheel, *J. Crystal Growth* **149** (1995) 187.
- 134 C. Klemenz and H. J. Scheel, *Physica C* **265** (1996) 126.
- 135 C. Klemenz and H. J. Scheel, *J. Crystal Growth* **129** (1993) 421.
- 136 P. Görnert, K. Fischer, and C. Dubs, *J. Crystal Growth* **128** (1993) 751.
- 137 C. Dubs, S. Bornmann, M. Schmelz, T. Schuler, F. Sandiumenge, G. Bruchlos, and P. Görnert, *J. Crystal Growth* **166** (1996) 836.

- 138 T. Aichele, S. Bornmann, C. Dubs, and P. Görnert, *Cryst. Res. Technol.* **32** (1997) 1145.
- 139 C. Dubs, K. Fischer, and P. Görnert, *J. Crystal Growth* **123** (1992) 611.
- 140 C. Dubs, T. Schuler, G. Bruchlos, M. Zeisberger, and P. Görnert, *J. Crystal Growth* **156** (1995) 216.
- 141 C. Klemenz, I. Utke, and H. J. Scheel, *J. Crystal Growth* **204** (1999) 62.
- 142 T. Kitamura, M. Yoshida, Y. Ikuhara, Y. Shiohara, I. Hirabayashi, and S. Tanaka, *Advances in Superconductivity VII* (Springer-Verlag, Tokyo, 1994) 617.
- 143 M. Mukaida, S. Miyazawa, C. Klemenz, and H. J. Scheel, *J. Crystal Growth* **169** (1996) 715.
- 144 X. Qi and J. L. MacManus-Driscoll, *J. Crystal Growth* **213** (2000) 312.
- 145 M. Yoshida, T. Nakamoto, T. Kitamura, Y. Yamada, I. Hirabayashi, Y. Shiohara, S. Tanaka, and A. Tsuzuki, *Physica C* **235** (1994) 353.
- 146 M. Yoshida, T. Nakamoto, T. Kitamura, O. B. Hyun, I. Hirabayashi, S. Tanaka, A. Tsuzuki, Y. Sugawara, and Y. Ikuhara, *Appl. Phys. Lett.* **65** (1994) 1714.
- 147 S. Miura, K. Hashimoto, F. Wang, Y. Enomoto, and T. Morishita, *Advances in Superconductivity IX* (Springer-Verlag, Tokyo, 1996) 1101.
- 148 T. Kitamura, S. Taniguchi, Y. Sugawara, Y. Ikuhara, Y. Shiohara, I. Hirabayashi, and S. Tanaka, *Physica C* **256** (1996) 64.
- 149 S. Taniguchi, T. Kitamura, Y. Shiohara, I. Hirabayashi, Y. Sugawara, Y. Ikuhara, and S. Tanaka, *Advances in Superconductivity VIII* (Springer-Verlag, Tokyo, 1995) 771.
- 150 M. Tagami, M. Nakamura, Y. Sugawara, Y. Ikuhara, and Y. Shiohara, *Physica C* **298** (1998) 185.
- 151 T. Kitamura, S. Taniguchi, Y. Shiohara, I. Hirabayashi, S. Tanaka, Y. Sugawara, and Y. Ikuhara, *J. Crystal Growth* **158** (1996) 61.
- 152 T. Kitamura, I. Hirabayashi, S. Tanaka, Y. Sugawara, and Y. Ikuhara, *Appl. Phys. Lett.* **68** (1996) 2002.
- 153 A. Takagi, I. Hirabayashi, and U. Mizutani, *J. Crystal Growth* **179** (1997) 444.
- 154 A. Takagi, I. Hirabayashi, and U. Mizutani, *J. Jpn. Inst. Met.* **61** (1997) 978.
- 155 A. Takagi, J. G. Wen, I. Hirabayashi, and U. Mizutani, *J. Crystal Growth* **193** (1998) 71.
- 156 Y. Niiori, Y. Yamada, I. Hirabayashi, T. Fujiwara, and K. Higashiyama, *Physica C* **301** (1998) 104.
- 157 Y. Yamada, Y. Niiori, I. Hirabayashi, and S. Tanaka, *Physica C* **278** (1997) 180.
- 158 Y. Yamada and I. Hirabayashi, *J. Jpn. Inst. Met.* **61** (1997) 937.
- 159 Y. Niiori, Y. Yamada, and I. Hirabayashi, *Physica C* **296** (1998) 65.
- 160 Y. Ishida, T. Kimura, K. Kakimoto, Y. Yamada, Z. Nakagawa, Y. Shiohara, and A. B. Sawaoka, *Physica C* **292** (1997) 264.
- 161 K. Kakimoto, Y. Sugawara, T. Izumi, and Y. Shiohara, *Physica C* **334** (2000) 249.
- 162 M. Kai, N. Hobara, K. Hasegawa, T. Izumi, S. Asada, Y. Nakamura, T. Izumi, T. Watanabe, and Y. Shiohara, *Extended Abstracts of the 5<sup>th</sup> ISTE C-MRS Intl. Workshop on Superconductivity* (Honolulu HI, USA, 2001) 150.
- 163 T. Kitamura, J. G. Wen, Y. Shiohara, N. Koshizuka, I. Hirabayashi, S. Tanaka, Y. Sugawara, and Y. Ikuhara, *Physica C* **262** (1996) 120.
- 164 T. Izumi, K. Kakimoto, K. Nomura, and Y. Shiohara, *J. Crystal Growth* **219** (2000) 228.

- 165 K. Nomura, S. Hoshi, X. Yao, K. Kakimoto, T. Izumi, Y. Nakamura, and Y. Shiohara, *J. Crystal Growth* **229** (2001) 384.
- 166 W. Bollmann, *Crystal Defects and Crystalline Interfaces* (Springer-Verlag, Berlin, 1970).
- 167 M. Kai, N. Hobara, K. Hasegawa, T. Izumi, H. Fuji, T. Honjo, Y. Nakamura, T. Izumi, and Y. Shiohara, *Physica C* **357-360** (2001) 1050.
- 168 K. Nomura, S. Hoshi, X. Yao, Y. Nakamura, T. Izumi, and Y. Shiohara, *Physica C* **357-360** (2001) 1377.
- 169 K. Nomura, S. Hoshi, Y. Nakamura, T. Izumi, and Y. Shiohara, *J. Mater. Res.* **16** (2001) 2947.
- 170 T. Kitamura, M. Yoshida, Y. Yamada, Y. Shiohara, I. Hirabayashi, and S. Tanaka, *Appl. Phys. Lett.* **66** (1995) 1421.
- 171 T. Kitamura, Y. Yamada, Y. Shiohara, I. Hirabayashi, S. Tanaka, Y. Sugawara, and Y. Ikuhara, *J. Crystal Growth* **166** (1996) 854.
- 172 C. Klemenz, *J. Crystal Growth* **187** (1998) 221.
- 173 I. Hirabayashi, M. Yoshida, T. Kitamura, O. B. Hyun, Y. Shiohara, S. Tanaka, A. Tsuzuki, Y. Sugawara, and Y. Ikuhara, *IEEE Trans. Appl. Supercond.* **5** (1995) 2015.
- 174 Y. Niiori, Y. Yamada, Y. Yoshida, and I. Hirabayashi, *Jpn. J. Appl. Phys. Pt 2-Lett.* **35** (1996) L1407.
- 175 T. Kitamura, Y. Sugawara, Y. Ikuhara, and I. Hirabayashi, *Advances in Superconductivity IX* (Springer-Verlag, Tokyo, 1996) 1077.
- 176 S. Miura, K. Hashimoto, F. Wang, Y. Enomoto, and T. Morishita, *Physica C* **278** (1997) 201.
- 177 Ch. Krauns, S. Koyama, T. Izumi, T. Izumi, Y. Nakamura, and Y. Shiohara, *Physica C* **357-360** (2001) 1055.
- 178 Y. Nakamura, A. Endo, and Y. Shiohara, *J. Mater. Res.* **11** (1996) 1094.
- 179 K. Nomura, S. Hoshi, X. Yao, Y. Nakamura, T. Izumi, and Y. Shiohara, *J. Jpn. Inst. Met.* **64** (2000) 323.
- 180 Y. Yamada, Y. Niiori, I. Hirabayashi, and S. Tanaka, *Advances in Superconductivity VIII* (Springer-Verlag, Tokyo, 1995) 337.
- 181 Y. Yamada, Y. Niiori, Y. Yoshida, I. Hirabayashi, and S. Tanaka, *J. Crystal Growth* **167** (1996) 566.
- 182 Y. Yamada and I. Hirabayashi, *J. Crystal Growth* **229** (2001) 343.
- 183 J. Maeda and Y. Shiohara, *J. Jpn. Inst. Met.* **63** (1999) 397.
- 184 N. Sakai, M. Deguchi, S.-I. Yoo, and M. Murakami, *J. Jpn. Inst. Met.* **61** (1997) 920.
- 185 B. J. Lee and D. N. Lee, *J. Am. Ceram. Soc.* **74** (1991) 78.
- 186 M. Tagami, Ch. Krauns, M. Sumida, M. Nakamura, Y. Yamada, T. Umeda, and Y. Shiohara, *J. Jpn. Inst. Met.* **60** (1996) 353.
- 187 M. Nakamura, Ch. Krauns, and Y. Shiohara, *J. Mater. Res.* **11** (1996) 1076.
- 188 K. W. Lay and G. M. Renlund, *J. Am. Ceram. Soc.* **73** (1990) 1208.
- 189 M. Nakamura, M. Kambara, T. Umeda, and Y. Shiohara, *Physica C* **266** (1996) 178.
- 190 M. Nakamura, Y. Yamada, and Y. Shiohara, *J. Mater. Res.* **9** (1994) 1946.
- 191 M. Murakami, N. Sakai, T. Higuchi, and S. I. Yoo, *Supercond. Sci. Tech.* **9** (1996) 1015.

- 192 Y. Koike, Y. Yamada, Y. Niiori, and I. Hirabayashi, *Extended Abstracts of the 2<sup>nd</sup> ISTEC-MRS Intl. Workshop on Superconductivity* (Naha-shi, Okinawa, Japan, 1998) 197.
- 193 T. Iwata, M. Hikita, and S. Tsurumi, *Advances in Superconductivity I* (Springer-Verlag, Tokyo, 1988) 197.
- 194 T. Izumi, N. Hobara, T. Izumi, M. Kai, K. Hasegawa, Ch. Krauns, Y. Nakamura, T. Watanabe, and Y. Shiohara, *Extended Abstracts of the 5<sup>th</sup> ISTEC-MRS Intl. Workshop on Superconductivity* (Honolulu HI, USA, 2001) 237.
- 195 T. Izumi, X. Yao, N. Hobara, K. Hasegawa, M. Kai, S. Asada, Y. Nakamura, T. Izumi, Y. Shiohara, and T. Watanabe, *Extended Abstracts of the 5<sup>th</sup> ISTEC-MRS Intl. Workshop on Superconductivity* (Honolulu HI, USA, 2001) 153.
- 196 T. Izumi, N. Hobara, K. Kakimoto, T. Izumi, K. Hasegawa, M. Kai, T. Honjo, X. Yao, H. Fuji, Y. Nakamura, and Y. Shiohara, *J. Crystal Growth* **229** (2001) 330.
- 197 N. Hobara, S. Asada, T. Izumi, X. Yao, K. Hasegawa, M. Kai, Ch. Krauns, Y. Nakamura, T. Izumi, and Y. Shiohara, *Extended Abstracts of the 5<sup>th</sup> ISTEC-MRS Intl. Workshop on Superconductivity* (Honolulu HI, USA, 2001) 156.
- 198 T. Izumi, X. Yao, N. Hobara, K. Kakimoto, K. Hasegawa, Y. Nakamura, T. Izumi, and Y. Shiohara, *J. Jpn. Inst. Met.* **64** (2000) 719.
- 199 T. Maeda, S. B. Kim, T. Suga, H. Kurosaki, T. Yuasa, Y. Yamada, H. Yoshino, M. Yamazaki, T. D. Thanh, T. Watanabe, K. Matsumoto, and I. Hirabayashi, *IEEE Trans. Appl. Supercond.* **11** (2001) 2931.
- 200 X. Yao, T. Izumi, N. Hobara, Y. Nakamura, T. Izumi, and Y. Shiohara, *Physica C* **357-360** (2001) 1063.
- 201 K. Kakimoto, N. Hobara, Y. Nakamura, T. Izumi, K. Fujino, K. Ohmatsu, and Y. Shiohara, *Physica C* **341-348** (2000) 2489.
- 202 N. Hobara, K. Kakimoto, Y. Nakamura, T. Izumi, and Y. Shiohara, *J. Jpn. Inst. Met.* **64** (2000) 727.
- 203 T. Izumi, N. Hobara, K. Kakimoto, T. Izumi, K. Hasegawa, M. Kai, T. Honjo, X. Yao, H. Fuji, Y. Nakamura, and Y. Shiohara, *Physica C* **357-360** (2001) 1027.
- 204 T. Suga, Y. Yamada, S. B. Kim, T. Maeda, Y. Yamada, I. Hirabayashi, T. D. Thanh, M. Yamazaki, and H. Yoshino, *Extended Abstracts of the 5<sup>th</sup> ISTEC-MRS Intl. Workshop on Superconductivity* (Honolulu HI, USA, 2001) 159.
- 205 T. Maeda, H. Kurosaki, T. Suga, S. B. Kim, T. Yuasa, Y. Yamada, T. Watanabe, and I. Hirabayashi, *Extended Abstracts of the 5<sup>th</sup> ISTEC-MRS Intl. Workshop on Superconductivity* (Honolulu HI, USA, 2001) 166.
- 206 Y. Yamada, T. Suga, H. Kurosaki, S. B. Kim, T. Maeda, Y. Yamada, I. Hirabayashi, Y. Iijima, K. Kakimoto, and T. Saitoh, *Advances in Superconductivity XIV* (Springer-Verlag, Tokyo, 2002) in press.
- 207 X. Qi and J. L. MacManus-Driscoll, *Extended Abstracts of the 5<sup>th</sup> ISTEC-MRS Intl. Workshop on Superconductivity* (Honolulu HI, USA, 2001) 162.
- 208 X. Qi, M. Soorie, and J. L. MacManus-Driscoll, *Proc. 5<sup>th</sup> European Conf. on Appl. Supercond.* (Copenhagen, Denmark, 2001) in press.
- 209 X. Qi, M. Soorie, Z. Lockman, and J. L. MacManus-Driscoll, "Rapid Growth of Nd<sub>2-x</sub>Ce<sub>x</sub>CuO<sub>4</sub> Thick Films as a Buffer on NiO/Ni for the Growth of Rare Earth Barium Cuprate Coated Conductors", preprint.
- 210 D. X. Huang, Y. Yamada, and I. Hirabayashi, *Physica C* **357-360** (2001) 1034.
- 211 T. Kitamura, S. Taniguchi, I. Hirabayashi, S. Tanaka, Y. Sugawara, and Y. Ikuhara, *IEEE Trans. Appl. Supercond.* **7** (1997) 1392.

- 212 T. Kitamura and I. Hirabayashi, *ISTEC Journal* **8** (1995) 19.
- 213 A. Takagi, U. Mizutani, T. Kitamura, S. Taniguchi, Y. Shiohara, I. Hirabayashi, S. Tanaka, and Y. Yamada, *IEEE Trans. Appl. Supercond.* **7** (1997) 1388.
- 214 A. Hayashi, K. Hasegawa, U. Nakamura, T. Izumi, and Y. Shiohara, *J. Jpn. Inst. Met.* **64** (2000) 307.
- 215 Y. Nakamura, N. Hobara, K. Kakimoto, T. Izumi, and Y. Shiohara, *Physica C* **341-348** (2000) 2323.
- 216 A. Vostner, H. W. Weber, A. Mathen, C. Jooss, J. Hoffmann, and H. C. Freyhardt, *Physica C* **341-348** (2000) 2487.
- 217 A. Vostner, Y. Sun, S. Tönies, H. W. Weber, Y. S. Cheng, A. Kursumovic, and J. E. Evetts, *Proc. 10<sup>th</sup> Intl. Workshop on Critical Current* (Göttingen, Germany, 2001) 291.
- 218 X. Yao, K. Nomura, M. Yoshizumi, M. Kuznetsov, Y. Nakamura, T. Izumi, and Y. Shiohara, *Physica C* **357-360** (2001) 1059.
- 219 H. J. Scheel, *MRS Bull.* **19** (1994) 26.
- 220 C. Klemenz, I. Utke, and H. J. Scheel, *J. Crystal Growth* **207** (1999) 62.
- 221 S. Rothman, J. L. Routboud, and U. Welp, *Phys. Rev. B* **44** (1991) 2326.
- 222 E. Olsson, A. Gupta, M. D. Thouless, A. Segmüller, and D. R. Clarke, *Appl. Phys. Lett.* **58** (1991) 1682.
- 223 T. Aichele, P. Gornert, R. Uecker, and M. Muhlberg, *IEEE Trans. Appl. Supercond.* **9** (1999) 1510.
- 224 J. Kawashima, Y. Yamada, and I. Hirabayashi, *Physica C* **306** (1998) 114.
- 225 Y. Yamada, J. Kawashima, J. G. Wen, Y. Niiori, and I. Hirabayashi, *Jpn. J. Appl. Phys. Pt 1* **39** (2000) 1111.
- 226 R. Kita, Y. Ishibe, and T. Suzuki, *Jpn. J. Appl. Phys. Pt 2-Lett.* **39** (2000) L1221.

<b>Chapter IV</b>	<b>A Review in Coated Conductor Development</b>	<b>44</b>
4.1	Introduction	44
4.2	Substrates	45
4.2.1	<i>Untextured metallic substrates</i>	48
4.2.2	<i>Textured metallic substrates</i>	48
4.3	Buffer Layers	50
4.3.1	<i>IBAD buffer</i>	50
4.3.2	<i>Inclined substrate deposition</i>	51
4.3.3	<i>Ceramic buffer on RABiTS</i>	52
4.3.4	<i>Metallic buffer on RABiTS</i>	54
4.3.5	<i>Self-oxidation epitaxy</i>	54
4.4	Superconducting Layer	55
4.4.1	<i>Thin film</i>	55
4.4.2	<i>Thick film</i>	56
4.5	Studies of Grain Boundaries as Weak Links Using Bicrystals	58
4.6	Summary of Coated Conductor Development	60
4.7	Liquid Phase Epitaxy of REBCO	60
4.7.1	<i>Early LPE of REBCO</i>	61
4.7.2	<i>Nucleation and growth of REBCO by LPE</i>	62
4.7.2(a)	Nucleation and growth of YBCO on NdGaO <sub>3</sub>	62
4.7.2(b)	Nucleation and growth of NdBCO on NdGaO <sub>3</sub>	64
4.7.2(c)	Nucleation and growth on seeded substrates	64
4.7.2(d)	Crystalline orientation of the LPE grown films	68
4.7.2(e)	Factors affecting the LPE growth rate	69
4.7.3	<i>Lowering the growth temperature</i>	70
4.7.4	<i>Recent developments</i>	72
4.7.5	<i>Transport properties</i>	75
4.7.6	<i>Crack formation</i>	76
4.8	Summary of the LPE of REBCO	78
	References	79

*This chapter describes all the experimental techniques used in sample preparation and characterisation of this work. Three different types of furnace set-ups were used for the LPE growth and various techniques including XRD and AFM were used to characterise the films.*

## **5.1 Sample Preparation**

Preparation of samples involves film growth on a suitable substrate and oxygenation to obtain proper oxygen stoichiometry.

### **5.1.1 Starting materials**

The starting materials used for the Ba-Cu-O flux were high purity BaO and CuO powders mixed in a ratio of Ba:Cu = 3:5 (pre-mixed and supplied by Praxair, 99.9%), whereas Y211 (Praxair, 99.9%) was used as a source of yttrium. The Y211 was pressed into pellets and sintered for several hours before use. Additional RE elements, Nd and Sm, were added as Nd422 and Sm211 (both by Praxair, 99.9%) in several experiments in the order of 1-2 at% in pressed and sintered form.

In cases where a Ba-Cu-O-F-Ag flux was used, besides BaO-CuO and Y211, approximately 5 mol% of pre-pressed BaF<sub>2</sub> (Alfa, 99.995%) pellets were added. Pre-pressed CuO (Sigma, 99%) pellets were also added in order to maintain the Ba:Cu ratio at 3:5. Ag (Advent, 99.9%) was added in the form of ribbon in the order of 7 at% (metal basis) to the melt in several experiments. An example of flux calculation is presented in the Appendix.

Different polished single crystalline substrate materials were investigated including (110) NdGaO<sub>3</sub>, (100) MgO, and (100) SrTiO<sub>3</sub>. With the exception of NdGaO<sub>3</sub>, all other single-crystalline substrates used required a YBCO seed layer. YBCO seeded metallic tapes (Ni, NiFe, NiCr, NiV, NiCrW) with various buffer architectures were also investigated. All seed and buffer layers were prepared by PLD technique with a KrF excimer laser (wavelength = 248 nm) with 20 ns pulse and at a repetition rate of 1-10 Hz [1-3].

### 5.1.2 Furnace set-up

Three different types of furnace set-up were used in this work for the LPE growth: (a) a box furnace with thermal-gradient crucible equipped with substrate rotation operating in air; (b) a box furnace operating in air using step cooling mode; and (c) a controlled-atmosphere furnace with thermal-gradient crucible equipped with substrate and/or crucible rotation capability.

In all three set-ups, excess amount of sintered RE211 pellets were placed at the bottom of a YSZ crucible and the top filled with pre-pressed Ba<sub>3</sub>Cu<sub>5</sub>O<sub>8</sub> pellets. The crucibles used were straight cylindrical open crucibles with 50 mm in diameter, 42 mm in height, and 1 mm thick supplied by Almath Crucibles Ltd. In furnaces with thermal-gradient crucible ((a) and (c) above), natural convection due to the thermal gradient was used to saturate the flux with RE prior to the growth stage. During growth, the substrates were rotated in order to establish forced convection of flux from bottom to top of the crucible, delivering melt supersaturated with Y or RE solutes.

The choices of crucible material were limited to high-melting oxide crucibles since metal crucibles such as platinum and gold were found, besides their high cost, unsuitable. Pt crucibles were found to be heavily corroded. Pt reacted with the flux forming Pt-rich Y-Ba-Cu-O phases such as Y<sub>2</sub>Ba<sub>2</sub>CuPtO<sub>8</sub> [4] and Y<sub>2</sub>Ba<sub>3</sub>Cu<sub>2</sub>PtO<sub>10</sub> [4,5]. Although a gold crucible was not as heavily corroded [6,7], however, a strong creeping of flux was observed [8] making the control of growth parameters difficult and did not allow for a long duration of experiments.

Among ceramic crucibles, Al<sub>2</sub>O<sub>3</sub> was considered due to its availability and relatively low cost. Al<sub>2</sub>O<sub>3</sub> crucible was initially used to grow YBCO in this work. However, the crucible was heavily corroded at the relatively high growth temperature leading to rapid rise in the flux viscosity. Severe flux creeping was also observed. Besides, Al substitutes for Cu in the Cu-O chains resulting in the formation of YBa<sub>2</sub>Cu<sub>3-x</sub>Al<sub>x</sub>O<sub>7-δ</sub> with values of  $x$  up to 0.22 [9] or even 0.5 [8]. YSZ was the next candidate, due to its higher melting point compared to Al<sub>2</sub>O<sub>3</sub>

(2700°C as opposed to 2040°C). However, YSZ has poor thermal shock resistance, which leads to cracking once cooled below the melting point of the flux, i.e. the flux could not be cooled down (solidified) and re-molten in the same crucible. The YSZ crucible was also found [9] to corrode over time forming barium zirconate with the formula  $\text{Ba}(\text{Y,Ca,Cu})\text{Zr}(\text{Cu})\text{O}_3$ . Nevertheless, the corrosion velocity was found to be acceptable [10] and contamination in the flux was found to be insignificant [8] where the YSZ crucible lasted for more than one week. Flux creeping was also observed on YSZ crucible, however, it was found acceptable for the duration of experiments in this work, which lasted up to ~10 days.

There are other materials such as  $\text{BaZrO}_3$  [11] and  $\text{RE}_2\text{O}_3$  crucibles where the latter were widely used at ISTECH in Japan. However, due to non-reliable supply and high cost,  $\text{BaZrO}_3$  crucibles were tested and abandoned in this work. Although  $\text{RE}_2\text{O}_3$  crucibles could reduce contamination as well as act as a source of RE solutes, they were not used mainly due to their high cost and limited availability.

### 5.1.2(a) *Box furnace with thermal-gradient crucible operating in air*

The first set-up was a modified box furnace equipped with a programmable temperature controller; the furnace set-up is shown schematically in Fig. 5.1.

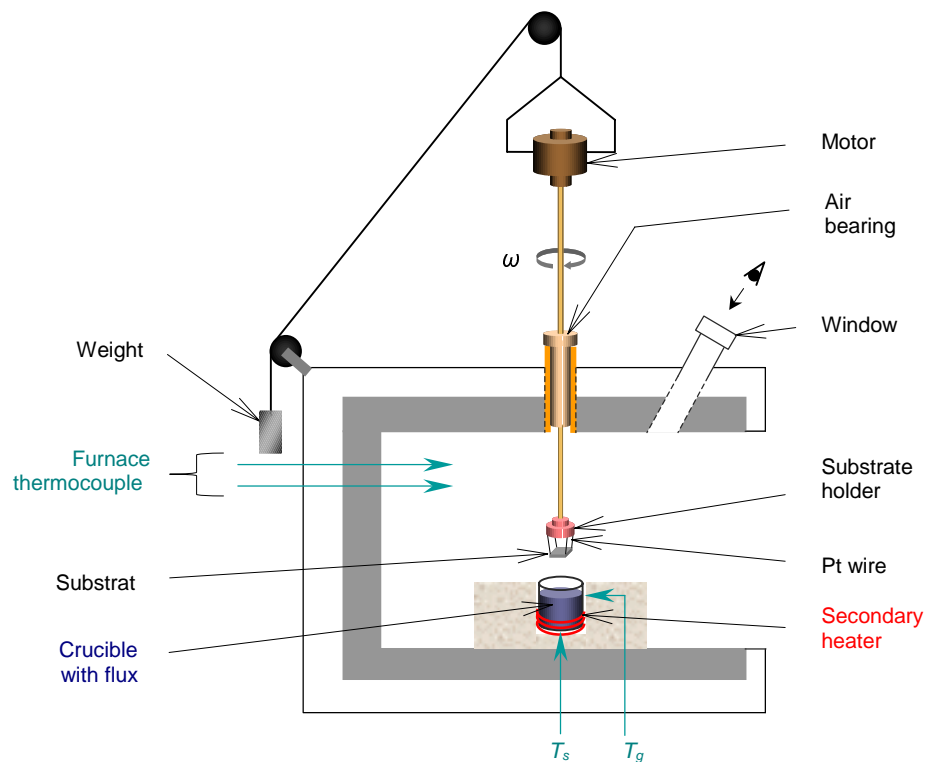


**Fig. 5.1** Schematic diagram of the LPE furnace with thermal-gradient crucible operating in air.

The furnace contains a set of primary heaters on both sides of the furnace walls and a secondary heating element at the bottom of the crucible, where molten flux was held. The growth atmosphere was air. Single crystalline substrates were horizontally attached by platinum wires at the lower end of a vertically placed ceramic rod that could be rotated around its axis. Besides furnace thermocouples, two type-K inconel-sheath thermocouples, one at the bottom of the crucible ( $T_s$ ) and one at 30 mm from the bottom ( $T_g$ ) as shown in Fig. 5.1, were attached halfway into the crucible wall for monitoring the undercooling. Optical pyrometer was also used to measure temperature at the surface of the flux through the observation window.

### **5.1.2(b) *Box furnace operating in air using step-cooling mode***

A conventional box furnace with side heating was also used for LPE growth in air using a step-cooling mode. No forced convection by substrate rotation was employed in this set-up. A YSZ crucible holding the melt was placed in the middle of the furnace and substrates were lowered into the melt from the top, held by platinum wire.

Step cooling was used to achieve the desired undercooling by controlling the overall furnace temperature. Additional thermocouples were attached halfway into the crucible wall for better monitoring of the flux temperatures. A secondary heating element was employed at the bottom of the crucible in order to avoid any temperature gradient across the entire flux.

Film growth was carried out ~30-35 minutes after the furnace temperature was reduced for the desired undercooling when the solution had reached thermal equilibrium, which was monitored by the thermocouples attached halfway into the crucible wall. The step-cooling mode has a major disadvantage compared to growth in a thermal-gradient crucible since the solute concentration in the former decreased from supersaturation to saturation level with time; thus, film growth had to be ceased after a certain period of time. However, the set-up was much simpler than the other two furnaces.

### **5.1.2(c) *Controlled-atmosphere furnace with thermal-gradient crucible***

In order to reduce the growth temperature and minimise high-temperature oxidation on metallic substrates, a growth condition with low  $pO_2$  is desired. Thus, a controlled-atmosphere furnace with three separate heating zones was built as shown schematically in Fig. 5.2. The topmost heating zone is retractable as part of a design for continuous reel-to-reel horizontal-fed configuration. The furnace is equipped with a crucible rotation capability

as well as substrate rotation in the vertically-fed arrangement. The growth atmosphere was 1%  $pO_2$  in Ar.

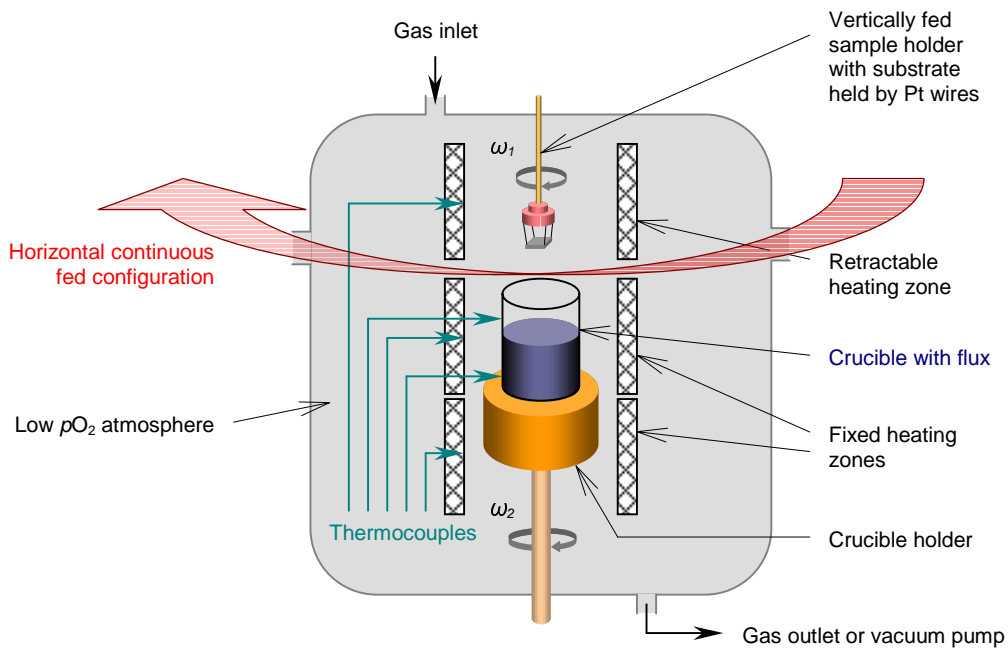


**Fig. 5.2** Schematic diagram of the controlled-atmosphere LPE furnace with thermal-gradient crucible.

### 5.1.3 Growth conditions

Growth conditions such as growth temperature varied according to the method used to achieve the desired undercooling and the use of additives in the melt. For YBCO growth from a Ba-Cu-O melt in the first furnace set-up, the bottom of the crucible was kept at 1020°C, while dissolution of the Y211 pellet was carried out at 1010°C which is above the peritectic temperature (~1005°C [12]). The 10°C gradient from 1020°C to 1010°C occurred through the bottom of the crucible and Y211 pellet where the temperature profile is shown in Fig. 5.3.

The solution is equilibrated at  $T_s$  (see Fig. 3.16) until the equilibrium "background" Y concentration ( $C_L$ ) was reached. The top of the melt, where growth occurs for equilibrium concentration  $C_e$ , was kept at 987-992°C at least ~10°C below  $T_p$  (~1005°C [12]). The critical parameters such as peritectic temperature and hence corresponding solubility data are not exactly known. However, the Y concentration ( $C_L$ ) in  $Ba_3Cu_5O_8$  solvent at ~1000°C is below 1 at% [12,13]. A solvent of composition Ba:Cu = 3:5 reacts with the Y211 pellet above  $T_p$ , enabling the growth of Y123 below  $T_p$  according to Eqn. (3.26).

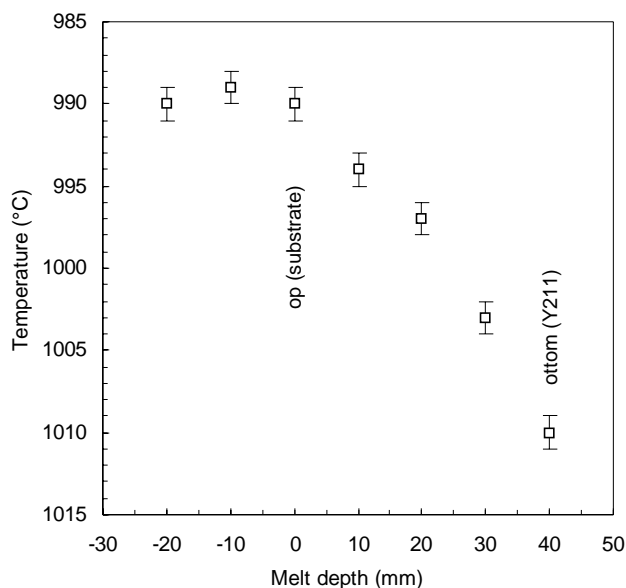


*Fig. 5.3 Temperature profile in a furnace set-up with thermal-gradient crucible.*

The amount of the melt decreases during growth without changing the average composition of the solution [14], which is the advantage of using a solvent with this composition. It was reported [13] that crucible corrosion might be the source of a significant change in the melt composition. However, in these rather short experiments (lasting up to ~10 days) contamination from YSZ crucibles was found to be insignificant.

#### **5.1.4 Film growth**

The substrate was slowly lowered (~0.2 mm/s) into the furnace and equilibrated for about 10 minutes prior to film growth. When forced convection was used, steady substrate rotation was started prior to its immersion into the melt. Various rotation rates ranging from 0 to 200±10 rpm were used. Films were grown isothermally at a temperature range of 900-990°C (higher for NdBCO) from 1 second to 9½ hours at a constant rotation rate.

Upon withdrawal of substrate (with films) from the melt, whenever possible, the substrate was rotated at a speed of 800-1500 rpm for 3-5 seconds in order to remove residual flux on the film by centrifugal force. The substrate with the film was subsequently removed from the furnace and cooled to room temperature in approximately 30 minutes.

### 5.1.5 Oxygenation

All samples were annealed in a conventional tube furnace at 500-700°C with a heating rate of 10°C/min for 48-168 hours under continuous flow of pure oxygen gas. Samples were furnace cooled under flowing oxygen gas after the power was cut off.

## 5.2 Characterisation

X-ray diffraction (XRD), optical microscopy, electron microscopy, and atomic force microscopy (AFM) were used for chemical and structural analyses. Superconductivity of the films was examined by measuring their  $T_c$  and  $J_c$ .

### 5.2.1 X-ray diffraction

All XRD measurements were performed on an automated Philips X'Pert diffractometer using Cu  $K_\alpha$  radiation (wavelength 1.542 Å).

#### 5.2.1(a) Diffractometer

A Philips X'Pert PW1710 diffractometer was used to carry out  $\theta$ - $2\theta$  and  $\omega$ -scans. The sample was aligned using plasticine such that its surface was parallel to the top of the sample holder, thus coinciding with the axis of rotation of the diffractometer as shown in Fig. 5.4.

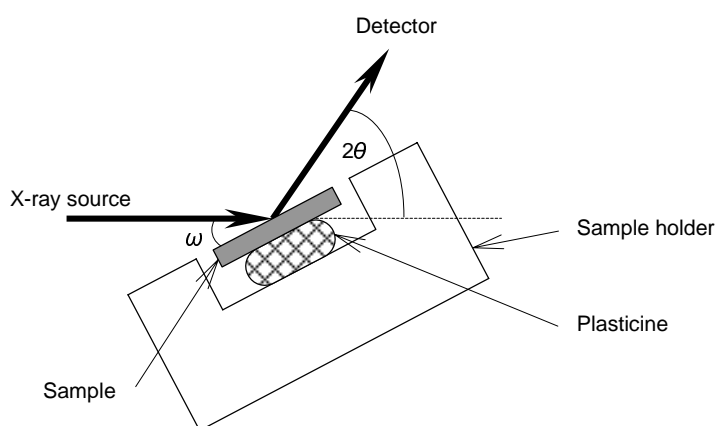


**Fig. 5.4** Set-up of the diffractometer.

In a  $\theta$ - $2\theta$  scan, the X-ray source remains fixed while the sample and the detector rotate at a ratio of 1:2. In this set-up, the incident X-ray beam makes an angle  $\theta$  with the sample whereby crystallographic planes parallel with the sample surface that satisfy the Bragg's Law

will diffract the X-ray beam to the detector.  $\theta$ - $2\theta$  scans were carried out in order to identify the phases present and its crystalline orientation for  $2\theta = 5^\circ$  to  $80^\circ$  at a scan rate of  $0.04^\circ/\text{s}$ .

By de-coupling the 1:2 rotation ratio, the angles made between the incident-beam/sample-surface and diffracted-beam/sample-surface are no longer equal. In this case, the angle made between the incident beam and sample surface is referred to as  $\omega$  (see Fig. 5.4). In the so-called rocking curve or  $\omega$ -scan, the positions of the incident beam and detector remain fixed for a  $2\theta$  angle of the relevant  $\{hkl\}$  reflections, for instance, (005) peak of *c*-oriented REBCO. The sample is then rotated in order to detect reflections from planes with the same  $\{hkl\}$  indices that are in slightly different orientations with respect to the angle  $\omega$ ; the resulting FWHM value from the measurement is an indication of the out-of-plane alignment of the sample. Rocking curves or  $\omega$ -scans were carried out on the (005) and (100)/(010) peak of *c*-axis oriented and *a,b*-axes oriented REBCO films, respectively, at a scan rate of  $0.02^\circ/\text{s}$ . The FWHM values from the  $\omega$ -scans were estimated using the PROFIT software developed by Langford *et al.* [15] and corrected for errors due to instrumental broadening.

### 5.2.1(b) *Texture goniometer*

In-plane alignment of the film was determined using a Philips X'Pert automated texture goniometer unit. The sample was mounted onto a brass stage and the height was adjusted using a retractable needle. The texture cradle on which the sample stage was mounted enabled the sample to be rotated in its own plane ( $\phi$ -scan) as well as the plane normal to both its surface and the plane containing the incident X-ray beam ( $\psi$ -scan). By measuring a series of  $\phi$ -scans from  $0^\circ$  to  $360^\circ$  at various  $\psi$  angles, which is limited between  $-70^\circ$  and  $+70^\circ$  due to defocusing effects, the variation of pole density with pole orientation for a selected set of crystal planes can be stereographically projected onto a 2-D representation known as a pole figure. The FWHM values obtained from the pole figure indicate the grain orientation within the plane. In-plane alignments were examined using  $\{103\}$  pole figures of REBCO for  $\phi = 0^\circ$  to  $360^\circ$  at a rate of  $2^\circ/\text{s}$  and  $\psi = 0^\circ$  to  $60^\circ$  at  $3^\circ$  interval.

### 5.2.2 *Optical microscopy*

Film thickness and surface morphologies (as-grown and post-annealed) were examined under reflected-light and polarised-light microscopes; the former is connected to a digital imaging tool while the latter is equipped with a 35 mm camera whereby photomicrographs were taken. The resolution of the optical microscopes used is about  $1\ \mu\text{m}$ .

### 5.2.3 Electron microscopy

Scanning electron microscopy (SEM), transmission electron microscopy (TEM), and high-resolution TEM (HREM) techniques were used to study the samples at atomic scale. A JEOL JSM-5800LV SEM equipped with energy dispersive X-ray spectroscopy (EDX) was used to study the chemical compositions of the films. All TEM and HREM works were carried out by Sibe Mennema [16] at the Delft University of Technology in the Netherlands.

### 5.2.4 Atomic force microscopy

Surface topographies of the samples were mapped using an AFM (Digital Instrument Nanoscope III). Microfabricated cantilevers with integrated  $\text{Si}_3\text{N}_4$  tips were employed and the images were recorded in tapping mode. In tapping mode AFM, the tip that is mounted on a flexible cantilever oscillates at a constant frequency as the AFM head scans across a selected area on the sample. The amplitude of the tip oscillation varies as the tip comes close to the specimen and interacts with the surface atoms. This information is used to deduce the surface height and topography of the sample. The AFM used was well calibrated in the  $z$ -direction with a resolution of  $\sim 2$  nm.

### 5.2.5 $T_c$ measurement

Two different methods were used to measure the transition temperature: (a) resistive transition, and (b) inductive method.

#### 5.2.5(a) Resistive transition

A standard four-probe method as shown in Fig. 5.5 was used to measure the resistive transition of oxygenated samples. The sample was mounted onto a probe and lowered into a helium dewar; voltage, current, and temperature readings were recorded for  $\Delta T \geq 0.5$  K and/or  $\Delta R \geq 0.2\%$ .

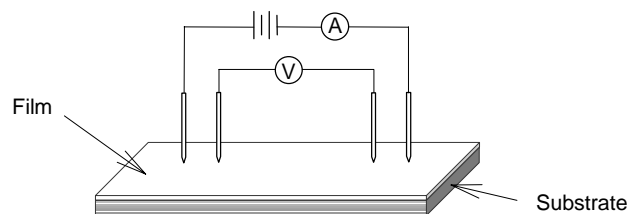
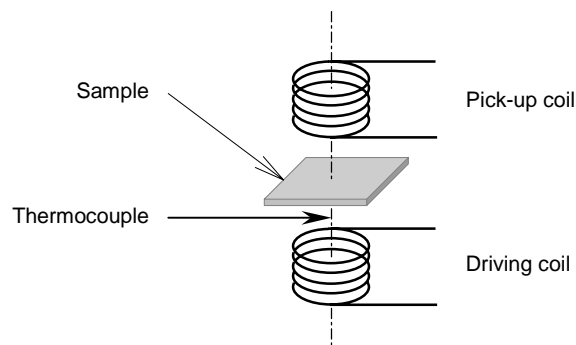


Fig. 5.5 Schematic diagram of the standard four-probe method for resistive transition measurement.

### 5.2.5(b) Inductive $T_c$ measurement

A simple inductive probe with a driving coil and a pick-up coil was used as an alternative, non-contact method to measure  $T_c$ . The sample with a thermocouple attached nearby was sandwiched between the coils as shown in Fig. 5.6. When an AC source was applied to the driving coil, it generated a magnetic field that went through the sample and induced the pick-up coil on the other side. Signals from the pick-up coil and the thermocouple were recorded as the probe was lowered into a helium dewar. When the sample reached its superconducting state, due to the Meissner effect, magnetic flux was expelled from the sample resulting in a drop of the pick-up signal. The corresponding temperature is  $T_c$ .



**Fig. 5.6** Schematic diagram of the inductive probe.

### 5.2.6 Transport $J_c$

All transport  $J_c$  measurements were carried out by Alexander Vostner [17] at the Atominstitut der Österreichischen Universitäten in Vienna, Austria where detailed procedures had been described in his Ph.D. dissertation. Making good low resistance electrical contact is an important step in measuring transport  $J_c$ . The contact terminals on the YBCO layer were made by vapour deposition of silver followed by a post-annealing process at 500°C in pure oxygen at 1 bar. The current and voltage leads were either soldered with Wood's metal or glued with silver paste onto the silver terminals. Fig. 5.7 shows a schematic diagram of the contacts used.

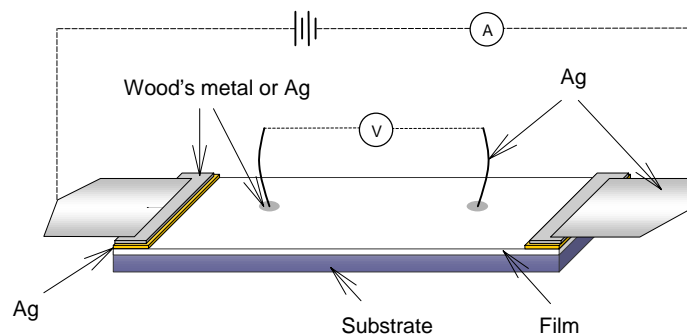


**Fig. 5.7** Schematic diagram of sample preparation for transport  $J_c$  measurement.

All transport current measurements were performed in a 6 T cryostat at various temperatures. Due to the lack of a protective shunt layer the currents through the samples had to be reduced by bridge patterning. The films were chemically etched to widths varying from 0.8 mm to 1.6 mm. However, a comparison of the  $J_c$  showed a small degradation due to etching, which was explained by partial etching of the bridges from the sides [17]. A standard electric field criterion of  $10^{-4}$  V/m ( $1 \mu\text{V}/\text{cm}$ ) was chosen for the evaluation of the critical transport current.

### 5.3 RE Solubility Measurement

The solubility of various RE solutes in the flux was measured using inductively coupled plasma atomic emission spectrometry (ICP-AES) at Qi *et al.* at Imperial College in London. The samples were taken from the high-temperature solution at 990-1010°C by dipping a platinum boat in the solution and then quickly withdrawing. The platinum boat was preheated to the same temperature as the solution at the position just above the surface of the solution to avoid segregation of solute phase. The samples were collected under similar conditions as film growth.

### References

- 1 R. I. Tomov, A. Kursumovic, D. J. Kang, B. A. Glowacki, M. Majoros, J. E. Evetts, A. Tuissi, and E. Villa, *Proc. 5<sup>th</sup> European Conf. on Appl. Supercond.* (Copenhagen, Denmark, 2001) in press.
- 2 R. I. Tomov, A. Kursumovic, M. Majoros, D.-J. Kang, B. A. Glowacki, and J. E. Evetts, *Supercond. Sci. Tech.*, in press.
- 3 R. I. Tomov *et al.*, unpublished data.
- 4 Y. Laligant, G. Ferey, M. Hervieu, and B. Raveau, *Europhys. Lett.* **4** (1987) 1023.
- 5 H. J. Scheel and F. Licci, *J. Crystal Growth* **85** (1987) 607.
- 6 D. L. Kaiser, F. Holtzberg, M. F. Chisholm, and T. K. Worthington, *J. Crystal Growth* **85** (1987) 593.
- 7 D. L. Kaiser, F. Holtzberg, B. A. Scott, and T. R. McGuire, *Appl. Phys. Lett.* **51** (1987) 1040.
- 8 C. Klemenz, PhD Dissertation, Swiss Federal Institute of Technology, Lausanne (2000).
- 9 H. J. Scheel, W. Sadowski, and L. Schellenberg, *Supercond. Sci. Tech.* **2** (1989) 17-21.
- 10 M. Berkowski, P. Bowen, T. Liechti, and H. J. Scheel, *J. Am. Ceram. Soc.* **75** (1992) 1005.
- 11 A. Erb, E. Walker, and R. Flukiger, *Physica C* **258** (1996) 9.
- 12 Ch. Krauns, M. Sumida, M. Tagami, Y. Yamada, and Y. Shiohara, *Z. Physik B* **96** (1994) 207.
- 13 C. Klemenz and H. J. Scheel, *J. Crystal Growth* **200** (1999) 435.

- 14 Y. Yamada, M. Nakamura, Ch. Krauns, M. Tagami, Y. Shiohara, and S. Tanaka, *J. Crystal Growth* **166** (1996) 804.
- 15 J. I. Langford, D. Louër, E. J. Sonneveld, and J. W. Visser, *Powder Diffraction* **1** (1986) 211.
- 16 S. Mennema, MSc Dissertation, Delft University of Technology, Delft (2001).
- 17 A. Vostner, PhD Dissertation, Atominstitut der Österreichischen Universitäten, Vienna (2001).

<b>Chapter V</b>	<b>Experimental Details</b>	<b>89</b>
5.1	Sample Preparation	89
5.1.1	<i>Starting materials</i>	89
5.1.2	<i>Furnace set-up</i>	90
5.1.2(a)	Box furnace with thermal-gradient crucible operating in air	91
5.1.2(b)	Box furnace operating in air using step-cooling mode	92
5.1.2(c)	Controlled-atmosphere furnace with thermal-gradient crucible	92
5.1.3	<i>Growth conditions</i>	93
5.1.4	<i>Film growth</i>	94
5.1.5	<i>Oxygenation</i>	95
5.2	Characterisation	95
5.2.1	<i>X-ray diffraction</i>	95
5.2.1(a)	Diffractionmeter	95
5.2.1(b)	Texture goniometer	96
5.2.2	<i>Optical microscopy</i>	96
5.2.3	<i>Electron microscopy</i>	97
5.2.4	<i>Atomic force microscopy</i>	97
5.2.5	<i>T<sub>c</sub> measurement</i>	97
5.2.5(a)	Resistive transition	97
5.2.5(b)	Inductive T <sub>c</sub> measurement	98
5.2.6	<i>Transport J<sub>c</sub></i>	98
5.3	RE Solubility Measurement	99
	References	99

*Among the substrates investigated, NdGaO<sub>3</sub> was the only substrate where YBCO could be grown directly by LPE due to its small lattice misfit (0.26%) with the Y123 phase. Although NdGaO<sub>3</sub> is not the ideal substrate for coated conductor applications, due to the ease of preparation as compared to YBCO seeded substrates, it was used to optimise growth parameters and to obtain fundamental scientific knowledge of the process such as nucleation and growth mechanisms. This chapter presents results from the growth of YBCO on (110) NdGaO<sub>3</sub> single crystalline substrates including its growth mechanism and growth kinetics.*

## 6.1 Crystalline Orientation

YBCO films between 1 μm and 350 μm thick were successfully grown on (110) NdGaO<sub>3</sub> substrates. XRD results show that both *c*- and *a,b*-axes oriented YBCO films were successfully grown. Typical XRD  $\theta$ - $2\theta$  scans for *c*-axis oriented films with characteristic (00*l*) peaks are presented in Fig. 6.1(a); (*hk*0)-type substrate peaks are visible on thinner films. Fig. 6.1(b) shows a typical XRD  $\theta$ - $2\theta$  scan for *a,b*-axes oriented film with (*h*00) and (0*k*0) peaks.

With a flux composition of Ba:Cu = 3:5 and a temperature gradient of about 2.5-20°C (undercooling) across the thermal-gradient crucible, the desired purely *c*-axis oriented film were grown at a temperature range of 987-992°C from a Ba-Cu-O flux while keeping the bottom temperature of the crucible constant. The "growth window" (or temperature range) of the growth temperature for *c*-axis orientation growth is a narrow 5°C, which is consistent with reported values [1] using similar experimental set up. Outside the stable *c*-axis growth regime

where faster growth was kinetically favoured, films with  $a,b$ -plane perpendicular to the substrate surface were nucleated and grown from the Ba-Cu-O flux.

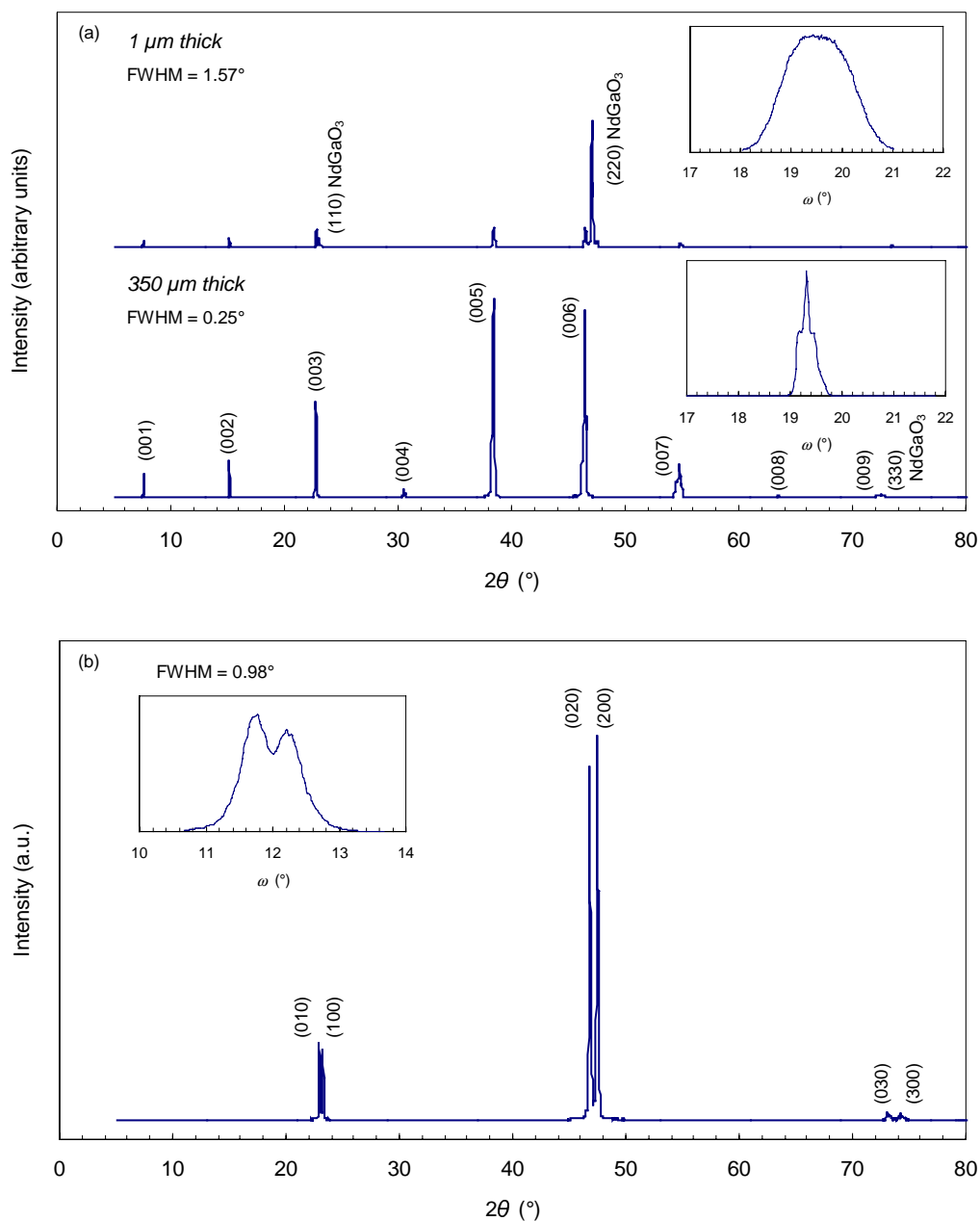


**Fig. 6.1** XRD  $\theta$ - $2\theta$  patterns of (a)  $c$ -axis and (b)  $a,b$ -axes oriented YBCO. The insets show rocking curves of (005) or (100)/(010) peaks.

The results above are in agreement with those from several researchers [2,3] who reported that  $c$ -axis oriented films were grown at about  $985$ - $993^\circ\text{C}$ , although from a flux with Ba:Cu = 3:7. However, they are different from those by Kitamura *et al.* [4,5] where only  $c$ -axis oriented films were reported to grow from a flux with Ba:Cu = 3.0:5.0.

The supersaturation created by undercooling determined the growth modes whereby outside the undercooling working window (2.5-20°C for YBCO grown at 990°C), *a,b*-oriented films were grown. At relatively low supersaturation, mixed *a/c*-oriented films were obtained. If the supersaturation was further decreased, the substrate would be attacked with the formation of a (Y,Nd)BCO layer (where Nd was from the substrate) by an etch-back and re-growth mechanism resulting in *a,b*-oriented films. When the supersaturation was increased beyond the working window, a mixture of *a/c*-oriented films were also obtained due to kinetic limitation of *c*-oriented growth. The substrate was found to be partially attacked and etched away even within the working window. However, the *c*-oriented epitaxy was retained, as will be discussed later in §6.6.1, where the growth can be considered as 3-dimensional epitaxial growth.

While the growth was kinetically more favourable for *a,b*-oriented films at high supersaturation, the growth of *a,b*-films at very low supersaturation could be related to the nucleation rate of the critical nuclei. At very low supersaturation, the driving force for nucleation was small and the critical size of stable nuclei required was large. It could be that the nucleation rate (of stable nuclei) was too "slow" for the subsequent lateral film growth to cover the entire substrate surface, thus exposing bare NdGaO<sub>3</sub> substrate to the highly corrosive BaO-CuO flux. As a result of etching, Nd dissolution from the substrate increased the supersaturation at the interface to a level that favoured *a,b*-oriented growth.

Good out-of-plane texture was achieved for growth at 987-992°C on NdGaO<sub>3</sub> substrates. The FWHM values from rocking curves of (005) peaks on *c*-axis oriented YBCO (insets in Fig. 6.1) varied from 1.57° for a 1-μm thick film to 0.25° for a 350-μm thick film showing increased crystallinity and/or grain size with increasing film thickness.

Fig. 6.2 shows a typical (103) pole figure of the *c*-axis oriented YBCO grown on NdGaO<sub>3</sub> substrates. The four-fold symmetry at  $\psi \approx 45^\circ$  indicates in-plane alignment of *a,b*-plane of the films. Sharp poles with a typical  $\phi$ -scan FWHM value of  $\sim 2.5^\circ$  on 1 μm thick film as shown on Fig. 6.2 indicate that the films produced have good in-plane alignment. The orientation of the *c*-oriented film can be described as  $[001]_{\text{YBCO}} \parallel [110]_{\text{NdGaO}_3}$ . Fig. 6.3 shows the epitaxial relationship of both *c*- and *a,b*-oriented films with NdGaO<sub>3</sub>.

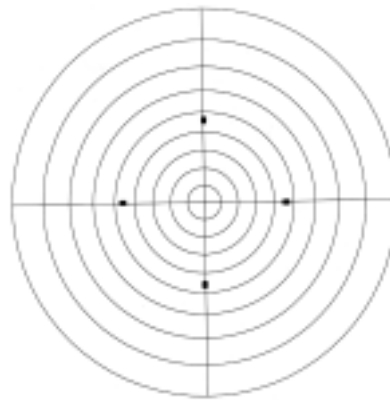


Fig. 6.2 A typical (103) pole figure of *c*-axis oriented YBCO grown on NdGaO<sub>3</sub> substrate.

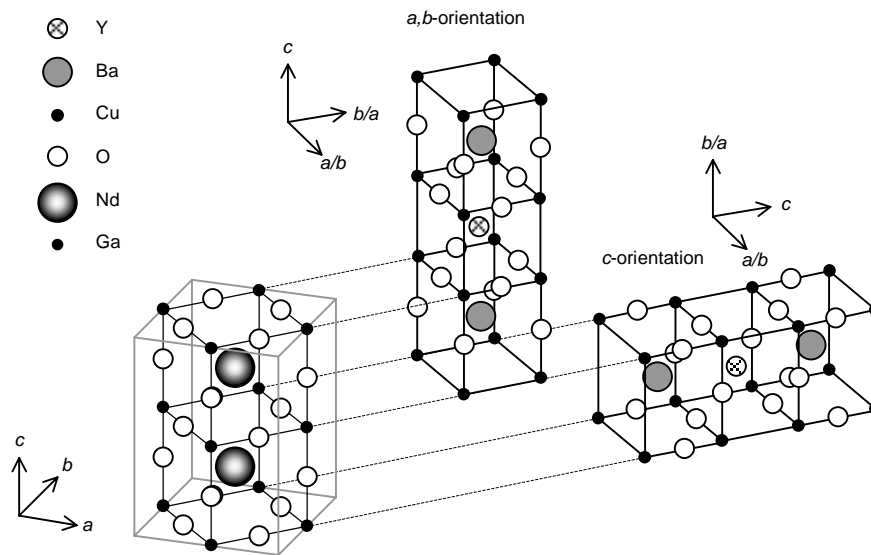
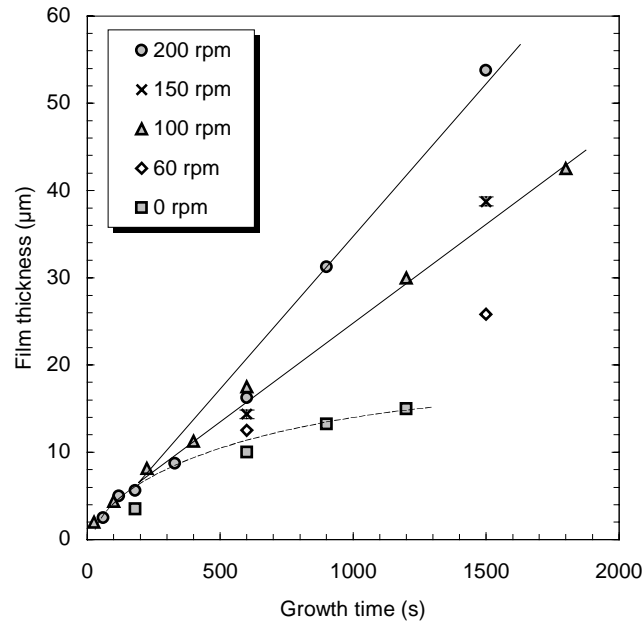


Fig. 6.3 Epitaxial relationship of both *c*- and *a,b*-oriented YBCO on NdGaO<sub>3</sub>.

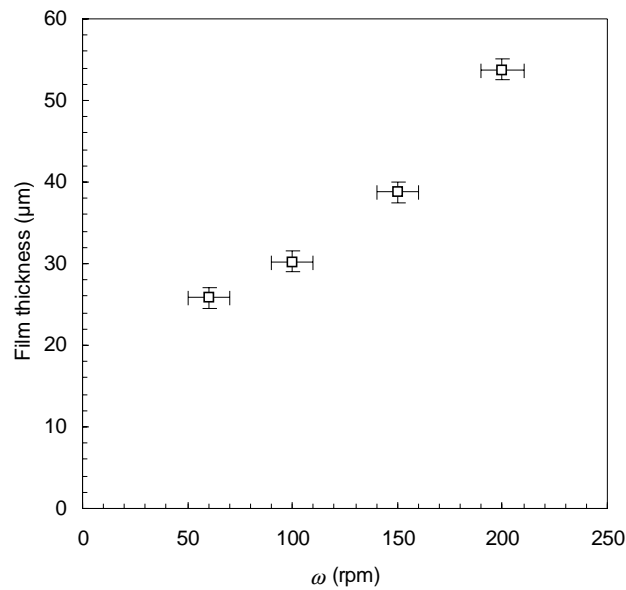
## 6.2 Growth Rate Dependence

Thicknesses of *c*-axis oriented films were measured using optical microscopy and confirmed using SEM. Fig. 6.4 shows a plot of film thickness versus growth time where there exists a common region of film growth from the start to about 180 s for both rotating and non-rotating substrate growths. In the initial transient regime ( $\leq 180$  s) growth was controlled by the long-range diffusion of Y and is parabolic with respect to time. Keeping the substrate stationary (no rotation) resulted in growth that coincided with the same parabolic curve (dashed line in Fig. 6.4). The growth rate became constant, i.e. the film thickness increased linearly with respect to time, when the steady-state convection of the supersaturated solution was achieved ( $\geq 300$  s). This result coincides with those obtained by Kitamura *et al.* [4], which also showed transient and steady-state growth regimes.



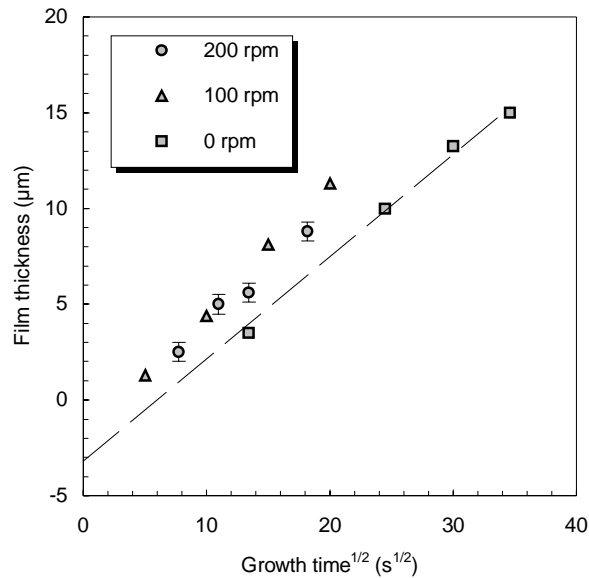
**Fig. 6.4** Growth rates dependence of *c*-axis oriented YBCO films with 20°C undercooling.

The dependence of film thickness on substrate rotation rate is further illustrated in Fig. 6.5 where various substrate rotation rates were investigated. All of the YBCO films were grown for 25 min under different substrate rotation rates and, as shown in Fig. 6.5, the film thickness increased proportionally with the substrate rotation rate.



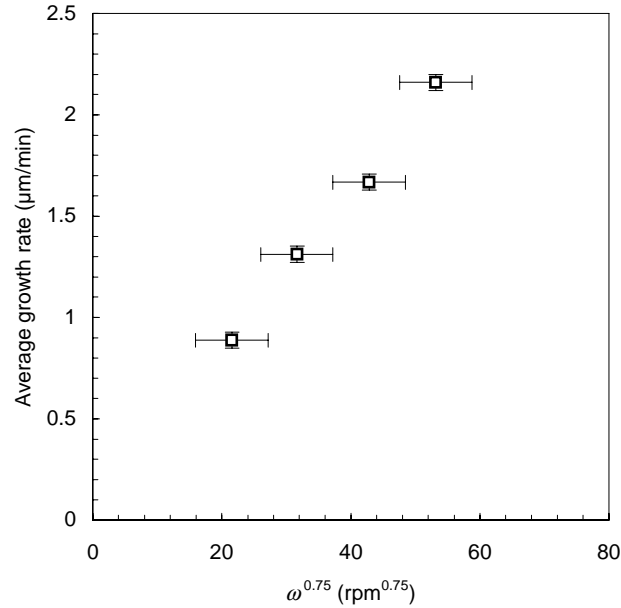
**Fig. 6.5** Growth dependence on substrate rotation rate. All films were grown for 25 min under similar condition with 20°C undercooling.

Fig. 6.6 shows a plot of the film thickness against  $\sqrt{t}$  for the initial transient growth. It can be seen that this transient growth for times  $t \lesssim 180$  s in stirred solutions coincides well with the unstirred (non-rotating substrate) growth. The  $\sqrt{t}$  kinetics was also observed for superconducting NdBa<sub>2</sub>Cu<sub>3</sub>O<sub>7- $\delta$</sub>  films grown by LPE in an unstirred undercooled solution [6], as well as for the case of unstirred solutions for garnet film LPE growth [7,8] and for the transient growth region in the case of rotating substrate forced convection [8]. For non-zero rotation rates, film thickness increased linearly with time after this initial transient stage.



**Fig. 6.6** Film thickness data from Fig. 6.4 for  $t < 1200$  s plotted against  $\sqrt{t}$  for the initial transient growth with 20°C undercooling.

The steady-state growth rate was determined to be  $\sim 2.5$   $\mu\text{m}/\text{min}$  for a rotation speed of  $200 \pm 10$  rpm and  $\sim 1.3$   $\mu\text{m}/\text{min}$  for  $100 \pm 10$  rpm from Fig. 6.4. These values are comparable with the data in the literature [9,10] for the same rotation speeds. The lower growth rate indicates that lower rotation speeds lead to a slower mass transport of solute atoms to the growth interface by forced convection as a result of the presence of a thicker solute-diffusion boundary layer (Eqn. (3.13)). In this study film growth was found to be dependent on the rotation rate according to power law as approximately  $\omega^{0.75}$  as shown in Fig. 6.7. This exponent is greater than the expected value of 0.5. The linear dependence of growth rate on  $\omega^{0.5}$  was not found in all cases [11] as it appeared to be valid only for low values of  $\omega$  ( $< 50$  rpm) and, as discussed by Elwell and Scheel, it could be partly due to the oversimplification of the assumptions used in deriving the expression (Eqn. (3.13)).



**Fig. 6.7** Plot of average growth rate in the steady-state growth regime as a function of substrate rotation rate  $\omega^{0.75}$  for LPE grown YBCO on NdGaO<sub>3</sub>, which shows a linear relationship.

### 6.3 Nucleation and Growth Mechanism

As shown in Fig. 6.8(a), the LPE growth of YBCO on NdGaO<sub>3</sub> substrate was initiated by multi-nucleation in a Stranski-Krastanov like mechanism, although layer-by-layer growth might be expected for very thin films. However, above a critical film thickness of  $\sim 2.5$   $\mu\text{m}$ , dislocations started to form as a lattice-misfit stress relieving mechanism, resulting in step formation and spiral growth as shown in Fig. 6.8(b).

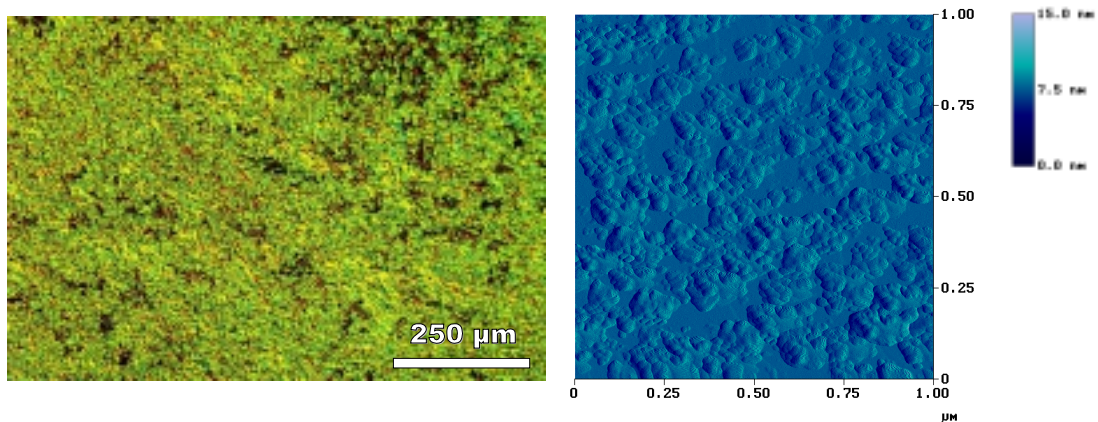


**Fig. 6.8(a)** Optical photomicrograph and AFM image showing initial growth stage with multi-nucleation in a Stranski-Krastanov like mechanism on a thin ( $<1$   $\mu\text{m}$ ) YBCO on NdGaO<sub>3</sub> substrate rotating at 200 rpm.

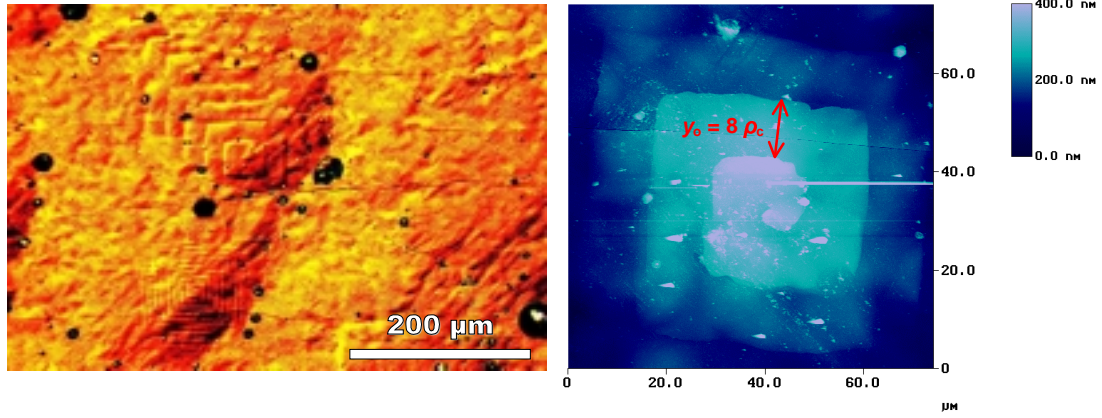


**Fig. 6.8(b)** Optical photomicrograph and AFM image showing spiral-mediated growth on a 5- $\mu\text{m}$  thick film with developed spirals around dislocation cores. From the AFM image of the spiral, the spiral-bunch height is  $h \approx 60 \text{ nm}$  and the inter-step distance  $y_0 \approx 14 \mu\text{m}$ ;  $\rho_c$  is the size of the critical nucleus if there was no step bunching.

### 6.3.1 Steady-state growth

The initial growth occurs via standard nucleation mechanism until some critical film thickness was reached, when screw dislocations started to form. The screw dislocations became a constant source of spiral steps growth according to the BCF theory [12]; hence the film continued to grow in a nucleation-free manner with the step growth rate  $f_{\text{st}} = Fh/y_0$  (Eqn. (3.21)), where  $h$  and  $y_0$  are defined in the caption of Fig. 6.8(b) and  $F$  is the growth rate determined to be  $\sim 2.5 \mu\text{m}/\text{min}$  from Fig. 6.4. For the growth conditions in this work at 200 rpm substrate rotation rate, the step growth rate was found to be  $f_{\text{st}} \approx 0.2 \text{ nm}/\text{s}$ .

The  $c$ -axis oriented YBCO films were grown under nominal undercooling conditions of about  $20^\circ\text{C}$ . According to the YBCO phase diagram [13], this corresponds to  $\sim 0.17$  at% Y supersaturation in the Ba-Cu-O solution at the growth temperature of  $990^\circ\text{C}$ . The nucleation and the initial film growth started under conditions of the background supersaturation level of  $C_L - C_e = 0.17\%$ , where  $C_L$  and  $C_e$  are the bulk and the equilibrium concentrations of the solute (Y) respectively; or in terms of relative supersaturation  $\sigma = (C_L - C_e)/C_e = 0.3$ . The solute concentrations are calculated in terms of Y atoms, being the lowest solubility among the Y-Ba-Cu-O species in the flux.

The interstep distance,  $y_0$ , for an Archimedian spiral, according to the BFC theory and rigorous calculations of Cabrera and Levine [14], is related to the critical nucleus size  $\rho_c$  as:  $y_0 = 19\rho_c$ . The critical nucleus size is an inverse function of the relative supersaturation next to its incorporating site,  $\sigma_{\text{st}}$ , giving  $y_0 = 19\gamma_m am / \epsilon k_B T \sigma_{\text{st}}$  (Eqn. (3.22)). The relative

supersaturation  $\sigma_{st} = (C_{st}-C_e)/C_e$  has the usual meaning where  $C_e$  and  $C_{st}$  are the Y concentration at equilibrium and next to its incorporation site, respectively. Here  $\gamma_m$  is the energy per growth unit, that is in the case of solution growth of the order of  $1/6$  of the heat of solution per growth unit [2,11] and  $a$  is the length of the growth unit (the growth unit is assumed to be a unit cell here). If step bunching occurs, the multiplier  $m \neq 1$  is the number of single spirals that combine in a step bunching process such as the AFM image shown in Fig. 6.8(b). However, for fully polygonized spirals the relationship  $y_o = 8\rho_c$  (Eqn. (3.20)) was suggested [15]. Therefore, for the spiral in Fig. 6.8(b) the interstep distance becomes:  $y_o = 8\gamma_m am/k_B T \sigma_{st}$ , taking into account step bunching as in Eqn. (3.22). For the present case,  $a = 0.39$  nm,  $m = 51$ ,  $y_o \approx 14$   $\mu$ m and  $\gamma_m = 4.01 \times 10^{-20}$  J (taken to be the same as in the case of Ba:Cu = 3.1:6.9 ratio [2]). The relative supersaturation calculated from the interstep distance is  $\sigma_{st} = 8\gamma_m am/k_B T y_o \approx 0.026$  corresponding to the value estimated by Klemenz and Scheel [2] for Ba:Cu = 3.1:6.9 ratio. Thus, the predicted relative supersaturation responsible for the spiral-step formation at 200 rpm ( $\sigma_{st} \sim 0.026$ ) is only a fraction of the overall relative supersaturation ( $\sigma \sim 0.3$ ) calculated from the solubility curve earlier. This lower local supersaturation level was a result of solutes being constantly consumed at the growth interface.

In the continuous growth regime, where spirals were dominating, the supersaturation at the growth interface was a function of the stirring conditions as well as diffusion coefficient in the liquid and surface kinetics for spiral/crystal growth. This supersaturation normally differs from the supersaturation that initiated growth; hence the critical nucleus size as discussed above refers to the new supersaturation condition. The critical nucleus size can be estimated from the interstep distance (Fig. 6.8(b)) to be  $\rho_c = y_o/8m \approx 34$  nm. This value (nucleation-free regime) is different from the size of the islands/nuclei in Fig. 6.8(a) (nucleation regime) due to different supersaturation in these two cases.

However, a pronounced spiral-made hillocks/sub-grains growth occurred in the steady-state growth regime under relatively high rotation rates (Figs. 6.8(b) and 6.9) with some initial size distribution. It was found that the average size/diameter of those hillocks that grew in time, or more precisely with film thickness, is independent of each other to a certain size ( $\sim 300$   $\mu$ m) whereby they became connected. In the connected regime as films grew thicker, larger sub-grains increased further in size at the expense of smaller ones, showing growth-death competition (Fig. 6.9). The actual height-to-width ratio of the hillocks depends on the relative supersaturation that is defining the spiral growth [11,12].

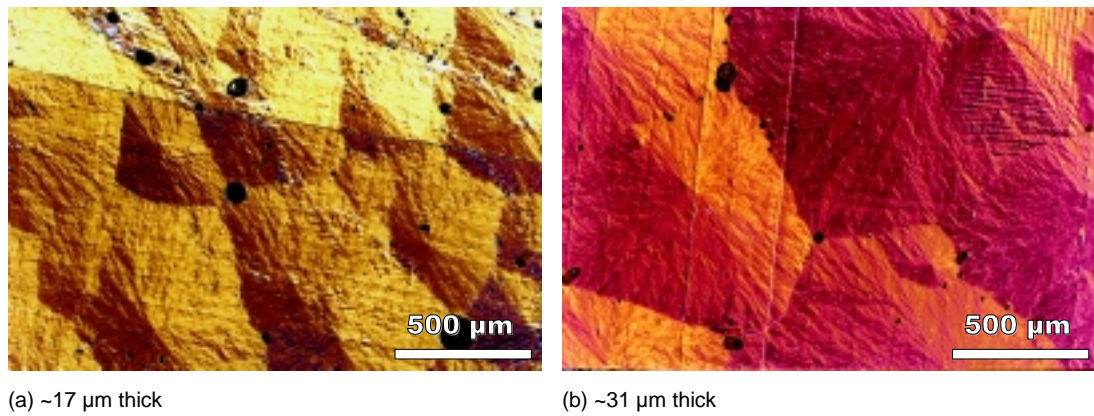


**Fig. 6.9** Photomicrographs of *c*-axis oriented films showing growth-death competition of sub-grains.

It is well known that atoms preferably go from small to big clusters (when elasticity is disregarded), or from regions of higher to lower stress. The reasons for the sub-grain "coarsening" can lie either in the liquid volume diffusion or surface kinetics. Since surface diffusion is known to be much slower than the diffusion in the flux, the hillock growth is mainly controlled by the solute atoms diffusing through the boundary layer  $\delta$  [5] in the growth regime (refer to §6.4.2 for details). The mass transfer diffusion through the boundary layer would favour large "hills" since they protruded more and thus had a shorter diffusion length promoting faster growth.

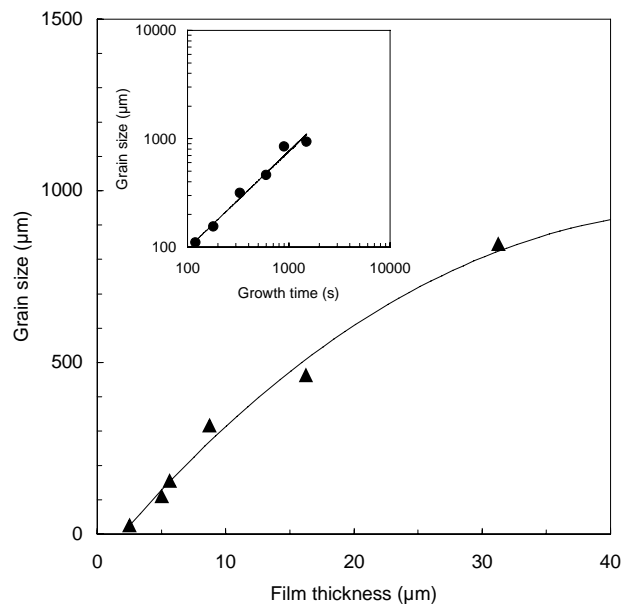


**Fig. 6.10** Kinetics of sub-grain growth for 200 rpm rotation rate.

It was noticed that the kinetics of this "coarsening" was sluggish for slow growth, i.e. in an unstirred solution and for moderate stirring. However, for high rotation rates (as in Fig. 6.10), the lateral growth rate of the sub-grains was appreciable, reaching  $\sim 1 \mu\text{m/s}$  for 200 rpm

substrate rotation rate. The kinetics of this grain growth is found to be of power law with the exponent  $<1$  ( $\propto t^{0.7}$  for 200 rpm). This hillock growth produced a significant relative surface roughness.

## 6.4 Growth Kinetics

The growth of epitaxial YBCO film from a supersaturated solution is analysed for both unstirred (stagnant) and stirred solutions. The initial transient growths in both cases did not involve a dynamic boundary layer and were thus independent of viscosity. On the other hand, the steady-state growth for a stirred solution involved a boundary layer  $\delta$  that was dependent on flux viscosity and the substrate rotation rate. The analyses have taken into account a surface kinetic contribution, which is introduced in terms of a phenomenological surface kinetic reaction constant  $k$ .

### 6.4.1 Unstirred solution and stirred solution transient growth

Growth in an unstirred solution and the initial transient growth in the stirred solution are shown in Fig. 6.6. As might be expected, film growth in the case of substrate rotation appeared to be faster than growth in an unstirred solution due to forced convection on a local scale prior to establishing the steady-state convection. However, in each case there is a negative intercept at  $t = 0$  in the thickness versus  $\sqrt{t}$  plot; this is a clear indication of an interface kinetics contribution to the growth [7]. The contribution of interface kinetics can be analysed quantitatively as follows.

Film growth normal to a plane surface is considered as one-dimensional growth, i.e. there is a concentration gradient only along the  $x$ -axis perpendicular to the interface. The concentration  $C(x,t)$  of the solute, in a convection-free solution, changes for a plane interface according to Fick's second law of diffusion in one dimension as:

$$dC/dt = Dd^2C/dx^2 \quad (6.1)$$

where  $D$  is the diffusion coefficient. This equation applies for the case where the diffusion length,  $l = (Dt)^{0.5}$ , is much smaller than substrate diameter and crucible dimensions.

The background-liquid concentration of the supersaturated solute is denoted as  $C_L$ , defining the first boundary condition:

$$C(\infty,t) = C_L. \quad (6.2)$$

The second boundary condition, for a substrate equilibrated at the growth temperature and immersed in the supersaturated solution at  $t = 0$  is:

$$C(x,0) = C_L. \quad (6.3)$$

The rate of transfer of diffusing material through unit area,  $J$ , is proportional to the concentration gradient  $J = -DdC/dx$  (Fick's first law). If a surface reaction is taken into account, the simplest possible assumption is to assume a first order reaction i.e. proportional to the difference between the actual solute concentration ( $C_i(t) = C(0,t)$ ) at the interface and the equilibrium concentration ( $C_e$ ) at the interface, as in Eqn. (3.23) with  $n = 1$ . A first order reaction has been suggested for the case of  $c$ -axis YBCO growth [16,17]. The coefficient of proportionality is the kinetic reaction constant  $k$ . This would define the third boundary condition at  $x = 0$  as [7,18]:

$$D \left. \frac{dC(x,t)}{dx} \right|_{x=0} = k[C(0,t) - C_e]. \quad (6.4)$$

Following a standard analysis [7,18], the concentration profile can be expressed as:

$$\frac{C(x,t) - C_L}{C_e - C_L} = \operatorname{erfc} \frac{x}{2\sqrt{Dt}} - \exp \frac{kx + k^2t}{D} \operatorname{erfc} \left( \frac{x}{2\sqrt{Dt}} + \frac{k\sqrt{Dt}}{D} \right). \quad (6.5)$$

Note that  $\operatorname{erfc}(z) = 1 - \operatorname{erf}(z)$ . The growth rate is defined [7] as  $F(t) = (D/C_{xt})dC/dx|_{x=0}$ , where  $C_{xt}$  is the solute concentration (density) within the growing crystal, hence:

$$F(t) = k \frac{(C_L - C_e)}{C_{xt}} \exp \left( \frac{k\sqrt{Dt}}{D} \right)^2 \operatorname{erfc} \frac{k\sqrt{Dt}}{D}. \quad (6.6a)$$

For large arguments  $\operatorname{erfc}(z)$  can be approximated as [19]:

$$\operatorname{erfc}(z) = 1 - \operatorname{erf}(z) \approx \frac{\exp(-z^2)}{z\sqrt{\pi}} \left( 1 - \frac{1}{2z^2} + \frac{1 \cdot 3}{(2z^2)^2} - \frac{1 \cdot 3 \cdot 5}{(2z^2)^3} + \dots \right), \text{ for } |z| \gg 1. \quad (6.6b)$$

Hence, if there was no surface kinetics involved ( $k \rightarrow \infty$ ) the growth rate would be given as:

$$F_{k \rightarrow \infty}(t) = \frac{(C_L - C_e)}{C_{xt}} \cdot \sqrt{\frac{D}{\pi t}}, \quad (6.6c)$$

would become infinite for very short times. The film thickness,  $H$ , is obtained by integration of the growth rate in Eqn. (6.6a),  $H = \int F dt$ , over the growth time, yielding for an unstirred solution:

$$H(t) = \frac{(C_L - C_e)}{C_{xt}} \left[ 2\sqrt{\frac{Dt}{\pi}} + \frac{D}{k} \left( \exp\left(\frac{k\sqrt{Dt}}{D}\right)^2 \operatorname{erfc}\frac{k\sqrt{Dt}}{D} - 1 \right) \right]. \quad (6.7)$$

For long times or more precisely for large arguments ( $k\sqrt{t/D} \gg 1$ ) in an unstirred solution, as well as in the transient part for a rotating substrate, the asymptotic approximation of Eqn. (6.7) can be used, giving [18,19]:

$$H(t) \approx \frac{(C_L - C_e)}{C_{xt}} \left( 2\sqrt{\frac{Dt}{\pi}} - \frac{D}{k} \right). \quad (6.8)$$

This is the function that fits the data in Fig. 6.6 as  $H(t) \approx (dH(t)/d\sqrt{t})\sqrt{t} + H(0)$ . The slope in Fig. 6.6 is independent of surface kinetics, and would have the same interpretation if growth was only limited by bulk diffusion in the solution [8]:

$$\frac{dH(t)}{d\sqrt{t}} \approx 2\sqrt{\frac{D}{\pi}} \frac{(C_L - C_e)}{C_{xt}}. \quad (6.9)$$

The negative intercept in Eqn. (6.8):

$$H(0) \approx -\frac{D}{k} \cdot \frac{(C_L - C_e)}{C_{xt}} \quad (6.10)$$

indicates a finite incorporation of kinetics at the growing interface [7]. This intercept would disappear only in the case of  $k \rightarrow \infty$  and  $C(0,t) = C_e$ , i.e. infinitely fast incorporation of kinetics at the interface, which is usually not the case.

The data on solute concentrations from the literature are not very reliable (i.e. are very sensitive to solution contamination [20] that varies from reference to reference). However, the present analysis is based on the diffusion coefficient estimated from a direct viscosity measurement ranging from  $2.9 \times 10^{-10}$  m<sup>2</sup>/s to  $4.3 \times 10^{-10}$  m<sup>2</sup>/s [21]. Hence, eliminating  $(C_L - C_e)/C_{xt}$  from Eqns. (6.9) and (6.10) and using data from Fig. 6.6 ( $H(0) = -3$  μm and  $dH(t)/d\sqrt{t} \approx 0.5 \times 10^{-6}$  m/s<sup>0.5</sup>), the kinetic reaction constant was estimated to be  $k \approx 2.5$  to  $3.1 \times 10^{-6}$  m/s. The corresponding  $(C_L - C_e)/C_{xt}$  ratio may be estimated to be in the range 0.021 to 0.026. Taking the Y concentration in the crystal  $C_{xt} = 8$  at% gives the Y supersaturation in the solution (Fig. 3.16) to be about  $C_L - C_e = 0.17$  to 0.21 at%.

Another relevant approximation of Eqn. (6.6a) is for very short times ( $t \rightarrow 0$ ) [7,22]. This gives the maximum growth rate in the course of the experiment, with fixed overall supersaturation ( $C_L - C_e$ ) as:

$$F_{\max} = F(0) \approx k \frac{(C_L - C_e)}{C_{xt}}. \quad (6.11)$$

This growth rate takes advantage of growth at the initial supersaturation; hence diffusion does not play any role, and growth is only limited by the interface kinetics. From the results above it follows that  $F_{\max} \approx 41\text{-}58 \text{ nm/s}$  (or  $2.5\text{-}3.5 \text{ }\mu\text{m/min}$ ).

The actual growth kinetics and corresponding relative concentration, of the solute at the interface is shown in Fig. 6.11.

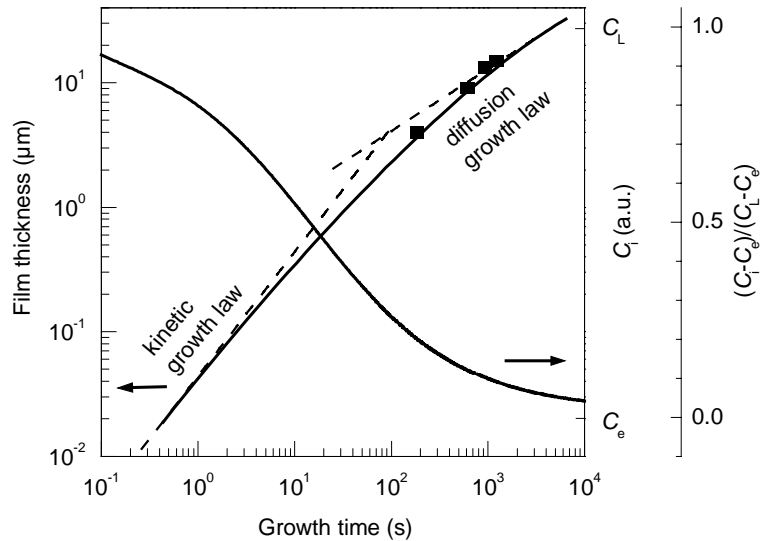


**Fig. 6.11** Thickness of the growing film and interface concentration versus time, showing the transition from interface to diffusion control in the unstirred solution and the transient part of the 200 rpm stirred solution growth (data from Fig. 6.6). Note that the growth law and the concentration gradients in the solution change together [23].

The relative supersaturation at the interface,  $\sigma_i = (C_i - C_e)/C_e$ , that is the driving force for the surface kinetics is not exactly known since  $C_i$  is uncertain. However, it can be seen that initially (for short times) there is linear growth limited only by the kinetics at the interface, while  $C_i$  is close to the maximum. For long times  $\sqrt{t}$  kinetics prevails where long range diffusion limits the growth and  $C_i$  approaches  $C_e$ , the equilibrium Y concentration. Therefore, for long times in an unstirred solution almost all the driving force (or undercooling as the surrogate for the driving force) goes into the diffusive transport process [23].

### 6.4.2 Stirred solution steady-state growth

In a simple approximation [24] there is a solute-diffusion boundary layer of thickness  $\delta$  between a region of an expected laminar liquid flow and the substrate. Transport by convection brings the supersaturated solution to the boundary layer ( $x = \delta$ ), while diffusion takes the solute atoms towards the growing surface ( $x = 0$ ) and rejects "undesirable" species away from it.

It is assumed that the solute concentration is at its background supersaturation level ( $C_L$ ) at  $x \geq \delta$ . The stagnant boundary layer approximation seems to have many critics [24], however, it remains a very convenient and easily exploited approach in the treatment of steady-state diffusion of this nature [11,24,25]. The problem becomes simple diffusion in a plane sheet of thickness  $\delta$  [18]. This layer, according to Cochran's approximation [25,26] in the case of substrate rotation at an angular velocity  $\omega$ , has thickness:

$$\delta = 2^{2/3} D^{1/3} \nu^{1/6} \omega^{-1/2}, \quad (6.12)$$

where  $\nu = \eta/\rho$  is the kinematic viscosity,  $\eta$  the dynamic viscosity and  $\rho$  the density. Hence, the diffusion boundary layer for any substrate rotation rates ( $\omega$ ) can be estimated from the kinematic viscosity and diffusion coefficient.

The viscosity of the Ba<sub>3</sub>Cu<sub>5</sub>O<sub>8</sub> flux at 990°C, from a direct viscosity measurement by a modified Stokes-pendulum viscometer,  $\eta \approx 0.0315$  Pa·s, was used [27]. The corresponding kinematic viscosity ( $\nu = \eta/\rho$ ) is therefore  $\sim 5.7 \times 10^{-6}$  m<sup>2</sup>/s (using the density of the solution  $\rho = 5500$  kg/m<sup>3</sup> [27,28]). The Reynolds number  $Re = r^2 \omega / \nu \ll 3000$  [8,29], where  $r$  is the substrate radius, defines the regime of laminar flow and thus the existence of the stagnant diffusion boundary layer of thickness  $\delta$  in Eqn. (6.12). In the case of this study the maximum  $Re \approx 20\omega \approx 400$  is well within the laminar flow regime. The diffusion boundary layer in Eqn. (6.12) estimated from the above data (for  $D = 2.9$  to  $4.3 \times 10^{-10}$  m<sup>2</sup>/s [21] and  $\nu = 5.7 \times 10^{-6}$  m<sup>2</sup>/s [27]) is shown in Fig. 6.12. It can be seen that the boundary layer thickness for 200 rpm is  $\sim 32$ - $36$   $\mu$ m, while it extends to  $\sim 50$   $\mu$ m for 100 rpm.

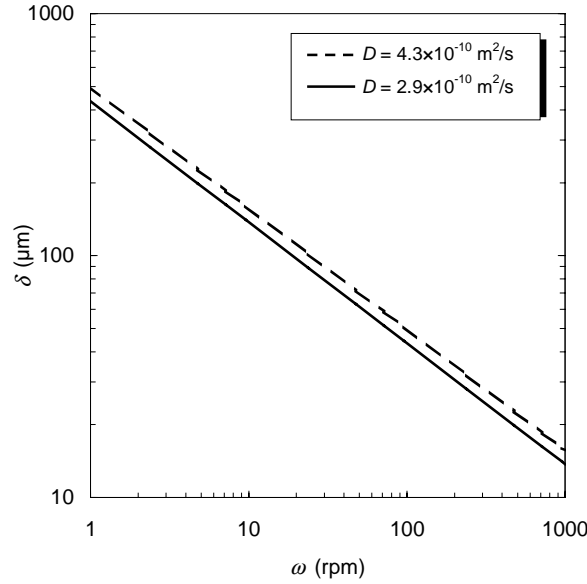


**Fig. 6.12** Steady-state diffusion boundary layer thickness calculated for  $D = 2.9\text{-}4.3 \times 10^{-10} \text{ m}^2/\text{s}$  and  $\eta = 0.0315 \text{ Pa}\cdot\text{s}$ .

After an initial transient growth, steady-state forced convection was achieved and the growth rate became constant, i.e. the film thickness increased linearly with time (Fig. 6.4). The duration of this transient is not in this case defined by the "relaxation" across the  $\delta$  boundary layer as suggested by Ghez and Giess [7]. If there was already steady-state forced convection at  $t = 0$  then this would be an appropriate approach. In the experiments carried out here, the liquid was stationary before the rotating substrate was immersed into the solvent, hence the transient was due to the establishment of the steady-state forced convection. During the transient stage, the growth rate passed through a minimum before recovering to the steady-state value. The apparent duration of the transient regime in this work is comparable with that in LPE grown YBCO [4] under similar conditions and magnetic garnet films [8]. In the stagnant diffusion boundary layer limit, only steady-state diffusion growth across  $\delta$  is important, reducing the diffusion Eqn. (6.1) to:

$$Dd^2C/dx^2 = 0. \quad (6.13)$$

The moving phase boundary (interface) is neglected in Eqn. (6.13). This is justifiable in the case of relatively slow growth rates [7,25] such that  $F\delta/D \ll 1$ , which is satisfied in this case. The boundary condition Eqn. (6.2) becomes:

$$C(\delta, t) = C_L. \quad (6.14)$$

The solution for steady-state growth when either diffusion or surface kinetics or both are rate limiting for the transport of growing species is thoroughly discussed by Wilcox [24]. The steady-state growth becomes [7,18]:

$$\frac{C(x,t) - C_L}{C_e - C_L} = \left(1 - \frac{x}{\delta}\right) \frac{\delta k}{\delta k + D} = \left(1 - \frac{x}{\delta}\right) \frac{1}{1 + R}. \quad (6.15)$$

The dimensionless parameter  $R = D/\delta k$  reflects the relative importance of volume diffusion to surface reaction kinetics as the rate limiting process [7]. The steady-state growth rate becomes in the same form as Eqn. (3.24):

$$F(t) = \frac{D (C_L - C_e)}{\delta C_{xt}} \frac{1}{1 + R}. \quad (6.16)$$

Hence, film thickness increases as  $H = \int F dt$ :

$$H = \frac{D (C_L - C_e)}{\delta C_{xt}} \frac{1}{1 + R} t + H_{tr}. \quad (6.17)$$

The constant  $H_{tr}$  ( $\sim 7 \mu\text{m}$  in Fig. 6.4) is the film thickness grown during the initial transient. It should be noted that the solution with the "attenuation" factor  $1/(1+R)$  can be obtained from the ordinary diffusion equation replacing the diffusion coefficient  $D$  with  $D/(R+1)$  [18]. The parameter  $R = D/\delta k$  can be estimated from the known materials and process parameters, using Eqn. (6.12) for  $\delta$ , as  $R = D(2^{2/3} D^{1/3} \nu^{1/6} \omega^{-1/2} k)^{-1}$ . Hence  $R$  is a linear function of  $\sqrt{\omega}$  for a given system. In the case of the system investigated here  $R \approx 0.9\sqrt{\omega}$  (for  $D = 3.5 \times 10^{-10} \text{ m}^2/\text{s}$ ), after the initial transient, surface kinetics becomes as important as volume diffusion for  $\omega = 1.1 \text{ rad/s} \approx 10 \text{ rpm}$  (for  $R = 1$ ) and becomes the predominant rate limiting process as  $\omega$  increases further.

The steady-state part of the curve in Fig. 6.4 was analysed for  $\omega = 200 \text{ rpm}$  rotation rate. The system of non-linear Eqns. (6.9), (6.10) and (6.16) can be solved simultaneously treating  $D$ ,  $k$  and  $(C_L - C_e)/C_{xt}$  as independent variables, and replacing  $R$  in Eqn. (6.16) by  $D\omega^{1/2}(2^{2/3} D^{1/3} \nu^{1/6} k)^{-1}$ . The roots of the non-linear equations gave the kinetic coefficient as about  $k \approx 2.5 \times 10^{-6} \text{ m/s}$ . The diffusion coefficient value used was  $D \approx 4 \times 10^{-10} \text{ m}^2/\text{s}$  [21]. The term  $(C_L - C_e)/C_{xt}$  was about 0.018 giving Y supersaturation in the solution to be about  $C_L - C_e \approx 0.14 \text{ at\%}$ , in satisfactory agreement with the value estimated from the results in the unstirred solution. From the available solubility data [20,30], this result suggests that the actual undercooling achieved was about  $20^\circ\text{C}$ , which is in agreement with the conditions used here with the highest undercooling under which  $c$ -axis growth was possible in the flux with Ba:Cu

$= 3:5$ . Furthermore, the maximum growth rate that was eventually achieved for vigorous stirring ( $\omega \rightarrow \infty$ ) resulting in the disappearance of the diffusion boundary layer ( $\delta \rightarrow 0$ ) in Eqn. (6.16) is predicted to be  $F_{\max} \approx 42$  nm/s (2.5  $\mu\text{m}/\text{min}$ ) very much in the range found from the results in the transient state of the stirred solution (Fig. 6.13).

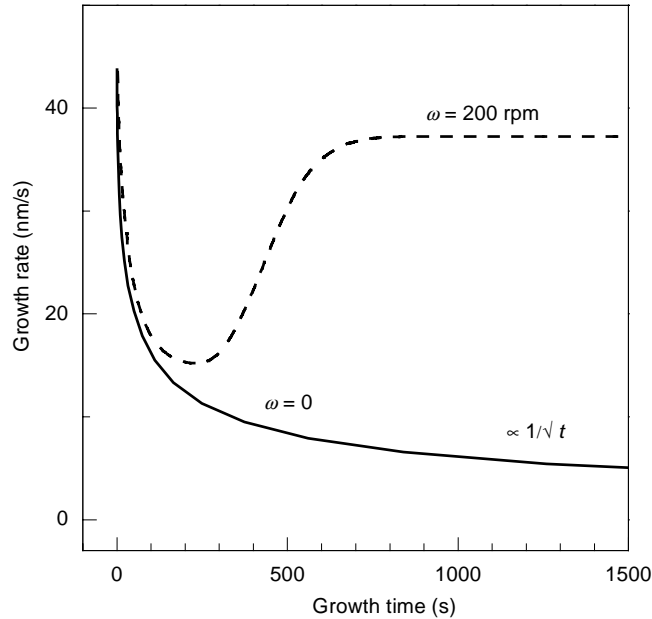


**Fig. 6.13** Calculated growth rates of LPE YBCO on NdGaO<sub>3</sub>, in unstirred and stirred solutions for the experimental conditions used.

YBCO film growth by LPE, with a rotating substrate as a stirrer clearly exhibited transient and steady-state regimes. In the unstirred solution, and in the transient regime of a stirred solution, growth started at a maximum rate at  $t = 0$  when the substrate is immersed in the supersaturated solution (Fig. 6.13). The initial maximum growth rate of  $\sim 42$  nm/s (or  $\sim 2.5$   $\mu\text{m}/\text{min}$ ) was determined by the surface kinetics (for the supersaturation used). However, this rapid growth lasted for less than  $\sim 10$  s and changed to a  $\sqrt{t}$  diffusion growth law, with the growth rate decaying as  $1/\sqrt{t}$ , when volume diffusion predominantly limits the growth. On the other hand, in a stirred solution the growth rate recovered to a higher value (Fig. 6.13) after the establishment of a relatively thin stagnant boundary layer between the supersaturated solution and the growing interface.

The growth rate calculated for volume diffusion between the background concentration  $C_L$  and the actual solute concentration at the interface  $C_i$  is given by a modified Eqn. (6.16) as [11]:  $F \approx (D/\delta)[(C_L - C_i)/C_{xt}]$ . Therefore, the supersaturation ( $C_L - C_i$ ) that drives Y diffusion across the diffusion boundary layer becomes:

$$C_L - C_i = C_{xt} \left( \frac{2}{D} \right)^{2/3} v^{1/6} F \omega^{-1/2}. \quad (6.18)$$

Hence, the solute concentration at the interface increases as  $\omega$  increases. The composition profile in the solution near the substrate would look as in Fig. 6.14. For comparison, in the case of an unstirred solution, growth became effectively independent of surface kinetics after a long enough period of time ( $t \gg 10$  s, Fig. 6.11), since there was no fixed boundary layer. The apparent boundary layer profile moves with time  $\delta_{app} \approx 2\sqrt{Dt}$ . The resulting  $R \ll 1$  means that bulk diffusion is now the rate limiting process with the solute concentration at the interface approaching the equilibrium value  $C_i \sim C_e$  (Figs. 6.11 and 6.14).

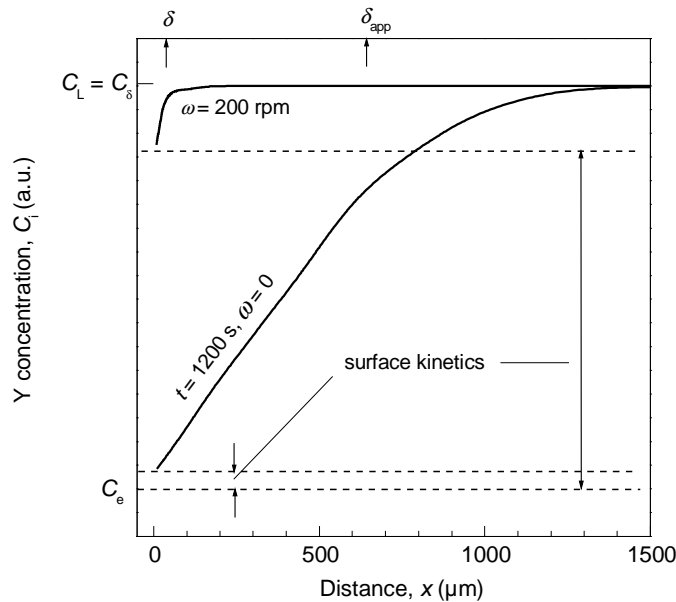


**Fig. 6.14** Schematic of the concentration profiles in the diffusion boundary layer for the unstirred ( $\delta_{app}$ , after 1200 s) and stirred ( $\delta$ ) solutions. Substrate is at  $x = 0$ .

## 6.5 Growth at Reduced Temperature in Air

Lowering the growth temperature was essential for the growth on metallic substrates as the tapes were found to dissolve in the highly corrosive Ba-Cu-O flux at high growth temperature around 990°C. Various additives such as BaF<sub>2</sub> and Ag had been demonstrated to be effective in lowering the growth temperatures of REBCO as presented in Table 4.2. Growth parameters with additives in the flux were first examined using NdGaO<sub>3</sub> substrates.

Using various additives in the flux, different ranges of growth temperature were exploited as presented in Fig. 6.15. The growth temperature in air was reduced to approximately 900°C

by BaF<sub>2</sub> addition, while the addition of Ag further reduced the growth temperature to 880°C. Film growth in atmosphere with reduced oxygen partial pressure succeeded in reducing the growth temperature to as low as 860°C; growth under reduced  $pO_2$  is discussed in details in Chapter IX.

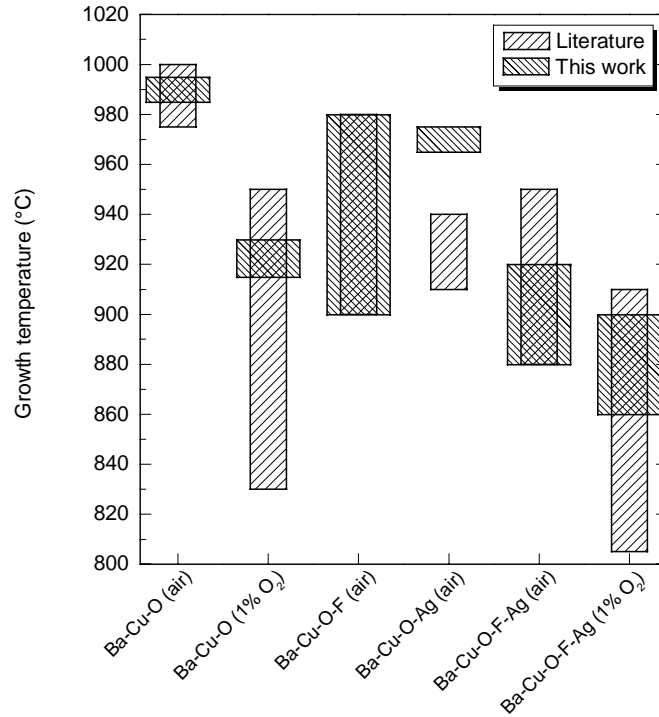


**Fig. 6.15** Range of flux composition exploited in lowering growth temperature. Literature data from refs. [31-33].

### 6.5.1 Growth from Ba-Cu-O-F flux in air

The window of growth temperature for purely  $c$ -oriented films from Ba-Cu-O-F flux (~5 mol% BaF<sub>2</sub>) was found to range from around 910 to 975°C at undercooling <20°C, which was much wider than growth from flux without BaF<sub>2</sub> addition. However, mixed  $c$ - and  $a,b$ -axes orientations were found on films grown from Ba-Cu-O-F flux with undercooling greater than 20°C within the similar temperature range. A typical XRD  $\theta$ -2 $\theta$  scan of a mixed  $c$ - and  $a,b$ -oriented film is presented in Fig. 6.16.

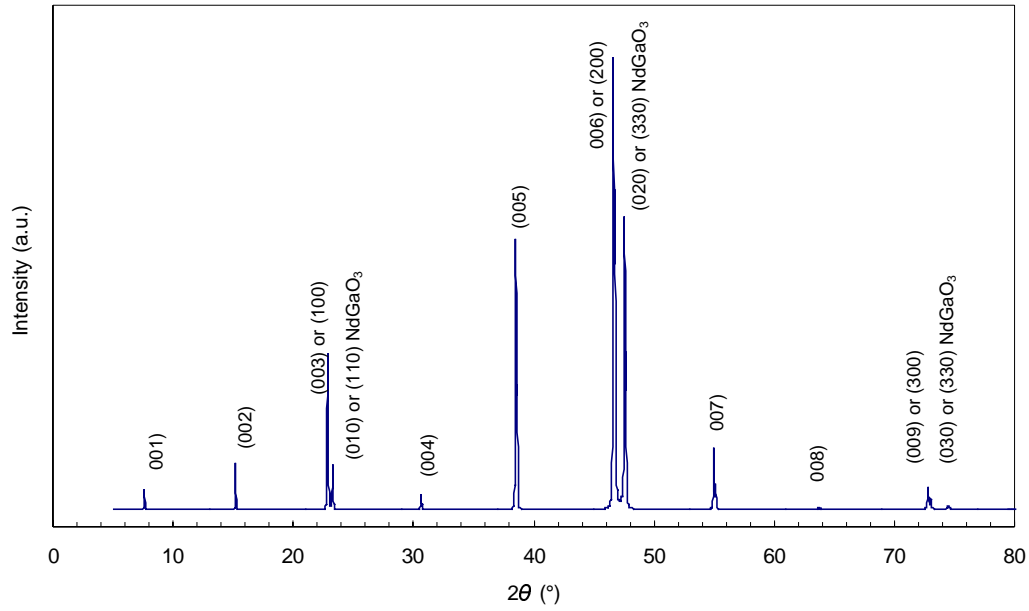


**Fig. 6.16** XRD  $\theta$ - $2\theta$  scan of a mixed c- and a,b-axes oriented YBCO grown on NdGaO<sub>3</sub> substrate from a Ba-Cu-O-F flux in air at 930°C with 25°C undercooling.

In general, samples grown at reduced temperature contained relatively more flux residues with randomly oriented crystallites of non-YBCO phases as compared to samples grown at 990°C; Fig. 6.17(a) shows an example of such film surface. Below 910°C, various randomly oriented BaO and CuO phases nucleated and grew and these flux residues covered almost the entire sample surface. Fig. 6.17(b) shows an optical image of a sample grown below 910°C that almost fully covered with flux residues.

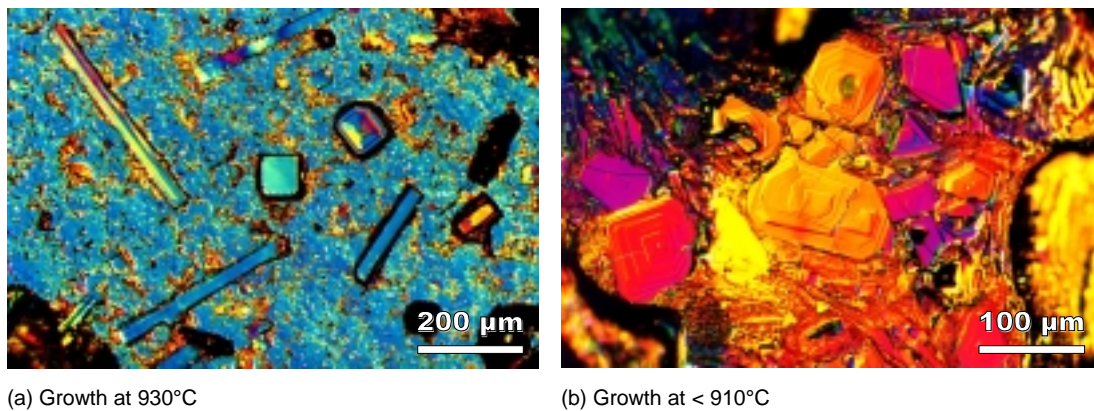


**Fig. 6.17** Optical photomicrographs showing two samples grown from a Ba-Cu-O-F flux in air where (a)  $\sim 1 \mu\text{m}$  thick YBCO film grown at 930°C with several randomly oriented non-YBCO crystallites, and (b) a sample covered with plenty of flux residues grown at  $< 910^\circ\text{C}$ .

The addition of BaF<sub>2</sub> into the flux seems to have widened the window of growth temperature for *c*-oriented film significantly (~65°C as compared to ~5°C in the case without BaF<sub>2</sub> addition) so long as the undercooling was kept below 20°C. However, it is not clear how the addition of BaF<sub>2</sub> affect the primary crystallisation field of YBCO. NdGaO<sub>3</sub> substrates were also found to be vulnerable in flux containing BaF<sub>2</sub> as severe etching of substrate was observed (see TEM and HREM analyses in §6.6.1).

### **6.5.2 Growth from Ba-Cu-O-Ag flux in air**

Although Yamada *et al.* [34] reported that the addition of Ag (~10 mol%, metal basis) into a Ba-Cu-O flux did not affect the growth temperature, two other reports [35,36] did mention the drop of peritectic temperature of Y-Ba-Cu-O system by approximately 35°C as a result of Ag addition.

In this work, YBCO films with *c*-axis orientation were grown on NdGaO<sub>3</sub> substrates at temperature as low as ~965-975°C with 10°C undercooling. However, these YBCO films grown from flux containing Ag had lower  $T_c$  and  $J_c$  than that without Ag addition (see §6.7 on Transport Properties). Hence only a limited number of experiments were carried out.

### **6.5.3 Growth from Ba-Cu-O-F-Ag flux in air**

The window for *c*-oriented growth from a Ag-saturated Ba-Cu-O-F flux was also exploited. It was found that the window for growth temperature could further decrease to as low as 885°C with the addition of Ag into a flux containing BaF<sub>2</sub>. Film growth below 885°C was possible, but the surface was usually almost fully covered with flux residues.

### **6.5.4 Growth rate dependence**

The LPE growth was found to be dependent on growth temperature as shown in Fig. 6.18. The average film growth rate with 200 rpm substrate rotation rate decreased from >2 μm/min at 990°C to <1 μm/min at growth temperature ≤915°C. There is no evidence showing the influence of BaF<sub>2</sub> or Ag on film growth rates. The slower growth was likely attributed to lower RE solubility and slower kinetics (diffusion) at reduced temperature. Kim *et al.* [37] also reported a decrease in LPE growth rate at reduced growth temperature (~0.25 μm/min at 860°C).

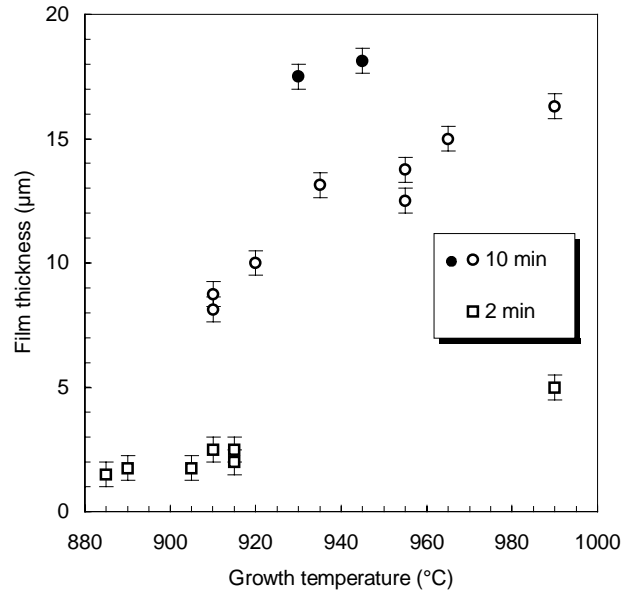


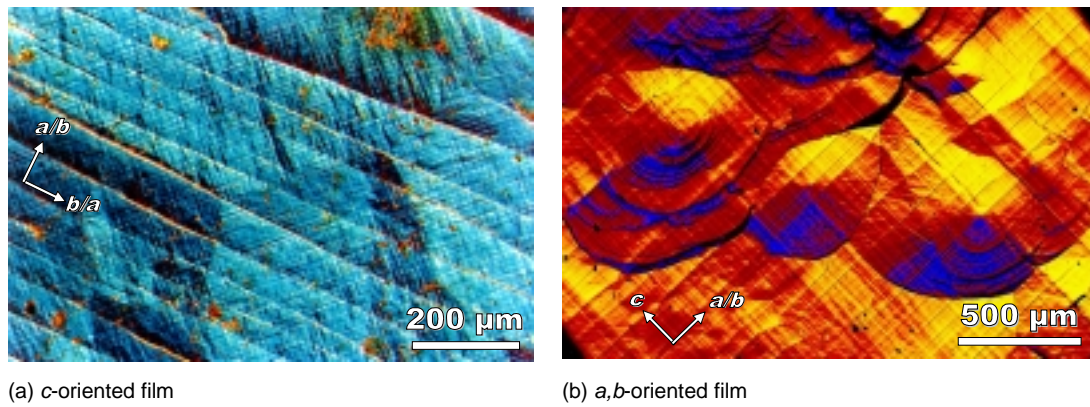
**Fig. 6.18** Growth of *c*-oriented YBCO films on NdGaO<sub>3</sub> as a function of growth temperature. Two sets of films grown for 2 and 10 minutes from Ba-Cu-O-Ag and Ba-Cu-O-F-Ag fluxes respectively (except those grown at 990°C) are shown here. All films were grown with 200 rpm substrate rotation rate.

Filled circles represent films with mixed *c*- and *a,b*-axes orientations.

## 6.6 Microstructural Analyses

Depending on the growth conditions, growth features such as spirals or hillocks could develop. Most of these growth features were coarse enough to be observed under optical microscope. Higher resolution images were obtained using AFM and electron microscopy techniques.

Among the defects generated during growth, misfit dislocations and stacking faults might reduce or compensate the misfit strain under certain conditions. After film growth, the strain generated by the difference in the thermal expansion coefficient between film and substrate during cooling and/or oxygenation could also be (at least partially) relaxed along specific directions by the formation of twins as shown in Fig. 6.19. Oxygenated *c*-oriented films showed the formation of twins along the [110] and  $[\bar{1}10]$  directions whereas *a,b*-oriented films developed twins along the [001] direction.



(a) c-oriented film

(b) a,b-oriented film

**Fig. 6.19** Optical photomicrographs of (a) c-oriented film showing crosshatch pattern of  $\{110\}$  twins and cracks along the  $[100]/[010]$  direction, and (b) a,b-oriented film showing unidirectional twins parallel to the  $[001]$  direction with cracks and elliptical hillocks elongated along the  $[100]/[010]$  direction.

During annealing, oxygen atoms incorporated into the Cu-O basal plane resulting in the split of the  $a$ -axis (=  $b$ -axis) of the tetragonal structure as well as the formation of twins within the crystal structure, which leads to surface roughening as illustrated schematically in Fig. 6.20.

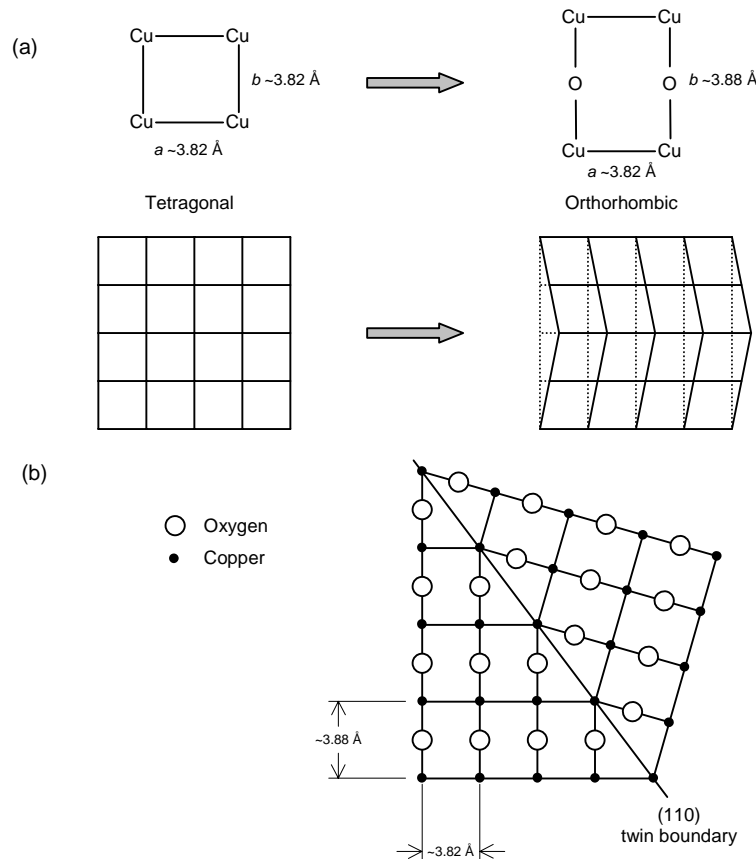


**Fig. 6.20** (a) Lattice parameters of non-oxygenated and oxygenated basal plane showing schematic of lattice deformation, and (b) schematic diagram showing how the lattice parameter difference is accommodated in a twin boundary in YBCO. Adapted from ref. [38].

As a result of the large difference in the thermal expansion coefficients between YBCO and NdGaO<sub>3</sub>, cracks usually formed on *c*-oriented films greater than a certain critical thickness upon cooling from the growth temperature. Theoretical modelling predicts [39] that the critical thickness of crack-free *a,b*-oriented YBCO films on (110) NdGaO<sub>3</sub> substrates is 0.17 μm, which is difficult to achieve due to the high growth rate of the LPE process (~1-2.5 μm/min). All YBCO films grown on NdGaO<sub>3</sub> substrates in this work developed cracks beyond a critical thickness of approximately 1-2 μm. As can be seen on all images of film surfaces (Figs. 6.8(b), 6.9 and 6.19), the cracks propagated through growth features such as growth spirals, which indicates that they were formed after film growth upon cooling from the growth temperature and/or due to partial oxygenation during the cooling process in air, as well as the subsequent oxygenation.

Fig. 6.21 shows the typical crack and twin patterns observed on both *c*- and *a,b*-oriented films grown on (110) NdGaO<sub>3</sub> substrates. The shape and orientation of the associated growth spirals are also shown.

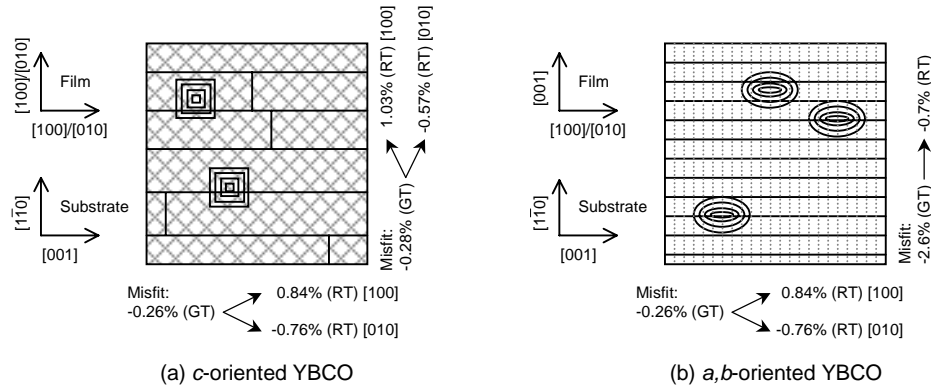


**Fig. 6.21** Growth features (dashed lines = twins, solid lines = cracks and spirals) generally observed on LPE grown (a) *c*-oriented, and (b) *a,b*-oriented YBCO films on (110) NdGaO<sub>3</sub> substrates. The misfit at growth temperature (GT = 990°C) and room temperature (RT = 25°C) along the different directions is taken from refs. [40,41]. Positive sign denotes tensile strain while negative one denotes compressive strain on the film.

At growth temperature, *c*-oriented films were under biaxial compressive strain of 0.28% and 0.26% for the orientations  $a_f \parallel d_s$  and  $a_f \parallel c_s$ , respectively, as shown in Fig. 6.21(a) where the subscripts *f* and *s* denote film and substrate respectively while *d* represents the [110]/2 lattice parameter. Upon cooling to room temperature, the splitting of *a*- and *b*-axis induced the tensile and compressive stress as indicated in Fig. 6.21(a). The twins formed along {110} planes resulted in crosshatch pattern.

For  $a,b$ -oriented films (Fig. 6.21(b)), the tetragonal  $a$ -axis ( $= b$ -axis) was under small compressive strain of 0.26% ( $a_f \parallel c_s$ ). A twinned film was formed upon cooling and subsequent oxygenation by which the compressive strain increased up to 0.76% in the [010] in-plane direction ( $b_f \parallel c_s$ ), whereas it became tensile with 0.84% in the [100] in-plane direction ( $a_f \parallel c_s$ ). Thus, the  $a/b$  twin domains that formed had an alternating compressive/tensile strain, which was effective in compensating the strain effect along the [001] substrate direction. However, the in-plane  $c$ -axis ( $c_f \parallel d_s$ ) was under a high compressive strain of 2.6% at growth temperature and upon cooling, this compressive strain was reduced to 0.7%, which could not be released by twinning and hence cracks developed along the [001] substrate direction.

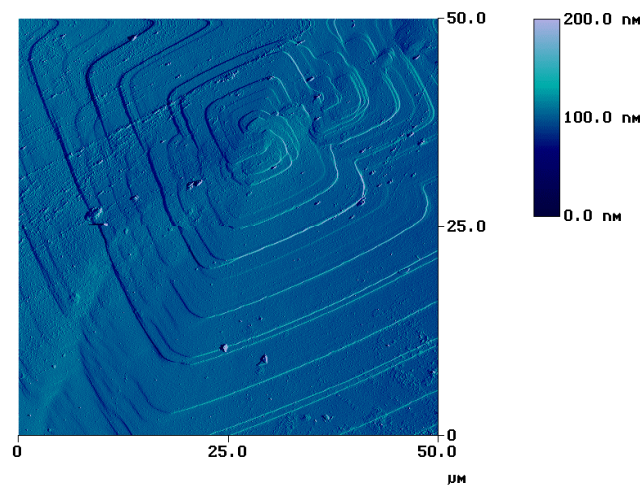
The mechanism that releases the strain during film growth is the formation of misfit dislocations. Klemenz *et al.* [42] estimated that strain in  $a,b$ -oriented film could be accommodated by the formation of misfit dislocations in the first few monolayers of  $\sim 2$  nm, whereas the critical thickness for  $c$ -oriented films is  $\sim 20$  nm. On the other hand, the strain in post-growth condition depends on the differential thermal expansion between film and substrate and the oxygenation process, with the phase transition accompanied by splitting of  $a$ - and  $b$ -axis, changing  $c$ -axis, and twinning. A large proportion of the post-growth strain was probably caused by the large difference in the thermal expansion coefficients between the film and substrate. NdGaO<sub>3</sub> substrate has a smaller coefficient of thermal expansion than YBCO (see Table 4.1); the substrate contracted less than the film upon cooling from growth temperature, thus inducing a tensile stress on the film. If the film forms {100} twins, a pseudo-tetragonal symmetry is established [42], resulting in reduced effective strains due to alternating compressive and tensile strains in adjacent twin domains. The formation of {110} twins partially relaxed the strain and when there were no mobile misfit dislocations to further accommodate the strain, cracking released the remaining effective strain energy by forming a new surface.

Upon cooling from the growth temperature, LPE grown film would be partially oxidised unless it is cooled in the absence of oxygen (e.g., N<sub>2</sub> atmosphere), in which the crystal would retain its tetragonal structure and depending on the differential thermal expansion between film and substrate, for film thickness below a critical value, strain could be further relaxed if the dislocation mobility is sufficient, or by bending. When the film is cooled in air, depending on the cooling rate and anisotropic oxidation rate, partially oxidised/twinned film is obtained. The strain can be accommodated by twinning and cracking if the film thickness exceeds the critical value for crack formation. In either case, further oxygenation was necessary in order to achieve the proper oxygen stoichiometry for optimum superconducting

properties. The oxygen diffusion in YBCO is highly anisotropic, with directional diffusion coefficients  $D_a = 10^{-13}$  cm<sup>2</sup>/s,  $D_b = 10^{-11}$  cm<sup>2</sup>/s, and  $D_c = 10^{-16}$  cm<sup>2</sup>/s [43]. Thus, an oxygen concentration gradient is expected in the film. The oxidation rate of the film would depend on the structural perfection, with more effective oxidation along cracks and other defects.

Surface morphology of *c*-oriented films showed straightedge spirals of typically 50-800 μm in diameter can be seen in Figs. 6.8(b) and 6.9(b), while those of *a,b*-oriented films were elliptical as shown in Fig. 6.19(b). It has been estimated [44,45] that the (001) face of YBCO is smoother than the (100) face; therefore, the polygonisation of growth spirals as observed on *c*-oriented films can be explained as in §3.1.6 where smooth steps lead to polygonised spirals. Comparable growth rates along both [100] and [010] directions resulted in the formation of straightedge spiral with its square edges parallel to [100] and [010] directions on *c*-oriented films (see Fig. 6.21(a)). On the other hand, anisotropic growth with higher growth rate along the *a,b*-direction (as compared to *c*-direction) led to a faster growth of the spiral along the same *a,b*-direction, resulting in the formation of elliptical spirals that elongated along the [100]/[010] direction (see Fig. 6.21(b)).

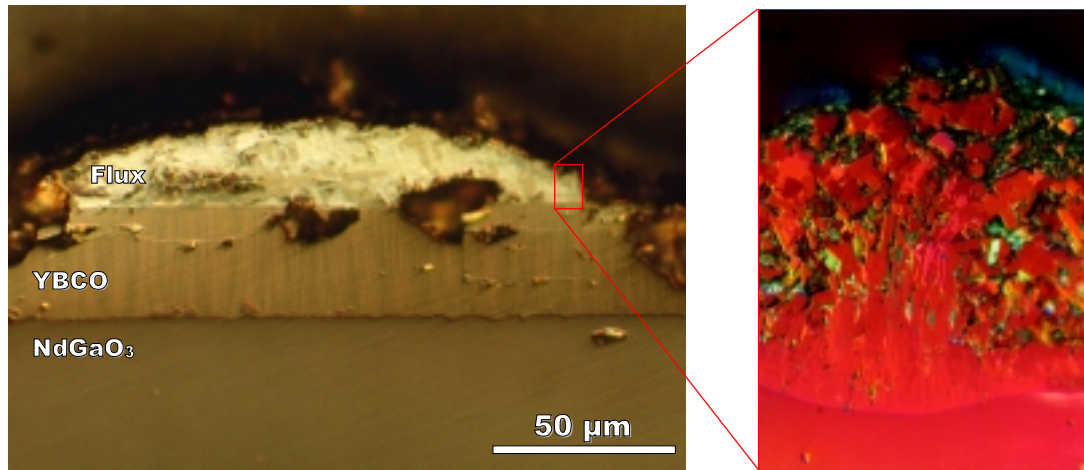
Most of the growth spirals observed on *c*-oriented films were non-Archimedean with bunching step height from one unit cell (~12 Å) to several tens of unit cell as shown in Fig. 6.8(b) and originated from more than one dislocation sources in pairs or groups close by as the one shown in Fig. 6.22. The macrospiral density on *c*-oriented films grown by LPE is estimated to be about  $5 \times 10^2$  to  $10^4$ /cm<sup>2</sup> [2,46].



**Fig. 6.22** AFM image showing a non-Archimedean growth spiral on *c*-axis oriented YBCO film grown on NdGaO<sub>3</sub> substrate.

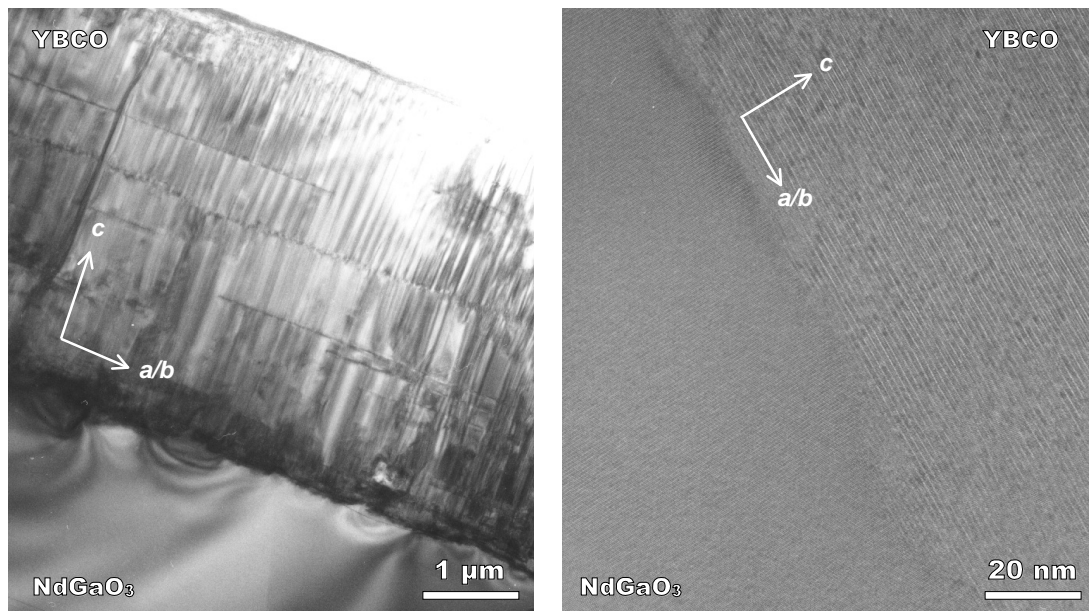
### 6.6.1 TEM and HREM analyses

Fig. 6.23 shows a polished cross-sectional image of YBCO/NdGaO<sub>3</sub> interface with flux residue on top, which clearly shows that the film grew epitaxially while the flux residue was randomly oriented (inset). It also shows that the film/substrate interface was not a smooth straight line indicating some chemical interaction took place at the high growth temperature (990°C) where the substrate was partially etched.



**Fig. 6.23** Optical images of a polished cross section of YBCO/NdGaO<sub>3</sub> interface with randomly-oriented flux residue on top. The inset shows a magnified image of the flux residue.

Detailed study using TEM and HREM revealed a high degree of epitaxy on LPE grown YBCO films as shown in Fig. 6.24.



**Fig. 6.24** TEM (left) and HREM (right) images showing high degree of epitaxy on LPE grown YBCO films on NdGaO<sub>3</sub>.

It is likely that there were some kind of chemical or physical interactions between the film and substrate at the relatively high growth temperature as observed on the optical photomicrographs (Fig. 6.23). Fig. 6.25(a) shows a HREM image of YBCO/NdGaO<sub>3</sub> interface, which is atomically straight. Some contrast differences are visible within the film, which indicate the presence of lattice strains that might be associated with misfit dislocations due to lattice mismatch between the film and substrate ( $\sim 0.26\%$ ). In contrast, HREM image in Fig. 6.25(b) shows an irregular YBCO/NdGaO<sub>3</sub> interface, which suggests that the substrate was attacked during the initial growth stage and partially dissolved. However, YBCO films further away from the interface show epitaxial growth. This indicates that the LPE growth of YBCO on NdGaO<sub>3</sub> substrate by etch-back and re-growth mechanism was of 3-dimensional epitaxial growth.

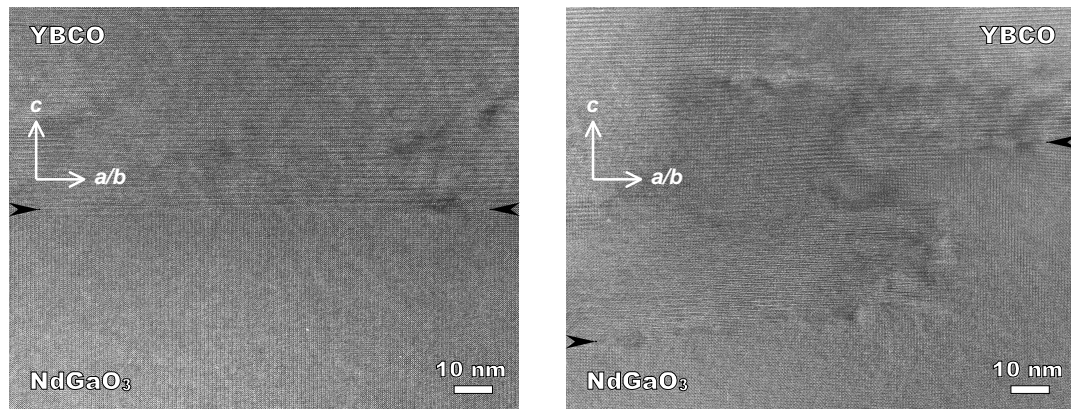


**Fig. 6.25** HREM images showing atomically straight (left) and a locally dissolved (right) of YBCO/NdGaO<sub>3</sub> interface. The arrowheads mark locations of the interface.

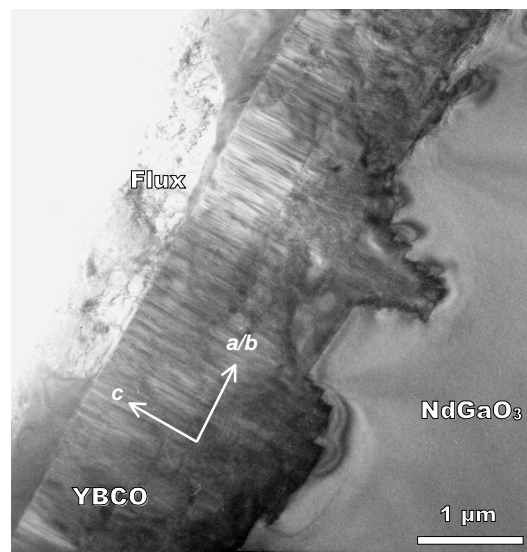


**Fig. 6.26** TEM image showing NdGaO<sub>3</sub> substrate heavily attacked or etched by flux containing BaF<sub>2</sub>. There was generally more flux residue left attached to the film at lower growth temperature.

It was expected that at reduced growth temperature the film/substrate interface would have less physical or chemical interactions. However, it was found that NdGaO<sub>3</sub> became vulnerable to the flux containing BaF<sub>2</sub>. As shown in Fig. 6.26, the substrate had been severely attacked or etched, however, the resulting YBCO film retained its 3-dimensional epitaxial growth.

## 6.7 Transport Properties

Fully-oxygenated YBCO films grown on NdGaO<sub>3</sub> substrates generally had high  $T_c$  approaching 92 K whereas  $J_c$  values were limited to the order of  $10^5$  A/cm<sup>2</sup> due to intrinsically low concentration of defects acting as effective pinning centres.

### 6.7.1 Critical temperatures

Both resistive and inductive methods were used to determine the critical transition temperatures of the samples prepared. The inductive method has the advantage of ease of preparation, as it was a non-contact method whereas the resistive method required good current and voltage contacts that could cause difficulties in cases where plenty of flux residues were left on the film surface.

Fully oxygenated YBCO film grown on NdGaO<sub>3</sub> substrate typically showed high  $T_c$  value of ~92 K with an average transition width of ~2-4 K. Fig. 6.27 shows a typical characteristically sharp resistive transition of an LPE grown film.

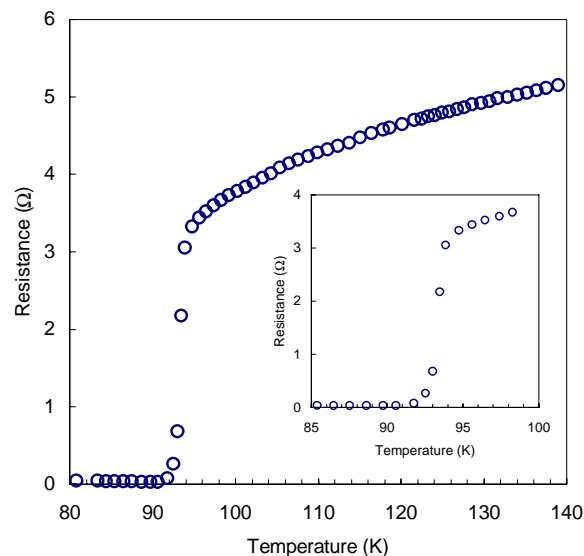


*Fig. 6.27 Resistive-transition of LPE grown YBCO on NdGaO<sub>3</sub>.*

Fig. 6.28 shows an example of  $T_c$  measured using inductive method with sharp transition around 92 K.

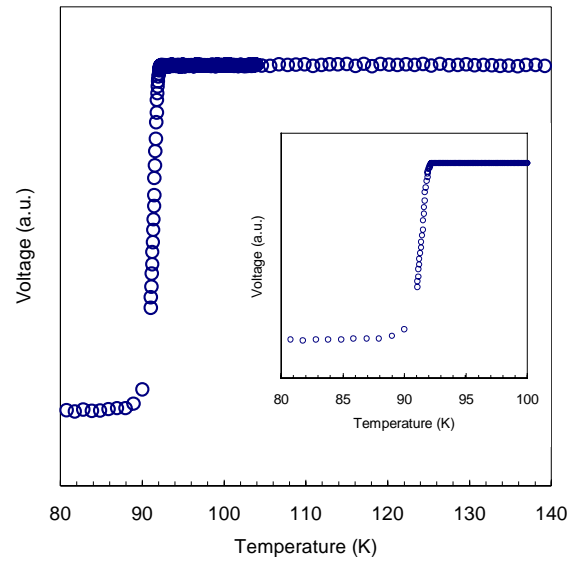


**Fig. 6.28** Critical transition temperature measured of LPE grown YBCO on NdGaO<sub>3</sub> using inductive method.

### 6.7.2 Critical currents

The magnetic field dependence of the transport  $J_c$  at 77 K is shown in Fig. 6.29 for three selected samples where sample 16-32 was grown from a Ba-Cu-O-Ag flux.

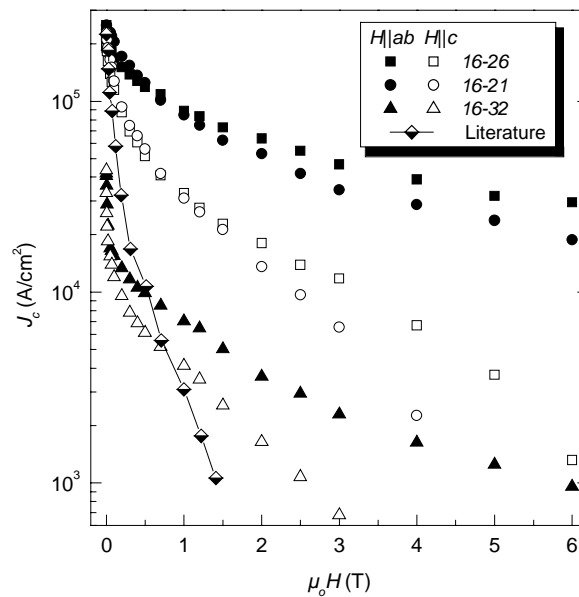


**Fig. 6.29** Field dependence of the critical transport current densities at 77 K; all three samples were  $\sim 1 \mu\text{m}$  thick. Full symbols represent  $J_c$  for  $H \parallel ab$  and open symbols for  $H \parallel c$ . Literature data from ref. [47].

The conditions of growth for each of the samples shown in Fig. 6.29 are presented in Table 6.1. The only difference between samples *16-21* and *16-26* is that the *16-26* was grown 3 days later than *16-21* from the same batch of flux.

**Table 6.1** Growth conditions for the samples shown in Fig. 6.29.

Sample	Growth $T$ (°C)	Undercooling (°C)	Growth time (s)	Substrate rotation rate (rpm)	Flux
16-21	990	15	30	100	Ba-Cu-O
16-26	990	15	30	100	Ba-Cu-O
16-32	955	15	30	100	Ba-Cu-O-Ag

The zero-field  $J_c$  of  $2.5 \times 10^5$  A/cm<sup>2</sup> of the coated conductors deposited by the "standard" LPE technique (without additives in the solution) were found to be much higher than the one grown from Ba-Cu-O-Ag flux, *16-32*, with  $J_c$  of  $4 \times 10^4$  A/cm<sup>2</sup>. In the latter case, a significant hysteresis of  $J_c$ , especially at low fields, for both field orientations  $H \parallel ab$  and  $H \parallel c$  was observed (e.g., a factor of 2 at 20 mT). This indicates a pronounced network of cracks or grain boundary grooves with low critical currents, where the magnetic flux can be trapped even at high temperatures. Silver in the solution seems to favour the formation of large grain boundaries leading to this hysteretic behaviour.

The in-field behaviour was similar for all films deposited on NdGaO<sub>3</sub> substrates. After a drop of  $J_c$  at relatively low fields the  $J_c$  show only a weak field dependence for  $H \parallel ab$ . The field dependence is more distinct for  $H \parallel c$ . In comparison to samples *16-26* and *16-21*, the worse in-field performance of *16-32* indicates inferior pinning.

The difference in the in-field performance between samples *16-21* and *16-26* indicates that the density of pinning centres is different between the two samples. Sample *16-26*, which was grown 3 days later than sample *16-21* may contain more defects due to the continuous deteriorating flux, thus leading to higher density of pinning centres as indicated by its higher  $J_c$ . The higher density of pinning sites leads to higher  $B_{irr}$  and thus the difference in the in-field  $J_c$  is larger at higher magnetic field. In addition, Fig. 6.29 shows that the difference in the in-field  $J_c$  between samples *16-21* and *16-26* is larger for  $H \parallel c$ , as compared to  $H \parallel ab$ . This is likely because flux pinning for  $H \parallel ab$  is largely determined by the intrinsic pinning mechanism, which is common to both samples. On the other hand when  $H \parallel c$ ,  $J_c$  is also determined by other external factors such as the density of point and  $c$ -axis correlated pinning centres. Given the sample to sample variation in the number of such defects, it is thus expected, and indeed observed, that the difference in  $J_c$  between the two samples is larger for  $H \parallel c$ .

Zero-field  $J_c$  value of  $2.5 \times 10^5$  A/cm<sup>2</sup> at 77 K of YBCO on NdGaO<sub>3</sub> substrate from this work is comparable to results from other researchers listed in Table 4.3. Nevertheless, these  $J_c$  values are one order in magnitude lower than that of films grown on MgO substrates mainly due to the lack of defects that act as effective pinning centres as discussed. However, comparing to those from other researchers as shown in Fig. 6.29, the  $J_c$  from samples prepared in this work show better in-field performance.

## 6.8 Summary

Both  $c$ - and  $a,b$ -oriented YBCO thick films were successfully grown on (110) NdGaO<sub>3</sub> substrates by LPE under carefully controlled growth temperature and undercooling. The undercooling working window for purely  $c$ -oriented growth was found to be between 2.5 and 20°C. The LPE grown films were highly epitaxial and biaxially aligned with good in-plane and out-of-plane textures. The initial growth of YBCO was found to be a multi-nucleation process in a Stranski-Krastanov like mechanism where initial layer-by-layer growth was followed by island formation. However, above a critical film thickness, dislocations started to form as a lattice-misfit stress relieving mechanism that led to step formation and spiral growth around dislocation cores. A pronounced spiral-made hillocks/sub-grain growth occurred in the steady-state growth regime under relatively high substrate rotation rate where growth-death competition was observed in which larger sub-grains increased in size at the expense of smaller ones.

The growth kinetics from an unstirred solution was found to obey a  $\sqrt{t}$  law, whereas the growth rate from a stirred solution was found to have two growth stages with initial transient and steady-state regimes. The transient regime extended to  $\sim 180$  s with  $\sqrt{t}$  growth kinetics. In the steady-state regime, diffusion across an established diffusion boundary layer led to a linear increase of film thickness with time. This diffusion layer was estimated to be  $\sim 35$   $\mu\text{m}$  for a substrate rotating at 200 rpm. Detailed study of the film growth suggested the presence of interface kinetics that limited the growth on a competitive basis with volume diffusion in the solution.

With the addition of BaF<sub>2</sub> and Ag into the flux, the growth temperature for  $c$ -oriented films in air was successfully reduced to as low as 885°C so long as the undercooling was kept below 20°C. Nevertheless, NdGaO<sub>3</sub> was found to be very vulnerable to etching in flux containing BaF<sub>2</sub>.

YBCO thick films grown on NdGaO<sub>3</sub> substrates by LPE showed high transition temperatures approaching 92 K and zero-field  $J_c$  at 77 K of  $2.5 \times 10^5$  A/cm<sup>2</sup> with much better in-field performance than that reported in the literature.

## References

- 1 T. Kitamura, M. Yoshida, Y. Yamada, Y. Shiohara, I. Hirabayashi, and S. Tanaka, *Appl. Phys. Lett.* **66** (1995) 1421.
- 2 C. Klemenz and H. J. Scheel, *Physica C* **265** (1996) 126.
- 3 T. Aichele, S. Bornmann, C. Dubs, and P. Görnert, *Cryst. Res. Technol.* **32** (1997) 1145.
- 4 T. Kitamura, S. Taniguchi, Y. Shiohara, I. Hirabayashi, S. Tanaka, Y. Sugawara, and Y. Ikuhara, *J. Crystal Growth* **158** (1996) 61.
- 5 T. Kitamura, Y. Yamada, Y. Shiohara, I. Hirabayashi, S. Tanaka, Y. Sugawara, and Y. Ikuhara, *J. Crystal Growth* **166** (1996) 854.
- 6 A. Takagi, I. Hirabayashi, and U. Mizutani, *J. Jpn. Inst. Met.* **61** (1997) 978.
- 7 R. Ghez and E. A. Giess, *MRS Bull.* **8** (1973) 31.
- 8 S. Knight, B. S. Hewitt, D. L. Rode, and S. L. Blank, *MRS Bull.* **9** (1974) 895.
- 9 T. Kitamura, I. Hirabayashi, S. Tanaka, Y. Sugawara, and Y. Ikuhara, *Appl. Phys. Lett.* **68** (1996) 2002.
- 10 M. Yoshida, T. Nakamoto, T. Kitamura, O. B. Hyun, I. Hirabayashi, S. Tanaka, A. Tsuzuki, Y. Sugawara, and Y. Ikuhara, *Appl. Phys. Lett.* **65** (1994) 1714.
- 11 D. Elwell and H. J. Scheel, *Crystal Growth from High-Temperature Solutions* (Academic Press, London, 1975).
- 12 W. K. Burton, N. Cabrera, and F. C. Frank, *Phi. Trans. A* **243** (1951) 299.
- 13 Ch. Krauns, M. Sumida, M. Tagami, Y. Yamada, and Y. Shiohara, *Z. Physik B* **96** (1994) 207.
- 14 N. Cabrera and M. M. Levine, *Phil. Mag.* **1** (1956) 450.
- 15 B. Mutaftschiev, in *Dislocations in Solids*, edited by F. R. N. Nabarro (North-Holland, Amsterdam, 1980) 90.
- 16 A. A. Chernov and H. J. Scheel, *J. Crystal Growth* **149** (1995) 187.
- 17 Y. Nakamura, A. Endo, and Y. Shiohara, *J. Mater. Res.* **11** (1996) 1094.
- 18 J. Crank, *The Mathematics of Diffusion* (Clarendon Press, Oxford, 1956).
- 19 M. L. Boas, *Mathematical Methods in the Physical Sciences*, 2<sup>nd</sup> edition (John Wiley & Sons, New York, 1983).
- 20 C. Klemenz and H. J. Scheel, *J. Crystal Growth* **200** (1999) 435.
- 21 A. Kursumovic, Y. S. Cheng, B. A. Glowacki, J. Madsen, and J. E. Evetts, *J. Crystal Growth* **218** (2000) 45.
- 22 M. Abramowitz and I. A. Stegun, *Handbook of Mathematical Functions* (Dover, New York, 1965).
- 23 J. W. Cahn, *Proc. Intl. Conf. on Crystal Growth* (Boston, USA, Pergamon Press, 1966) 681.
- 24 W. R. Wilcox, in *Preparation and Properties of Solid State Materials*, edited by R. A. Lefever, Vol. 1 (Marcel Dekker, New York, 1971).

- 25 J. A. Burton, R. C. Prim, and W. P. Slichter, *J. Chem. Phys.* **21** (1953) 1987.
- 26 W. G. Cochran, *Proc. Camb. Phil. Soc.* **30** (1934) 365.
- 27 A. Kursumovic *et al.*, unpublished data.
- 28 Y. Namikawa, M. Egami, and Y. Shiohara, *J. Jpn. Inst. Met.* **59** (1995) 1047.
- 29 H. Schlichting, *Boundary-Layer Theory*, 6<sup>th</sup> edition (McGraw Hill, New York, 1968).
- 30 M. Nakamura, Ch. Krauns, and Y. Shiohara, *J. Mater. Res.* **11** (1996) 1076.
- 31 Y. Yamada, Y. Niiori, I. Hirabayashi, and S. Tanaka, *Physica C* **278** (1997) 180.
- 32 Y. Niiori, Y. Yamada, and I. Hirabayashi, *Physica C* **296** (1998) 65.
- 33 Y. Yamada, T. Suga, and I. Hirabayashi, *J. Crystal Growth*, in press.
- 34 Y. Yamada and I. Hirabayashi, *J. Crystal Growth* **229** (2001) 343.
- 35 J. Maeda and Y. Shiohara, *J. Jpn. Inst. Met.* **63** (1999) 397.
- 36 N. Sakai, M. Deguchi, S.-I. Yoo, and M. Murakami, *J. Jpn. Inst. Met.* **61** (1997) 920.
- 37 S. B. Kim, T. Maeda, Y. Yamada, T. Suga, Y. Yamada, T. Watanabe, and I. Hirabayashi, *Extended Abstracts of the 5<sup>th</sup> ISTE-C-MRS Intl. Workshop on Superconductivity* (Honolulu HI, USA, 2001) 244.
- 38 M. D. Vazquez-Navarro, PhD Dissertation, University of Cambridge, Cambridge (1998).
- 39 T. Aichele, P. Görnert, R. Uecker, and M. Muhlberg, *IEEE Trans. Appl. Supercond.* **9** (1999) 1510.
- 40 I. Utke, C. Klemenz, H. J. Scheel, M. Sasaura, and S. Miyazawa, *J. Crystal Growth* **174** (1997) 806.
- 41 I. Utke, C. Klemenz, H. J. Scheel, and P. Nüesch, *J. Crystal Growth* **174** (1997) 813.
- 42 C. Klemenz, I. Utke, and H. J. Scheel, *J. Crystal Growth* **207** (1999) 62.
- 43 S. Rothman, J. L. Routboud, and U. Welp, *Phys. Rev. B* **44** (1991) 2326.
- 44 Y. Yamada, M. Nakamura, Y. Shiohara, and S. Tanaka, *J. Crystal Growth* **148** (1995) 241.
- 45 C. Klemenz, PhD Dissertation, Swiss Federal Institute of Technology, Lausanne (2000).
- 46 H. J. Scheel, C. Klemenz, F. K. Reinhart, H. P. Lang, and H. J. Guntherodt, *Appl. Phys. Lett.* **65** (1994) 901.
- 47 T. Kitamura and I. Hirabayashi, *ISTEC Journal* **8** (1995) 19.

<b>Chapter VI Growth of YBCO on NdGaO<sub>3</sub></b>	<b>101</b>
6.1 Crystalline Orientation	101
6.2 Growth Rate Dependence	104
6.3 Nucleation and Growth Mechanism	107
6.3.1 <i>Steady-state growth</i>	108
6.4 Growth Kinetics	111
6.4.1 <i>Unstirred solution and stirred solution transient growth</i>	111
6.4.2 <i>Stirred solution steady-state growth</i>	115
6.5 Growth at Reduced Temperature in Air	119
6.5.1 <i>Growth from Ba-Cu-O-F flux in air</i>	120
6.5.2 <i>Growth from Ba-Cu-O-Ag flux in air</i>	122
6.5.3 <i>Growth from Ba-Cu-O-F-Ag flux in air</i>	122
6.5.4 <i>Growth rate dependence</i>	122
6.6 Microstructural Analyses	123
6.6.1 <i>TEM and HREM analyses</i>	128
6.7 Transport Properties	130
6.7.1 <i>Critical temperatures</i>	130
6.7.2 <i>Critical currents</i>	131
6.8 Summary	133
References	134

*Studies of LPE growth from a thermal-gradient crucible with substrate rotation in previous chapter revealed the presence of interface kinetics as a competing factor with volume diffusion as the rate-limiting process in film growth. In order to study the effect of the presence of more than one RE element in the solution on film growth, LPE growth from unstirred, isothermal (without thermal gradient) solution was used to minimise the effect of interface kinetics. The justification for this is that in the absence of natural (thermal gradient) and forced (stirring) convection to deliver fresh supersaturated solution to the growth interface, volume diffusion would be the predominate rate-determining step, since interface kinetics is thought to be much faster than volume diffusion process. This chapter presents results from the growth of mixed (Y,RE)BCO (where RE = Nd and Sm) on NdGaO<sub>3</sub> single crystalline substrates including the undercooling working windows (temperature ranges) of various RE and mixed Y-RE systems, as well as the cumulative effect of multiple RE solubility on growth rate.*

### **7.1 Undercooling Growth Windows of Various REBCO Systems**

SmBCO and NdBCO films were grown in Sm- and Nd-saturated Ba-Cu-O solution respectively. The growth temperatures used in both cases were kept at 990°C for comparison with YBCO growth. It has been reported that the growth rates of SmBCO [1] and NdBCO [2] bulk single crystals are 2 and 5 times, respectively, higher than that of YBCO in air due to the higher solubility of Sm and Nd in the Ba-Cu-O solution at the growth temperatures near  $T_p$ . However, the temperature range used for undercooling lies in the primary crystallisation field for both SmBCO and NdBCO systems where moderate growth rates were achieved due

to relatively low RE solubility at the growth temperature used as compared to that at  $T_p$ . In addition, mixed (Y,Nd)BCO and (Y,Sm)BCO films were grown by further saturating the solution with yttrium.

It was found that different RE-Ba-Cu-O systems have a different range of undercooling where films would grow. The supersaturation created by undercooling determined the growth modes whereby outside the stable  $c$ -oriented undercooling working windows (or temperature ranges) as indicated in the shaded areas in Fig. 7.1,  $a,b$ -oriented films were grown. An undercooling created by cooling from any temperature within the shaded areas in Fig. 7.1 to the growth temperature of  $990^\circ\text{C}$  would result in  $c$ -oriented films. Note that the working windows referred to in Fig. 7.1 are windows of undercooling whereby predominately  $c$ -oriented films would grow.

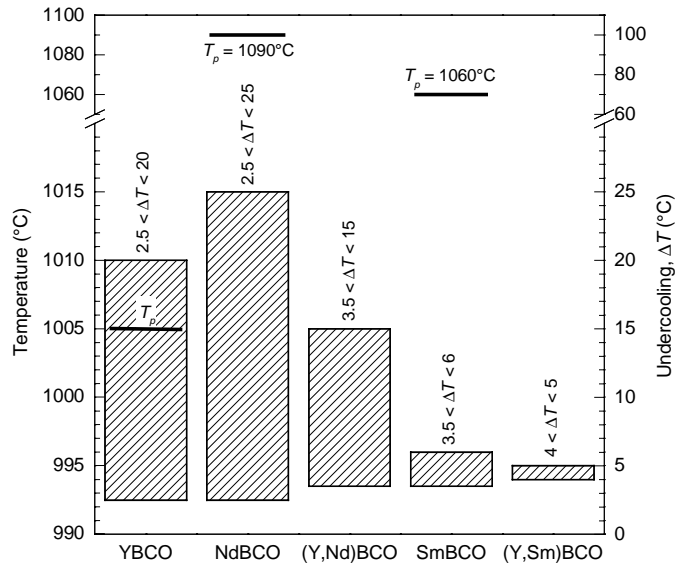


**Fig. 7.1** Undercooling working windows for various REBCO systems grown on  $\text{NdGaO}_3$  substrates at  $990^\circ\text{C}$ . An undercooling created by cooling from a temperature within the shaded area to the growth temperature of  $990^\circ\text{C}$  would result in  $c$ -oriented growth. The undercooling ranges of Sm- and Nd-systems lie within their primary crystallisation fields.  $T_p$  denotes the peritectic temperatures for the REBCO systems [3,4].

At relatively low supersaturation, mixed  $a$ -/ $c$ -oriented films were obtained. If the supersaturation was further decreased, the substrate was found partially dissolved with the formation of a (RE,Nd)BCO layer (where Nd was from the substrate) by a dissolution and re-growth process resulting in  $a,b$ -oriented films. When the supersaturation was increased beyond the working window, mixed  $a$ -/ $c$ -oriented films were also obtained due to kinetic limitation of  $c$ -oriented growth. Some dissolution of the substrate was found even within the

working window. However, the *c*-oriented epitaxy was retained as shown in Fig. 7.2 where the growth can be considered as 3-dimensional epitaxial growth.

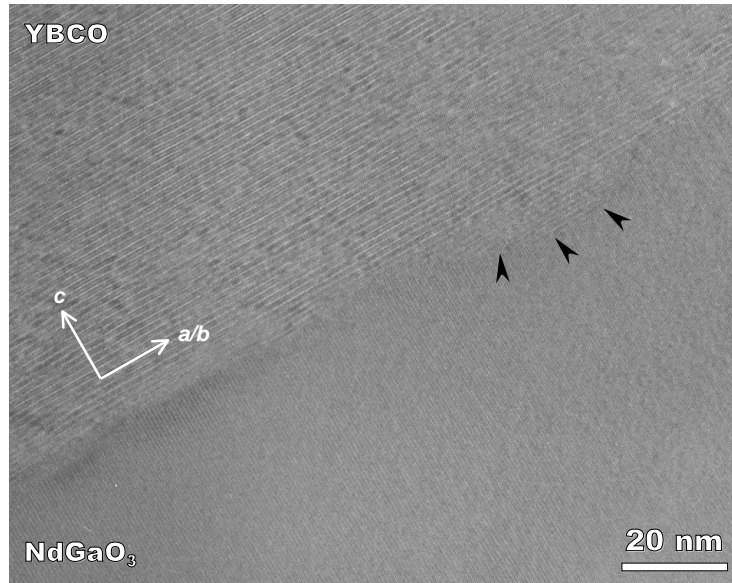


**Fig. 7.2** HREM image of a *c*-oriented YBCO on NdGaO<sub>3</sub> substrate showing dissolution (indicated by arrowheads) and re-growth process whereby 3-dimensional epitaxy was retained.

The widest undercooling working window was found for NdBCO between 2.5 and 25°C, while SmBCO had a very narrow range between 3.5 and 6°C. The addition of Y to both Sm- and Nd-saturated solutions resulted in narrower working windows and generally produced films with higher roughness as compared to films with only a single RE.

## 7.2 Growth of NdBCO and (Y,Nd)BCO from Unstirred Solutions

Fig. 7.3 shows a typical XRD  $\theta$ - $2\theta$  scan of NdBCO or (Y,Nd)BCO film grown on NdGaO<sub>3</sub> substrates with (00*l*) peaks indicating *c*-axis orientation. SEM EDX analyses show that the Y:Nd ratio is typically around 3:7 for films grown at 10°C undercooling, i.e., the (Y,Nd)BCO films had a composition of Y<sub>0.3</sub>Nd<sub>0.7</sub>Ba<sub>2</sub>Cu<sub>3</sub>O<sub>7- $\delta$</sub> . Fig. 7.4 shows the (103) pole figures of both NdBCO and (Y,Nd)BCO films. The four-fold symmetry at  $\psi = 45^\circ$  indicates in-plane alignment of *a*,*b*-plane of the films. The orientation of the film grown can be described as [001]<sub>REBCO</sub> || [110]<sub>NdGaO<sub>3</sub></sub>. Sharp poles with a typical  $\phi$ -scan FWHM value of  $\sim 3^\circ$  for a 1  $\mu\text{m}$  thick film indicate that the films produced have good in-plane alignment.

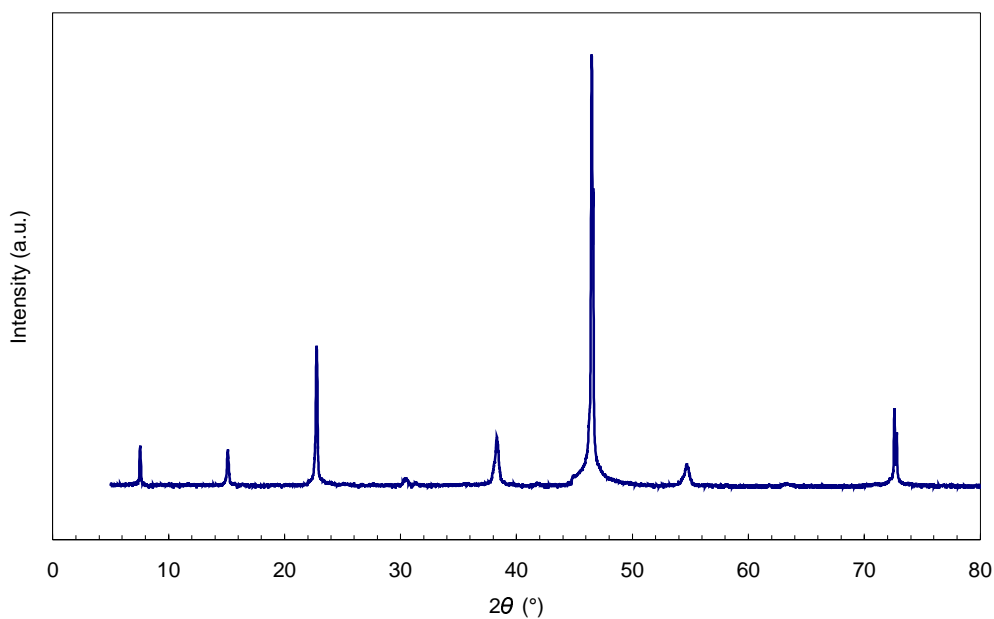


**Fig. 7.3** XRD  $\theta$ - $2\theta$  scan of NdBCO film grown on NdGaO<sub>3</sub> substrates.

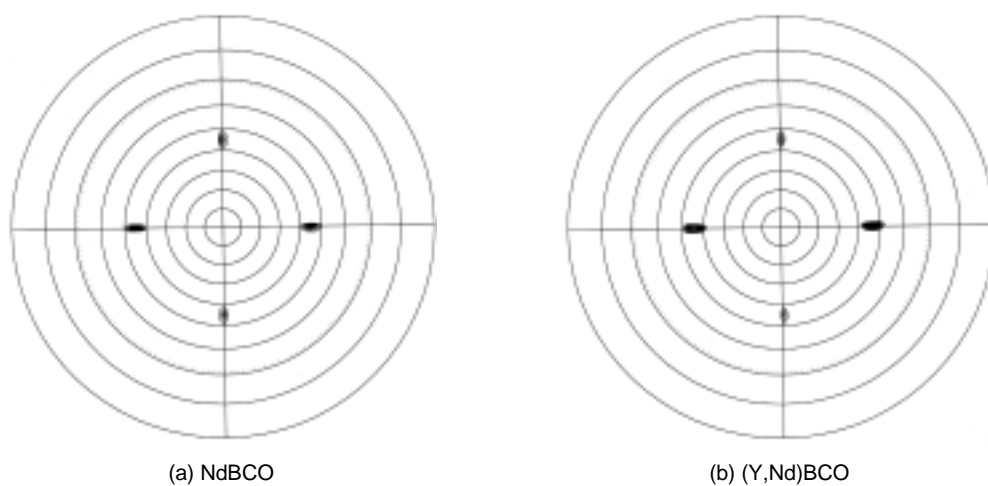


**Fig. 7.4** (103) pole figures of (a) NdBCO and (b) (Y,Nd)BCO grown on NdGaO<sub>3</sub> substrates.

The growth of YBCO, NdBCO, and (Y,Nd)BCO systems from unstirred solutions are shown in Fig. 7.5. For comparison, growth of YBCO from stirred solution (substrate rotation) is also shown in the figure. In the absence of the forced convection induced by substrate rotation in the solution (i.e., unstirred solution), the film thickness increased as the  $\sqrt{t}$  with a "negative intercept" indicating the presence of interface kinetics that limited the growth on a competitive basis with volume diffusion in the solution as discussed in the previous chapter.

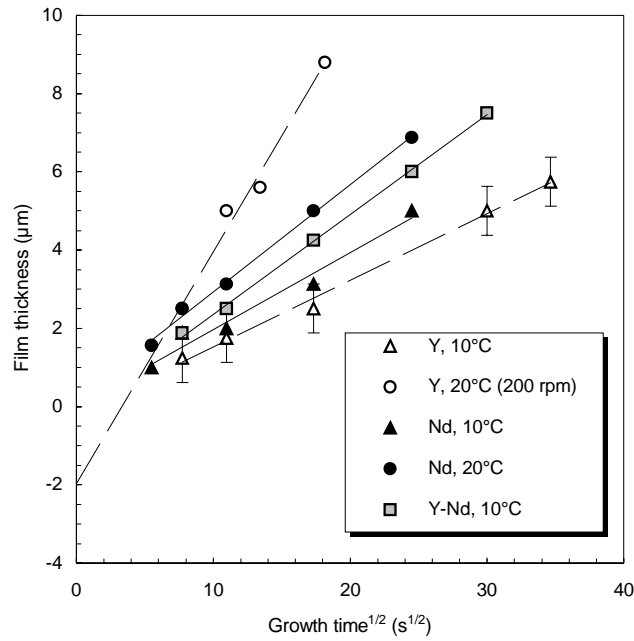


**Fig. 7.5** Film thickness of YBCO, NdBCO, and (Y,Nd)BCO as a function of the square root of growth time for c-oriented films grown on NdGaO<sub>3</sub> substrates from unstirred solutions. For comparison, growth of YBCO from stirred solution (substrate rotation) is also shown.

Film growth with a rotating substrate shows a higher growth rate than that from an unstirred solution; the former also shows a larger negative intercept, suggesting that interface kinetics played a larger role in growth with a rotating substrate. In contrast, in the case of growth from an unstirred solution, the delivery of fresh supersaturated solution to the growth interface was limited to volume diffusion of solutes from the bulk solution due to a concentration gradient in the flux. This concentration gradient was caused by the consumption of solute atoms at the growth interface, resulting in the decrease of supersaturation level at the growth interface. These results confirm that volume diffusion of solutes was a more dominant rate-determining step than interface kinetics in the growth from an unstirred solution.

According to Eqn. (6.10), the intercept from a plot of film thickness versus  $\sqrt{t}$  is dependent on the supersaturation level ( $C_L - C_e$ ). In the growth from a thermal-gradient crucible with substrate rotation as discussed in Chapter VI, a constant supersaturation level was maintained; hence, the kinetic reaction constant  $k$  can be determined quantitatively. In contrast, in the growth from an unstirred, isothermal (without thermal gradient) solution, as in this case, due to the constantly decreasing supersaturation level where  $C_L \rightarrow C_e$ ,  $H(0) \rightarrow 0$ . Thus, the intercepts of film growths from unstirred, isothermal solutions (Fig. 7.5) show values closer to the origin.

Study of the film growth at different undercoolings revealed that higher undercooling led to higher growth rate due to higher RE supersaturation as shown in Fig. 7.6. Film growth rate is dependent on the level of supersaturation as shown in Eqn. (3.14). Thus, it is expected that higher supersaturation would result in a higher growth rate.

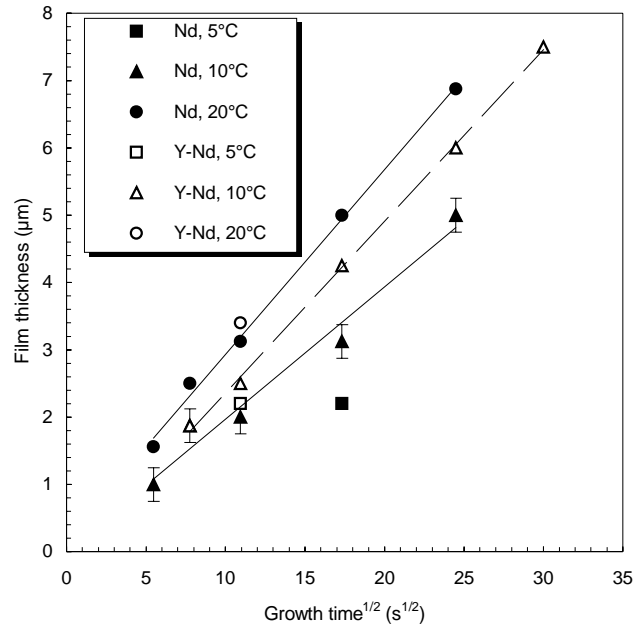


**Fig. 7.6** Film thickness as a function of square root of growth time of *c*-oriented NdBCO and (Y,Nd)BCO films grown on  $\text{NdGaO}_3$  substrates showing the effect of different undercoolings on growth rates.

For a given undercooling at  $10^\circ\text{C}$ , Fig. 7.5 shows that the growth of NdBCO is faster than that of YBCO from unstirred solutions mainly due to the higher solubility limit of Nd in the solution. However, the growth rate of NdBCO was not 5 times higher than that of YBCO as reported for the growth of NdBCO single crystals [2] since the RE solubility limit of Nd at  $990^\circ\text{C}$  is only marginally higher than Y [3,4], which is much smaller than that for the single crystals grown at higher temperature. Furthermore, the LPE growth rate of mixed (Y,Nd)BCO is higher than that of either YBCO or NdBCO. These results, together with the results from RE solubility measurements as presented in Fig. 7.7, indicate that the presence of more than one RE element had a cumulative effect on the individual RE solubility limit in the solution, producing higher supersaturation that led to faster growth. Studies of RE solubility with various RE combinations by Qi *et al.* [5-7] also revealed a cumulative effect on the individual RE solubility limit in the solution.

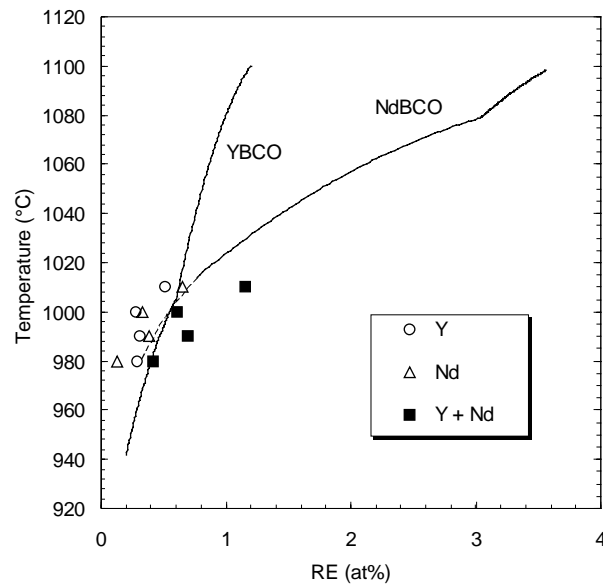


**Fig. 7.7** ICP-AES analyses of Y and Nd solubility showing a cumulative effect of individual RE solubility in the solution. Literature data from refs. [3,4].

As mentioned earlier, the major drawback of using step cooling as a mean of achieving the desired undercooling for film growth from an unstirred solution is the gradual depletion of solute atoms over time from the initial supersaturation level to the equilibrium saturation level at the growth temperature. Fig. 7.8 shows a plot of NdBCO film thickness as a function of the time elapsed from the start of step cooling for a 10°C undercooling growth. Once the undercooling was created by step cooling, all films were grown for 10 min at 15-45 min intervals without further increase in the supersaturation level, i.e., another step cooling process. As shown in Fig. 7.8, the thickness of NdBCO films (grown for the same period of time) decreased as time elapsed, which indicates the decrease in the growth rate due to the depletion of solute atoms (or supersaturation level) with time. However, this effect is not important in the present work (data in Figs. 7.5 and 7.6) because the time frame considered, from the start of step cooling until the end of film growth, was too short (a maximum of 60 min in total, with 25 min of film growth as indicated by the shaded area in Fig. 7.8) to cause a very significant depletion in solute concentration (or supersaturation level).

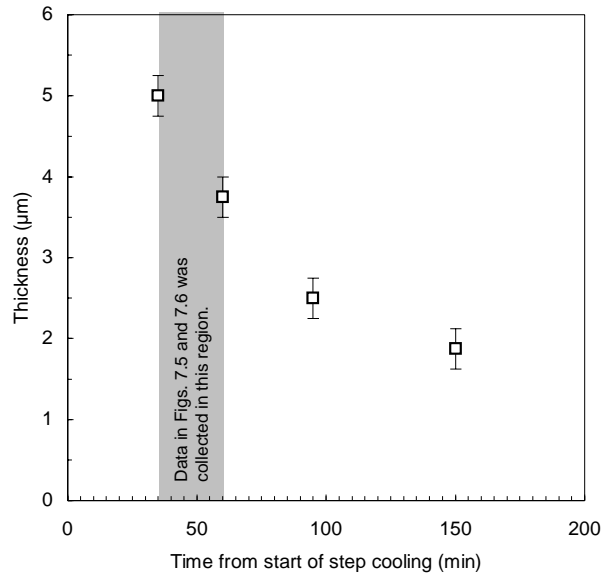


**Fig. 7.8** Film thickness as a function of time elapsed from the start of step cooling for NdBCO films grown on NdGaO<sub>3</sub> substrates from an unstirred solution. All films were grown for 10 min.

### 7.3 Growth of SmBCO and (Y,Sm)BCO from Unstirred Solutions

The growth of SmBCO and (Y,Sm)BCO at 10°C undercooling are shown in Fig. 7.9. At 10°C undercooling, the growth of SmBCO and (Y,Sm)BCO were outside of the stable *c*-oriented growth as indicated in Fig. 7.1.

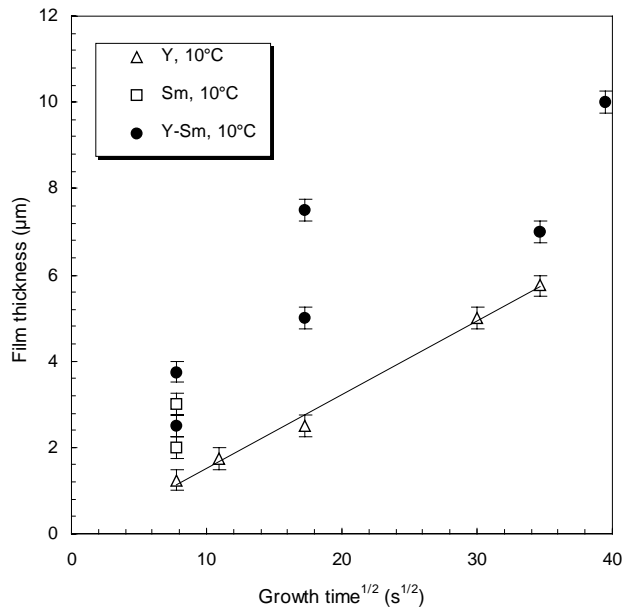


**Fig. 7.9** Growth of YBCO, SmBCO, and (Y,Sm)BCO with 10°C undercooling at 990°C on NdGaO<sub>3</sub> substrates from an unstirred solution. At 10°C undercooling, the growth of SmBCO and (Y,Sm)BCO were outside of the stable *c*-oriented growth windows, thus producing mixed *c*-/*a*-oriented films.

Although the supersaturation level of Sm in the solution at 990°C with 10°C undercooling is similar to that of Y [3], the growth of SmBCO resulted in a roughly equal mixture of *c*- and *a,b*-oriented film as shown by the XRD  $\theta$ - $2\theta$  scan in Fig. 7.10. This suggests that the higher growth rate of SmBCO as compared to YBCO at 10°C undercooling, which resulted in the presence of *a,b*-oriented component in SmBCO films, is likely to be related to other growth parameters such as the diffusion coefficients of Sm and Y in the solution.

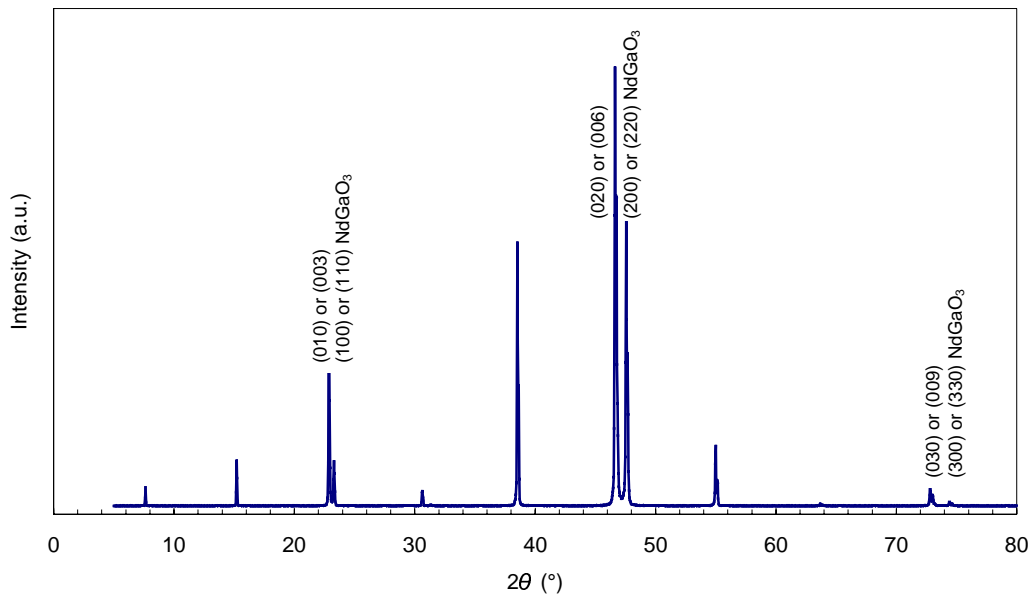


*Fig. 7.10* XRD  $\theta$ - $2\theta$  scan of SmBCO grown on NdGaO<sub>3</sub> substrates from an unstirred solution showing equal mixture of *c*- and *a,b*-orientations.

#### 7.4 The Effects of the Presence of Multiple REs

The presence of more than one RE elements in the solution resulted in a higher growth rate; however, it also yielded narrower undercooling working windows (Fig. 7.1). The cumulative effect of individual RE solubility limits created a higher RE supersaturation in the solution for a given undercooling, resulting in higher growth rate. This higher growth rate, in turn, appears to be limiting the growth of purely *c*-oriented films by encouraging the growth of the kinetically more favourable *a,b*-oriented films. Therefore, in order to obtain pure *c*-oriented films, lower undercooling was necessary in the presence of more than one RE element, hence resulting in narrower undercooling working windows.

In summary, the growth mode (*c*- or *a,b*-oriented growth) is controlled by the growth rate of the process, which is directly related to the level of supersaturation in the solution. The level of supersaturation, in turn, is controlled by the magnitude of undercooling along with the amount of total RE solubility in the solution. This is illustrated in the growth spiral as shown

in Fig. 7.11 where the initial elliptical growth spiral indicates *a,b*-oriented growth at a high supersaturation level. The eventual depletion of solute at the growth interface lowered the supersaturation level leading to *c*-oriented growth, indicated by the polygonised (straightedged) growth spirals on top.

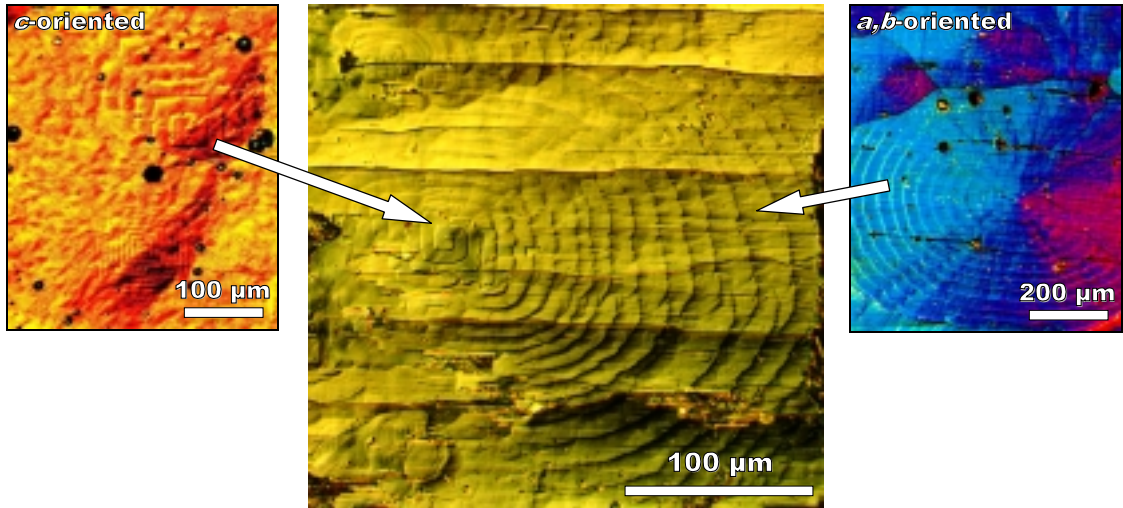


**Fig. 7.11** A growth spiral containing both *c*- and *a,b*-oriented phases characterized by polygonized (straightedged) and elliptical spirals, respectively, as shown in the insets. The initial growth of an elliptical spiral indicates *a,b*-oriented growth at the higher supersaturation level, whereas the polygonized spiral that developed at a later stage indicates the slower *c*-oriented growth that started after the depletion of solutes (or supersaturation level) at the growth interface.

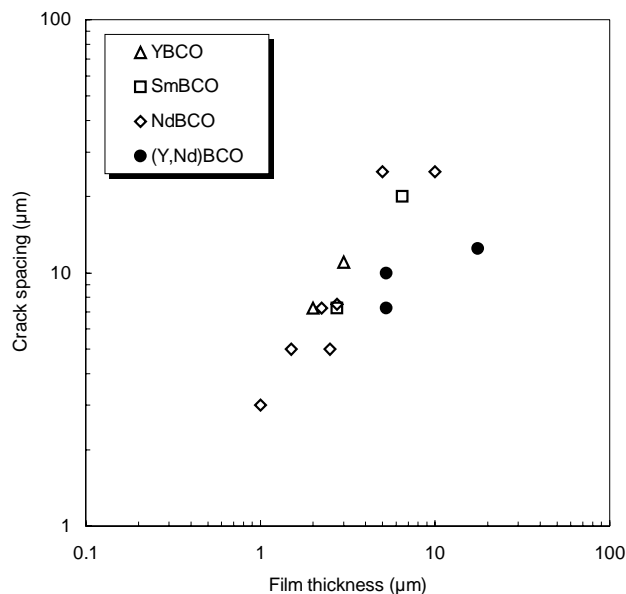


**Fig. 7.12** Crack spacing as a function of film thickness of single-RE and multiple-RE films on NdGaO<sub>3</sub> substrates.

As discussed earlier in §6.6, cracks developed on YBCO films grown on NdGaO<sub>3</sub> substrates beyond a certain critical thickness. As shown in Fig. 7.12, mixtures of REs reduced the crack density but not to a great extent, since most of the cracks were developed at lower temperature where diffusion of species that could accommodate stresses was negligible.

## 7.5 Summary

The undercooling working windows for the desired *c*-oriented films were found to vary significantly according to the RE-Ba-Cu-O system. Furthermore, the addition of more RE in the solution resulted in narrower working windows. However, the presence of more than one RE elements had a cumulative effect on the individual RE solubility limit in the solution, resulting in higher RE supersaturation that lead to higher growth rates. The film growth mode (*c*- or *a,b*-oriented growth) is determined by the growth rate, which is directly related to the level of RE supersaturation that could be controlled by the undercooling used along with the amount of total RE solubility in the solution.

## References

- 1 Ch. Krauns, M. Tagami, M. Nakamura, and Y. Shiohara, *Advances in Superconductivity VII* (Springer-Verlag, Tokyo, 1994) 641.
- 2 M. Nakamura, H. Kutami, and Y. Shiohara, *Physica C* **260** (1996) 297.
- 3 Ch. Krauns, M. Sumida, M. Tagami, Y. Yamada, and Y. Shiohara, *Z. Physik B* **96** (1994) 207.
- 4 C. Klemenz and H. J. Scheel, *J. Crystal Growth* **200** (1999) 435.
- 5 X. Qi and J. L. MacManus-Driscoll, *J. Crystal Growth* **213** (2000) 312.
- 6 X. Qi, G. K. Perkins, A. D. Caplin, and J. L. MacManus-Driscoll, *IEEE Trans. Appl. Supercond.* **11** (2001) 2897.
- 7 X. Qi and J. L. MacManus-Driscoll, *Curr. Opin. Solid State & Mat. Sci.* **5** (2001) 291.

<b>Chapter VII</b>	<b>Growth of Mixed (Y,RE)BCO on NdGaO<sub>3</sub></b>	<b>136</b>
7.1	Undercooling Growth Windows of Various REBCO Systems	136
7.2	Growth of NdBCO and (Y,Nd)BCO from Unstirred Solutions	138
7.3	Growth of SmBCO and (Y,Sm)BCO from Unstirred Solutions	143
7.4	The Effects of the Presence of Multiple REs	144
7.5	Summary	146
	References	146

---

## Chapter VIII Growth on Seeded Single Crystalline Substrates

---

*Of all the substrate materials investigated, (110) NdGaO<sub>3</sub> was the only substrate where YBCO could be grown directly by LPE. A YBCO seed layer, usually prepared by PVD techniques, is required for other substrate candidates due to the large lattice mismatch with YBCO. This chapter presents results from the LPE growth of YBCO on seeded single crystalline (100) MgO and (100) SrTiO<sub>3</sub> substrates. All seed layers were prepared by PLD technique using a KrF excimer laser (wavelength = 248 nm) with 20 ns pulse at a repetition rate of 1-10 Hz. The seed layer varied from 50 to 450 nm thick. The stability of the seed layer is also discussed.*

### 8.1 X-Ray Characterisation

YBCO films were grown by LPE on (100) SrTiO<sub>3</sub> substrates with a YBCO seed layer (*c*-axis oriented, ~200 nm thick). Purely *c*-axis oriented films were grown at 990°C from Ba-Cu-O flux and as low as 910°C from Ba-Cu-O-F flux. Fig. 8.1 shows XRD  $\theta$ - $2\theta$  scans of *c*-axis oriented YBCO seed layer and the LPE grown YBCO on SrTiO<sub>3</sub>.

The  $\omega$ -scan FWHM value of YBCO (005) peak was found to decrease from 0.42° on the seed layer to 0.08° for LPE grown layer of 5- $\mu$ m thick (insets in Fig. 8.1), showing improved crystallinity of the film by the LPE process. This small FWHM value of 0.08° suggests that the LPE grown film was almost a single crystal.

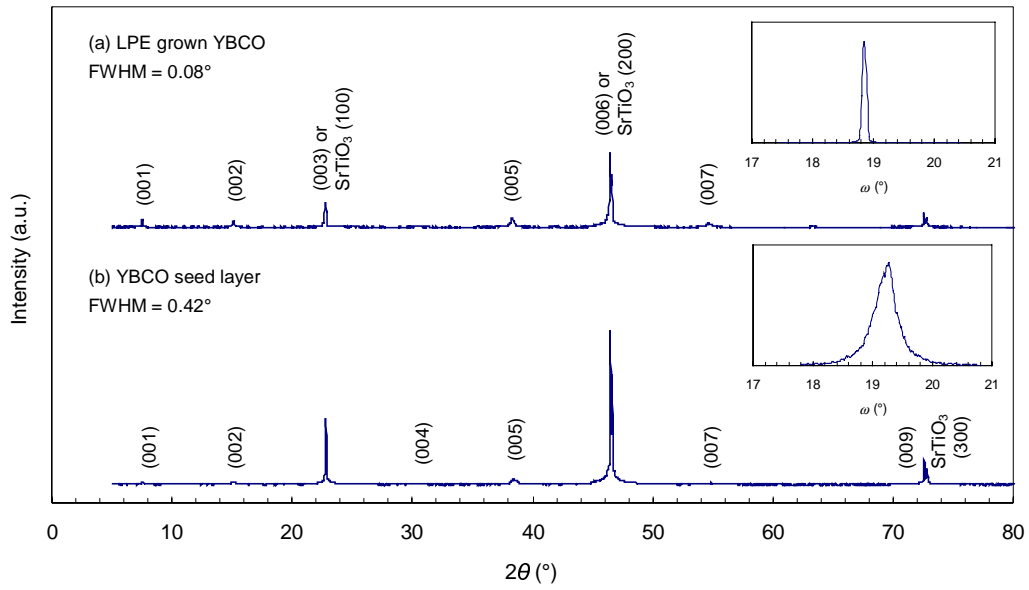


**Fig. 8.1** XRD  $\theta$ - $2\theta$  scans and (005) rocking curves of c-oriented (a) 5- $\mu\text{m}$  thick LPE grown YBCO and (b) YBCO seed layer on  $\text{SrTiO}_3$ .

At a growth temperature of  $990^{\circ}\text{C}$ , the  $\text{SrTiO}_3$  substrate (together with YBCO film) was found to dissolve in the flux after approximately 5 minutes. Thus, only films with thicknesses up to  $\sim 8\text{-}9\ \mu\text{m}$  were successfully grown at  $990^{\circ}\text{C}$ . In contrast, the substrate was not attacked at reduced growth temperature of  $910^{\circ}\text{C}$  with  $\text{BaF}_2$  addition in the flux; hence, thicker films up to  $\sim 20\ \mu\text{m}$  were successfully grown.

Fig. 8.2 shows that the pole figure of LPE grown YBCO is similar to that of the seed layer, with four-fold symmetry at  $\psi = 45^{\circ}$  indicating good in-plane alignment of  $a, b$ -plane of the film.

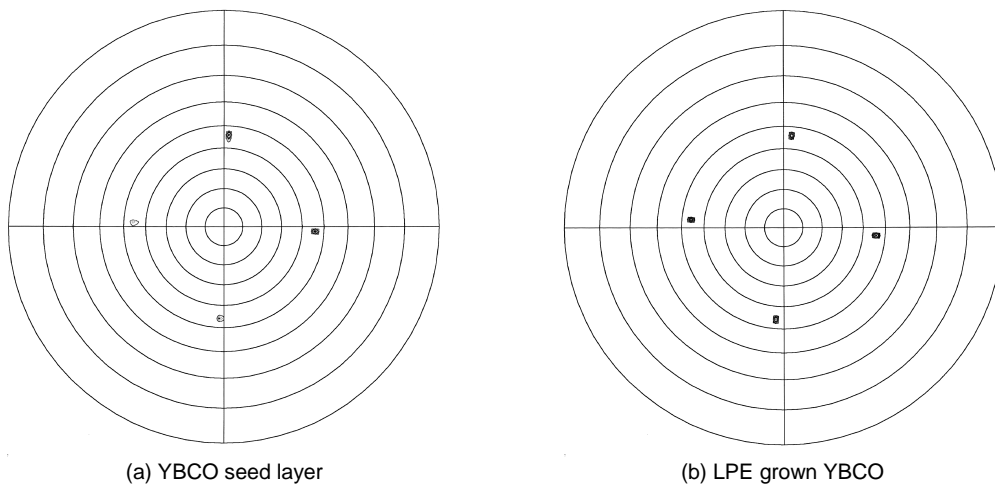


**Fig. 8.2** (103) pole figures of (a) YBCO seed layer and (b) LPE grown YBCO on  $\text{SrTiO}_3$ .

Sharp poles on the figure with typical FWHM value of  $\sim 2\text{-}4^\circ$  indicates that the LPE grown films were highly in-plane aligned. Nevertheless, YBCO films grown on  $\text{SrTiO}_3$  substrates developed cracks after oxygenation (see §8.4 later), hence, the subsequent work focused on seeded MgO substrates.

YBCO films with  $c$ -axis orientation were successfully grown on (100) MgO substrates with YBCO seed layer ranging from 50-450 nm thick at growth temperature ranging from 910 to 990°C from Ba-Cu-O-F and Ba-Cu-O fluxes. All the seed films grown by PLD on MgO substrates were  $c$ -axis oriented with typical  $\omega$ -scan FWHM value of  $0.3\text{-}0.5^\circ$ . Fig. 8.3 shows XRD  $\theta$ - $2\theta$  scans of  $c$ -oriented seed layer and LPE grown YBCO on MgO with typical rocking curve FWHM value of (005) reflection of  $0.1\text{-}0.2^\circ$  for the LPE grown layer.

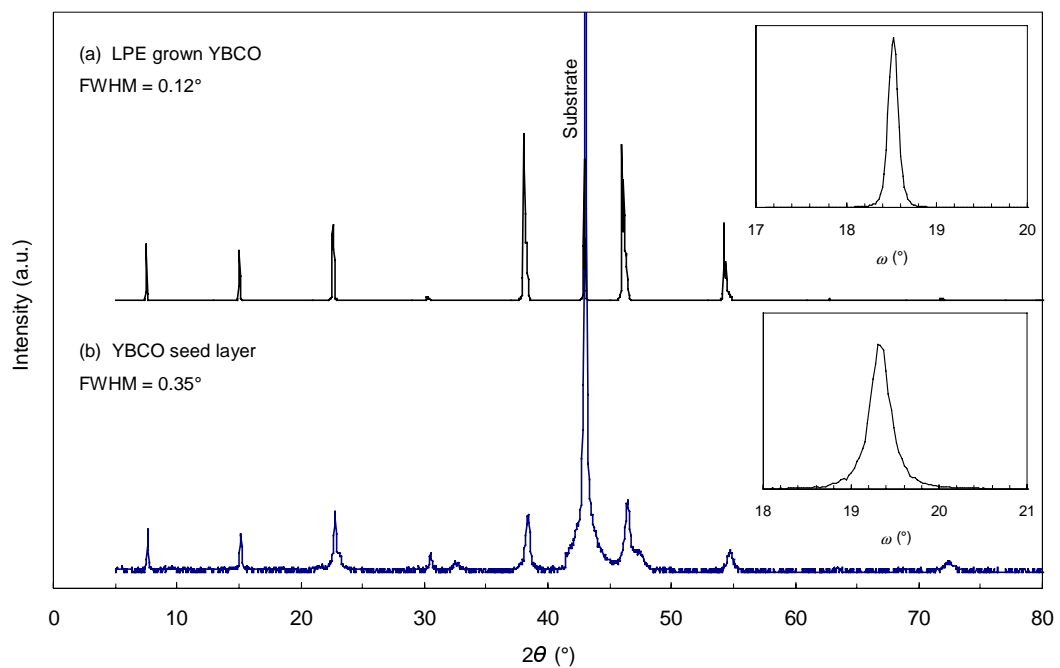


**Fig. 8.3** XRD  $\theta$ - $2\theta$  scans of  $c$ -axis oriented YBCO (a) LPE grown film and (b) seed layer on MgO substrate. Insets are rocking curves of (005) reflections.

Fig. 8.4 shows pole figures of typical YBCO seed layer on MgO and the LPE grown YBCO layer. Both pole figures show 4-fold symmetry at  $\psi = 45^\circ$  indicating good in-plane alignment of  $a,b$ -plane of the film. Sharp poles with typical FWHM value of  $\sim 3^\circ$  on a 3- $\mu\text{m}$  thick film indicate that the LPE grown films were highly in-plane aligned and an improvement in crystallinity from the seed layer with FWHM of  $\sim 5\text{-}6^\circ$ .

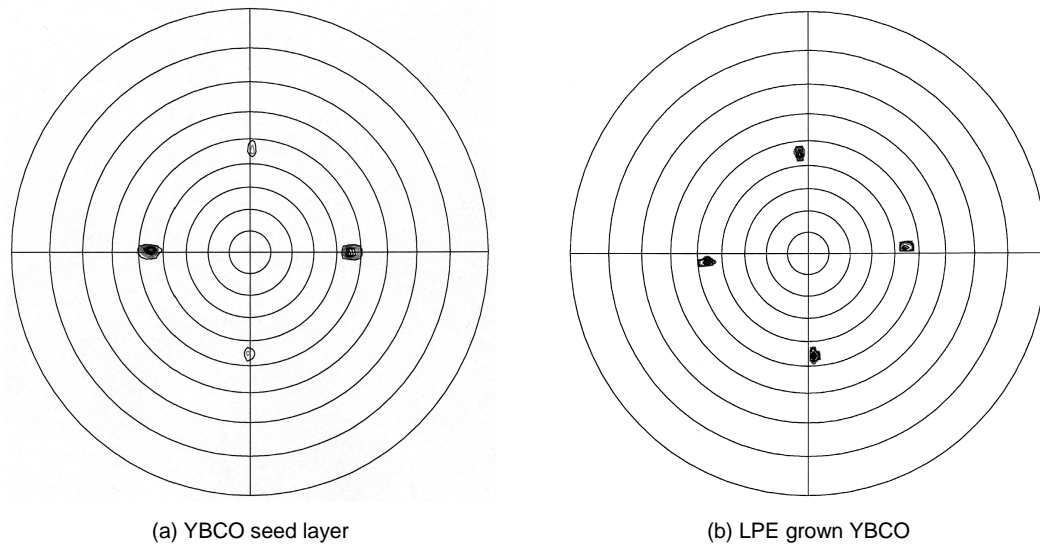


**Fig. 8.4** (103) pole figures of (a) YBCO seed layer and (b) LPE grown YBCO on MgO substrate.

## 8.2 Stability of the Seed Layer

The stability of the seed layer was found to be an important factor in determining the success in growing YBCO by LPE. YBCO grains on the seed layers with two different orientations have been reported [1-6] such that the [100]/[010] direction of YBCO grains aligned with either [100] or [110] direction of the MgO substrate, which were termed 0°- and 45°-oriented grains, as in §4.7.2(c). Furthermore, they also observed the preferential dissolution of the 45°-oriented grains due to: (i) the coarsening mechanism as a result of the difference in grain boundary curvature, and (ii) the difference in interfacial energies between the different grains (0° or 45°) with the substrate as mentioned in §4.7.2(c). In the former case, the presence of grains with non-uniform size resulted in a difference in the concentration gradient according to the Gibbs-Thomson effect [7]. The coarsening of the larger grains (0°) at the expense of the smaller ones (45°) occurred as a result of the concentration gradient.

Results from this work showed that the type of seed films with surface morphologies as shown in Fig. 8.5 (termed seed A hereafter) dissolved into the flux prior to the LPE growth and thus resulted in unsuccessful LPE growth. Seed A contained grains with non-uniform size distribution and some may also contain 45°-oriented grains. In cases where seed A contained 45° grains, the percentage of these grains was in the order of 10-20% as indicated in the 3-D pole figure in Fig. 8.6. This percentage is a much smaller percentage than that reported in the literature [1-6] where almost equal amount of both 0° and 45° grains were observed.

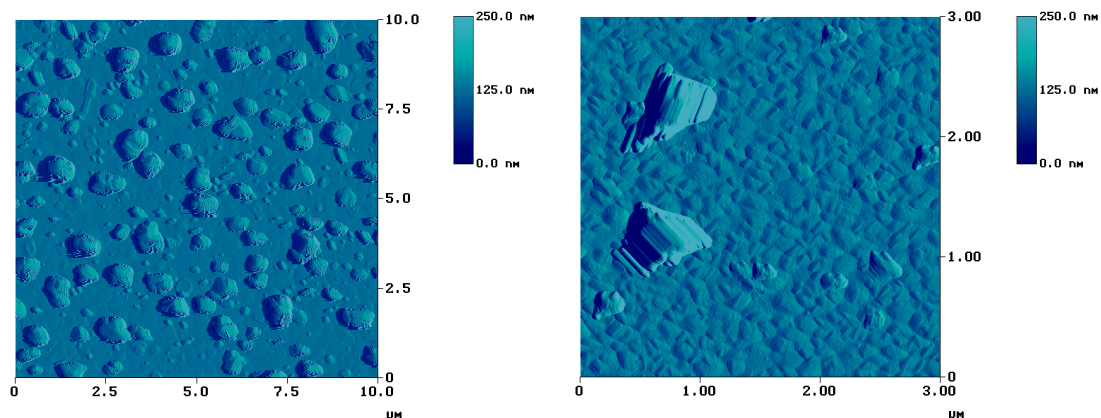


**Fig. 8.5** AFM images of unstable YBCO seed layers (seed A) on MgO substrates prepared by PLD technique showing non-uniform grain size distribution.

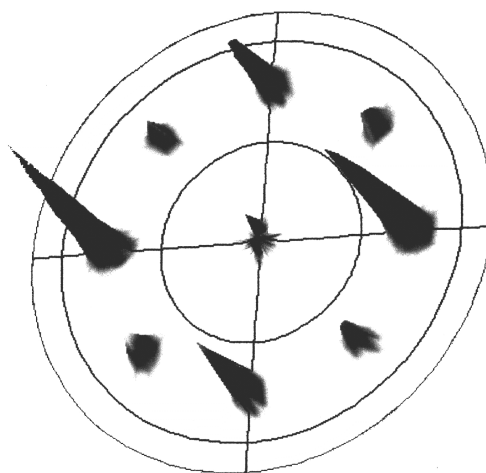


**Fig. 8.6** 3-D (103) pole figure of a YBCO seed layer type A on MgO showing both 0°- and 45°- oriented grains with 8-fold symmetry but the amount of 45° grains is in the order of 10-20%.

On the other hand, if the seed layers contained grains with uniform size distribution as shown in Fig. 8.7 (termed seed B hereafter), subsequent LPE growth was possible.

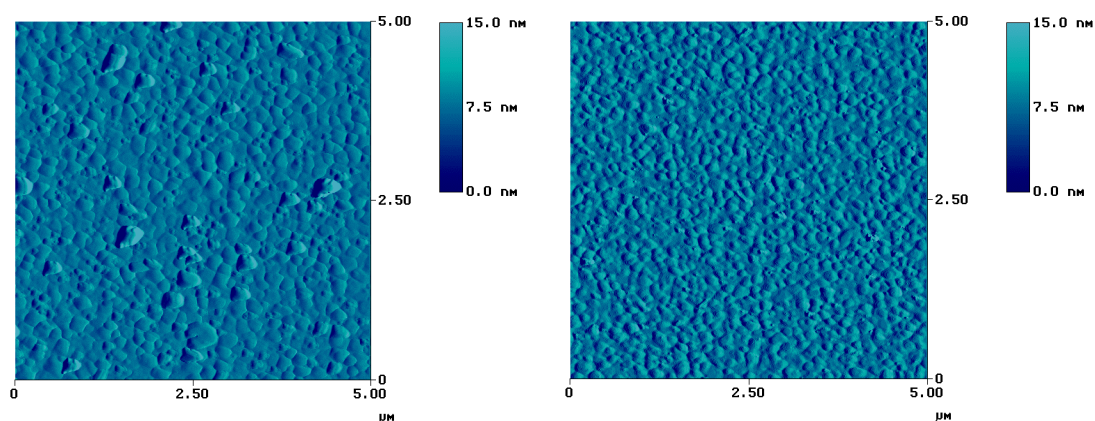


**Fig. 8.7** AFM images of stable seed layers (seed B) showing uniform grains.

In this work, it was found [8,9] that as long as the PLD deposition temperature was within the range of  $720\pm 30^\circ\text{C}$  and  $p\text{O}_2$  of 15-20 Pa where almost exclusively uniform,  $0^\circ$  grains were grown, a seed layer as thin as  $\sim 50$  nm was sufficient to initiate the LPE growth. On the other hand, if the seed layer contained predominately non-uniform grains, even a layer as thick as up to  $\sim 450$  nm would dissolve in the flux prior to the LPE growth. This suggests that the mechanism of preferential dissolution of seed layer type A is different from that observed by other researchers [1-6] where significant amount of  $45^\circ$  grains was observed.

### **8.2.1 Surface modification of the seed layer prior to the LPE growth**

Proper oxygen stoichiometry in YBCO films is necessary in order to obtain the optimum superconducting properties by post-deposition annealing in oxygen atmosphere. Oxygenation of YBCO film is usually performed at around  $500^\circ\text{C}$  and does not seem to affect its surface morphology. However, the influence of heat treatment approaching the peritectic temperature of YBCO ( $\sim 1005^\circ\text{C}$  [10]) in air has not been studied in detail and is crucial in the present work. This is because prior to the LPE growth, the YBCO seeded MgO substrate would be slowly lowered from room temperature into the furnace at  $\sim 980\text{-}985^\circ\text{C}$  and held for several minutes in order to achieve thermal equilibrium.

In order to study the influence of high-temperature annealing in air on the surface morphology of thin YBCO films, seed layers (both type A and B) on MgO substrates were annealed at 950, 970, 975, 980, and  $985^\circ\text{C}$  in air for 1 minute and followed by a further 5 minutes annealing at  $985^\circ\text{C}$ . It appeared that there was a significant surface modification of the seed layer, depending on the type of the seed films (A or B), when heated up to elevated temperature in air prior to the LPE growth. Seed A (Fig. 8.5) showed a significant change in its surface morphology after heat treatment as presented in Fig. 8.8.

The AFM image in Fig 8.8(b) shows that the surface modification started at  $\sim 970^\circ\text{C}$  with the formation of small "islands" on the relatively flat surface that were subsequently drawn towards the larger islands/grains (as shown in Figs. 8.5 and 8.8(a)) by surface diffusion and gradually transformed into needle-like whiskers. After a total of 6 minutes of heat treatment at  $985^\circ\text{C}$  (Fig. 8.8(f)), the entire films were covered with the needle-like whiskers as shown by the SEM image in Fig. 8.9.

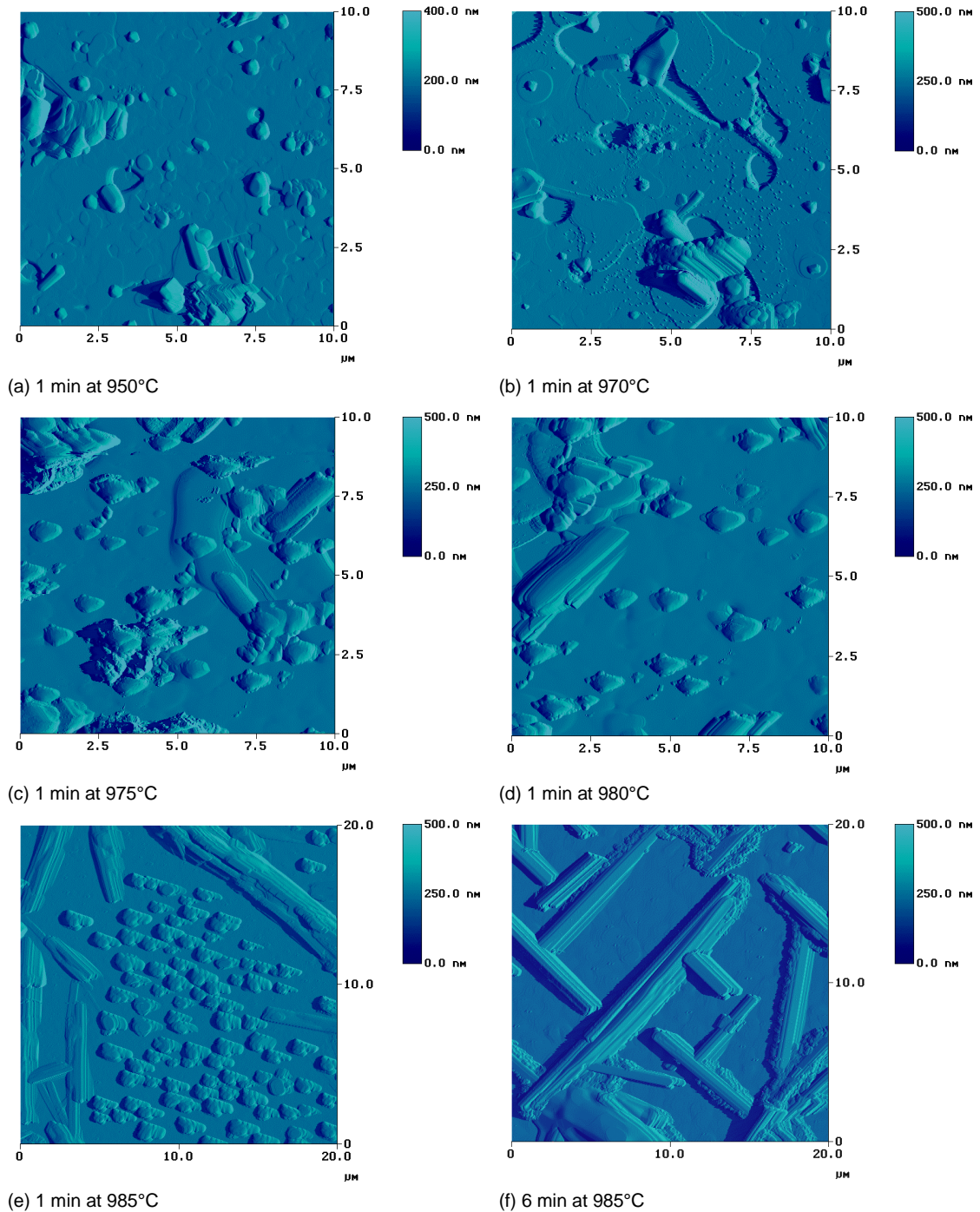


**Fig. 8.8** AFM images of seed A (unstable) after heat treatment for 1 min in air at (a) 950°C, (b) 970°C, (c) 975°C, (d) 980°C, (e) 985°C, and (f) a further 5 min at 985°C, showing significant surface modification that started at ~970°.

The SEM image in Fig. 8.9 of the annealed seed layer A shows that the length and width of the whiskers are approximately 5-50  $\mu\text{m}$  and 0.5-5  $\mu\text{m}$ , respectively. Most of the whiskers were aligned in two specific directions suggesting growth along two specific crystallographic orientations on the MgO and the whiskers are therefore epitaxial.

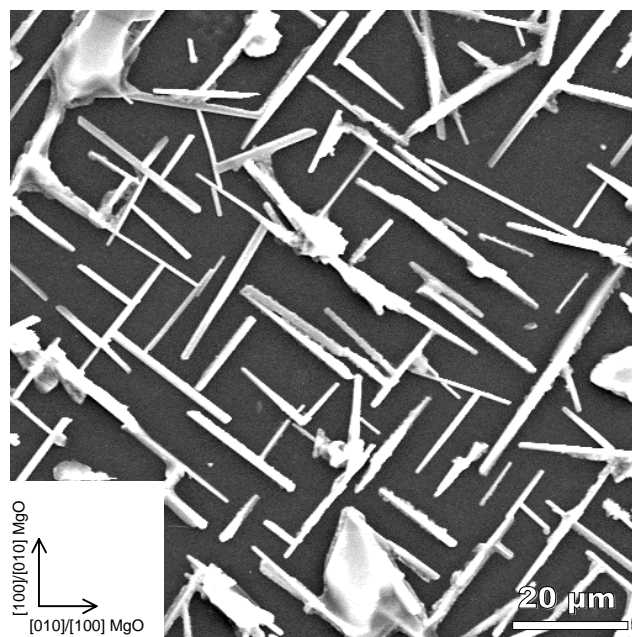


**Fig. 8.9** SEM image showing the modified seed layer A on MgO with the formation of needle-like whiskers after 6 minutes of heat treatment at 985°C in air.

XRD analysis showed no traces of Y123 left on the film as shown in Fig. 8.10. This is likely due to the fact that the small area that the whiskers covered was not sufficient to diffract the incident X-ray beam.

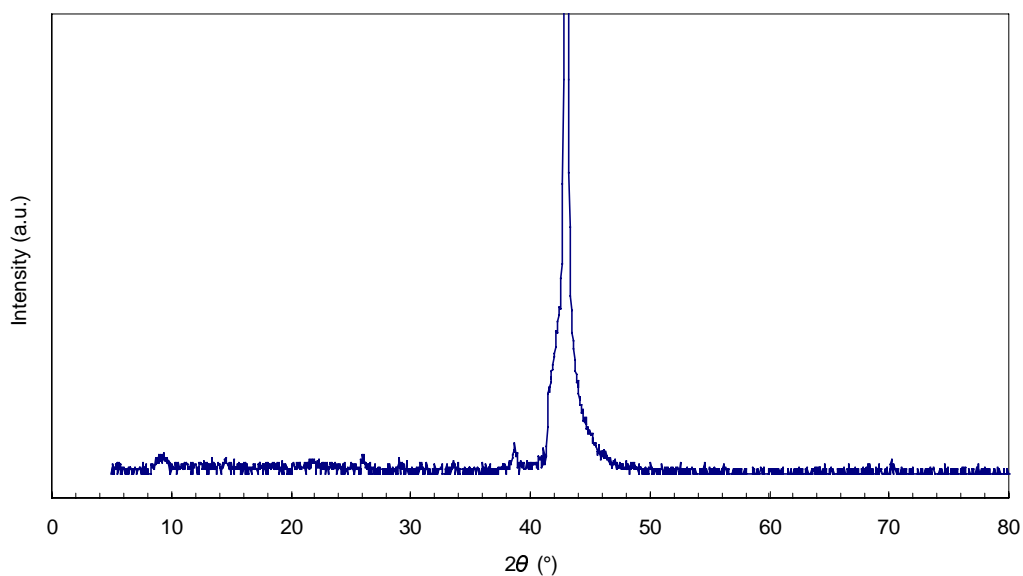


**Fig. 8.10** XRD  $\theta$ - $2\theta$  scans showing the seed layer A after annealing at 985°C in air for 6 minutes where no traces of Y123 are observed.

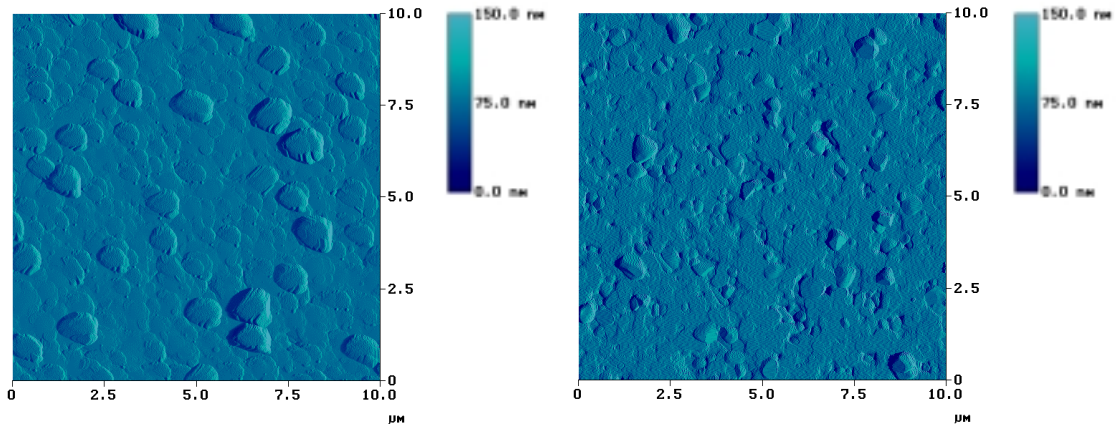
EDX analyses revealed that the composition of Y:Ba:Cu of the whiskers varied between 1:0.4:1 and 1:1.6:2.2, which suggests that the whiskers were more Y-rich than the

stoichiometric 1:2:3 YBCO. Based on the result from electron-diffraction [11], the  $a$ ,  $b$ , and  $c$  lattice parameters were estimated to be approximately 7, 12, and 5.6 Å respectively. These values strongly suggest that the whiskers consisted of the Y-rich compound Y211 with  $a = 7.132$  Å,  $b = 12.181$  Å, and  $c = 5.658$  Å [12]. Furthermore, compositional analyses by EDX on the flat regions between the whiskers show no evidence of the presence of yttrium; while the presence of Ba and Cu in those flat regions suggests that Y123 had been decomposed and transformed into Y211 whiskers and only BaO-CuO were left in the areas. As a result of the surface modification of the seed layer into Y211 whiskers and leaving no traces of Y123 phase prior to the LPE growth, the subsequent LPE growth was thus impossible in the absence of Y123 seed.

Huang *et al.* [13] also observed similar Y211 needle-like whisker formation of the seed layer on MgO while studying the possibility in using YBCO as a seed for growing the higher- $T_p$  NdBCO via LPE. However, the whiskers Huang *et al.* observed were formed as a result of exposure of the seed film at a temperature above the  $T_p$  of YBCO. Further EDX studies on the as-grown PLD seed layer revealed that the larger grains as shown in Fig. 8.5 were Y-rich with Y:Ba:Cu ratio that varied between 1:0.3:0.5 and 1:0.4:0.7, whereas the smaller grains were approximately stoichiometric 1:2:3 YBCO. These results suggest that the mechanism of Y211 whisker formation as observed in this work is different from that reported by Huang *et al.* [13].

The driving force for the surface modification of seed layer type A can be at least partially explained by the coarsening mechanism due to differences in grain boundary curvature mentioned earlier. The coarsening of the larger grains at the expense of the smaller ones occurred via surface diffusion in the presence of a concentration gradient due to the difference in grain boundary curvature as a result of the presence of non-uniform grains on seed A (Fig. 8.5). Furthermore, the  $c$  lattice parameter of Y211 (5.66 Å) matches relatively well with the [110] lattice parameter of MgO (5.95 Å), hence, the lattice misfit with crystallographic orientation such that  $[001]_{\text{Y211}} \parallel [110]_{\text{MgO}}$  is smaller (~5.12%) when compared to the mismatch between Y123 and [100]/[010] of MgO (~9.35%). In addition, the Y211 whiskers as shown in Fig. 8.9 are oriented approximately in the  $\langle 110 \rangle$  directions of MgO. Therefore, it is likely that the smaller lattice misfit between Y211 and MgO compared to that between Y123 and MgO played a major role in the formation of the Y211 whiskers along the  $\langle 110 \rangle_{\text{MgO}}$ .

In contrast, no significant changes in the surface morphologies were observed after heat treatment of seed layer type B (Fig. 8.7) as shown by the AFM images in Fig. 8.11.



(a) 1 min at 950°C

(b) 1 min at 985°C

*Fig. 8.11 AFM images of seed B (stable) after heat treatments showing no significant changes.*

### 8.3 Growth Mechanism

The growth of YBCO layer via LPE on seeded MgO is investigated. Fig. 8.12 shows a cross sectional image of a LPE grown YBCO on seeded MgO substrate. The film, which was grown at 990°C for 3 min with 100 rpm substrate rotation rate at 15°C undercooling, has a thickness of  $\sim 3.8 \mu\text{m}$ . This average growth rate of  $\sim 1.3 \mu\text{m}/\text{min}$  was consistent with the growth of YBCO on  $\text{NdGaO}_3$  substrate under similar conditions (§6.2). The film surface was quasi-atomically flat, however, there were some irregularities along the film/substrate interface as shown in the inset of Fig. 8.12. The seed layer is not clearly visible in Fig. 8.12.



*Fig. 8.12 TEM images of a LPE grown YBCO on MgO substrate. The inset shows an enlargement of an interfacial disturbance.*

Fig. 8.13 shows optical images of a sample that had been brought into contact with the flux in three different stages (after 5, 10, and 40 s) where photomicrographs were taken after each

stage of the growth. Fig. 8.13(a) shows islands of Y123 crystallites where multiple nucleation is expected to start immediately on a stable seed film when the substrate was brought into contact with the supersaturated flux. Figs. 8.13(b) and (c) show that the islands coalesced and expanded laterally connecting isolated grains into a continuous film and eventually covered the entire substrate. Similar growth mechanism is also reported by Huang *et al.* [13] in the study of growth of NdBCO film from YBCO seeded MgO substrate.

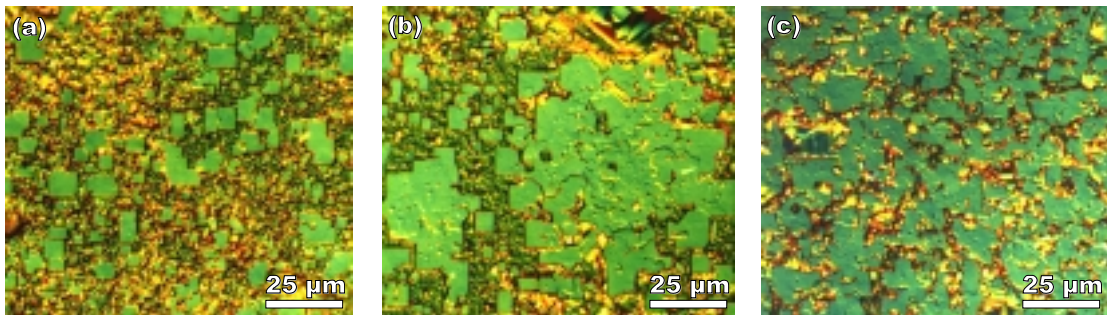


**Fig. 8.13** Optical photomicrographs showing different LPE growth stages on a seeded MgO substrate: (a) initial growth after  $\sim 5$  s showing the presence of small YBCO crystallites that served as nuclei, (b) lateral growth connecting these isolated grains (after  $\sim 10$  s), and (c) well connected grains covering almost the entire substrate with flux residues on the film surface (after  $\sim 40$  s).

#### 8.4 Surface Morphology of LPE Grown YBCO

Surface morphology studies of the LPE grown YBCO films on seeded substrates revealed similar features such as growth spirals and hillocks as those grown on NdGaO<sub>3</sub>. There were significantly more growth spirals on films grown on SrTiO<sub>3</sub> and MgO than that on NdGaO<sub>3</sub> as shown in Fig. 8.14. This implies the presence of more screw dislocations, which served as the cores of growth spirals, as a result of larger lattice mismatch between YBCO and SrTiO<sub>3</sub> ( $\sim 1.56\%$ ) or MgO ( $\sim 9.35\%$ ) as compared to NdGaO<sub>3</sub> ( $\sim 0.26\%$ ).

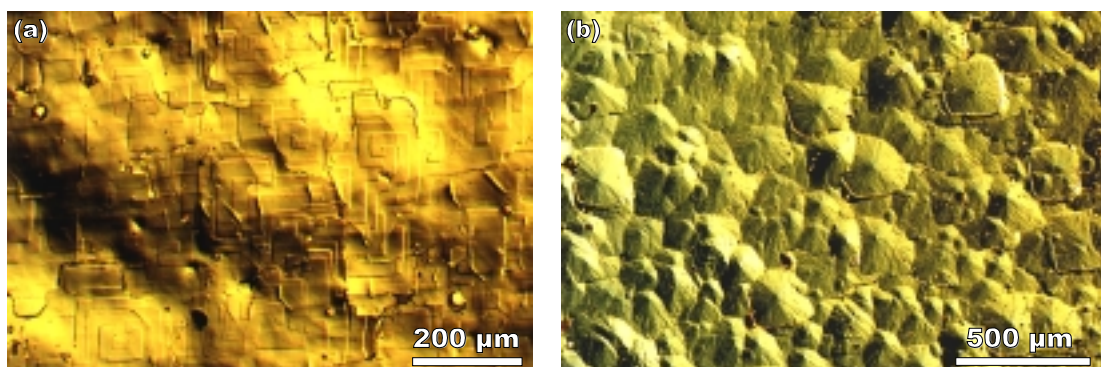


**Fig. 8.14** Optical photomicrographs of *c*-oriented YBCO grown by LPE on seeded (a) SrTiO<sub>3</sub> and (b) MgO substrates showing high density of growth spirals.

YBCO films grown on MgO substrates did not develop cracks upon cooling from the growth temperature due to the close matching of thermal expansion coefficients between YBCO and MgO. Furthermore, these films on MgO did not develop cracks even after oxygenation. In addition, as-grown YBCO films on SrTiO<sub>3</sub> substrates were free of cracks up to the maximum thickness attempted, which was approximately 20  $\mu\text{m}$ . This crack-free thickness on SrTiO<sub>3</sub> was far thicker than the critical crack-free thickness of films grown on NdGaO<sub>3</sub> substrates. However, cracks developed on the films on SrTiO<sub>3</sub> after oxygenation as shown in Fig. 8.15.

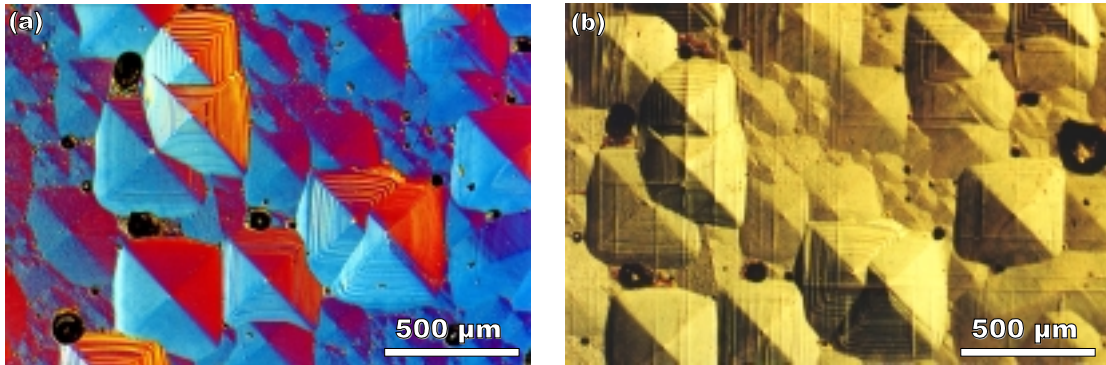


*Fig. 8.15 Photomicrographs of a LPE grown YBCO on seeded SrTiO<sub>3</sub> (a) before oxygenation and (b) after after oxygenation showing cracks.*

## 8.5 Transport Properties and Mg Contamination

The onset  $T_c$  of LPE grown YBCO on seeded MgO showed a wide variation ranging from ~70 to 85 K depending on the film thickness as shown in Fig 8.16.

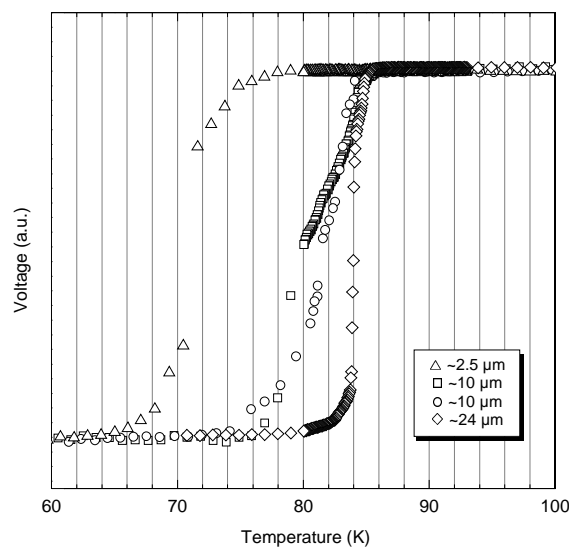


*Fig. 8.16 Transition temperatures of LPE grown YBCO on seeded MgO measured by inductive method showing a wide range of variation.*

The  $T_c$  values on samples grown on seeded MgO substrates are lower as compared to films grown on NdGaO<sub>3</sub>. If the samples were under-doped with oxygen, the thinner sample should have a higher  $T_c$  than thicker sample, as oxygenation should be faster on thinner samples. Furthermore, it is unlikely that the samples were over-doped at the annealing temperature of 500°C for 96 hours, since films grown on NdGaO<sub>3</sub> substrates with plenty of cracks did not show the sign of over-doping under similar annealing condition where oxygen are known to diffuse through cracks and other defects.

It has been shown [14] that Mg from the substrate diffused up to 40 μm into the LPE grown NdBCO layer from the film/substrate interface during the relatively high growth temperature and degraded its superconducting properties. Since all of the LPE layers grown on MgO substrates in this work were under 40 μm thick, it can be assumed that all films prepared in this work were contaminated with Mg from the substrates. The lower  $T_c$  values on thinner films (Fig. 8.16) suggest the presence of larger amount of Mg. EDX analyses revealed approximately 0.5-1.0 at% and 0.9-1.3 at% of Mg on the surface of 7 μm and 10 μm thick film, respectively. This result confirms the presence of Mg in the film and the effect of Mg contamination on the superconducting properties is further examined.

Fig. 8.17 shows three samples that had been oxygenated twice at two different temperatures. Filled symbols represent the  $T_c$  measurements after first oxygenation at 500°C for 96 hours, while open symbols denote the  $T_c$  measurements after second oxygenation for a further 48 hours at 500°C for sample 26-5, and at 700°C for samples 26-6 and 26-8.

As shown in Fig. 8.17, the  $T_c$  for thinner film was lower after first oxygenation, which is due to the presence of larger amount of Mg as discussed above. The smaller drop in the  $T_c$  value of sample 26-5 ( $\Delta T \approx 2-5$  K) as compared to sample 26-6 ( $\Delta T \approx 8-10$  K) with similar thickness indicates that Mg diffusion was more significant at higher temperature for sample 26-6 (at 700°C compared to 500°C). In addition, the thinner film (26-8) showed an even larger drop in  $T_c$  of ~12-15 K compared to ~5-10 K in the thicker films (26-5 and 26-6) due to the presence of larger amount of Mg as a result of shorter diffusion length. All the above results confirm that Mg contamination was the cause in deteriorating superconductivity in films grown on MgO substrates in this work.

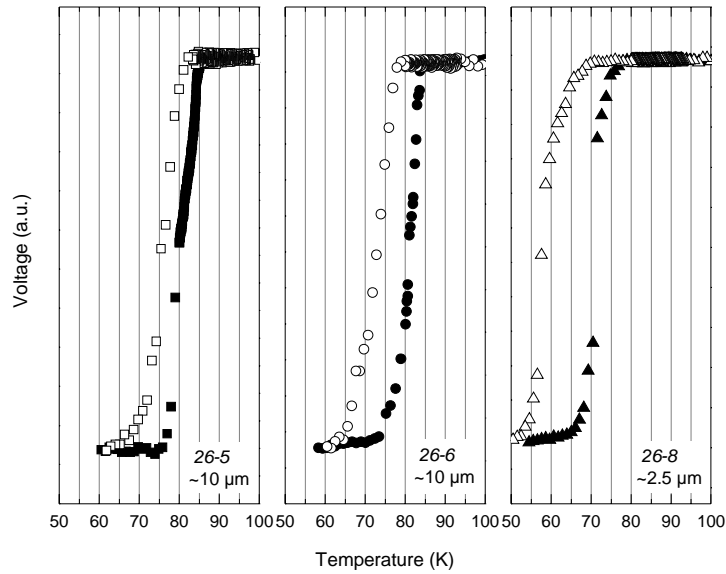


**Fig. 8.17** Inductive  $T_c$  measurements of three LPE grown YBCO samples on seeded MgO substrates.

Full symbols represent measurements after first oxygenation at 500°C for 96 hours, while open symbols denote measurements after second oxygenation for a further 48 hours at 500°C for sample 26-5 and at 700°C for samples 26-6 and 26-8.

Similarly, YBCO grown on seeded MgO typically had zero-field  $J_c$  at 77 K of  $\sim 1.3 \times 10^5$  A/cm<sup>2</sup>, which is an order lower in magnitude than reported in the literature (Table 4.3). Due to limited resources, full characterisation of transport  $J_c$  properties was restricted to only a small number of samples. The field dependence of  $J_c$  of two samples grown on MgO is presented in Fig. 8.18.

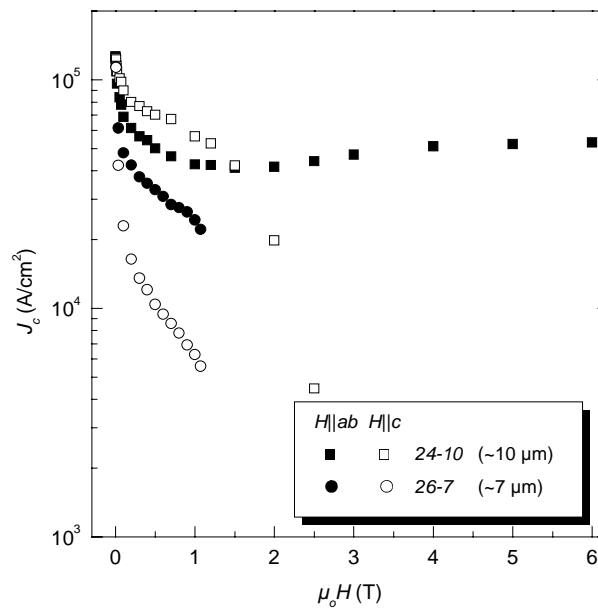


**Fig. 8.18**  $J_c$  field dependence of LPE grown YBCO on seeded MgO substrate.

The  $J_c$  field dependence of sample grown on MgO is somewhat different from that of the samples grown on NdGaO<sub>3</sub> (Fig. 6.29). The sharp drop of the critical current densities at low fields is absent both for  $H \parallel ab$  and  $H \parallel c$  for sample 24-10; instead it shows a fishtail-like field dependence for  $H \parallel c$  at about 1 T. Above 1.5 T a weak increase of  $J_c$  with increasing field can be observed for  $H \parallel ab$ . However, the cause of this behaviour is unclear.

## 8.6 Summary

YBCO films with  $c$ -axis orientation have been successfully grown by LPE on single crystalline substrates having large lattice mismatch with YBCO such as (100) SrTiO<sub>3</sub> and (100) MgO using a YBCO seed layer prepared by PLD technique. It was found that the stability of the seed layer was critical in determining the success of subsequent LPE growth. The stability of the seed layer was found to be related to the surface morphology and the presence of Y-rich grains in the seed film, which was determined by the PLD growth parameters such as the growth temperature and  $pO_2$ . In the presence of a non-uniform grain size distribution, coarsening of the larger grains at the expense of the smaller ones lead to the formation of Y211 whiskers along the  $\langle 110 \rangle_{MgO}$ , which eventually dissolved into the flux resulting in unsuccessful LPE growth. On a stable seed film, the growth started with multiple nucleation and was followed by lateral grain coarsening that eventually connected all grains and covered the entire substrate. Spiral-mediated growth on  $c$ -oriented films was observed on the later stage of the growth.

It was found that the LPE grown films on SrTiO<sub>3</sub> substrates developed cracks upon oxygenation whereas all YBCO films grown on MgO were free of cracks. However, films grown on MgO substrates showed degraded superconductivity due to Mg contamination as a result of Mg diffusion from the substrate into the film during film growth at the relatively high growth temperature.

## References

- 1 Y. Ishida, T. Kimura, K. Kakimoto, Y. Yamada, Z. Nakagawa, Y. Shiohara, and A. B. Sawaoka, *Physica C* **292** (1997) 264.
- 2 K. Kakimoto, Y. Sugawara, T. Izumi, and Y. Shiohara, *Physica C* **334** (2000) 249.
- 3 M. Kai, N. Hobara, K. Hasegawa, T. Izumi, S. Asada, Y. Nakamura, T. Izumi, T. Watanabe, and Y. Shiohara, *Extended Abstracts of the 5<sup>th</sup> ISTE C-MRS Intl. Workshop on Superconductivity* (Honolulu HI, USA, 2001) 150.
- 4 T. Izumi, K. Kakimoto, K. Nomura, and Y. Shiohara, *J. Crystal Growth* **219** (2000) 228.

- 5 K. Nomura, S. Hoshi, X. Yao, K. Kakimoto, T. Izumi, Y. Nakamura, and Y. Shiohara, *J. Crystal Growth* **229** (2001) 384.
- 6 K. Nomura, S. Hoshi, Y. Nakamura, T. Izumi, and Y. Shiohara, *J. Mater. Res.* **16** (2001) 2947.
- 7 W. W. Mullins, in *Structure, Energetics, Kinetics* (American Society for Metals, Metals Park, 1963) 17.
- 8 R. I. Tomov *et al.*, unpublished data.
- 9 A. Kursumovic *et al.*, unpublished data.
- 10 Ch. Krauns, M. Sumida, M. Tagami, Y. Yamada, and Y. Shiohara, *Z. Physik B* **96** (1994) 207.
- 11 S. Mennema, MSc Dissertation, Delft University of Technology, Delft (2001).
- 12 C. Michel and B. Raveau, *J. Solid State Chem.* **43** (1982) 73.
- 13 D. X. Huang, X. Yao, K. Nomura, Y. Wu, Y. Nakamura, T. Izumi, and Y. Shiohara, *J. Mater. Res.*, in press.
- 14 X. Yao, K. Nomura, M. Yoshizumi, M. Kuznetsov, Y. Nakamura, T. Izumi, and Y. Shiohara, *Physica C* **357-360** (2001) 1059.

<b>Chapter VIII</b>	<b>Growth on Seeded Single Crystalline Substrates</b>	<b>147</b>
8.1	X-Ray Characterisation	147
8.2	Stability of the Seed Layer	150
8.2.1	<i>Surface modification of the seed layer prior to the LPE growth</i>	152
8.3	Growth Mechanism	156
8.4	Surface Morphology of LPE Grown YBCO	157
8.5	Transport Properties and Mg Contamination	158
8.6	Summary	161
	References	161

*The ultimate goal in the development towards implementing HTS materials in electric power applications is to produce commercially affordable high- $J_c$  coated conductors in long lengths. The most promising substrate candidate is thought to be metallic tapes. Hence, attempts had been made to grow YBCO on metallic substrates and tapes with various buffer architectures. This chapter presents results from the growth of YBCO on Ni-based metallic substrates. Efforts were made to lower the growth temperature in order to reduce the corrosion in air and dissolution of the metallic tapes in the highly corrosive Ba-Cu-O flux by means of BaF<sub>2</sub> and Ag additions, as well as growth under low oxygen partial pressure. High-temperature oxidation of the metallic tapes was another major problem but was significantly reduced by using a controlled-atmosphere furnace under reduced oxygen partial pressure.*

### **9.1 Growth of YBCO on Metallic Substrates in Air**

The initial attempt to grow on metallic substrates at 990°C in air was not successful because the tapes dissolved completely into the flux. Hence, lowering the growth temperature, by means of BaF<sub>2</sub> and Ag additions, was the next obvious step to follow in order to avoid substrate dissolution.

Metallic substrates with a wide range of buffer architectures were exploited at reduced growth temperatures (900-950°C) under various undercoolings (5-20°C) in air. Single (YSZ/seed), double (CeO<sub>2</sub>/YSZ/seed), and triple (CeO<sub>2</sub>/YSZ/CeO<sub>2</sub>/seed and CeO<sub>2</sub>/YSZ/Y<sub>2</sub>O<sub>3</sub>/seed) buffer architectures (deposited by PLD technique) on various Ni-based substrates (Ni, NiV, NiCr,

NiFe, and NiCrW) were explored. The total thickness of the buffer layers was in the order of 300-400 nm and the thickness of the YBCO seed layer varied from 50-400 nm. The best result on metallic tape prepared by PLD was on a ternary NiCrW substrate with triple-buffer architecture ( $\text{CeO}_2/\text{YSZ}/\text{Y}_2\text{O}_3/\text{seed}$ ) [1,2] and was therefore largely used for the subsequent LPE growth.

It was found that none of the metallic substrates considered was stable at the growth temperature of  $990^\circ\text{C}$  and all suffered severe high-temperature oxidation, especially on the bare metallic tapes. However, even at reduced growth temperature, substrate oxidation (in air) remained since both YSZ and  $\text{CeO}_2$  are good oxygen ion conductors. Growth of a continuous YBCO layer by LPE was found impossible in air. Fig. 9.1 shows XRD  $\theta$ - $2\theta$  scans of a double-buffered ( $\text{CeO}_2/\text{YSZ}/\text{seed}$ ) NiCrW tape prepared by PLD and an unsuccessful LPE growth at  $925^\circ\text{C}$  in air showing severe substrate oxidation.

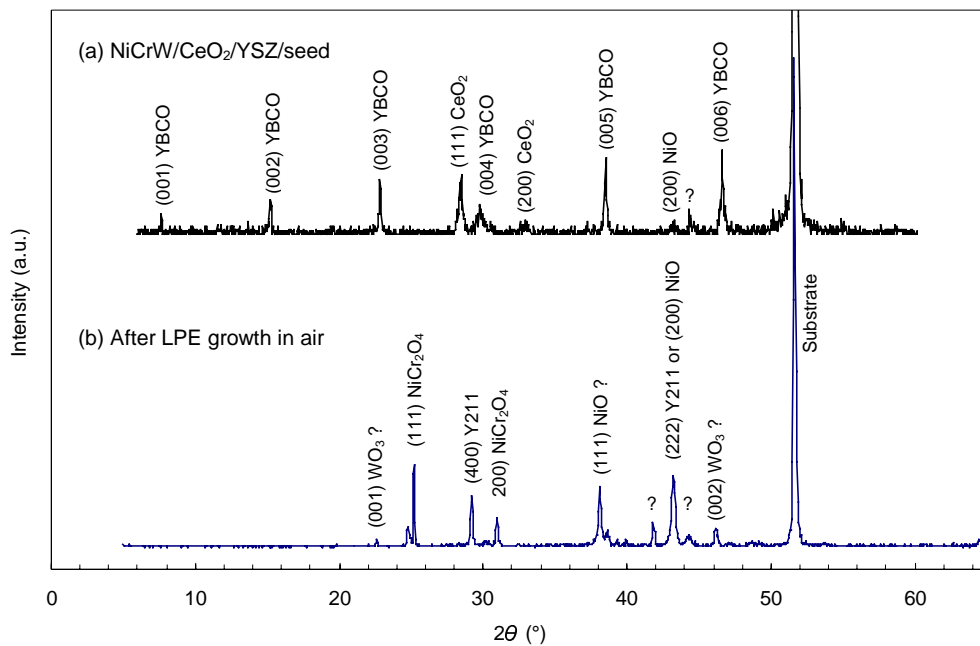


**Fig. 9.1** XRD  $\theta$ - $2\theta$  scans showing (a) c-oriented seed layer on a double-buffered ( $\text{CeO}_2/\text{YSZ}/\text{seed}$ ) NiCrW tape, and (b) severe substrate oxidation from an unsuccessful LPE growth at  $925^\circ\text{C}$  in air.

## 9.2 Growth under Controlled Atmosphere

In order to minimise high-temperature oxidation of the metallic substrates prior to the LPE growth, a controlled-atmosphere furnace was built (§5.1.2(c)) where film growth was performed under reduced  $p\text{O}_2$ . A growth environment with 1%  $\text{O}_2$  in Ar was used for the LPE growth from a Ba-Cu-O flux. The additions of  $\text{BaF}_2$  and Ag were not carried out at the

initial stage in order to study the growth behaviour under reduced  $pO_2$  alone, as it is known that the peritectic temperature of the YBCO system decreases as the  $pO_2$  decreases.

High-temperature oxidation on the metallic substrates was significantly reduced under low  $pO_2$  atmosphere. The growth temperature was reduced to as low as  $\sim 890^\circ\text{C}$  using 1%  $O_2$  in Ar alone. LPE grown YBCO layer on metallic substrates at reduced temperature was found to be much rougher with plenty of flux residues attached than that on single-crystalline substrates.

The microstructure of the LPE grown films was found to be directly related to the substrate-buffer-seed texture. The initial growth of YBCO on seeded metallic substrate closely followed that of the seed texture as presented by the (103) pole figures in Fig. 9.2, whereby a seed layer with good in-plane texture (4-fold symmetry) yielded an epitaxial LPE layer whereas a seed layer with 12-fold symmetry resulted in LPE grown YBCO crystallites having similar orientation. Fig. 9.2 shows optical images of these two LPE grown YBCO samples with different seed textures. The surfaces were rough and had plenty of flux residues attached.

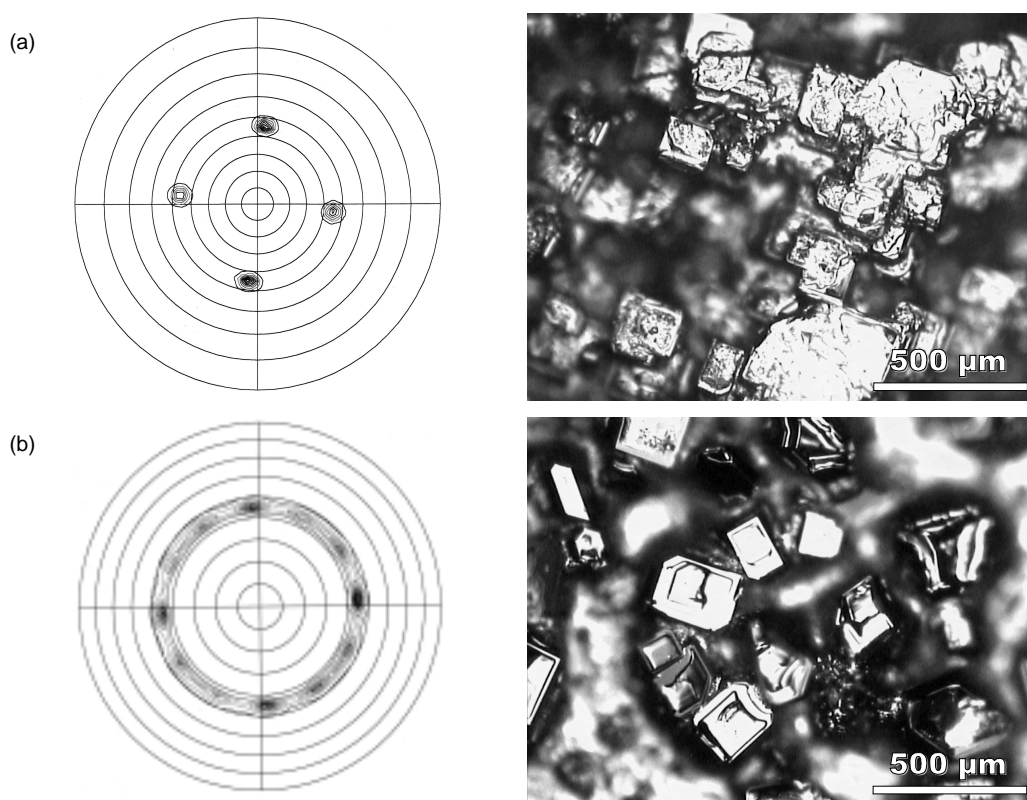


**Fig. 9.2** Optical images of well textured but rough LPE grown YBCO at  $900^\circ\text{C}$  on triple-buffer ( $\text{CeO}_2/\text{YSZ}/\text{Y}_2\text{O}_3/\text{seed}$ ) tapes with different seed textures: (a) 4-fold symmetry seed on NiCrW alloy and (b) 12-fold symmetry seed on pure Ni. The (103) pole figures are of the YBCO seed layers.

Continuous deposition on metallic substrate with reel-to-reel configuration was tested using the controlled-atmosphere furnace with a uniquely designed "split" heating zone (see Fig. 5.2). Long lengths of the commercially available NiFe tapes were successfully coated continuously as shown in Fig. 9.3. However, deposition of the necessary buffer and/or seed layers using scalable and cost-effective techniques would be the minimum requirement for continuous deposition of YBCO layer by LPE.

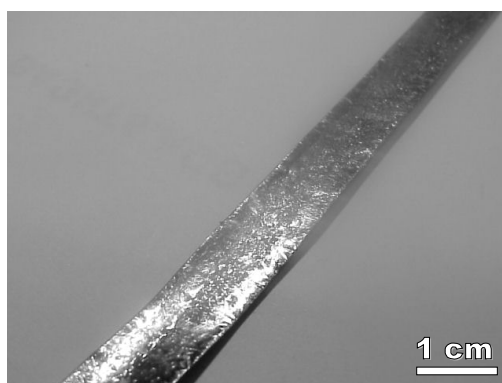


*Fig. 9.3 Continuous tape processing had been tested at a preliminary level on commercially available NiFe tape (bare) showing scalability of the LPE process.*

### 9.3 Summary

There were several problems associated with the LPE growth on metallic substrates including substrate dissolution at high growth temperature and high-temperature oxidation of substrate in air. Substrate dissolution was overcome by lowering the growth temperature while growing under low oxygen partial pressure significantly reduced substrate oxidation. The major stumbling block towards continuous deposition of coated conductor in long lengths by LPE is the lack of non-vacuum techniques capable in producing long lengths of suitably buffered substrate or a closely-matched substrate where YBCO can be deposited directly. However, despite the lack of buffered and/or seeded substrates in long lengths, continuous tape processing through a liquid bath had been tested at a preliminary level showing scalability of the process.

### References

- 1 Y. S. Cheng, A. Kursumovic, R. I. Tomov, B. A. Glowacki, A. Vostner, H. W. Webber, A. Tuissi, E. Villa, and J. E. Evetts, *Extended Abstracts of the 5<sup>th</sup> ISTE-C-MRS Intl. Workshop in Superconductivity* (Honolulu HI, USA, 2001) 185.
- 2 R. I. Tomov, A. Kursumovic, D. J. Kang, B. A. Glowacki, M. Majoros, J. E. Evetts, A. Tuissi, and E. Villa, *Proc. 5<sup>th</sup> European Conf. on Appl. Supercond.* (Copenhagen, Denmark, 2001) in press.

<b>Chapter IX Growth on Metallic Substrates</b>	<b>163</b>
9.1 Growth of YBCO on Metallic Substrates in Air	163
9.2 Growth under Controlled Atmosphere	164
9.3 Summary	166
References	166

*This chapter presents conclusions drawn from this work and provides an outlook for the continuing work of coated conductor development by LPE.*

### **10.1 Conclusions**

LPE has been successfully used to grow YBCO thick films with both *c*- and *a,b*-orientations on (110) NdGaO<sub>3</sub> substrates under carefully controlled growth temperature and undercooling. The undercooling working windows for the desired *c*-oriented films were found to vary significantly according to the RE-Ba-Cu-O (RE = Y, Nd, Sm) system. Furthermore, the addition of more RE in the solution resulted in narrower working windows. However, the presence of more than one RE elements had a cumulative effect on the individual RE solubility limit in the solution, resulting in higher RE supersaturation that led to higher growth rates. The film growth mode (*c*- or *a,b*-oriented growth) is determined by the growth rate, which is directly related to the level of RE supersaturation that could be controlled by the undercooling used together with the amount of total RE solubility in the solution.

The addition of BaF<sub>2</sub> and/or Ag into the flux resulted in reducing the growth temperature in air to as low as 885°C and the desired *c*-oriented films were grown so long as the undercooling was kept within the working window for each of the RE-Ba-Cu-O system. Nevertheless, NdGaO<sub>3</sub> was found to be very vulnerable to etching in fluxes containing BaF<sub>2</sub>.

The initial growth of YBCO on NdGaO<sub>3</sub> substrate was found to be a multi-nucleation process in a Stranski-Krastanov like mechanism where initial layer-by-layer growth was followed by island formation. However, above a critical film thickness, dislocations started to form as a lattice-misfit stress relieving mechanism that led to step formation and spiral growth around

screw dislocation cores. A pronounced spiral-made hillocks/sub-grain growth occurred in the steady-state growth regime under relatively high substrate rotation rate where growth-death competition was observed in which larger sub-grains increased in size at the expense of the smaller ones.

The growth kinetics from an unstirred solution was found to obey a  $\sqrt{t}$  law, whereas the growth rate from a stirred solution (rotating substrate) was found to have two growth stages with initial-transient and steady-state regimes. The transient regime extended to  $\sim 180$  s with  $\sqrt{t}$  growth kinetics. In the steady-state regime, diffusion across an established diffusion boundary layer led to a linear increase of film thickness with time. This diffusion layer was estimated to be  $\sim 35$   $\mu\text{m}$  for a substrate rotating at 200 rpm. Detailed study of the film growth suggested the presence of interface kinetics that limited the growth on a competitive basis with volume diffusion in the solution. This extensive precision work has shown that the phenomenology for the kinetics of layer growth can be applied in a quantitative way to the growth of YBCO by LPE where the value of the kinetic reaction constant  $k$  was determined to be  $\sim 2.5 \times 10^{-6}$  m/s.

YBCO films with  $c$ -axis orientation have also been successfully grown by LPE on single crystalline substrates having large lattice mismatch with YBCO including (100)  $\text{SrTiO}_3$  and (100)  $\text{MgO}$  using a YBCO seed layer prepared by PLD technique. The stability of the seed layer was found to be critical in determining the success of subsequent LPE growth, which is related to the surface morphology and the presence of Y-rich grains in the seed film. In the presence of non-uniform grain size distribution, coarsening of the larger grains at the expense of the smaller ones led to the formation of Y211 whiskers along the  $\langle 110 \rangle_{\text{MgO}}$ , which eventually dissolved into the flux resulting in unsuccessful LPE growth. On a stable seed film, the growth started with multiple nucleation and was followed by lateral grain coarsening that eventually connected all grains and covered the entire substrate. Spiral-mediated growth on  $c$ -oriented films was observed at the later stage of the growth.

The LPE grown films were highly epitaxial and biaxially textured with good in-plane and out-of-plane alignments. YBCO thick films grown on  $\text{NdGaO}_3$  substrates by LPE showed high transition temperatures approaching 92 K and zero-field  $J_c$  at 77 K of  $2.5 \times 10^5$  A/cm<sup>2</sup> with much better in-field performance than that reported in the literature. However, films grown on  $\text{MgO}$  substrates showed degraded superconductivity (an order of magnitude lower in  $J_c$ ) due to Mg contamination as a result of Mg diffusion from the substrate into the film during film growth at the relatively high growth temperature.

LPE growth on metallic substrates is much more difficult to achieve due to several problems including substrate dissolution at high growth temperature and high-temperature oxidation of substrate in air. Substrate dissolution was overcome by lowering the growth temperature with  $\text{BaF}_2$  and/or Ag addition together with reduced  $p\text{O}_2$ , whereas growing under low oxygen partial pressure significantly reduced substrate oxidation. The major obstacle towards continuous deposition of coated conductor in long length by LPE is the lack of non-vacuum techniques capable of producing long length of suitably buffered substrate or a closely-matched substrate where YBCO can be deposited directly. However, despite the lack of buffered and/or seeded substrates in long lengths, continuous tape processing through a liquid bath had been tested at a preliminary level showing scalability of the process.

## 10.2 Future Outlook

The real challenge towards large-scale production of coated conductor by LPE is to deposit the thick films on long lengths of flexible metallic substrates. The most successful work in this aspect has thus far been on relatively short textured NiCr tapes with in-plane aligned, *c*-oriented films that were grown at reduced temperature of  $\sim 820^\circ\text{C}$  from a Ba-Cu-O-F-Ag flux by Yamada *et al.* [1]. The films have zero-field transport  $J_c$  values at 77 K of 1.7-1.9 MA/cm<sup>2</sup>. This encouraging result has proved the viability of LPE in the processing of coated conductors. However, the NiCr tape mentioned above required a rather complex buffer architecture (IBAD-YSZ and PLD- $\text{Y}_2\text{O}_3$ ) with a YBCO seed layer deposited by vacuum technique, which may cause concerns for large-scale, cost-driven industrial implementation.

The development towards fabrication of cost-effective coated conductor by LPE is largely dependent on the development of a suitable metallic substrate where YBCO can be deposited directly or non-vacuum deposition techniques in preparing the required buffer and seed layers. The most important requirements for the buffer layer and substrate are close lattice matching (<1%) and resistance to corrosion in air and in the flux. In terms of substrate candidates, the most commonly used metallic tapes are Ag and Ni-based alloys. While the former does not seem to be the best choice from the economic point of view, the latter is more promising since the development of well-textured SOE-NiO is straightforward and cost-effective. However, diffusion of Ni into the superconducting layer is known to poison the superconductivity severely. Therefore, the need of buffer layer(s) seems inevitable.

Nevertheless, recent development of  $\text{Nd}_{2-x}\text{Ce}_x\text{CuO}_4$  buffer layer via non-vacuum techniques by Qi *et al.* [2-4] with high growth rate shows encouraging results that the buffer candidate is suitable for subsequent LPE processed REBCO. These results from Qi *et al.*, together with

the high  $J_c$  LPE processed films by Yamada *et al.* [1], have shown promising future towards the development of REBCO coated conductor by LPE.

## References

- 1 Y. Yamada, T. Suga, H. Kurosaki, S. B. Kim, T. Maeda, Y. Yamada, I. Hirabayashi, Y. Iijima, K. Kakimoto, and T. Saitoh, *Advances in Superconductivity XIV* (Springer-Verlag, Tokyo, 2002), in press.
- 2 X. Qi and J. L. MacManus-Driscoll, *Extended Abstracts of the 5<sup>th</sup> ISTEC-MRS Intl. Workshop on Superconductivity* (Honolulu HI, USA, 2001) 162.
- 3 X. Qi, M. Soorie, and J. L. MacManus-Driscoll, *Proc. 5<sup>th</sup> European Conf. on Appl. Supercond.* (Copenhagen, Denmark, 2001) in press.
- 4 X. Qi, M. Soorie, Z. Lockman, and J. L. MacManus-Driscoll, "Rapid Growth of  $\text{Nd}_{2-x}\text{Ce}_x\text{CuO}_4$  Thick Films as a Buffer on NiO/Ni for the Growth of Rare Earth Barium Cuprate Coated Conductors", preprint.

## Appendix: Flux Calculation

Atomic/molecular weights:

Ag = 107.868	Ba <sub>3</sub> Cu <sub>5</sub> O <sub>8</sub> = 857.712
Ba = 137.33	Y <sub>2</sub> CuBaO <sub>5</sub> = 458.683
Cu = 63.546	BaF <sub>2</sub> = 175.326
F = 18.998	CuO = 79.545
O = 15.999	
Y = 88.906	

Define:

Ba <sub>3</sub> Cu <sub>5</sub> O <sub>8</sub> used = $x$ g	BaF <sub>2</sub> = $p$ wt%	
Y <sub>2</sub> CuBaO <sub>5</sub> used = $y$ g	BaF <sub>2</sub> = $q$ mol% (BaO-CuO-BaF <sub>2</sub> basis)	
Y <sub>2</sub> CuBaO <sub>5</sub> min. = $z$ g	Ag = $r$ g	
BaF <sub>2</sub> = $m$ g	Ag = $s$ wt%	
CuO (Ba:Cu=3:5) = $n$ g	Ag = $t$ mol% (metal basis)	

- Minimum Y<sub>2</sub>CuBaO<sub>5</sub> required for saturation (assuming 0.6 at% Y):

$$z \text{ (g)} = \frac{0.6 \times 16 \times \left(\frac{x}{857.712}\right)}{(2 \times 100) - (0.6 \times 9)} \times 458.683 \quad (\text{A.1})$$

- Atomic percentage of Y in Ba<sub>3</sub>Cu<sub>5</sub>O<sub>8</sub> (+ Y<sub>2</sub>CuBaO<sub>5</sub>):

$$Y \text{ (at\%)} = \frac{2\left(\frac{y}{458.683}\right)}{9\left(\frac{y}{458.683}\right) + 16\left(\frac{x}{857.712}\right)} \times 100 \quad (\text{A.2})$$

- BaF<sub>2</sub> (with Ba:Cu=3:5) needed for  $p$  wt% of BaF<sub>2</sub>:

$$m \text{ (g)} = \frac{p(x+z)}{100 - p\left(1 + \frac{5}{3} \cdot \frac{79.545}{175.326}\right)} \quad (\text{A.3})$$

- BaF<sub>2</sub> (with Ba:Cu=3:5) needed for  $q$  mol% of BaF<sub>2</sub> (on BaO-CuO-BaF<sub>2</sub> basis):

$$m \text{ (g)} = \frac{q\left(\frac{8x}{857.712}\right)}{100 - q\left(1 + \frac{5}{3}\right)} \times 175.326 \quad (\text{A.4})$$

- CuO needed to maintain Ba:Cu=3:5:

$$n \text{ (g)} = \frac{5}{3} \times \frac{m}{175.326} \times 79.545 \quad (\text{A.5})$$

- Ag needed for  $s$  wt% of Ag:

$$r \text{ (g)} = \frac{s(x+z+m+n)}{100 - s} \quad (\text{A.6})$$

- Ag needed for  $t$  mol% of Ag (on metal basis):

$$r \text{ (g)} = \frac{t\left[\left(\frac{3x}{857.712} + \frac{z}{458.683} + \frac{m}{175.326}\right) + \left(\frac{5x}{857.712} + \frac{z}{458.683} + \frac{n}{79.545}\right)\right]}{100 - t} \times 107.868 \quad (\text{A.7})$$

An example of the calculations is presented in the following page.



## List of Publications and Conference Presentations

### Publications

1. "Microstructure Development in Thick YBCO Films Grown by Liquid Phase Epitaxy"  
A. Kuršumović, **Y.S. Cheng**, A.P. Bramley, B.A. Glowacki and J.E. Evetts, *Inst. Phys. Conf. Ser. No. 167, 1* (EUCAS, Sitges, Barcelona, Spain, September 1999) 147-150.
2. "Transport Critical Current Measurements in a Pressurized Liquid Nitrogen Vessel"  
B. Zeimet, B.A. Glowacki, **Y.S. Cheng**, A. Kuršumović, E. Mendoza, X. Obradors, S.X. Dou, J.E. Evetts and T. Puig, *Inst. Phys. Conf. Ser. No. 167, 2* (EUCAS, Sitges, Barcelona, Spain, September 1999) 1033-1036.
3. "Study of the Rate Limiting Processes in Liquid Phase Epitaxy of Thick YBaCuO Films"  
A. Kuršumović, **Y.S. Cheng**, B.A. Glowacki, J. Madsen and J.E. Evetts, *J. Crystal Growth* **218** (2000) 45-56.
4. "Irreversibility Properties of Coated Conductors Deposited by LPE on Single Crystalline Substrates"  
A. Vostner, Y. Sun, S. Tönies, H.W. Webber, **Y.S. Cheng**, A. Kuršumović and J.E. Evetts, *Proc. 10<sup>th</sup> Intl. Workshop on Critical Currents* (Göttingen, Germany, June 2001) 291-293.
5. "Development of High Critical Current (RE)BCO Coated Conductors via Low-Cost High-Rate Liquid Phase Epitaxy Route"  
**Y.S. Cheng**, A. Kuršumović, R.I. Tomov, B.A. Glowacki, A. Vostner, H.W. Webber, A. Tussi, E. Villa and J.E. Evetts, *Proc. 5<sup>th</sup> ISTEC-MRS Intl. Workshop in Superconductivity* (Honolulu HI, USA, June 2001) 185-187.
6. "Growth of Mixed  $(Y_xRE_{1-x})Ba_2Cu_3O_{7-\delta}$  (RE = Nd, Sm) Thick Films by Liquid Phase Epitaxy"  
**Y.S. Cheng**, A. Kuršumović, B.A. Glowacki, H.W. Zandbergen and J.E. Evetts, *J. Mater. Res.*, to be published.
7. "Irreversibility Properties of Coated Conductors Deposited by LPE on Single Crystalline Substrates"  
A. Vostner, S. Tönies, H.W. Webber, **Y.S. Cheng**, A. Kuršumović, J.E. Evetts, S.H. Mennema and H.W. Zandbergen, *J. Appl. Phys.*, to be published.
8. Some of the results from this work will appear in the chapter of "Superconductivity and Superconductors" by B.A. Glowacki, as part of the *Kirk-Othmer Encyclopedia of Chemical Technology* (John Wiley & Sons, New York), to be published.

## Conference Presentations

1. *Inst. Phys. Superconductivity Group Annual Conf.*, 31<sup>st</sup> March 1999, Birmingham, UK.  
A. Kuršumović, **Y.S. Cheng**, A.P. Bramley, E.A. Robinson, B.A. Glowacki and J.E. Evetts.
2. *4<sup>th</sup> European Conference on Applied Superconductivity (EUCAS)*, 14-17 September 1999, Sitges, Barcelona, Spain.
  - i. A. Kuršumović, **Y.S. Cheng**, A.P. Bramley, B.A. Glowacki and J.E. Evetts.
  - ii. **B. Zeimetz**, B.A. Glowacki, **Y.S. Cheng**, A. Kuršumović, E. Mendoza, X. Obradors, S.X. Dou, J.E. Evetts and T. Puig.
3. *Inst. Phys. Superconductivity Group Annual Conf.*, 12 April 2000, Birmingham, UK.  
**Y.S. Cheng**, A. Kuršumović, B.P. Zeimetz, B.A. Glowacki, A. Vostner, H.W. Weber and J.E. Evetts.
4. *Workshop on High Current Conductors*, 25 October 2000, London, UK.  
**A. Kuršumović**, R.I. Tomov, **Y.S. Cheng**, Z.H. Barber, B.A. Glowacki and J.E. Evetts.
5. *Inst. Phys. Superconductivity Group Annual Conf.*, 4 April 2001, Birmingham, UK.  
**Y.S. Cheng**, A. Kuršumović, B.A. Glowacki, X. Qi, J.L. MacManus-Driscoll and J.E. Evetts.
6. *10<sup>th</sup> International Workshop on Critical Current (IWCC)*, 4-7 June 2001, Göttingen, Germany.  
**A. Vostner**, Y. Sun, S. Tönies, H.W. Weber, **Y.S. Cheng**, A. Kuršumović and J.E. Evetts.
7. *5<sup>th</sup> ISTECH-MRS International Workshop on Superconductivity*, 24-27 June 2001, Honolulu HI, USA.  
**Y.S. Cheng**, A. Kuršumović, R.I. Tomov, B.A. Glowacki, A. Vostner, H.W. Weber, A. Tuissi, E. Villa and J.E. Evetts.
8. *Inst. Phys. Superconductivity Group Annual Conf.*, 10 January 2002, Cambridge, UK.  
**A. Kuršumović**, **Y.S. Cheng**, R.I. Tomov, B.A. Glowacki and J.E. Evetts,
9. *Materials Congress*, 9-11 April 2002, London, UK.  
**A. Kuršumović**, **Y.S. Cheng**, R.I. Tomov, B.A. Glowacki and J.E. Evetts.
10. *104<sup>th</sup> Annual Meeting of the American Ceramic Society*, 28 April - 1<sup>st</sup> May 2002, St. Louis MO, USA.  
**A. Kuršumović**, **Y.S. Cheng**, R.I. Tomov, B.A. Glowacki and J.E. Evetts.

<b>Chapter X</b>	<b>Conclusions and Future Outlook</b>	<b>167</b>
10.1	Conclusions	167
10.2	Future Outlook	169
	References	170
	<b>Appendix: Flux Calculation</b>	<b>171</b>
	<b>List of Publications and Conference Presentations</b>	<b>173</b>